北京大学

博士研究生学位论文

题目：通过同电荷 WW 散射和 Wγ 联合产生精确检验标准模型并搜寻超出标准模型的新物理

姓　　名：肖杰

学　　号：1701110100

院　　系：物理学院

专　　业：粒子物理与原子核物理

研究方向：高能物理实验

导　　师：李强 长聘副教授

PAGANONI Marco 教授

GOVONI Pietro 副教授

二〇二二 年 六 月

SCUOLA DI DOTTORATO
UNIVERSITÀ DEGLI STUDI DI MILANO-BICOCCA

Dipartimento di / Department of

FISICA "Giuseppe Occhialini"

Dottorato di Ricerca in / PhD program FISICA e ASTRONOMIA Ciclo / Cycle XXXV

Curriculum: FISICA SUBNUCLEARE

Precise testing of the Standard Model and search for new physics beyond the Standard Model through same-sign WW scattering and Wγ production

Cognome / Surname XIAO Nome / Name JIE

Matricola / Registration number 863938

Tutore / Tutor: Prof. PIETRO GOVONI

Cotutore / Co-tutor: Dr. ANDREA MASSIRONI

Supervisor: Prof. MARCO PAGANONI

Coordinatore / Coordinator: Prof. MARTA CALVI

ANNO ACCADEMICO / ACADEMIC YEAR 2021/2022

版权声明

摘要

2012 年，基于大型强子对撞机 (LHC) 在 2011-2012 年的质子-质子对撞数据，超环面仪器（ATLAS）和紧凑缪子螺线管（CMS）实验同时发现了希格斯 (Higgs) 玻色子。作为标准模型（SM）的最后一块拼图，希格斯 (Higgs) 玻色子的发现，标志着粒子物理实验进入了一个新的时代。为了更加精确地检验标准模型以及寻找超出标准模型的新物理，一方面，人们利用超出标准模型的理论或者模型无关的有效场论（EFT）方法直接或间接地搜寻标准模型之外的新物理；另一方面，人们对标准模型允许的过程进行高精度测量，或者测量标准模型预测的稀有过程。同时，随着 LHC 第二阶段运行的结束，其上的 CMS 实验，在 2016 至 2018 年间，收集了大量质心系对撞能量为 13 TeV 的质子-质子对撞数据，对应的积分亮度约为 137 fb^{-1}。基于这些数据，人们开展进行了大量物理分析工作。因为多玻色子过程蕴藏着丰富的物理目标，其中很多工作都围绕着多玻色子过程进行。

在 LHC 上的实验中，多玻色子过程通常是指包含两个及以上电弱矢量玻色子（$\mathrm{W}^{\pm}$，Z，γ）产生的反应过程，这允许在电弱（EW）和量子色动力学（QCD）的理论框架下测试标准模型，研究标准模型粒子的特性，并搜寻超出标准模型（BSM）的新物理现象。多玻色过程可以精确检验电弱对称性自发破缺（EWSB）机制。同时，多玻色过程包含三规范玻色子耦合（TGC）或四规范玻色子耦合（QGC）的相互作用顶点，因此也可以研究这些相互作用耦合常数是否符合标准模型预测。历史上，许多实验已经对多玻色子过程做了大量研究。在 LHC 之前，多玻色子过程的研究以玻色子对产生（即反应过程包含两个玻色子）为主。比如大型正负电子对撞机（LEP）实验研究了 WW 和 WZ 玻色子对产生与质心系对撞能量的关系。这些实验发现三规范玻色子作用顶点是限制截面随能量增长的关键，这有力地证实了标准模型的正确性。LEP 实验首次对反常三规范玻色子耦合（aTGCs）设立了限制，这些限制在 LHC 的出现之前一直是最严格的。在粒子加速器 Tevatron 上的探测器实验 CDF 和 D0，也对规范玻色子对产生进行了测量，并将测量过程扩展到 WW、WZ、ZZ、Wγ、Zγ 和 $\gamma\gamma$ 的产生。在更大质心能量下，这些过程可以用来进一步检验标准模型。

现在，已经有一批分析利用 LHC 上的 ATLAS 和 CMS 实验所收集的数据研究了多玻色子过程。随着 LHC 质心对撞能量的提高和相关过程产生截面的大幅增加，对三规范玻色子和四规范玻色子作用顶点的能量已被提高到 TeV 能级。随着大型强子对撞机的能量和积分亮度的继续增加，更多的精确测量正在逐步展开。LHC 上质子-质子对撞的取数主要分为两个阶段，2011 年和 2012 年分别进行质心系对撞能量为 7 和 8 TeV 的

对撞取数，一般称为 Run-1 阶段，也就是利用这批数据，首次发现了 Higgs 粒子。2016 年至 2018 的对撞取数，一般称为 Run-2 阶段。基于 Run-1 或 Run-2 的数据，所有玻色子对产生的反应道，即 WW、WZ、ZZ、Wγ、Zγ 和 $\gamma\gamma$ 都被进一步研究。对于反常三规范玻色子耦合的限制现在已经超过了先前 LEP 和 Tevatron 的结果。同时，利用 Run-1 与 Run-2 的数据，对多玻色子过程的研究拓展到了三规范玻色子联合产生，首次探索了 W$\gamma\gamma$、Z$\gamma\gamma$ 和 VVV（V 可以是 W 或者 Z）的反应道，这类过程可以限制反常四规范玻色子耦合（aQGCs）。同时，还可以通过矢量玻色子散射（VBS）过程对 aQGCs 做出限制。VBS 是指两个由对撞部分子夸克辐射而来的规范玻色子进行的散射，通常在探测器上会有两个大张角并具备很大不变质量的喷注（jet）。目前，ATLAS 和 CMS 实验对 $\mathrm{W^{\pm}W^{\pm}}jj$、$\mathrm{W^{\pm}W^{\mp}}jj$、$\mathrm{W}\gamma jj$、$\mathrm{Z}\gamma jj$、$\mathrm{WZ}jj$ 和 $\mathrm{ZZ}jj$ 等过程（其中符号 j 表示喷注）进行了研究，也对相应的的 aQGC 进行了限制。

本文的其中一个分析会报道在 13 TeV 质心系对撞能量下，对 Wγ 过程的首次精确测量。对 $\mathrm{pp} \rightarrow \mathrm{W}\gamma$ 截面的精确测量可以探测 WWγ 三规范玻色子耦合（TGC）顶点是否符合标准模型预测。同时该过程产生截面较大，是其他分析，如 $\mathrm{W}\gamma jj$ 的主要本底，精确测量该过程，能够提高其他分析的测量精度。精确测量 $\mathrm{pp} \rightarrow \mathrm{W}\gamma$ 过程存在诸多困难，该分析通过高精度模拟，数据驱动本底估计等方法，提高了观测精度。该分析考虑 W 玻色子衰变到轻子（电子或缪子），因此末态粒子包含一个满足条件的轻子，一个较高能量的光子以及中微子。其中，在 CMS 上，中微子无法被探测，一般通过测量丢失横动量，来反映中微子的贡献。为了精确模拟信号过程，该分析使用 MadGraph5_*a*mc@nlo 和 powheg 这两个先进的蒙特卡洛（Monte Carlo）产生子软件，在次领头阶精度（NLO）水平，模拟了该过程，为精确测量奠定了基础。

此外，本底估计是该分析的一大难点。对于瞬发光子和轻子，即在短时间或短距离下立即衰变产生的光子和轻子。产生子模拟软件大都能给出精确预测，诸如 Zγ，$\mathrm{t\bar{t}}\gamma$，VVγ（其中 V 为 W 或 Z 玻色子）等本底过程，都是通过蒙特卡洛模拟进行估计。该分析还存在不可忽略的非瞬发轻子与非瞬发光子本底，这类本底可能是来自于探测器的误鉴别，或者喷注中产生的轻子或光子。这部分本底过程，难以通过蒙特卡洛方法进行估计，因此采用数据驱动的估计方法。首先对于非瞬发轻子本底，通过在双喷注控制区间，根据轻子赝快度（η）和横动量（p_{T}）的所在区间，测量得到的高品质轻子与较低品质轻子之间的比值，并以此得到信号测量区间非瞬发轻子本底贡献到瞬发轻子的转换因子，从而通过非瞬发轻子及对应转换因子，得到其在信号测量区间的贡献。对于非瞬发光子，首先定义 W+jet 控制区间，通过模版拟合的方法，即对光子在电磁量能器上的簇射相关变量的拟合，确定非瞬发的较低品质光子所占的比例，从而对信号区间的该类本底进行估计。其中，对同时包含非瞬发轻子和光子的本底，该分析进行了单独估计，并且会在单独的非瞬发轻子和光子本底中扣除，以避免重复计算。最后，电子被鉴别为光子的本底，在电子道测量中非常重要。造成这类本底的原因是电子径迹未能与电磁量能器簇射正确匹配，电子因此被误鉴别为光子。$\mathrm{Z} \rightarrow ee$ 过程是这一本底的主要来源，因此轻子与光子不变质量（$m_{\ell\gamma}$）在 Z 共振峰附近的事例会急剧增加。该分析通过蒙特卡洛模拟获取 $\mathrm{Z} \rightarrow ee$ 过程产生的 $m_{\ell\gamma}$ 形状（也称为模版），通过一个浮动的比例系数，来调整该过程的贡献，并在最后同实验数据的 $m_{\ell\gamma}$ 分布进行拟

合时，确定该系数，从而准确估计该过程的贡献。

该分析精确测量了 Wγ 过程的基准区截面。为了测量基准区截面，需要在信号区间选择条件的基础上，定义基准区选择条件。基准区选择条件要求模拟信号在产生子水平有一个满足条件的光子和轻子，未满足条件的信号样本事例则视为本底。在通过 $m_{\ell\gamma}$ 分布进行拟合时，基准区内信号事例通过一个信号强度系数进行浮动，而基准区外信号事例则遵循蒙特卡洛模拟给出的截面。最终通过拟合实验数据得到的信号强度，推导出实际测量的基准区截面。最终测量的基准区截面为 $\sigma = 15.58 \pm 0.05(\text{stat}) \pm 0.73(\text{syst}) \pm 0.15(\text{theo})\,\text{pb} = 15.58 \pm 0.75\,\text{pb}$，测量结果与产生子 MadGraph5_aMC@NLO 预测截面 $\sigma = 15.4 \pm 1.2(\text{scale}) \pm 0.1(\text{PDF})\,\text{pb}$ 一致，但低于另一产生子 POWHEG 的预测值 $\sigma = 22.4 \pm 3.2(\text{scale}) \pm 0.1(\text{PDF})\,\text{pb}$，为校验产生子软件提供了重要参考。

除了对标准模型的精确测量，本论文的另一个工作是对标准模型稀有过程的测量。该工作在世界上首次测量了同电荷 WW 玻色子极化散射过程。首先，同电荷 WW 散射过程是首个发现的 VBS 过程。但是对 VBS 过程的总截面测量只是研究此类过程的开始。对于大质量的矢量玻色子，其螺旋度可分为横向极化或纵向极化。假设没有 Higgs 玻色子存在，纵向极化的矢量玻色子散射截面是发散的，这将破坏幺正性。Higgs 机制的存在可以保证幺正性不被破坏，同时也预测了在 1.2 TeV 下，可能会存在 Higgs 粒子。现在实验已经发现了质量约为 125 GeV 的 Higgs 玻色子，但这不代表研究纵向极化的矢量玻色子散射没有意义。相反，纵向极化的矢量玻色子散射能够深入研究 EWSB 机制，探索是否存在额外的 Higgs 玻色子，以及 Higgs 玻色子与矢量玻色子的耦合常数是否符合标准模型。因此，研究极化的矢量玻色子散射具有非常重要的意义。

该分析的关键是如何模拟信号样本，产生子软件 MadGraph5_aMC@NLO 从 2.7.0 版本开始，支持相应的语法规则来产生某一过程的不同极化态分量。对于同电荷 WW 玻色子极化散射过程，实际上有三种成分：两个玻色子都为纵向极化（$\mathrm{W}^\pm_\mathrm{L}\mathrm{W}^\pm_\mathrm{L}$）；一个玻色子纵向极化，另一个玻色子横向极化（$\mathrm{W}^\pm_\mathrm{L}\mathrm{W}^\pm_\mathrm{T}$）；以及两个玻色子都是横向极化 ($\mathrm{W}^\pm_\mathrm{T}\mathrm{W}^\pm_\mathrm{T}$)。同时，螺旋度本征态的定义与所选取的参考系有关。在实验分析中，一般选择实验室参考系，在这种情况下，纵向极化分量 $\mathrm{W}^\pm_\mathrm{L}\mathrm{W}^\pm_\mathrm{L}$ 占比约为 7%。而相关的理论唯象研究中，一般选取 $\mathrm{W}^\pm\mathrm{W}^\pm$ 质心系。考虑 VBS 散射顶点，$\mathrm{W}^\pm\mathrm{W}^\pm$ 质心系是很自然的选择。同时，模拟发现在 $\mathrm{W}^\pm\mathrm{W}^\pm$ 质心系中，$\mathrm{W}^\pm_\mathrm{L}\mathrm{W}^\pm_\mathrm{L}$ 分量在总的 $\mathrm{W}^\pm\mathrm{W}^\pm jj$ 过程中占比约为 11%，可以提升测量该分量的显著度。该分析同时考虑了实验室参考系和 $\mathrm{W}^\pm\mathrm{W}^\pm$ 质心系，该过程的末态粒子包含有两个同电荷的满足鉴别条件的孤立轻子 (电子或缪子)，丢失横动量，以及两个具有较大张角的和较大不变质量的喷注。以上信号模拟精度均为领头阶（LO），为提高精度，作者对模拟信号进行了 NLO 修正。NLO 修正基于理论计算，作为参考的理论计算对同电荷 WW 散射整体过程考虑了 NLO 的 QCD 和 EW 修正。由于极化过程的 NLO EW 效应在含有 $\mathrm{W}^\pm_\mathrm{L}$ 时并不显著，因此，对于 $\mathrm{W}^\pm_\mathrm{T}\mathrm{W}^\pm_\mathrm{T}$ 的 NLO 修正，同时考虑了 QCD 和 EW 效应，而对于 $\mathrm{W}^\pm_\mathrm{L}\mathrm{W}^\pm_\mathrm{L}$ 与 $\mathrm{W}^\pm_\mathrm{L}\mathrm{W}^\pm_\mathrm{T}$ 分量，仅考虑 NLO QCD 修正。

该分析以非极化的 $\mathrm{W}^\pm\mathrm{W}^\pm jj$ 测量为基础，本底估计方法相同，信号区间内一大主要本底是非瞬发轻子本底，该本底通过数据驱动估计得到，其余本底过程都是基于产生子模拟得到。由于极化分量和总过程的运动学变量极其相似，进一步设置选择条件来

区分各极化分量，会降低事例筛选效率，导致结果的不稳定性。当然，通过产生子水平的对比，可以发现在诸多运动学变量中，如双喷注极角差（$\Delta\phi_{\mathrm{jj}}$）、双轻子极角差（$\Delta\phi_{\ell\ell}$）等，各极化分量都表现出了一定的差异性。所以，该分析运用了决策树模型（BDT）和深度神经网络（DNN），来提高信号和本底区分能力。以测量 $\mathrm{W^{\pm}W^{\pm}}$ 质心系中的 $\mathrm{W_L^{\pm}W_L^{\pm}}$ 分量为例，过程中训练了两个 DNN 模型，其中一个模型用来区分 $\mathrm{W_L^{\pm}W_L^{\pm}}$ 分量和其他极化分量；另一个 DNN 用来区分同电荷 WW 散射总过程和非 VBS 本底（主要是非瞬发轻子）。最后，通过同时拟合信号区间，两个 DNN 构造的二维分布，以及控制区间的运动学变量分布，如双喷注不变质量（m_{jj}）谱，得到 $\mathrm{W_L^{\pm}W_L^{\pm}}$ 的信号强度系数，设立截面上限。同时，该分析也依次训练新模型，对其他极化分量进行研究，给出显著度或者测量截面。其中包括在 $\mathrm{W^{\pm}W^{\pm}}$ 质心参考系下，设立了同电荷 WW 散射纵向极化分量产生截面在 95% 置信度的观测（预期）上限 1.17(0.88) fb，以及给出了单纵向 W 玻色子散射分量的观测（预期）显著度达 2.3（3.1）个标准偏差。同时也对实验室系下的对应过程，进行了类似研究。

同电荷 WW 玻色子散射，除了进行标准模型稀有过程的研究，还可以用来搜寻超出标准模型的新物理现象。本论文也展示了通过同电荷 WW 玻色子散射对重马约拉纳（Majorana）中微子的搜寻。中微子振荡实验表明中微子质量是非零的，标准模型并不能解释中微子质量的问题。这是目前实验上发现的明确超出标准模型范畴的现象。揭开中微子微小质量和大混合角的谜团因此成为当今粒子物理学中最紧迫的问题之一。为了解释中微子质量来源，一个可能的方法是对中微子引入狄拉克（Dirac）质量。然而，这将引入右手中微子，由于右手中微子从来没有被发现，所以人们会寻求另一种机制，即所谓的跷跷板模型（Seesaw model）。跷跷板模型是一类模型的统称，这类模型通过假设各种与标准模型轻子以及 Higgs 玻色子耦合的新粒子来产生中微子质量。这些新粒子可以是带电的或惰性的费米子、具有奇异量子数的标量粒子或者是具有新对称性的规范玻色子。根据引入新粒子的方案不同，跷跷板模型可以被分为第一类、第二类、第三类跷跷板模型。这些新粒子可能会导致轻子数破缺和/或带电轻子味破缺。标准模型中微子质量可以表示为 $m_\nu \sim \frac{C\mathrm{v}^2}{\Lambda}$，其中 v 是真空期望值（vacuum expectation value），约为 246 GeV，C 是无量纲耦合常数，Λ 是和新粒子相关的质量尺度。尽管有这些可行的解决方案，但仍缺乏来自实验和理论的明确指导。因此，有必要在高能物理实验中广泛地对这类模型进行测试。

本论文中的分析通过第一类跷跷板模型，引入一个重马约拉纳中微子，该马约拉纳中微子质量越大，则对应的中微子质量越小。在 CMS 实验中，对于重马约拉纳中微子，已经有多个分析对上百 GeV 至 1 TeV 的质量区间进行了搜寻。这些分析主要通过正反夸克对湮灭或者 $\mathrm{W}\gamma$ 熔合产生重马约拉纳中微子，然后对不同质量的重马约拉纳中微子与标准模型轻子的混合矩阵元（mixing element）相关参数 $|V_{\ell N}|^2$ 作出限制。其实，考虑矢量玻色子散射过程，LHC 可以被视为电弱玻色子对撞机。通过非共振重马约拉纳中微子让两个 $\mathrm{W^{\pm}}$ 熔合，亦可对 $|V_{\ell N}|^2$ 进行限制。本论文的分析在同电荷缪子对衰变道中进行的。对应的信号特征，大体与同电荷 WW 散射过程类似，只是由于末态不包含中微子从而导致丢失横动量较小。模拟研究也发现，因为信号过程末态不包含中微子，两个末态同电荷缪子更倾向于背靠背产生，所以最终导致两个缪子极角之差比较大。

该分析的整体分析策略也借鉴了对极化同电荷 WW 散射过程的研究。信号模拟通过第一类的跷跷板模型，选取近 20 个不同的马约拉纳中微子质量点（从 50 GeV 到 25 TeV），使用 MadGraph5_aMC@NLO 进行了高精度模拟，精度达到 NLO 水平。本底估计中，非瞬发轻子也是通过数据驱动的方法进行估计。在该分析中，信号区间最大的本底来自于标准模型下的 $\mathrm{W}^{\pm}\mathrm{W}^{\pm}$ 散射过程。同时，该分析有着与极化同电荷 WW 散射分析类似的信号区间和控制区间。经过研究，该分析也对部分选择条件进行了优化，作者发现更大的 m_{jj} 阈值，可以提高实验对该过程的敏感度。因而，m_{jj} 在该分析中选择了更大的阈值。同时，考虑到末态轻子更倾向于背靠背产生，对信号区间，进一步分出正交的高 $\Delta\phi_{\ell\ell}$ 区域和低 $\Delta\phi_{\ell\ell}$ 区域，进一步提升了区分信号和本底的能力。通过同时拟合信号区间和控制区间，设立了对 $|V_{\ell N}|^2$ 的限制，对比以往对重马约拉纳中微子的研究，该分析大大扩展了探测的质量范围, 直至 20 余 TeV，同时在重马约拉纳中微子质量大于 650 GeV 时，给出了最好的限制。

由于没有明确的理论指导，不同于给定具体的理论模型进行新物理搜寻，与模型无关的 EFT 方法被提出并且受到了越来越多的关注。理论上，标准模型的拉格朗日量包含二维和四维质量算子。在 EFT 框架下，通过设定一个很大的能量尺度 Λ，人们可以利用高维算子对标准模型拉格朗日量进行扩展，这些高维算子带来的效应同时被能标 Λ 所抑制，可以表示为 $\mathcal{L}_{\mathrm{SM}} = \mathcal{L}_{\mathrm{SM}}^{(4)} + \frac{1}{\Lambda}\sum_k C_k^{(5)} Q_k^{(5)} + \frac{1}{\Lambda^2}\sum_k C_k^{(6)} Q_k^{(6)} + \mathcal{O}\left(\frac{1}{\Lambda^3}\right)$，其中 $Q_k^{(n)}$ 表示 n 维算子，$C_k^{(n)}$ 为其对应的耦合常数。标准模型常常被视为 EFT 方法在低能量情况下的近似，因此，EFT 方法能够捕捉任何超出标准模型的新物理现象。

在 EFT 中，只有一个满足规范变换不变的五维算子，也被称为温伯格（Weinberg）算子。温伯格算子也可以解释马约拉纳中微子的质量，它会导致标准模型中微子相互作用顶点。在 $\mathrm{W}^{\pm}\mathrm{W}^{\pm}$ 散射的双缪子衰变道中，W 玻色子衰变产生的中微子会因为相互反应，发生湮灭，所以末态只包含两个大张角、高动量的喷注以及两个同电荷的缪子。中微子湮灭的作用顶点，在目前产生子软件中，难以模拟。如果将该作用顶点简化为等效的马约拉纳中微子，该过程就可以借助第一类的跷跷板模型进行近似模拟。经过检验，在 EFT 能量尺度 Λ 很大时，该近似是有效的。所以在通过同电荷 WW 散射研究中微子质量起源的工作中，作者也同时考虑了利用五维算子诠释中微子的质量。同样，这部分工作使用 MadGraph5_aMC@NLO 产生了 NLO 精度的信号样本。与重马约拉纳中微子不同的是，$\Delta\phi_{\ell\ell}$ 对于该信号过程没有很好的区分度，考虑到信号末态没有中微子产生，所以信号区间，通过丢失横动量 $p_{\mathrm{T}}^{\mathrm{miss}}$ 划分为低 $p_{\mathrm{T}}^{\mathrm{miss}}$ 和高 $p_{\mathrm{T}}^{\mathrm{miss}}$ 两个区间。通过同时结合控制区间进行拟合，最后得到了等效马约拉纳中微子质量上限 $|m_{\mu\mu}|$ 的观测（预期）值为 10.8 (12.8) GeV。

事实上，EFT 的六维算子在多玻色子过程中更为普遍。在对 $\mathrm{W}\gamma$ 过程的分析中，除了精确测量其基准区截面，还可以通过 EFT 方法研究三规范玻色子作用顶点 $\mathrm{WW}\gamma$ 的反常耦合。一般来说，如果超出标准模型的反常 $\mathrm{WW}\gamma$ 耦合存在，$\mathrm{W}\gamma$ 的产生截面会增加。这种增加影响到相空间的大部分高能区域，特别是光子高横动量（p_{T}）的区间。虽然六维算子数目众多，但考虑 $\mathrm{WW}\gamma$ 的反常耦合，只需要涉及到五个独立的六维算子。该信号过程的模拟，首先选取特定的 EFT 模型，基于该模型，扫描五个独立六维算子对应的耦合系数，即 c_{WWW}、c_W、c_B、$c_{W\tilde{W}W}$、$c_{\tilde{W}}$，最后产生一个重新加权的 $\mathrm{W}\gamma$ 样本，

该信号样本的每个事例具有多个权重，每个权重对应不同的模型参数设置。该模拟过程依然使用 MadGraph5_aMC@NLO 进行 NLO 精度的模拟。首先，对系数 c_{WWW} 设为 25 的 Wγ 样本进行未加权（权重 =1 或-1）产生。然后计算出每个事例的权重，并将权重存储起来。这些权重，可以将未加权事例转换到其对应参数的相空间去。通过对光子 p_{T} 的极大似然拟合，分析给出了反常三规范玻色子作用顶点相关的六维算子的系数在 95% 置信度下的限制，特别是对 c_{WWW} 参数给出了世界最好限制，从而为间接寻找标准模型之外的新物理提供了重要输入信息。

上述物理分析工作紧密相关，既有对双玻色子产生截面的精细测量，也有对极化矢量玻色子散射这样的稀有物理过程的首次探测。既有对 TeV 乃至 10 TeV 质量区间的重中微子效应的直接探测，也有通过五维温伯格算子和六维质量算子对新物理的间接探测。这些工作为后续进一步测量矢量玻色子极化散射、全局性地探索高维度有效理论算子奠定了基础。作者在这批工作中发挥了重要作用，如给予分析的最终审核 (Approval) 报告、担当合作组内分析负责人等。此外，作者还在 CMS 大型合作组的产生子软件测试及检验等方面做出了服务性贡献，担任了产生子检验工作组三级召集人以及标准模型分析组的机器学习联络人。

关键词：多玻色子过程，纵向极化，马约拉纳中微子，有效场论, 温伯格算子，六维算子

ABSTRACT

The Higgs boson discovery in 2012, the final piece of the Standard Model (SM) puzzle, marked a new era in particle physics. At the Large Hadron Collider (LHC), it is a hot research topic at the high–energy frontier of high–energy physics to precisely test the SM by measuring processes such as multibosons or exploring new physical phenomena beyond the Standard Model (BSM). The compact muon solenoid (CMS) detector at the LHC has collected a data sample in proton–proton collisions with an integrated luminosity of about 137 fb^{-1} at a center-of-mass energy of 13 TeV. The author has carried out the following three analyses around multi–boson processes based on the recorded data.

The thesis reports the first measurement of the associated production of a W boson and a photon at $\sqrt{s} = 13\,\mathrm{TeV}$. Both the electron and the muon decay modes of the W boson are used to extract the cross section by a maximum likelihood fit to the lepton–photon mass distribution. The measured cross section in a defined fiducial region is $\sigma = 15.58 \pm 0.75\,\mathrm{pb}$. The measured cross section is compared with theoretical expectations at next-to-leading order in quantum chromodynamics. This study further searches for new physics by reporting the 95% confidence level limits on the coefficients of the dimension–six operators relevant to anomalous triple gauge couplings with the effective field theory (EFT) approach. In particular gives a world's best limit on the c_{WWW} parameter, thus providing important input information for the indirect search for new physics beyond the SM.

The second work studied the polarized same-sign W boson pairs for the first time in the world. The longitudinally polarized vector boson scattering can verify if the Higgs boson preserves the unitary and be used to deeply understand the electroweak symmetry breaking (EWSB). The final state of polarized same-sign WW scattering consists of exactly two well–identified isolated leptons, electrons or muons, with the same charge, moderate missing transverse momentum, and two jets with a large rapidity separation as well as a large dijet mass. With the helicity eigenstates defined in the diboson center-of-mass reference frame, the observed (expected) 95% CL upper limit on the production cross section for longitudinally polarized same-sign WW scattering is set to 1.17 (0.88) fb. The electroweak induced same-sign WW boson scattering with at least one of the W bosons longitudinally polarized is measured at the same time with an observed (expected) significance of 2.3 (3.1) standard deviations.

Based on the same-sign WW scattering, the thesis also probes heavy Majorana neutrinos at the TeV energy scale and the dimension-five Weinberg operator for the first time at a collider. Both are important benchmark theories for solving the mystery of the origin of neutrino mass. The search is performed in the same–charge dimuon channel, with similar final state topology as the polarized same-sign WW scattering. The results are found to be consistent with the predictions from the SM. For heavy Majorana neutrinos, constraints on the squared muon-heavy neutrino mixing element are derived at 95% confidence level in the mass range 50 GeV–25 TeV; for masses above 650 GeV these are the most stringent constraints from searches at the LHC to date. A first test of the Weinberg operator at colliders is also provided. The observed (expected) upper limit at 95% confidence level on the effective $\mu\mu$ Majorana mass is 10.8 (12.8) GeV.

The above analyses are closely related to precise measurements of the diboson production cross section and the first detection of rare physical processes such as the polarized vector boson scattering. There are direct detections of heavy Majorana neutrino effects in the TeV and even 10 TeV mass scale and indirect searches of new physics via the dimension-five Weinberg operator and the dimension-six operators in the EFT. These works lay the foundation for further subsequent polarized vector boson scattering measurements and global exploration of high dimension EFT operators. The author played an essential role in these works, giving the final approval report of the analysis and taking the lead role in analyzing the collaborative group. In addition, the author has played an essential role in these works, such as giving approval reports for the analyses and acting as the analysis contact person. In addition, the author has made service contributions to the CMS collaboration on generators software testing and validation, serving as the level 3 convener of the generator validation group and as the machine learning contact person in the standard model analysis group.

KEY WORDS: Multiboson processes, Longitudinal polarization, Majorana neutrino, EFT, Weinberg operator, Dimension–six operator

Contents

Chapter 1

Introduction

In 2012, the critical and the final building block in the Standard Model (SM), the Higgs boson, was observed[1-2], which provides an explanation that the fermions and gauge bosons acquire mass via the Brout–Englert–Higgs mechanism (BEH mechanism)[3-5]. The SM became the most successful theory of particle physics and ushered in a new era of particle science. Since then, more precision testing on the SM are carried out exploiting the data collected in the Run-2 phase[6] at the Large Hadron Collider (LHC)[7].

After the discovery of the Higgs boson, the first vector boson scattering (VBS) process, the electroweak (EW) production of a same-sign W boson pair in association with two jets, was observed[8-9]. This is another milestone of the Standard Model. Not only because it is a rare process that can again prove the correctness of the standard model, but also because it can test electroweak symmetry breaking (EWSB) at high energy scale. In fact, the Higgs boson plays an important role in the VBS processes. If we go back to the construction of the LHC, there are two key questions to be answered, namely, is there a Higgs boson? If the Higgs boson exists, what is its mass? In fact, without Higgs boson, the scattering of longitudinally polarized gauge bosons will not preserve perturbative unitarity. Introducing a Higgs boson with mass below 1 TeV ensures the unitarity of the longitudinally polarized scattering of gauge bosons[10-11]. It was this strong constraint that motivated the construction of the LHC collider at the TeV energy scale. Studying the longitudinally polarized gauge boson scattering is a further precise measurement of the SM. Although the Higgs boson has been found so far, this can also address whether there are additional Higgs bosons that participated in EWSB and whether the Higgs boson couples to vector bosons as the SM predict[12-13]. The first measurement of the longitudinally polarized VBS process, the EW-induced polarized same-sign WW scattering[14], was performed with the data collected in Run-2[15-17] with the Compact Muon Solenoid (CMS) detector[18] in proton-proton collisions at $\sqrt{s} = 13$ TeV, which is one of the topics in this thesis.

Despite the great success of the SM, there are still many phenomena that cannot be explained by it. The observation of neutrino oscillations[19-20], which confirms that at least two types of SM neutrinos have a tiny, but nonzero, mass. It definitely goes beyond the SM. In order to solve this problem, the neutrino mass models, collectively referred to as the seesaw models, are realized by assuming various states couple to the SM lepton and Higgs sectors[21]. At present, it is unclear which of these states is more natural. New charged or sterile fermions, new symmetric gauge bosons, and scalar particles with exotic gauge quantum numbers can be considered[22-25]. A number of analyses at the LHC have tested the seesaw models, including searches for dijet resonances[26-27], multi–lepton final states[28-33], and lepton number violation (LNV) processes[29,34-36]. Constrains on the active–sterile neutrino mixing matrix elements $V_{\ell N}$, $\ell \in \{e, \mu\}$, are given in the Ref[29,34] for sterile neutrino masses up to ~ 1 TeV. Since the LHC can probe the VBS processes, based on the type I seesaw model, Ref[37] discussed the upper limits on $|V_{\ell N}|^2$, $\ell = \mu$, for the sterile neutrino masses up to $O(10)$ TeV by introducing a t–channel heavy Majorana neutrino to the same-sign WW scattering. The analysis of dimuon final state for production in this same-sign WW scattering process in CMS is also a part of this thesis.

Although there are many models beyond the SM (BSMs) on the market, including the seesaw models, no additional new states have been observed at the LHC (to date) since the discovery of the Higgs boson. Under such a circumstance, the effective field theory (EFT) approach is getting more and more attention. Given the EFT Lagrangian is an extension of Lagrangian of the SM[38], the EFT approach has adequate ability to capture any physics beyond the SM. In the SM, all operators in the Lagrangian have mass dimension–four. The only gauge-invariant dimension–five operator, known as the Weinberg operator[39], can address the mass origin of the SM neutrinos. The first test of the Weinberg operator at colliders is discussed together with the t–channel heavy Majorana neutrino in same-sign WW scattering in present thesis. Not all the processes are sensitive to the dimension–five operator, more commonly, processes receive the EFT correction to the SM Lagrangian mainly from the dimension–six operators. This thesis includes measurements of the associated production of a W boson and a photon[40], besides giving the first measurement of the Wγ cross section in proton–proton (pp) collisions at $\sqrt{s} = 13$ TeV, constrains on the Wilson coefficients of the relevant dimension–six operators are reported. In fact, there are many dimension–six operators, for the given Wγ production process, only a few operators have an effect to the its featured triple boson coupling WWγ[41-43].

After the introduction, Chapter 2 and Chapter 3 provide an overview of the theoretical framework and the experimental background on the LHC and the CMS detector. Chapter 4 outlines the reconstruction and identification of physics objects. Chapter 5, Chapter 6, and Chapter 7 describe in detail of searching the polarized same-sign WW scattering, probing heavy Majorana neutrinos and the Weinberg operator in $W^{\pm}W^{\pm}$ scattering, and measuring the Wγ using the Run-2 data samples collected by the CMS detector in proton-proton (pp) collisions at a center-of-mass energy of 13 TeV, respectively. Finally, the conclusions are presented in Chapter 8.

Chapter 2

Theoretical Overview

2.1 The Standard Model

The Standard Model (SM)[44-47] is currently the most successful theoretical framework describing elementary particles and their interactions. It is constructed through the language of quantum field theory (QFT). The SM has successfully explained almost all particle physics phenomena and verified them by experiments. One of the keys in the Standard Model is the BEH mechanism, which solves the most crucial problem of the gauge theory in the SM, namely the origin of the mass of the elementary particles. This section introduces the particles and interactions in the SM and explains how the BEH mechanism is implemented.

2.1.1 Elementary Particles

Elementary particles are subatomic particles with no substructure. According to the spin, the particles can be summarized into spin-0 Higgs boson, spin-1/2 fermions, and spin-1 vector bosons, as described in Figure 2.1. Bosons carry integer spin and obey the Bose-Einstein statistics, fermions have half-integer spin and follow the Fermi-Dirac statistics.

Higgs Boson There is only one experimentally observed fundamental scalar boson in the Standard Model known as the Higgs boson (H) with a mass close to 125 GeV and without any charge, color charge, or parity. It is the product of electroweak symmetry breaking (EWSB). Measuring the properties of the Higgs boson is quite crucial for understanding the EWSB. Only massive particles can directly couple with the Higgs boson, and the strength of the coupling is related to the mass of the particle.

Spin-1/2 fermion In the SM, the fundamental fermions are the main components that build the matter in the universe. The fermions contain six quarks, six leptons. These six quarks are further divided into three generations, each consisting of up-type and down-type quarks with charges of +2/3 and -1/3, respectively. The leptons can also be divided into charged leptons

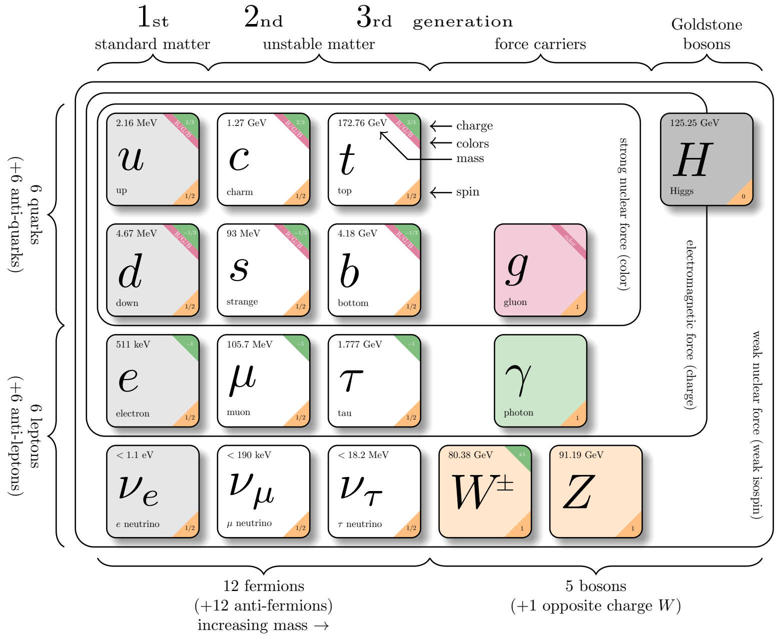

Figure 2.1 The elementary particles in the Standard Model, categorized into fermions, gauge bosons, and Higgs boson, with their mass, charge, and spin. The fundamental forces and the particles involved are described. Taken from Ref[48] with values from Ref[49].

(with a charge of -1) and neutral leptons (named neutrinos). On the other hand, all fermions have their antiparticles, which have opposite charge but the same mass and flavor. Antiquarks also contain anti-color charges. Experimentally, each fermion has a different mass, which violates the global chiral symmetry of fermions, which prohibits large mass fermions. The BEH mechanism could explain this.

Quarks contain three quantum numbers, electric charge, color charge, and flavor, which take part in three interactions, electromagnetic, weak, and strong interactions. The three generations of up-type quark flavors are the up (u) quark, the charm (c) quark, and the top (t) quark, while the down-type quarks are the down (d) quark, the strange quark (s), and the bottom (b) quark. Due to the color confinement in quantum chromodynamics (QCD), particles carrying color charges cannot exist in space alone. Hence, only colorless particles with quark-antiquark pairs and baryons consisting of three quarks with red, green, and blue color charges, which together are called hadrons, can be observed. However, most hadrons are unstable and decay immediately into other particles. Only protons and neutrons are relatively stable. Still, these quarks still allow asymptotic freedom at very short distances in high energies, resulting in protons that can be stably accelerated in the LHC and inelastic scattering.

The electron is a stable particle that dominates electromagnetic interactions in our life. On the other hand, due to the absence of color charge, leptons only incorporate electromagnetic and weak interactions. There are three different flavors of charged leptons, namely electrons

(e^-), muons (μ^-), and taus (τ^-), corresponding to three generations. Muons are heavier than electrons, relatively unstable, and almost decay into electrons. Taus are the heaviest but most unstable leptons, it can decay into electrons and muons, and hadrons. There are also three types of neutral leptons: electron neutrino (ν_e), muon neutrino (ν_μ), and tau neutrino (ν_τ). Since they have no electric charge, neutrinos interact with other particles only through weak interactions, and they pass through matter with almost no interaction. Numerous experiments have observed the phenomenon of neutrino flavor oscillations, i.e., the time variation of neutrino flavor during neutrino propagation. Such observation suggests that neutrinos have a non-zero mass, which the SM cannot explain.

Spin-1 Vector boson Vector bosons are the force carriers of three fundamental interactions in the SM, the photon (γ) of electromagnetic interaction, the massive $W^\pm$ and Z bosons of the weak interaction, and the gluons (g) of the strong interaction. When the fermions interact, they exchange the vector bosons and change their physical quantities. All three interactions obey gauge symmetry. Thus these vector bosons are also called gauge bosons. The gauge symmetry does not allow the existence of massive gauge bosons. The $W^\pm$ and Z bosons explicitly violate the gauge symmetry in the weak interaction, which the BEH mechanism could explain.

2.1.2 Interactions

The Lagrangian formalism ($\mathcal{L}$) is one of the main tools for describing the dynamics of various physical systems and the leading principle for the construction and development of theories of elementary particle interactions is based on QFT. In QFT, particles can be considered as quantized excitations of physical fields in a vacuum state. Propagation and interaction of these particles can be described by the Lagrangian. Based on the principle of action, the Euler-Lagrange Equation 2.1 is derived to describe the system's motion.

$$\frac{\partial \mathcal{L}}{\partial \phi} = \partial_\mu \left(\frac{\partial \mathcal{L}}{\partial \left(\partial_\mu \phi \right)} \right). \tag{2.1}$$

The Lagrangian actually satisfies the principle of relativity, which requires the Lagrangian is invariant under the Lorentz transformation, and in turn, that the fields within the Lagrangian be Lorentz transformed with a specific representation under the Lorentz group. In group language, the Lorentz group is described by a *SO(3, 1)* group. The three SM fundamental forces can be represented as a gauge group

$$SU(3)_c \times SU(2)_L \times U(1)_Y. \tag{2.2}$$

This gauge group consists of strong interactions ($SU(3)_c$) and electroweak (EW) interactions ($SU(2)_L \times U(1)_Y$), where c represents the color charge, L refers to left-handed fields, and Y refers to the weak hypercharge. The Lagrangian of the SM respects the above symmetry is given by

$$\mathcal{L}_{SM} = \mathcal{L}_{EW} + \mathcal{L}_{Higgs} + \mathcal{L}_{Yukawa} + \mathcal{L}_{QCD}. \tag{2.3}$$

These interactions under gauge theory are introduced below through the language of QFT.

2.1.2.1 Electroweak interaction

Electroweak interaction is unified descripes electromagnetic interaction and weak interaction.

The electromagnetic interaction obeys $U(1)$ gauge symmetry and is described by quantum electrodynamics (QED). The fields of Fermions under the $U(1)$ transformation are described as

$$\psi \longrightarrow \psi' = e^{i\mathrm{Qe}\alpha}\psi \sim (1 + iQe\alpha)\psi, \tag{2.4}$$

where Q is the charge of the fermions and e is a real value interpreted as the coupling strength of the electromagnetic force. In general, a Dirac Lagrangian can describe free fermions carrying mass as

$$\mathcal{L}_{\text{free}} = \bar{\psi}\left(i\gamma^{\mu}\partial_{\mu} - m\right)\psi. \tag{2.5}$$

Only one generator corresponds to spin-1 field of photon, A_{μ}, involved in the gauge-invariance Lagrangian form based on Lagrangian 2.5 with a covariant derivative

$$\partial_{\mu}\psi \longrightarrow D_{\mu}\psi = \left(\partial_{\mu} + iQeA_{\mu}\right)\psi, \tag{2.6}$$

with the photon under the $U(1)$ gauge transformation form as

$$A_{\mu} \longrightarrow A'_{\mu} = A_{\mu} + \frac{i}{Qe}\left(\partial_{\mu}U\right)U^{\dagger} \approx A_{\mu} - \partial_{\mu}\alpha. \tag{2.7}$$

Under the $U(1)$ gauge symmetry, an overall Lagrangian of the QED ($\mathcal{L}_{QED}$) with the kinetic term of the photon is given by

$$\mathcal{L}_{QED} = \bar{\psi}\left(i\gamma^{\mu}D_{\mu} - m\right)\psi - \frac{1}{4}F^{\mu\nu}F_{\mu\nu}, \tag{2.8}$$

where $D_{\mu} = \left(\partial_{\mu} + iQeA_{\mu}\right)$ is the covariant derivative and $F_{\mu\nu} = \partial^{\mu}A^{\nu}$ is the field stress tenser of photon.

For weak interaction, it should obey a non-Abelian $SU(2)$ gauge symmetry. Madam Wu's experiment[50] shows that only left-handed fermions take part in weak interaction. Therefore, the weak interaction is described by a $SU(2)_L$ (L shows this only related to the left-handed fermions) gauge-invariance Lagrangian

$$\mathcal{L}_{\text{weak}} = i\bar{\psi}_L\gamma^{\mu}D_{\mu}\psi_L - \frac{1}{4}W^{(a)\mu\nu}W^{(a)}_{\mu\nu}, \tag{2.9}$$

$$D_\mu = \partial_\mu + ig_W W_\mu^a \sigma^a, \tag{2.10}$$

where D_μ is the covariant derivative, g_W is the weak interaction strength, and σ^a represents the Pauli matrices corresponding to three spin-1 fields W_μ^a. The second term is a kinetic term of the W fields with $W_{\mu\nu}^a$ defined by

$$W_{\mu\nu}^a = \partial_\mu W_\nu^a - \partial_\nu W_\mu^a - g_W f_{abc} W_\mu^b W_\nu^c, \tag{2.11}$$

where f_{abc} is the structure constant.

In the SM, quarks (Q) and leptons (L) can be written as the $SU(2)_L$ left-handed doublets as

$$Q = \begin{pmatrix} u_L \\ d_L \end{pmatrix}, \begin{pmatrix} c_L \\ s_L \end{pmatrix}, \begin{pmatrix} t_L \\ b_L \end{pmatrix} \quad L = \begin{pmatrix} \nu_{eL} \\ e_L \end{pmatrix}, \begin{pmatrix} \nu_{\mu L} \\ \mu_L \end{pmatrix}, \begin{pmatrix} \nu_{\tau L} \\ \tau_L \end{pmatrix}. \tag{2.12}$$

The weak isospin quantum number is introduced to each doublet with $I_W^{(3)} = \frac{1}{2}$ for the upper component and $I_W^{(3)} = -\frac{1}{2}$ for the lower component. The real involved gauge bosons are W± and Z in the weak interaction. Then the W± bosons related to the $W^{(1)}$ and $W^{(2)}$ are expressed as

$$W_\mu^\pm = W_\mu^{(1)} \mp iW_\mu^{(2)}. \tag{2.13}$$

Experiments show that the Z boson can couple both left-handed and right-handed particles which violates the properties of the weak interaction. Sheldon Glashow proposed a theory to unified electromagnetic and weak interactions[51], which provides a new gauge symmetry, $U(1)_Y$, replacing the A_μ field with a new gauge field B_μ. $U(1)_Y$ offers a new quantum number weak hypercharge, so that the fermions under the U(1) transformation are defined as

$$\psi \longrightarrow \psi' = e^{ig'\frac{Y}{2}\alpha}\psi \sim \left(1 + ig'\frac{Y}{2}\alpha\right)\psi. \tag{2.14}$$

Finally, the complete electroweak Lagrangian is

$$\mathcal{L}_{EW} = i\bar{\Psi}_L\gamma^\mu D_\mu \Psi_L + i\bar{\psi}_R\gamma^\mu D'_\mu \psi_R - \frac{1}{4}B_{\mu\nu}B^{\mu\nu} - \frac{1}{4}W_{\mu\nu}^{(a)}W^{(a)\mu\nu}, \tag{2.15}$$

$$D_\mu = \partial_\mu + ig'\frac{Y}{2}B_\mu + ig_w W_\mu^a \sigma^a, \tag{2.16}$$

$$D'_\mu = \partial_\mu + ig'\frac{Y}{2}B_\mu. \tag{2.17}$$

In the electroweak model, the photon and Z boson now can be expressed by the linear combinations of the $W_\mu^{(3)}$ and B_μ field as

$$A_\mu = +B_\mu cos\theta_W + W_\mu^{(3)} sin\theta_W, \tag{2.18}$$

$$Z_\mu = -B_\mu sin\theta_W + W_\mu^{(3)} cos\theta_W, \tag{2.19}$$

where θ_W is the weak mixing angle. The relationship also derives

$$Y = 2(Q - I_W^{(3)}), \tag{2.20}$$

$$e = g_W sin\theta_W = g' cos\theta_W. \tag{2.21}$$

In mathematical form, electromagnetic and weak interactions are successfully unified. However, experiments measured massive $W^\pm$ and Z boson, which breaks the gauge theory. Then the BEH mechanism was developed to address this problem.

2.1.2.2 BEH mechanism

A key point of gauge symmetry in particle physics is that the gauge bosons must, in principle, be massless particles. In 1964, spontaneous symmetry breaking was introduced to explain the acquisition of mass by vector bosons[3-5]. Then in 1967, this concept was introduced into the electroweak theory, which theoretically solved the problem of massive gauge bosons. The BEH mechanism predicted a new single scalar boson named the Higgs boson.

Spontaneous symmetry breaking To explain the spontaneous symmetry breaking, consider a general Lagrangian of a complex scalar field satisfying the global U(1) symmetry, with an additional potential $V(\phi) = \mu^2\phi^2 + \lambda\phi^4$, as

$$\mathcal{L} = \left(\partial_\mu \phi\right)^* \left(\partial^\mu \phi\right) - V\left(\phi\right). \tag{2.22}$$

As illustrated in Figure 2.2, when $\mu^2 > 0$, the physical vacuum state is always at $V = 0$. When $\mu^2 < 0$, the potential shape looks similar to a Mexican hat. The vacuum state is no longer located at the origin but inside the red dashed circle with a non-zero vacuum expectation value (v.e.v, or v), defined by $\phi_1 + \phi_2 = -\frac{\mu^2}{\lambda} = \mathrm{v}^2$. The field standing in the original vacuum state is now unstable, and it must fall to one of the new vacuum states (red dashed circle). Once the field begins falling, the global $U(1)$ symmetry is spontaneously broken by the non-zero vacuum expectation value. This concept can be extended to $U(1)$ gauge symmetry, known as the BEH mechanism.

To understand the physics near the vacuum state after spontaneous symmetry breaking, consider the physical vacuum state chosen at $\phi_1 + i\phi_2 = \mathrm{v}$. The excitation of the complex scalar field nearby is like the disturbance of this scalar field, denoted by

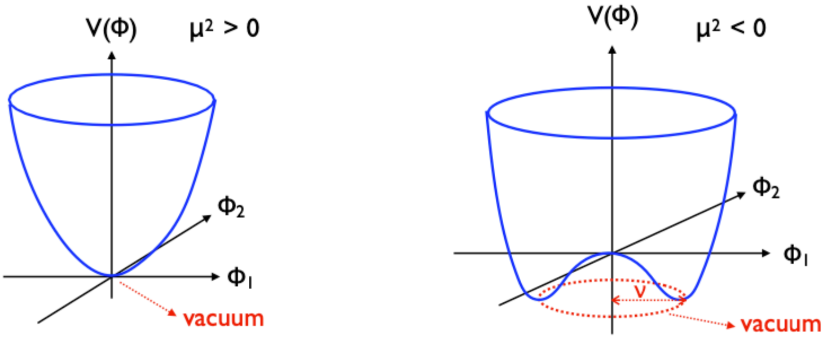

Figure 2.2 Potential ($V(\phi)$) for the complex scalar field for the $\mu^2 > 0$ (left) and $\mu^2 < 0$ (right).

$$\phi(x) = \frac{1}{\sqrt{2}}(\nu + \eta(x) + i\omega(x)). \tag{2.23}$$

A scalar field Lagrangian with $U(1)$ local gauge symmetry can be described by

$$\mathcal{L} = -\frac{1}{4}F_{\mu\nu}F^{\mu\nu} + \left(D_\mu\phi\right)^* (D^\mu\phi) - \mu^2\phi^2 - \lambda\phi^4, \tag{2.24}$$

with D_μ being the covariant derivative given by $D_\mu = \partial_\mu + igB_\mu$ being the field stress tensor by $F_{\mu\nu} = \partial_\mu B_\nu - \partial_\nu B_\mu$.

Then, the Lagrangian of the scalar field with $U(1)$ local gauge symmetry can be expressed by

$$\mathcal{L} = \underbrace{\frac{1}{2}\left(\partial_\mu\eta\right)(\partial^\mu\eta) - \lambda \mathrm{v}^2\eta^2}_{\text{massive } \eta} + \underbrace{\frac{1}{2}\left(\partial_\mu\omega\right)(\partial^\mu\omega)}_{\text{massless } \omega} \underbrace{- \frac{1}{4}F_{\mu\nu}F^{\mu\nu} + \frac{1}{2}g^2\mathrm{v}^2 B_\mu B^\mu}_{\text{massive gauge field}} + g\mathrm{v}B_\mu\partial^\mu\omega + V_{int}, \tag{2.25}$$

in which V_{int} includes three- and four-point interactions of the η, ω and B fields. This Lagrangian consists of a massive scalar field η, a massless scalar field ω referred to as the Goldstone boson, and a massive gauge field B_μ. To eliminate the unphysical interaction term, $g\mathrm{v}B_\mu\partial^\mu\omega$, following equation is considered

$$\frac{1}{2}\left(\partial_\mu\omega\right)(\partial^\mu\omega) + g\mathrm{v}B_\mu\partial^\mu\omega + \frac{1}{2}g^2\mathrm{v}^2 B_\mu B^\mu = \frac{1}{2}g^2\mathrm{v}^2\left[B_\mu + \frac{1}{g\mathrm{v}}\partial_\mu\omega\right]^2, \tag{2.26}$$

in which $\frac{1}{g\mathrm{v}}\partial_\mu\omega$ can be treated as an $U(1)$ gauge transformation on the B_μ field, i.e., the ω is "eaten" by the B_μ field to another B'_μ field which keep the physical prediction. So $\phi(x)$ can be adapted to

$$\phi(x) = \frac{1}{\sqrt{2}}(\nu + \eta(x) + i\omega(x)) \longrightarrow \phi(x)' = \frac{1}{\sqrt{2}}(\nu + h(x)), \tag{2.27}$$

here, $h(x)$ is the Higgs field. Finally, Lagrangian in Equation 2.26 can be rewritten as

$$\begin{aligned}\mathcal{L} = & \underbrace{\frac{1}{2}\left(\partial_\mu h\right)\left(\partial^\mu h\right) - \lambda \mathrm{v}^2 h^2}_{\text{massive } \eta} - \underbrace{\frac{1}{4}F_{\mu\nu}F^{\mu\nu} + \frac{1}{2}g^2\mathrm{v}^2 B_\mu B^\mu}_{\text{massive gauge field}} \\ & + \underbrace{g^2 \mathrm{v} B_\mu B^\mu h + \frac{1}{2}g^2 B_\mu B^\mu h^2}_{h,B \text{ interactions}} - \underbrace{\lambda v h^3 - \frac{1}{4}\lambda h^4}_{h \text{ self-interactions}} .\end{aligned} \tag{2.28}$$

In conclusion, after the spontaneous symmetry breaking, the Goldstone boson arising from the degree of freedom of the broken $U(1)$ symmetry is ”eaten” by the spin-1 gauge boson B_μ. The extra freedom degrees become the longitudinal degrees of freedom of B_μ and give B_μ its mass. However, in this Lagrangian 2.28, the $U(1)$ gauge symmetry is not explicitly violated but hidden. The BEH mechanism also predicts the existence of a new spin-0 particle, the Higgs boson.

BEH mechanism in the Standard Model Experimental observations show that the three massive gauge bosons W± and Z come from the ”broken” $SU(2)_L$ gauge symmetry and a massless photon from the $U(1)_{EM}$ gauge symmetry. That is, in the SM, the EBH mechanism should happen in the electroweak symmetry. To deduce the EWSB, a Higgs field H with an electroweak doublet form is considered, which consists of a charged h^+ and a neutral h^0 field for offering longitudinal degrees of freedom for the $\mathrm{W}^\pm$ and Z bosons.

$$H = \begin{pmatrix} h^+ \\ h^0 \end{pmatrix}. \tag{2.29}$$

The Lagrangian of the Higgs field respecting the electroweak symmetry is written as

$$\mathcal{L}_{Higgs} = -\frac{1}{4}B_{\mu\nu}B^{\mu\nu} - \frac{1}{4}W^{(a)}_{\mu\nu}W^{(a)\mu nu} + \left(D_\mu H\right)^\dagger\left(D^\mu H\right) - \mu^2 H^\dagger H - \lambda\left(H^\dagger H\right)^2, \tag{2.30}$$

in which $\mu^2 H^\dagger H + \lambda\left(H^\dagger H\right)^2$ is the Higgs potential. After spontaneous symmetry breaking, $\mu^2 < 0$, the vacuum states satisfy

$$H^\dagger H = \frac{\mathrm{v}^2}{2} = -\frac{\mu^2}{2\lambda}. \tag{2.31}$$

Consider the vacuum state and H as

$$\langle 0|H|0\rangle = \frac{1}{\sqrt{2}}\begin{pmatrix} 0 \\ \mathrm{v} \end{pmatrix} \quad H = \frac{1}{\sqrt{2}}\begin{pmatrix} 0 \\ \mathrm{v} + h \end{pmatrix}. \tag{2.32}$$

By substituting the Higgs field in Equation 2.32 to the $\mathcal{L}_{Higgs}$, the Lagrangian expanded around the vacuum is:

$$\begin{aligned}\mathcal{L}_{Higgs} = &\frac{1}{2}\left(\partial_\mu h\right)\left(\partial^\mu h\right) - \lambda \mathrm{v}^2 h^2 - \lambda \mathrm{v} h^3 - \frac{\lambda}{4} h^4 \\ &+ (\mathrm{v}+h)^2 \left(\frac{g^2}{4} W^+_\mu W^{-\mu} + \frac{g^2}{8\cos^2\theta_W} Z_\mu Z^\mu\right).\end{aligned} \tag{2.33}$$

The masses of W$^\pm$, Z bosons, and the Higgs boson, can be obtained by

$$m\left(\mathrm{W}^\pm\right) = \frac{1}{2}\mathrm{vg}; m(\mathrm{Z}) = \frac{\mathrm{vg}}{2\cos\theta_\mathrm{W}} = \frac{m\left(\mathrm{W}^\pm\right)}{\cos\theta_\mathrm{W}}; m(H) = \sqrt{2\lambda}\mathrm{v}. \tag{2.34}$$

The v.e.v. is the only free dimensional parameter of the SM. The current best estimation is $\mathrm{v} \approx 246$ GeV[49]. However, λ is a free parameter hence the mass of the Higgs is not predicted by the SM. The Higgs boson mass with combining CMS and ATLAS results is $m(H) = 125.25 \pm 0.17$ GeV[49].

On the other hand, to describe the interaction between left, right handed fermions and the Higgs field, which still obeys the $SU(2)_L \times U(1)_Y$ symmetry, a Lagrangian is defined as (take the b quark for example)

$$\mathcal{L}_{Yukawa} = -y_f \left[\begin{pmatrix} \bar{t} & \bar{b} \end{pmatrix}_L \begin{pmatrix} h^+ \\ h^0 \end{pmatrix} b_R + \bar{b}_R \begin{pmatrix} h^{+*} & h^{0*} \end{pmatrix} \begin{pmatrix} t \\ b \end{pmatrix}_L \right], \tag{2.35}$$

in which y_f is the Yukawa coupling constant of the b quarks and the Higgs field. After EWSB, with Equation 2.32, the $\mathcal{L}_{Yukawa}$ can be written as

$$\mathcal{L}_{Yukawa} = -\frac{y_f}{\sqrt{2}}\mathrm{v}\left(\bar{b}_L b_R + \bar{b}_R b_L\right) - \frac{y_f}{\sqrt{2}} h \left(\bar{b}_L b_R + \bar{b}_R b_L\right). \tag{2.36}$$

The first term in above Lagrangian is the b quark mass term, which means the Yukawa coupling be expressed via the observed b quark mass given by

$$y_b = \sqrt{2}\frac{m_b}{\mathrm{v}}. \tag{2.37}$$

In this case, the Lagrangian 2.36 can be rewritten by

$$\mathcal{L}_{Yukawa} = -m_b \bar{b} b - \frac{m_b}{\mathrm{v}} h \bar{b} b. \tag{2.38}$$

The first term can be explained by the fact that the fermion mass originates from the non-zero vacuum expectation value coupling with massless left-handed and right-handed fermions. Thus, the mass scale is actually driven by the strength of the fermion coupling to the Higgs field. The second term is the coupling of the Higgs boson to the fermions via Yukawa interactions. The Higgs mechanism not only succeeds in solving the question about how the weakly gauge bosons can gain mass, but also gives an answer to the question about the origin of the fermion mass.

2.1.3 Strong interaction

In the SM, the theory that governs the strong interaction is quantum chromodynamics (QCD), which describes the interaction between quarks and gluons in the SM and obeys the $SU(3)_c$ group symmetry[52]. Each quark flavor has three colors, which transform to triplets under $SU(3)_c$ gauge transformation. The local gauge invariance introduces eight gluon fields G_μ^a through the covariant derivatives as following

$$D_\mu = \partial_\mu + ig_s \frac{\lambda_a}{2} G_\mu^a, \tag{2.39}$$

here, g_s is the strong coupling constant, the sum in a goes from 1 to 8, while λ_a represents the 8 Gell-Mann matrices. To keep quantum invariance and to describe the self-interaction of gluons, the following equation is introduced

$$G_{\mu\nu}^a = \partial_\mu G_\nu^a - \partial_\nu G_\mu^a - g_s f_{abc} G_\mu^b G_\nu^c, \tag{2.40}$$

in which $\partial_\mu G_\nu^a - \partial_\nu G_\mu^a$ are kinetic terms while $g_s f_{abc} G_\mu^b G_\nu^c$ is interaction between two gluons. The complete QCD Lagrangian is given by

$$\mathcal{L}_{QCD} = \bar{\psi}\left(i\gamma^\mu D_\mu - m\right)\psi - \frac{1}{4} G^{(a)\mu\nu} G_{\mu\nu}^{(a)}. \tag{2.41}$$

There are two important phenomenological characteristics in QCD:

- color confinement: the coupling constant is significant at low energies (large distances), and a perturbative method is not applicable. The confinement is why quarks and gluons are observed only as colored singlets into bound states, i.e., hadrons. Hadrons can split into mesons (quark-antiquark pairs), baryons (quark/antiquark triplets). Once two quarks start to separate in hadrons, the color field created by the exchange of gluons increases until it is more favorable to make a quark-antiquark pair from the vacuum to increase the interaction potential further. This confinement is also responsible for the hadronization process, which creates a cascade of mesons and baryons called jets.
- asymptotic freedom: with increasing energy scales, the coupling constant decreases and approaches zero. Thus, quarks and gluons can be considered free particles, whereas perturbative methods can describe hard processes.

2.2 Multiboson production at the LHC

At LHC, multiboson production usually refers to production including two or more electroweak vector bosons ($W^\pm$, Z, γ), which allows testing the SM in both electroweak and QCD domains, extracting properties of the SM particles, and testing BSM theories. The latter are often concentrated on potential new physics effects leading to anomalous triple (aTGC) and quartic (aQGC) gauge couplings of electroweak bosons. A common way to look for deviations from

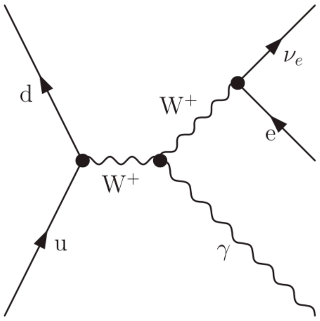

Figure 2.3 Representative Feynman diagram for pp → $e^+\nu_e\gamma$ production with a TGC vertex.

the SM is to put constraints on coefficients of EFT operators of mass dimension greater than four[53].

2.2.1 Inclusive Wγ production

The associated production of a W boson and a photon in pp collisions, whose representative Feynman diagram is shown in Figure 2.3, corresponds to a fundamental process that bearing on the basic ingredients of the SM. A precise measurement of the pp → Wγ cross section allow probing the WWγ triple-gauge coupling (TGC) and higher-order corrections to it. The structure and strength of the WWγ TGC are closely related to the $SU(2) \times U(1)$ gauge symmetry of the SM and the mechanism for EWSB, which the presence of new physics can change with alternative symmetries or symmetry breaking mechanisms. Previous measurements of Wγ production from the LHC use the data collected in 2011 at $\sqrt{s} = 7\,\text{TeV}$[54-55], the differential cross sections and anomalous triple gauge couplings are measured. The present thesis reports the first measurement of the pp → Wγ cross section at $\sqrt{s} = 13\,\text{TeV}$ based on data collected by the CMS experiment in 2016-2018, corresponding to an integrated luminosity of about 137 fb^{-1}[40], which is one of the analyses the authors participated in.

2.2.2 Vector Boson Scattering and EW-induced W$^\pm$W$^\pm$ scattering

The definition of VBS processes between the theoretical point of view and the experimental perspective are not exactly the same. Based on the theoretical simulations, particular selections in the experimental analyses are applied to select the VBS events. The typical picture of VBS consists of two gauge bosons radiated off two separate quarks lines to scatter. Take the same sign WW scattering process as the example, as illustrated in Figure 2.4. Typical Feynman diagrams in the top row indicates that the VBS process is defined at Born level at the order $O(\alpha^6)$, upon including the decay up to four leptons in the final states. This implies that three possible VBS signatures at the LHC are: 2 jets and 4 leptons (fully leptonic), 4 jets and 2 leptons (semi-leptonic/semi-hadronic), or 6 jets (fully hadronic). This definition has the advantage to be clearly gauge invariant and to describe all non-resonant, off-shell, and interference effects.

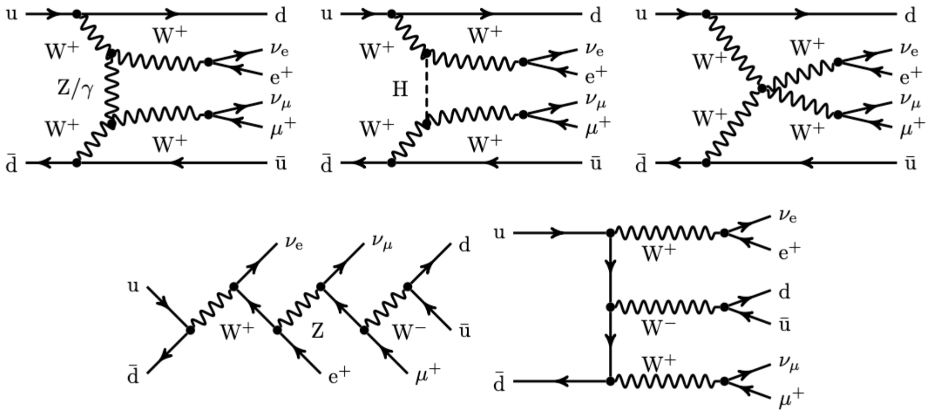

Figure 2.4 Representative Feynman diagrams for VBS contributions (top) as well as non-VBS contributions (bottom) contributing to the process pp → $\mu^+\nu_\mu e^+\nu_e jj$. These figures are taken from Ref[64].

In particular, it means that many other diagrams beyond the VBS ones such as tri-boson contributions are included, some are shown in bottom row of Figure 2.4. In order to select VBS diagrams only, approximations to the full process like the effective vector-boson[56-60] or the vector-boson scattering ones have to be used[61-63].

The $\mathrm{W}^\pm\mathrm{W}^\pm jj$ process is considered to be the golden channel in the study of VBS. The cross-section ratio of the EW component containing the VBS production compared to the QCD-induced same-sign W boson pairs is very large. The observation and differential measurements of these processes are performed in Ref[8-9,65], which are just the beginning of the studies of the VBS properties. Within the various features of the SM that are particularly relevant to the VBS, the possibility of obtaining different polarization states of the vector boson is undoubtedly one of the most intriguing features. After the EWSB, the massive vector boson has three physical polarization states two transverse ones (left-handed and right-handed) and one longitudinal one. It's calculated that the amplitude of purely longitudinally scattering of VBS processes violate the perturbative unitarity bound when the energy scale grows up. However, this divergence can be canceled if the Higgs boson also join this process which limits the mass of Higgs to less than around 1.2 TeV[63,66]. In fact, this is one the main motivations to build the LHC at the TeV scale. Even if the Higgs boson is now observed, studying the longitudinally polarization states of the VBS process is still interesting. As illustrated in Figure 2.5, the total cross section of $\mathrm{W}_\mathrm{L}^+\mathrm{W}_\mathrm{L}^+$ as a function of the center of mass energy behaves differently depending on both the Higgs mass and Higgs couplings. The measurements of polarized $\mathrm{W}^\pm\mathrm{W}^\pm jj$ are important for a precise test of the SM and a study of the additional scalar boson or non-SM HWW coupling of the BSM. One of the analyses in this thesis is the first measurement of the polarized $\mathrm{W}^\pm\mathrm{W}^\pm jj$ using data collected by the CMS experiment.

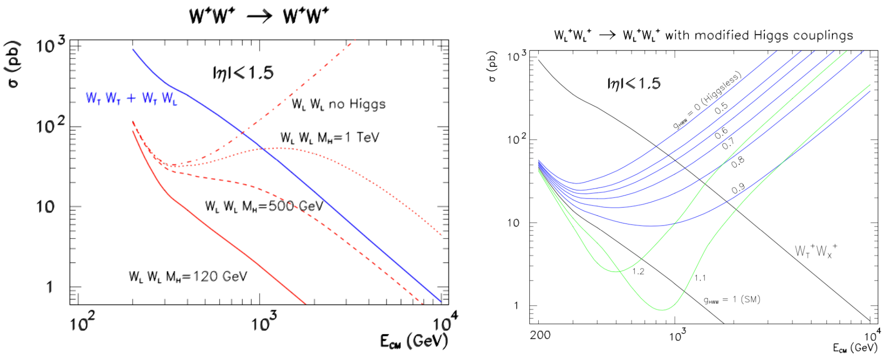

Figure 2.5 The total W^+W^+ scattering cross sections as a function of the center of mass energy for different final (and initial) state polarizations and for different Higgs masses (left), the total $W_L^+W_L^+$ scattering cross sections as a function of the center of mass energy for different values of the HWW coupling, g_{HWW}. These figures are taken from Ref[66].

2.3 Type-I Seesaw model

Despite the success of the Standard Model, there are still many physical phenomena that cannot be explained. For example, neutrinos should be massless in the SM since no Yukawa coupling for neutrinos with the Higgs field, observations of the neutrino oscillation indicates that neutrinos do have mass[19,67]. To address the non-zero mass of neutrinos, Ettore Majorana came up a hypothesis that neutrinos are their own antiparticles in 1937[68], the mass of the SM neutrinos can thus be explained via the "seesaw" mechanism[69-72].

For example, consider the Type-I seesaw model, which introduces the heavy Majorana neutrinos ($N_{k'}$) that couple to SM particles through mass mixing with light neutrinos (ν_k). The Lagrangian of the theory can be written as

$$\mathcal{L}_{Type-I} = \mathcal{L}_{SM} + \mathcal{L}_{Kin} + \mathcal{L}_{Y}, \tag{2.42}$$

where $\mathcal{L}_{Kin}$ is the Majorana mass terms for $n_R \geq 2$ right-handed (RH) neutrinos (ν_R^i), and $\mathcal{L}_Y$ is the Yukawa couplings between the SM Higgs field, the SM lepton doublets and ν_R^i. After EWSB, flavor eigenstates of active, left-handed (LH) neutrinos ($\nu_{L\ell}$) can be decomposed into light (ν_k) and heavy ($N_{k'}$) mass eigenstates with mass eigenvalues m_{ν_k} and $m_{N'}$:

$$\nu_{L\ell} = \sum_{k=1}^{3} U_{\ell k}\nu_k + \sum_{k'=4}^{n_k+3} V_{\ell k'}N_{k'}. \tag{2.43}$$

In the above equation, the matrix elements $U_{\ell k}(V_{\ell k'})$ represent the mixing between the LH interaction state $\nu_{L\ell}$ and the light (heavy) mass eigenstate $\nu_k(N_{k'})$[37].

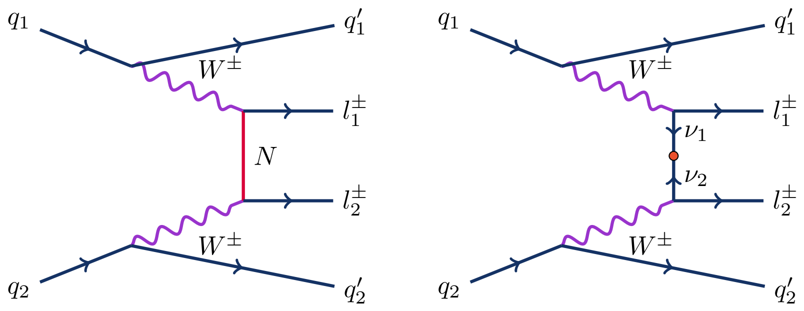

Figure 2.6 Example Feynman diagrams of VBF processes with heavy Majorana neutrino production (left) and processes mediated by the dimension-five Weinberg operator (right) at the LHC.

2.3.1 Heavy Majorana neutrino in $W^\pm W^\pm$ scattering

A phenomenological study[37] suggests studying the production of same-sign dimuon channel via the t-channel exchange of a heavy Majorana neutrino in $W^\pm W^\pm$ scattering ($W^\pm W^\pm \rightarrow \mu^\pm\mu^\pm$), as shown in the left of Figure 2.6.

A key feature of this process is that, the m_N can reach ~ 20 TeV, since it's less suppressed by the center-mass-of-energy of the LHC. Although the t-channel cross section, which in general has the form

$$\sigma^{\ell\ell'}(s) \equiv \left|V_{\ell N}V^*_{\ell' N}\right|^2 \times \sigma_0^{\ell\ell'}(s), \tag{2.44}$$

is negligible if the heavy Majorana neutrino has hundred GeV mass scale, it would be the dominant processes at LHC energy with multi-TeV mass heavy Majorana neutrino. Compared with $W\gamma$ fusion or $s-$channel production[29,34], it brings the sensitivity to high mass phase space. The present thesis also introduces the analysis using the CMS data.

2.4 Effective field theory

EFT, a model-independent approach to capture any BSM physics, has become more and more popular since there is no explicit theoretical guidance. It applies to energies up to a certain scale Λ and satisfies the following requirements[38]:

1. its guage group contains $SU(3)_c \times SU(2)_L \times U(1)_Y$ of the SM,
2. all SM degrees of freedom should be incorporated as fundamental or composite fields,
3. at low energies, it should reduce to SM without the presence of undiscovered but weakly coupled light particles such as axions or sterile neutrinos.

EFT usually does the expansion of the SM Lagrangian by means of high-dimensional operators that are suppressed by powers of Λ, which can be expressed as

$$\mathcal{L}_{\text{SM}} = \mathcal{L}_{\text{SM}}^{(4)} + \frac{1}{\Lambda}\sum_{k} C_k^{(5)} Q_k^{(5)} + \frac{1}{\Lambda^2}\sum_{k} C_k^{(6)} Q_k^{(6)} + O\left(\frac{1}{\Lambda^3}\right), \tag{2.45}$$

where $\mathcal{L}_{\text{SM}}^{(4)}$ is the SM Lagrangian, which only contains dimension-two and -four operators. And $Q_k^{(n)}$ denote dimension-n operators, $C_k^{(n)}$ stand for the corresponding dimensionless coupling constants (Wilson coefficients).

2.4.1 Dimension-five Weinberg operator in same-sign WW scattering

The EFT method can also explain the Majorana neutrino masses via the Weinberg operator[73], which is the only gauge-invariant operator at dimension five. The Lagrangian for the dimension-five Weinberg operator is

$$\mathcal{L}_5 = \frac{C_5^{\ell\ell'}}{\Lambda}\left[\Phi\cdot\bar{L}_\ell^c\right]\left[L_{\ell'}\cdot\Phi\right], \tag{2.46}$$

where Λ is the EFT scale; $C^{\ell\ell'}$ is a flavor-dependent Wilson coefficient, $L_\ell^T = (\nu_\ell, \ell)$ is the left-handed (LH) lepton doublet, and Φ is the SM Higgs doublet. The v.e.v of the SM Higgs doublet generates the quantity

$$m_{\ell\ell'} = C_5^{\ell\ell'} \mathrm{v}^2/\Lambda. \tag{2.47}$$

The EFT method can be implemented in a specific seesaw model, this analysis mainly focuses on the phenomenological parameters, i.e., Λ and $C^{\ell\ell'}$, $\ell, \ell' = e, \mu, \tau$. After EWSB, the the Higgs field can be expanded around its v.e.v, in the unitary gauge, which reads $\sqrt{2}\Phi \approx \mathrm{v}+h$, h is the Higgs boson. The Lagrangian becomes

$$\mathcal{L}_5 = -\frac{C_5^{\ell\ell'}}{2\Lambda} hh\overline{\nu_\ell^c}\nu_{\ell'} - \frac{C_5^{\ell\ell'}\mathrm{v}}{\Lambda} h\overline{\nu_\ell^c}\nu_{\ell'} - \frac{C_5^{\ell\ell'}\mathrm{v}^2}{2\Lambda}\overline{\nu_\ell^c}\nu_{\ell'} + \text{H.c.}\ . \tag{2.48}$$

The minus signs above originate from the SU(2)$_L$-invariant product $\Phi\cdot\overline{L^c} = \Phi^i\varepsilon_{ij}\overline{L^{cj}}$, with $\varepsilon_{12} = 1$. The first two terms in Equation 2.48, represent double- and single-Higgs couplings to neutrinos of flavors $\ell\ell^{prime}$, the third term generates the 3×3 LH Majorana mass matrix $m_{\ell\ell^{prime}}$ in the Equation 2.47. By rotating $m_{\ell\ell^{prime}}$ into the mass basis, the generated eigenvalues parametrize the three SM neutrino mass eigenstates m_{ν_k} as

$$|m_{\ell\ell}| = \left|\sum_{k=1}^{3} U_{\ell k} m_{\nu_k} U_{\ell k}\right|, \tag{2.49}$$

where $U_{\ell k}$ is the Pontecorvo-Maki-Nakagawa-Sakata (PMNS) mixing matrix elements.

The Equation 2.48 introduces the coupling between SM neutrinos, just as the Feynman diagrams of $0\nu\beta\beta$ experiments, namely the VBS process. This BSM interaction, represented by the heads-on fermion lines, as shown in right plot of the Figure 2.6, can explain the $\mathrm{m_N}$

mass. However, commonly used event Monte-Carlo simulation generators, such as MADGRAPH5_AMC@NLO, can not handle such fermion lines, leaving us a large difficulty in performing researches along this direction. Recently, a novel approach[74] is proposed for solving this dilemma partially. As discussed in the literature, one can assume through effectively treating the heads-on fermion line as a Majorana particle. The mass is correspondingly determined as

$$\mathrm{m_N} = |\sum_{\ell=e,\mu,\tau}\sum_{\ell'=e,\mu,\tau} C_5^{\ell\ell'}|\frac{\mathrm{v}^2}{\Lambda}, \tag{2.50}$$

while the approximated cross section for the VBS process is thus

$$\sigma(s) = \frac{2-\delta_{\ell\ell'}}{2\pi 3^2}|\frac{C_5^{\ell\ell'}}{\Lambda}|^2 + O(\frac{m_W^2}{M_{WW}^2}) \tag{2.51}$$

This assumption is valid at $\mathrm{m_N^2}/p^2 \rightarrow 0$, which is valid when the EFT scale Λ is very large. The authors of Ref[74] checks this approximation carefully by analytically calculating the cross sections at different EFT scale. As a result, they found that when $\Lambda \sim 100$ TeV the assumption works well with less than 1% relative error. Under this assumption, the $0\nu\beta\beta$-like process is thus simplified to the $\mathrm{W^\pm W^\pm}$ VBS with t-channel Majorana neutrino similar to the heavy Majorana neutrino ones. Since many nuclear experiments give stringent constraints on the $0\nu\beta\beta$ process and the study of tau leptons is experimentally challenging, the final state with same-sign muons is investigated in the present thesis.

2.4.2 Dimension-six operators in production of Wγ

Besides precisely measuring the cross section of the inclusive Wγ, mentioned in Section 2.2.1, the s-channel production of Wγ events can happen associating with the triple-boson coupling WWγ. The analysis also makes use of an EFT approach to the anomalous coupling. In general, if the anomalous coupling WWγ of new physics existed, the Wγ production cross section would increase. This increase affects most the high-energy regions of the phase space and in particular the high-p_{T} tail of the photon p_{T} distribution.

Taking the BSM parts in to account, the dimension-six operators described in Equation 2.45 are considered. In fact, there are many dimension-six operators, however, for the given Wγ production process, only a few operators have an effect[42-43]. When C and P are conserved, only three independent dimension-six operators need to be considered of which there are several options of combination. Refer to Ref[41], the three independent dimension-six operators seleted when C and P are conservation written as follows

$$\begin{aligned} O_{WWW} &= Tr[W_{\mu\nu}W^{\nu\rho}W^{\mu}_{\rho}] \\ O_{W} &= (D_{\mu}\Phi)^{\dagger}W^{\mu\nu}(D_{\nu}\Phi) \\ O_{B} &= (D_{\mu}\Phi)^{\dagger}B^{\mu\nu}(D_{\nu}\Phi) \end{aligned} \tag{2.52}$$

If the C and/or P violation are allowed, there are two additional operators, which can be written as follows

$$\begin{aligned} O_{W\tilde{W}W} &= Tr[\tilde{W}_{\mu\nu}W^{\nu\rho}W^{\mu}_{\rho}] \\ O_{\tilde{W}} &= (D_{\mu}\Phi)^{\dagger}\tilde{W}^{\mu\nu}(D_{\nu}\Phi) \end{aligned} \tag{2.53}$$

where Φ is the Higgs doublet field, D_{μ} the SM electroweak covariant derivative, and $W^{\mu\nu}$ and $B^{\mu\nu}$ are the SU(2)×U(1) field strength tensors, $\tilde{W}^{\mu\nu}$ is defined as $\epsilon^{\mu\nu\rho\sigma}W_{\rho\sigma}/2$ ($\epsilon^{\mu\nu\rho\sigma}$ is totally antisymmetric with $\epsilon^{0123} = 1$). And the five operators are only constrained by electroweak vector boson pair production[75] contributed by gauge boson self-interactions without the coupling of the electroweak vector bosons to fermions. The five operators have corresponding coefficients c_{WWW}, c_{W}, c_{B}, $c_{W\tilde{W}W}$ and $c_{\tilde{W}}$, respectively. From all above, the effective field theory Lagrangian is written as follows

$$\mathcal{L} = \mathcal{L}_{SM} + \frac{c_{WWW}}{\Lambda^2}O_{WWW} + \frac{c_{W}}{\Lambda^2}O_{W} + \frac{c_{B}}{\Lambda^2}O_{B} + \frac{c_{W\tilde{W}W}}{\Lambda^2}O_{W\tilde{W}W} + \frac{c_{\tilde{W}}}{\Lambda^2}O_{\tilde{W}} \tag{2.54}$$

From which the first term belongs to standard model, the following three terms respect C and P, and the remaining two terms violate C and/or P.

According to Ref[42], using the following formulas, these coefficients can be converted into the parameters in the so-called LEP framework:

$$\begin{aligned} g_1^Z &= 1 + c_W\frac{m_Z^2}{2\Lambda^2} \\ \lambda_\gamma = \lambda_Z &= c_{WWW}\frac{3g^2m_W^2}{2\Lambda^2} \\ \tilde{\kappa}_\gamma &= c_{\tilde{W}}\frac{m_W^2}{2\Lambda^2} \\ \tilde{\kappa}_Z &= -c_{\tilde{W}}\tan^2\theta_W\frac{m_W^2}{2\Lambda^2} \\ \tilde{\lambda}_\gamma = \tilde{\lambda}_Z &= c_{W\tilde{W}W}\frac{3g^2m_W^2}{2\Lambda^2} \end{aligned} \tag{2.55}$$

where

$$g = \frac{2\sqrt{\alpha_{EW}\pi}}{\sin\theta_W} = 0.6298. \tag{2.56}$$

Chapter 3

Experimental Setup

Collider experiments are an essential part of particle physics research. It can provide high-quality data for precise physical analysis. The Large Hadron Collider (LHC) is now the biggest and highest-energy particle collider globally. As the energy frontier, it hosts eight experiments using detectors to analyze the particles from collisions. The Compact Muon Solenoid (CMS) detector is one of the biggest. In this chapter, the LHC and CMS experiments are described.

3.1 The Large Hadron Collider

The LHC[7] at European Organization for Nuclear Research (CERN) is located underground the border between Switzerland and France with an average depth of 100 meters, Figure 3.1. It is a two-ring-superconducting-hadron accelerator installed in the 27-kilometer tunnel for the Large Electron-Positron (LEP) collider. As a particle-particle collider, the two rings carry counter-rotating beams are designed as "twin-aperture" magnets to adapt to the limitation of the geometry space in the tunnel. A common cold mass and cryostat surround two beam pipes with magnetic flux in opposite directions.

As a part of the CERN accelerator complex, shown in Figure 3.2, the LHC is connected to other components through two transfer tunnels. Particle acceleration starts with the LINear ACcelerator (LINAC), the synchrotron Booster, the Proton Synchrotron (PS), and the Super Proton Synchrotron (SPS). When the beam energy reaches 450 GeV, they are extracted and injected into LHC ring. The machine is expected to accelerate two beams of protons to an energy of 7 TeV, or two beams of heavy ions to an energy of 2.76 TeV, in the case of Pb ions. Each proton beam consists of 2800 bunches at full intensity, and each beam containing about 10^{11} protons.

The LHC is composed of 16 radiofrequency (RF) cavities, 1232 main dipole magnets, and 392 quadrupole electromagnet. An oscillating electric field accelerates the hadrons and packs them into separate bunches. These bunches are spaced 25 ns apart, providing a bunch collision rate of 40 MHz. The dipole magnets generate a field of 8.3 T, that keeps the hadrons in their

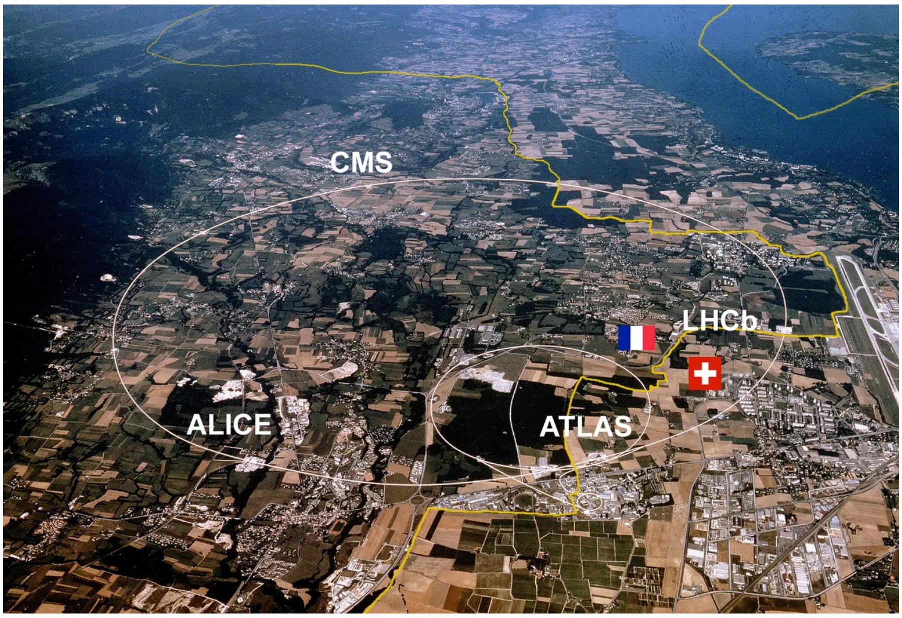

Figure 3.1 Location of the LHC tunnel across France and Switzerland[76].

circular path. The dipole magnets are operated by superconducting coils with a current of 11080 amperes (11.08 kA) composed of NbTi/Cu Rutherford-type cables cooled down to 1.9 K by superfluid helium. The LHC is divided into eight arcs due to eight straight sections in Figure 3.3. Quadrupole magnets are installed in the straight sections to focus and squeeze the beam to force more particles collisions when the beam paths cross. The LHC also uses sextupole and octupoles electromagnets in these straight segments to make small changes in the direction of the beam.

Only four of the rectilinear regions are chosen to be the interaction points (IPs). Each of the IPs is equipped with detectors. As shown in Figure 3.3, the fours detectors are as follows:

- A Toroidal LHC Apparatus (ATLAS) and the CMS detectors at point 1 and point 5, respectively, are two general-purpose detectors. They are designed to perform precision measurements of the SM and to search for any possible signal beyond the SM. Due to different design, the two detectors can cross-check with each other.
- A Large Ion Collider Experiment (ALICE) is an experiment for studying the quark-gluon plasma in heavy ions collisions.
- The LHC-beauty (LHCb) is an experiment designed to study CP violation in electroweak interactions and flavor physics.

At or near the main detector sites, there are also some small experiments that have carried out very specialized research: LHCf (LHC-forward), TOTEM (TOTal Elastic and diffractive cross section Measurement), MoEDAL (Monopole and Exotics Detector At the LHC), and FASER (ForwArd Search ExpeRiment).

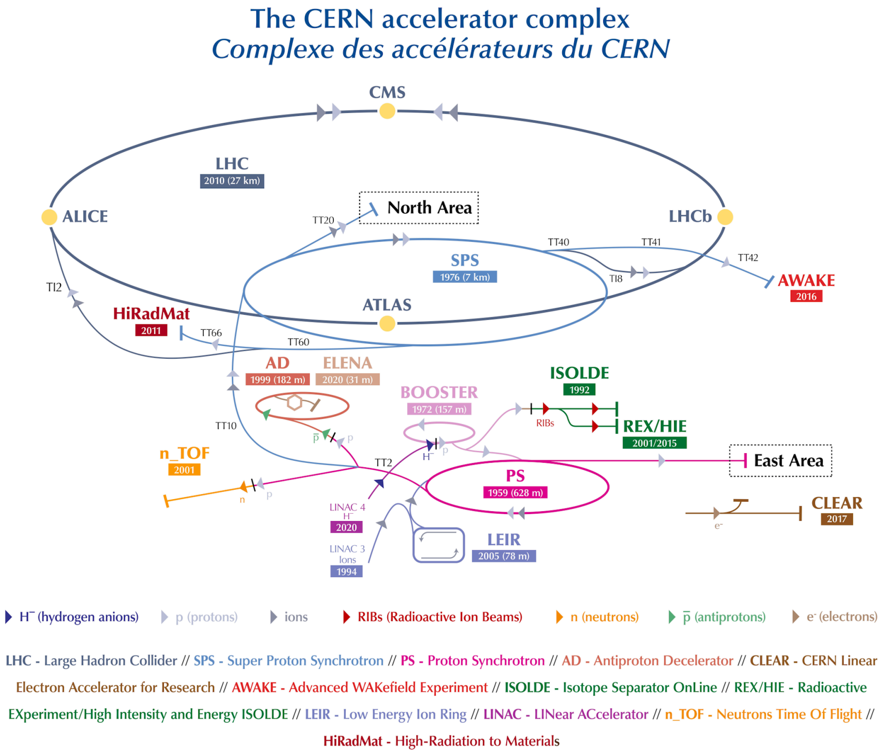

Figure 3.2 The CERN accelerator complex**accelerator_complex**.

3.1.1 Luminosity and pileup

The beam focuses and collides at four selected IPs when the LHC reaches the operating energy. In each crossover, only a small number of hadrons interact, and the beam remains in circulation until the instantaneous intensity decreases due to the small loss accumulated in time. At this point, the beam is dumped and a new beam is injected.

The quantity Luminosity, L, is used to reflect the number of proton-proton collisions per second. Consider the cross section for process pp $\rightarrow X$, $\sigma_{\mathrm{pp}\rightarrow X}$, the number of of events generated per second $N_{\mathrm{pp}\rightarrow X}$ is given by:

$$N_{\mathrm{pp}\rightarrow X} = L_{inst} \times \sigma_{\mathrm{pp}\rightarrow X}, \tag{3.1}$$

where L_{inst} is the instantaneous luminosity. Assuming that the proton beam density function obeys the Gaussian distribution and the two colliding beams have the same beam parameters, the instantaneous luminosity can be expressed as

$$L_{inst} = \frac{N_b^2 n_b f_{\mathrm{rev}} \gamma_r}{4\pi \epsilon_n \beta^*} F, \tag{3.2}$$

where N_b is the number of particles per bunch, n_b the number of bunches per beam, f_{rev} the revolution frequency, γ_r the relativistic gamma factor, ϵ_n the normalized transverse beam

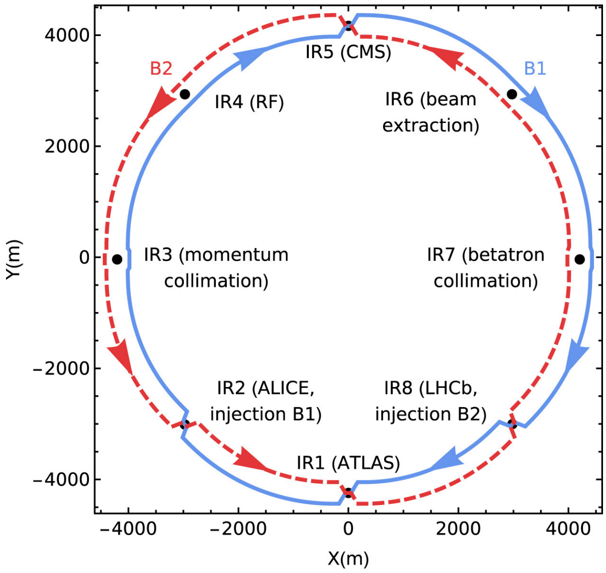

Figure 3.3 The LHC layout (Beam 1 - clockwise, Beam 2 - anticlockwise) from Ref[77].

emittance, β^* the beta function at the collision point, and F the geometric luminosity reduction factor due to the crossing angle at the IP:

$$F = \left(1 + \left(\frac{\theta_c \sigma_z}{2\sigma^*}\right)^2\right)^{-1/2}, \tag{3.3}$$

where θ_c is the full crossing angle at the IP, the root mean square (RMS) of the bunch length σ_z , and the transverse RMS beam size at the IP σ^*[7].

For data analysis, people are more interested in the integrated luminosity, L_{int}, which is the time integral of the instantaneous luminosity. The integrated luminosity is given by

$$L_{int} = \int L_{inst} dt. \tag{3.4}$$

The higher the instantaneous luminosity, the higher the integrated luminosity, the more data available for analysis. However, high instantaneous luminosity can lead to a large pileup (PU), μ, defined as the number of inelastic proton-proton collisions per bunch crossing. The following formula estimate the average PU, $\langle \mu \rangle$,

$$\langle \mu \rangle = \frac{L_{inst} \sigma_{\mathrm{pp}}^{inel}}{n_b f_{\mathrm{rev}}}, \tag{3.5}$$

where $\sigma_{\mathrm{pp}}^{inel}$ is the inelastic cross section for proton-proton collisions.

Typical PU interactions are soft and have a very high probability of occurring. To detect a single primary collision in the background of the other interactions, the higher PU is a challenge. Still, it makes higher the probability of an interesting event occurring. Thus, the PU has a significant impact on the physics reach of the experiment.

3.1.2 Run period

The CERN Council approved the LHC project in December 1994, and the first protons circulated inside the LHC on September 10, 2008. But after a few days, a magnet quench incident led to a loss of approximately six tonnes of liquid helium, caused extensive damage to over 50 superconducting magnets, their mountings, and the vacuum pipe. The LHC had to cease operations. The repairs lasted one year[78].

On 20 November 2009, two proton beams at a center-of-mass energy of $\sqrt{s} = 0.9\,\text{TeV}$ circulated in the tunnel for the first time since the incident. On 30 March 2010, LHC set a new record for high-energy collisions by colliding proton beams at a combined energy level of 7 TeV.

The first main research program of proton-proton collision, the Run-1 data-taking period, lasted from 2011 until 2012. In the first year, a total integrated luminosity of 6.1 fb^{-1} was delivered at a centre-of-mass energy of $\sqrt{s} = 7\,\text{TeV}$. The search for the Higgs boson yielded encouraging results, so it was decided to increase the beam energy to $\sqrt{s} = 8\,\text{TeV}$ for the 2012 data run. At the end of Run-1, the Higgs boson was discovered by the ATLAS and CMS collaborations with nearly 30 fb^{-1} of recorded data.

During the period 2013 to 2015, the LHC was shut down for a 2-year upgrade known as Long Shutdown 1 (LS1). On 5 April 2015, the second operational run (Run-2) started at a centre-of-mass energy of $\sqrt{s} = 13\,\text{TeV}$, and ended on 3 December 2018. The analyses in this thesis are carried out with the CMS Run-2 data. According to Ref[79], the parameters of the LHC operation for each year of Run-2 are in Table 3.1. In 2016, machine operators focused on increasing luminosity. The design value was reached for the first time on June 29, and further improvements brought the collision rate up to 40% higher. In 2017, the luminosity was increased further, reaching twice the design value. At the end of the Run-2, a total delivered integrated luminosity of about 163 fb^{-1} for this period (Figure 3.4 (a)), which corresponds about about 137 fb^{-1} valid luminosity for data analysis. As shown in Figure 3.4 (b), larger $\langle\mu\rangle$ values of 2017, 2018 than 2016 are observed.

Table 3.1 Parameters of the LHC for 2016, 2017 and 2018.

Symbol	**Parameter**	**2016**	**2017**	**2018**
$\sqrt{s}$	Centre-of-mass energy (TeV)	13	13	13
Δt	Bunch spacing (ns)	25	25	25
L_{inst}	Instantaneous luminosity peak (10^{34} $\text{cm}^{-2}\text{s}^{-1}$)	1.4	2.1	2.1
$\langle\mu\rangle$	Average pileup	25	38	37
n_b	Max. No. bunches per beam	2220	2556/1868	2556
N_b	No. protons per bunch (stable beam) (10^{11})	1.0-1.25	1.0-1.25	1.0-1.25
ϵ	Transverse emittance (stable beam) (μm)	2.2	2.2	1.9
f_{rev}	Revolution frequency (Hz)	11245	11245	11245
β^*	Beta function (cm)	40	40-30	30-25

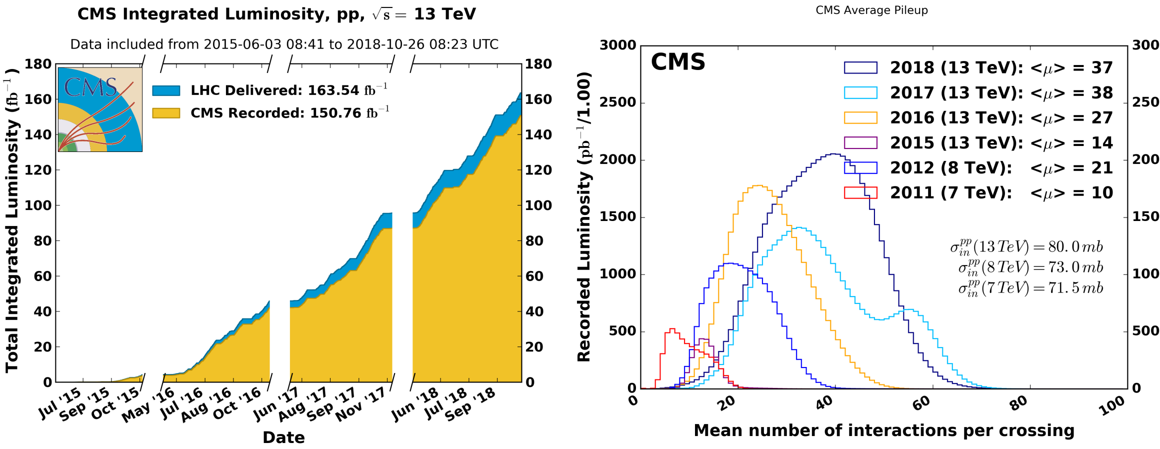

(a) The integrated luminosity of Run-2 period (b) Average PU for each data-taking period

Figure 3.4 Figure (a) shows the integrated luminosity of the pp collisions at a centre-of-mass energy of $\sqrt{s}$ = 13 TeV during the Run-2 period. The integrated luminosity delivered from the LHC is 163.54 fb^{-1} and recorded by the CMS is 150.76 fb^{-1}. The total valid luminosity for data analysis is about 137 fb^{-1}. Figure (b) shows the distribution of the mean number of inelastic interactions per crossing (PU) for each data-taking period for pp collisions in 2016 (orange curve), 2017 (light blue curve), and 2018 (navy blue curve). A minimum bias cross section of 80.0 mb is chosen. The mean number per bunch crossing and year of inelastic interactions is provided in the legend.

3.1.3 The Worldwide LHC Computing Grid

The challenge of the LHC experiment lies not only in the construction and operation of the accelerator and detectors, but also in the necessary computational resources. Due to the high cost and very specific requirements, these data storage and computational requirements are difficult to find in the market. In addition, since most LHC researchers do not work at CERN, the computational resources must be globally accessible. Therefore, a distributed computing infrastructure, called the Worldwide LHC Computing Grid (WLCG or Grid), was established. This system provides computational capabilities for all LHC experiments and provides a range of services needed to process and store data for LHC experiments, as well as to generate Monte Carlo (MC) samples. The grid is arranged in a multi-layer system, as shown in Figure 3.5. And the grid is classified according to its processing power, storage capacity and Internet connection speed, following is the CMS example,

- The first tier is known as Tier-0 (T0), which are responsible to accept the raw data (RAW format) that comes from the LHC detectors. Thus, the T0 must provide enough storage to save all the data collected by the LHC experiments. The T0 also performs prompt first pass reconstruction (RECO format), and then distributes to the Tier-1.
- Tier-1 (T1), responsible for large-scale, centrally organized activities. In the CMS experiment, there are seven T1 sites, which are large centers in CMS collaborating countries.

These T1 sites provide substantial CPU power for scheduled Analysis Object Data (AOD) extraction and distribute them to the Tier-2.

- Tier-2 (T2), provides capacity for user analysis, calibration studies, and Monte Carlo production. T2 sites are used for production of the compact version of the reconstructed data (miniAOD and nanoAOD formats). The T2 are mainly located in laboratories and universities.

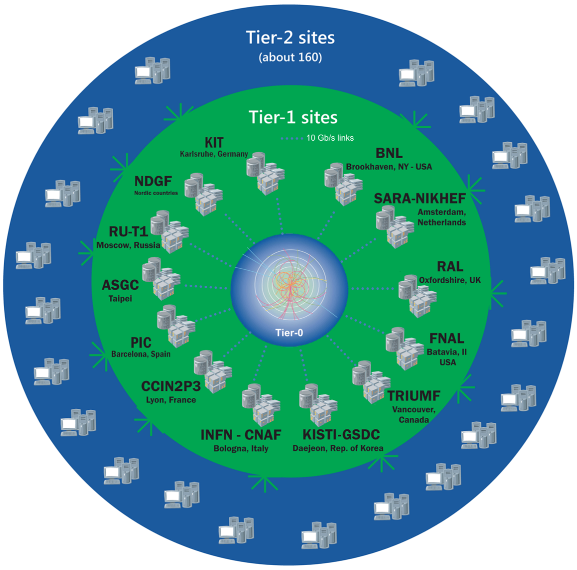

Figure 3.5 The WLCG architecture and the Tier hierarchy.

3.2 The CMS detector

Mentioned in Section 3.1, the CMS[18] is a general-purpose detector located at the LHC IP5, around 100 meters underneath Cessy, France. The primary motivation for the LHC is to elucidate the nature of EWSB. The Higgs mechanism is believed to be the reason. Since the CMS detector covers almost a solid angle of 4π steradians around the interaction point except for the space near the beamline, it can identify and reconstruct virtually all of the physics objects produced in pp collisions. So the CMS detector can perform analyses such as precise measurements of SM parameters, searches for the Higgs boson, and even BSM processes

The sandwich structure of the CMS is shown in Figure 3.6. It is divided in three regions: two forward regions also known as the endcaps, and and a central barrel region. The installed high-granularity subdetectors inside the CMS are described in the following sections. From innermost to outermost, the inner tracker system with a pixel detector (inner) and a silicon strip tracker (outer) provides accurate and efficient measurements of charged particle trajectories in Section 3.2.2; an electromagnetic calorimeter (ECAL) absorbs electrons and photons for particle identification and energy measurements, and a hadron calorimeter (HCAL) plays a similar role for hadrons are described in Section 3.2.3 and Section 3.2.4, respectively; the most accurate momentum measurement and the best time resolution for muons are further given by the outermost muon system in Section 3.2.6. The superconducting solenoid magnet between the HCAL and muon detectors is an important feature of the CMS detector, which provides a constant magnetic field of 3.8 T, is introduced in Section 3.2.5. The high magnetic field allows to bend charged particles in the tracking system, then the momenta can be measured precisely through the curvature of their trajectories. The magnetic field is then constrained by a return yoke between the muon detectors, resulting in a better measurement of the muon momenta. Considering the electromagnet and steel yoke, the CMS detector weighs up to 14,000 tons, which is really compact for a cylindrical volume of only 22 meters long and 15 meters in diameter.

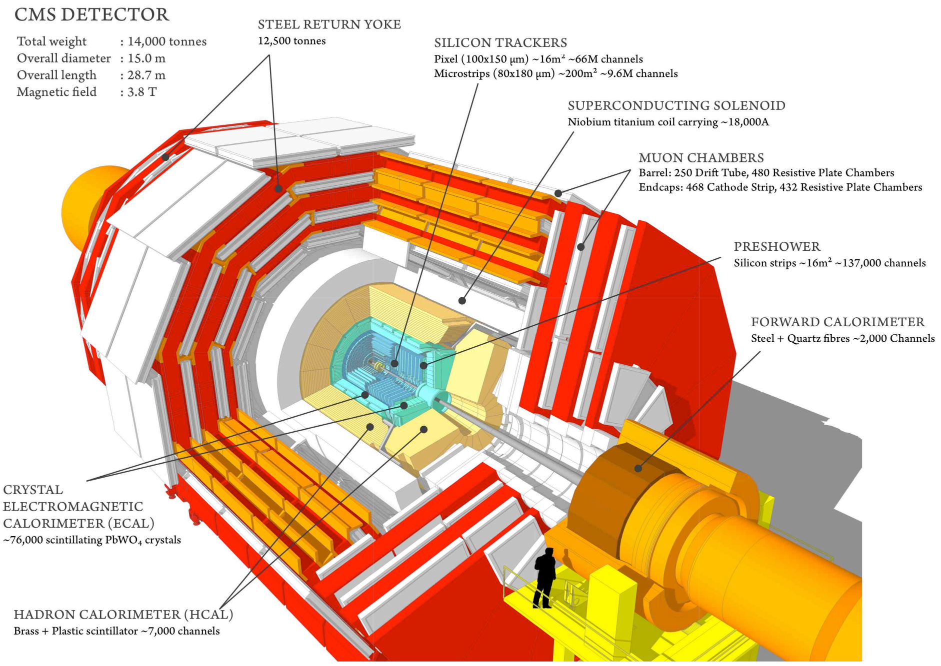

Figure 3.6 Cross section of the CMS with a sandwich structure.

3.2.1 Coordinate system

A right-handed coordinate system is used in the CMS experiment, where the origin is centered at the interaction point, the x-axis points toward the center of the LHC ring, the y-axis points vertically upwards to the plane of the LHC ring, and the z-axis points along the counterclockwise beam direction, the azimuthal angle ϕ is measured from the x-axis in the xy-plane and the polar angle θ is measured from the positive z-axis, described in Figure 3.7.

In experimental particle physics, the quantity rapidity, y, is prefered than the polar angle. It's defined

$$y = \frac{1}{2}\ln(\frac{E + p_z}{E + p_z}), \tag{3.6}$$

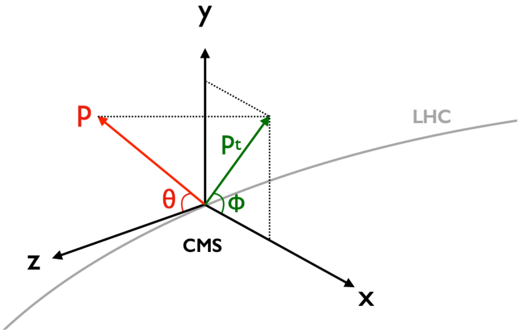

Figure 3.7 The coordinate system used in the CMS experiment.

where E is the particle energy, p_z is the momenta at the z component. In pp collisions, the y-component of the particle momenta is always positive, and the z-component is always negative. Due to the parton density function, partons from the protons carry unknown momenta at the z-axis. Thus, the products from collisions could be longitudinally boosted, but the exact amount of boost is unknown. The advantage of rapidity is that the rapidity difference remains constant under longitudinal boosting. At high energy, the mass of the products can be negligible, the rapidity can approximate to the so-called pseudorapidity, given by

$$\eta = \ln(\tan(\theta/2)), \tag{3.7}$$

where θ is the polar angle. Both ϕ and transverse momentum, p_T, which is defined by

$$p_\mathrm{T} = \sqrt{p_x^2 + p_y^2}, \tag{3.8}$$

are invariant under longitudinal boosting. So in the high energy physics, the four-momentum of the particle is usually described by $(p_\mathrm{T}, \eta, \phi, E)$ for convenience. Other kinematic variables that are invariant under longitudinal boosting, such as the spatial angle distance between two particles, defined by $\Delta R = \sqrt{\Delta\eta^2 + \Delta\phi^2}$, and transverse energy, $E_T = m^2 + p_\mathrm{T}^2$, are also widely used in high energy physics.

3.2.2 Inner Tracking System

In a magnetic field, the transverse momentum of a charged particle is given by

$$p_\mathrm{T} = qrB, \tag{3.9}$$

where q is the electric charge of the particle, r is the radius of the particle trajectory, and B is the magnetic field. The inner tracking system of CMS[18] is designed to accurately and efficiently measure the trajectory of charged particles generated by pp collisions. The momentum of a charged particle can be determined by its trajectory with a precision of up to 10 μm.

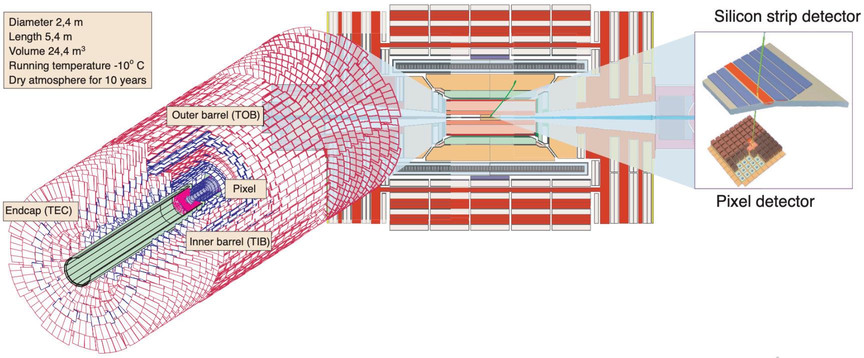

Figure 3.8 A schematic view of the inner tracker system of CMS[80].

Those parameters are usually used to describe a track: p_{T}, η, ϕ, d_{xy}, and d_z, where d_{xy} is and d_z the transverse impact parameter, d_z is the longitudinal impact parameter. The reconstructed charged tracks plays an important role in interaction vertices and secondary vertices reconstruction. The vertices are further used in reconstructing physical objects, identifying particles, and tagging heavy flavor jets.

At the LHC design luminosity ($\approx 10^{34} cm^{-2} s^{-1}$), there will be on average about 1000 particles from more than 20 overlapping pp interactions traversing the tracker with 25 ns bunch spacing. A detector technology with high granularity and fast response is therefore needed to identify trajectories and attribute them to the correct bunch reliably. To avoid multiple scattering, the tracker keeps the amount of material as low as possible. The internal tracker system has a higher granularity pixel detector and a lower granularity silicon strip tracker surrounding the interaction point and covering a $|\eta| < 2.5$ region. It has a length of 5.8 m and a diameter of 2.5 m, a schematic view is shown in Figure 3.8. The CMS solenoid offers a uniform magnetic field of 3.8 T over the entire tracker volume.

The pixel detector consists of three barrel layers (BPix) and two endcap discs (FPix), which are arranged as shown in Figure 3.9 (bottom). This arrangement provides 3 tracking points in the $|\eta| < 2.5$ region. The layout of the pixel detector has been changed since the 2017 phase 1 upgrade[81] to four layers in the barrel section and three disks in the endcap section, with the new arrangement shown in Figure 3.9 (top). This geometry structure provides a complete set of four tracking points in the $|\eta| < 2.5$ region to cope with the higher pileup environment. The pixel detector uses silicon sensors comprising 124 million high dose n-type pixels with a size of 100 μm by 150 μm, embedded in a high resistance n-substrate of 285 μm thickness. A high dose p-type backplane featuring a reverse bias voltage is placed under the bulk. When charged particles with enough energy go through a pixel, they ionize electron-hole pairs in the bulk. These electron-hole pairs are brought out to the surface by a reverse bias voltage and induce small electrical signals. These electrical signals are eventually passed to the readout plane.

Outside the silicon pixel detector is the silicon strip tracker. It has 25000 single sided p-on-

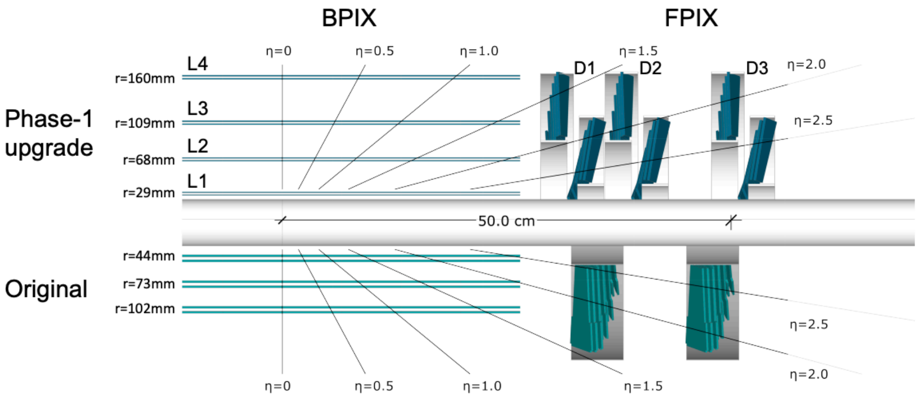

Figure 3.9 Arrangement of the Pixel detector (top) with the original detector (bottom) after the phase 1 upgrade.

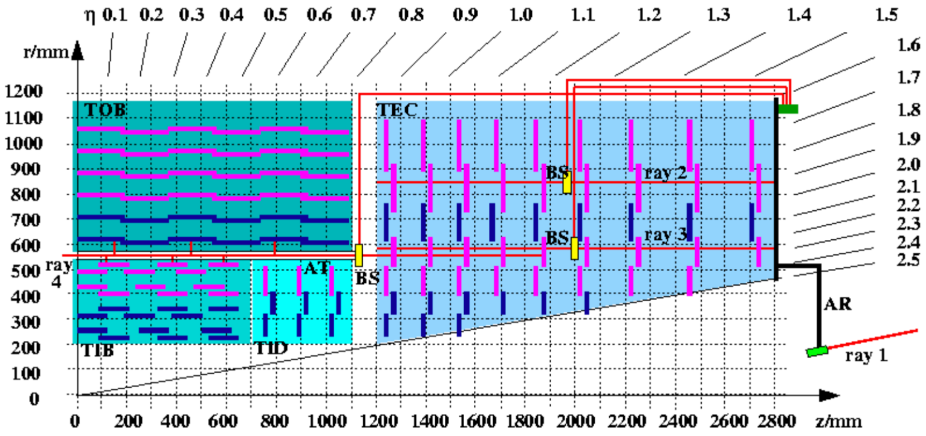

Figure 3.10 Sketch of one quarter of the silicon strip tracker system.

n type silicon micro-strip sensors distributed in four regions: the Tracker Inner Barrel (TIB), Tracker Outer Barrel (TOB), Tracker Inner Disks (TID), and Tracker End Caps (TEC). There are 10 layers in TIB and TOB. The TID and TEC have three wheels and nine wheels per side respectively. Figure 3.10 shows the sketch of one quarter of the silicon strip tracker system.

3.2.3 Electromagnetic calorimeter

Contrary to the tracking system, which must interact minimally with the particles and do not affect the measurement of their trajectory, the calorimeter detector has to absorb the particles to measure their energy. Because of this reason, the calorimeter is installed after the tracker detector. The principle of a calorimeter is that particles entering it will produce particle shower, the secondary particles from showering deposit energy and produce more particles until all the energy is absorbed. The shape and size of the particle shower depend on the energy and the primary particle type.

The Electromagnetic Calorimeter (ECAL) of the CMS detector[18] is a hermetic homoge-

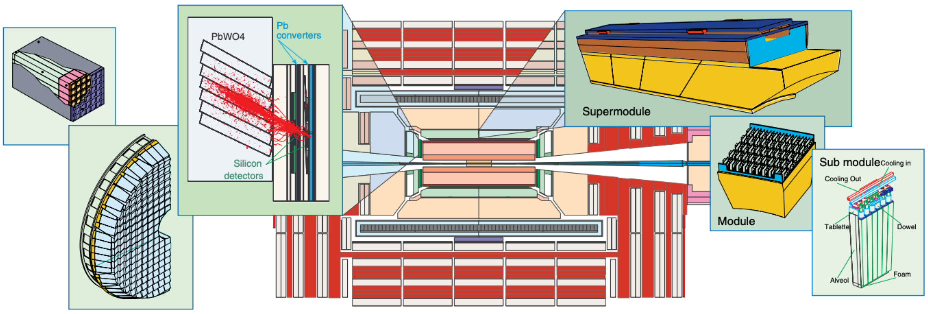

Figure 3.11 A schematic view of the ECAL of CMS[82].

neous calorimeter made of 61200 lead tungstate (PbWO4) crystals mounted outside the inner tracking system, closed by 7324 crystals in each of the two endcaps, covering the region of $|\eta|$ up to 3. In front of the endcap crystals, a preshower detector is located. Avalanche photodiodes (APDs) and vacuum phototriodes (VPTs) are used as photodetectors in the barrel and endcaps. A sketch of the ECAL is shown in the Figure 3.11.

Recently, the scintillation properties and other qualities of PbWO4 have been gradually improved, leading to the mass production of optically clear, fast and radiation-resistant crystals. The PbWO4 crystal has a high degree of transparency and scintillates when electrons or photons go through, emitting radiation proportional to their energy. This crystal is heavier than stainless steel with a density of $\rho = 8.28$ g/cm^3, which results in a short radiation length of $X_0 = 0.89$ cm. In additional, small Molière radius (2.2 cm) of this crystal provides the ECAL with high energy resolution and a fine granularity. The PbWO4 crystal has a fast scintillation decay time of the same order of magnitude as the LHC bunch crossing time: about 80% of the light is emitted in 25 ns, making it able to avoid signal overlapping between events. However, The light yield is relatively low and varies with temperature, at 18°C about 4.5 photoelectrons/MeV are collected in both APDs and VPTs.

The central barrel section (EB) of ECAL covers $|\eta| < 1.479$, two endcaps (EE) in the forward and backward regions, which cover the range $1.479 < |\eta| < 3.0$, as shown in Figure 3.12. The EB crystals have a conical shape that varies slightly with η position. In the ϕ and η projections, their axes form a slight angle (3°) concerning the vector from the nominal interaction vertex to avoid cracks in alignment with the particle trajectories. The crystal cross section is approximately 0.0174×0.0174 corresponding to $\eta - \phi$, i.e., 22×22 mm^2 at the front and 26×26 mm^2 at the back. The length of the crystal is 230 mm, which is equivalent to 25.8 X_0. In the EE part, identically shaped crystals are grouped into mechanical cells of 5×5 crystals (supercrystals, or SCs), consisting of a carbon fiber alveola structure. Each endcap is split into two halves or Dees. The crystals and SCs are arranged in a rectangular $x - y$ grid, with the crystals pointing to a focal point 1300 mm beyond the point of interaction, giving a deviation angle of 2 to 8 degrees. The crystals have a rear surface cross-section of 30×30 mm^2 and

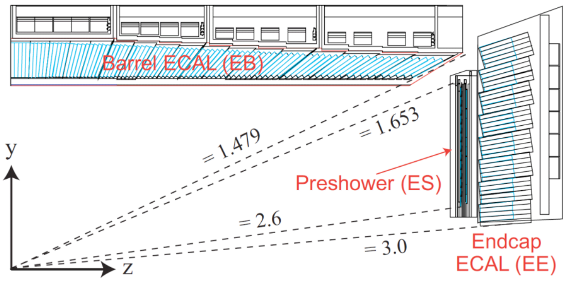

Figure 3.12 Geometric view of one quarter of the ECAL[83].

a front surface cross-section of 28.62×28.62 mm^2 and a length of 220 mm ($24.7X_0$). The preshower detector (ES) in front of the endcap crystal has a high granularity photon sensitive detector covering $1.65 < |\eta| < 2.5$. The main purpose is to separate the individual photons from the boosted π_0, where their diphoton decay is close to each other and may be mistaken for a single photon. Therefore, ES employs a sampling calorimeter consisting of two layers with high spatial resolution. Each layer consists of a $2X_0$ lead absorber and a X_0 silicon strip sensor positioned behind the absorber to measure energy deposition and high-granularity of the transverse shower profiles.

The photodetectors (APDs in the EB and VPTs in the EE) amplify and digitize the electrical signals and then store the signals in a frond-end readout card pipeline for 256 bunch crossings awaiting a Level1-accept (L1A) trigger. Each readout card receives data corresponding to 5×5 crystals, the so-called tower, and sums the transverse energy in each tower at each bunch crossing.

The energy (E) resolution of ECAL is decoupled into three terms (in GeV):

$$\left(\frac{\sigma(E)}{E}\right)^2 = \left(\frac{S}{\sqrt{E}}\right)^2 + \left(\frac{N}{E}\right)^2 + c^2, \tag{3.10}$$

where S is considered as a random term for fluctuations in the number of photoelectrons generated and collected, N is a noise term originating from electronic noise and PU events, and c is a constant term depending on the non-uniformity of the longitudinal light collection. The measured parameters for EB with electron test beams are S =2.8%, N = 12% and c^2 = 0.3%. The overall energy resolution of EB is below 1% in general, as described in Ref[84].

3.2.4 Hadron Calorimeter

Surrounding the ECAL, a Hadron Calorimeter (HCAL) installed is a sampling calorimeter covering $|\eta|$ up to 5.2. It consists mainly of duplicated dense absorber layers and plastic scintillator tiles that produce fast light pulses when the hadronic showers travel through these scintillators. The absorber is made up of a flat brass alloy absorber plate of 70% Cu/30% Zn with a known radiation length of 1.49 cm and an interaction length (λ_I) of 16.42 cm. The HCAL absorbs particles that survive in the ECAL except for muons and weakly interacting particles and measures the jets' energy and direction. Due to its hermetic structure, the HCAL can also measure the transverse energy imbalance, which is typical of non-interacting particles such as neutrinos or possible exotic particles.

Figure 3.13 displays the layout of the HCAL. It is composed of four major parts: the hadron barrel (HB), the hadron endcap (HE), the hadron forward (HF), and the hadron outer (HO) calorimeters. The HB is located between radii of 1775 and 2876.5 mm covering $|\eta| < 1.39$. The HB is divided into two half-barrel sections in the direction along the z-axis, each assembled from 18 wedges. A wedge contains absorber plates made of brass that are bolted together. The inner and outer plates are made out of stainless steel. There are 17 layers per wedge that house the plastic scintillator tiles. The HB effective thickness absorbers increase with the polar angle from 5.82 interaction lengths (λ_I) to 10.6 λ_I. The HB has about 40000 scintillator tiles. A set of scintillators with the same value of η and ϕ in different layers is grouped together as a tower. The HE calorimeter is also formed with brass absorber plates with 18 sampling layers of plastic scintillator and covers $1.30 < |\eta| < 3.00$. The total length of the calorimeter, including electromagnetic crystals, is about 10 λ_I. Due to the limited absorber material in HB, a HO subdetector is installed outside the magnet coil to measure the remaining energy that leaks from the HB. The iron return yoke acts as an additional absorption layer to enhance the energy resolution, which extends the effective depth to 11.8 λ_I. The HO calorimeter covers $|\eta| < 1.26$. The $\eta-\phi$ segmentation of the HO calorimeter closely matches that of the HB calorimeter. The optical signals from the scintillator detectors in the HB, HE, and HO is detected by wavelength shifting fibers, summed with successive tile optics to form an energy towers, and then converted to electrical signals using multichannel hybrid photodiodes (HPDs). The other calorimeter HF measures forward activities, installed at 11.2 m from the center of the CMS detector, and covers the range of $2.9 < |\eta| < 5.2$. To stand with a higher flux of particles, the HF is made of steel absorbers like a cylindrical structure with radiation-hard quartz fibers inserted, which provide the collection of the Cherenkov lights produced by charged shower particles. Photomultiplier tubes (PMTs) collect the light in the fibers of the energy towers. The HF also serves as part of the online measurement of the luminosity system in the CMS detector. The back-end electronics of the four subdetectors finally send signals to the data acquisition system for event triggering. A test beam experiment[85] (beam energy from 2 to 350 GeV) measured the combined calorimeter (ECAL + HCAL) energy resolution, which is given by the following formula:

$$\frac{\sigma_E}{E} = \frac{84.7\%}{\sqrt{E(\mathrm{GeV})}} \oplus 7.4\%. \tag{3.11}$$

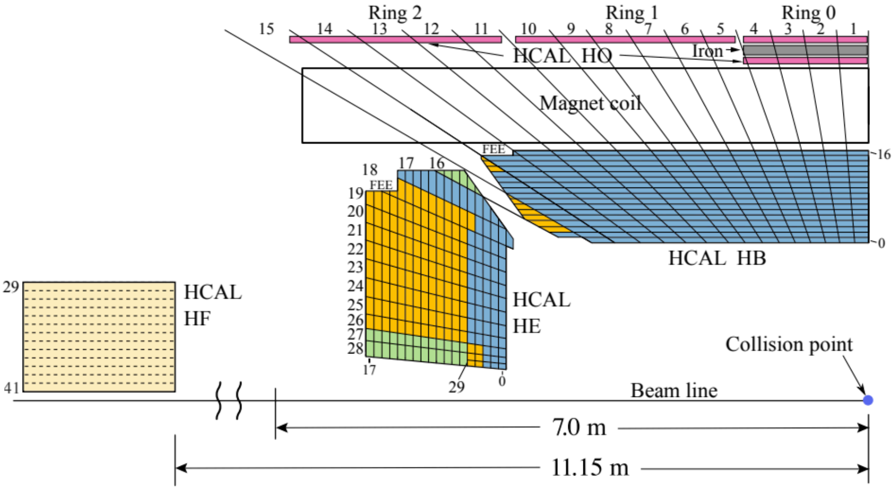

Figure 3.13 A schematic view of one quarter of the CMS HCAL during 2016 LHC operation[86].

3.2.5 Superconducting magnet

One distinctive feature of the CMS is that it can provide a 3.8 T magnetic field, achieved by a superconducting solenoid[18,87]. It is shaped like a cylinder with a length of 12.5 meters and a diameter of 6.4 meters and is constructed of four layers of coils made of stable reinforced NbTi conductors. A cold mass of 220 tons cools the coils to a temperature of 1.8 K, resulting in stored energy of 2.6 GJ at full current. The magnet is enclosed inside a 12000 tons yoke, composing of five barrel wheels and three endcap disks at each end with common structural steel. The overall geometry is shown in Figure 3.14 from Ref[87]. The yoke accounts for only 8% of the central magnetic flux density; its main role is to improve the field uniformity within the tracker volume and to reduce stray fields by returning flux to the solenoid. In addition, the steel plates act as absorbers in the four interleaved layers (”stations”) of muon chambers. The Figure 3.15 shows the magnetic field strength distribution of the magnet.

3.2.6 The Muon System

Muons are about 200 times heavier than electrons, and the relatively small bremsstrahlung radiation makes them less affected than electrons at energies of a few to several hundred GeV. Muons are the only charged particles that are not absorbed by the CMS calorimeters or return yoke. The detection of muons is essential because they are expected to be one of the final decay products of many vital processes. As the middle name of the experiment suggests, the detection of muons is of great importance to CMS: accurate and robust muon measurements have been a central subject from its earliest design stages. The three functionalities of the muon system are muon identification, momentum measurement, and triggering. The high field solenoid magnet and its flux return yoke enable a good muon momentum resolution and triggering capability.

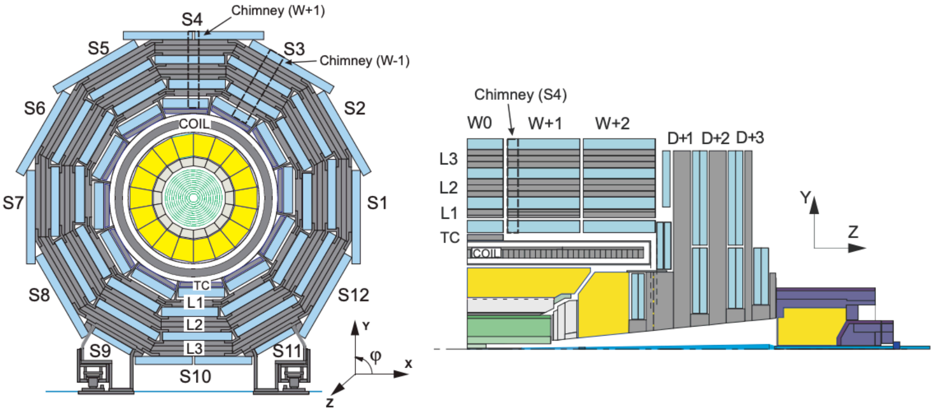

Figure 3.14 Schematic of the CMS detector, including the numbering conventions for the azimuthal sectors (S), wheels (W), barrel yoke layers (L), and end cap discs (D). Left: transverse view at z=0. Right: longitudinal view of the detector quarter.

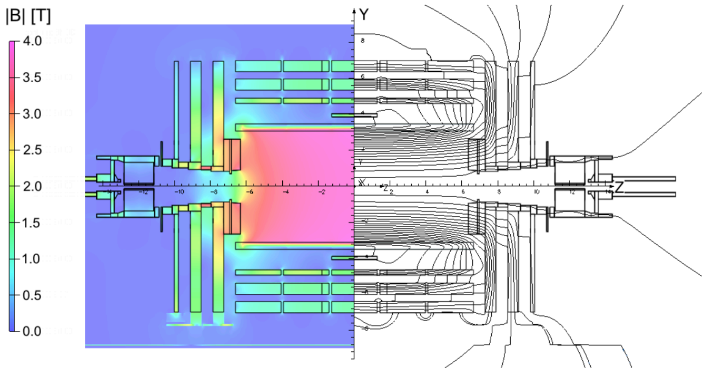

Figure 3.15 At a central magnetic flux density of 3.8 T, the left half of the figure is the value of the magnetic field strength, and the right half is field lines predicted on a longitudinal section of the CMS detector. Each field line represents a magnetic flux increment of 6 Wb.

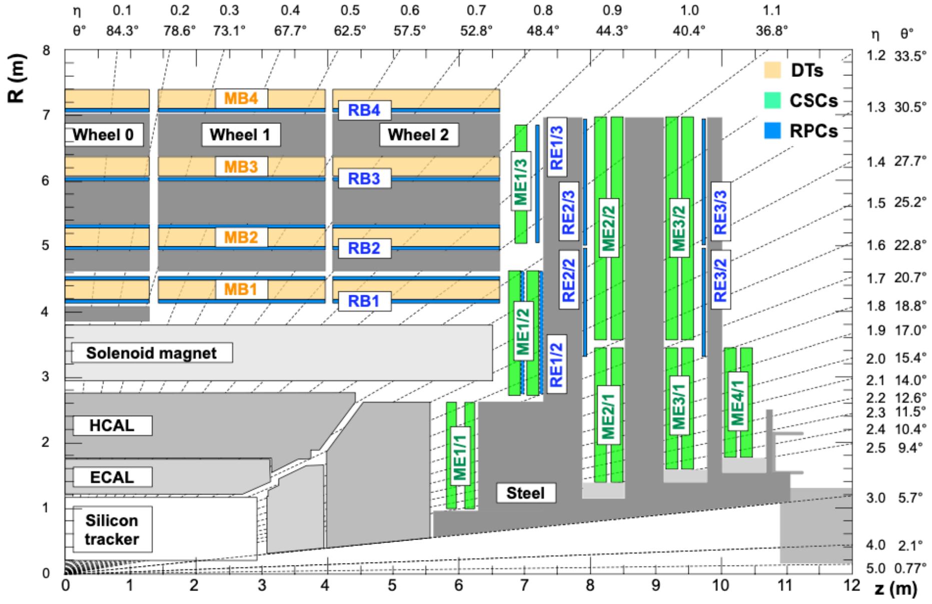

Figure 3.16 Sketch of a quarter of the CMS detector in r-z view, running horizontally parallel to the axis of the beam (z) and increasing in radius (r) upwards[88]. The intersection point is located in the lower left corner. The four drift tubes (DTs, light orange) stations are denoted as MB (muon buckets) and the cathode strip chamber (CSC, green) is denoted as ME (muon endcap). Resistive plate chambers (RPCs, blue) is located in both the CMS barrel and the endcap, which are labeled RB and RE, respectively.

The CMS muon system is located outside the solenoid. Due to the shape of the solenoid magnet, the muon system is naturally driven to have a cylindrical barrel section and two flat end-cap regions. CMS uses three types of gaseous particle detectors to reconstruct the muon tracks covering the region $|\eta| < 2.4$, as shown in Figure 3.16. They are the drift tube chambers (DTs), cathode strip chambers (CSCs), and resistive plate chambers (RPCs).

The neutron-induced background is small in the barrel region, the muon rate is low, and the magnetic field is uniform using drift chambers with standard rectangular drift cells. The DTs cover the region $|\eta| < 1.2$. A DT is a drift tube cell with a transverse size of 42×13 mm^2 and a variable length of 2 to 4 m, filled with a mixture of the Ar (85%) and CO_2 (15%) gas. A gold-plated stainless-steel anode wire is centered inside each tube, four electrodes are used to shape the effective drift field shown as Figure 3.17 (a). The electrical signal is read out by electrodes. Four layers of these drift tubes make a super layer and three super layers form a drift chamber as a station. In each chamber, two superlayers with anode lines parallel to the beam direction and one perpendicular to the beam direction provide three measurements for each impact location: two r-ϕ coordinates and one z coordinate. The spatial resolution per chamber was 80-120 μm in the DTs[88].

The muon rates and background level are higher in the endcaps, and the magnetic field is not uniform. The CSCs with fast response time, covering a region of $0.9 < |\eta| < 2.4$, can provide

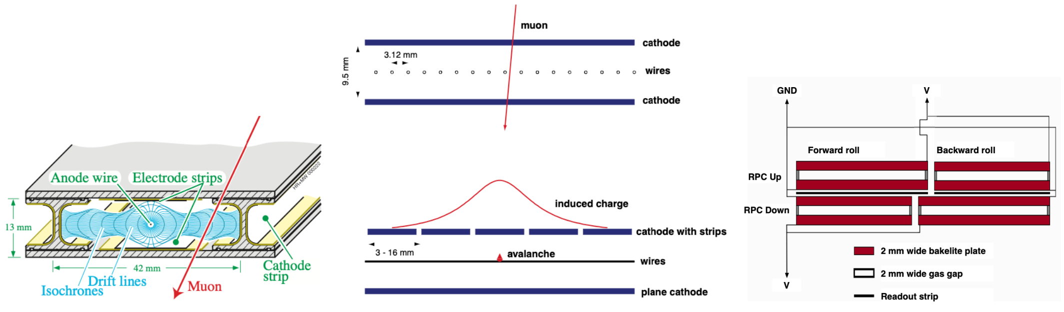

(a) (b) (c)

Figure 3.17 Schematic of each sub-detector in the muon system. Figure (a), section of a drift tube cell showing the drift lines and isochrones. Figure (b), cross-sectional views of the gas gap in a CSC gap with the anode wires and cathode planes, and a schematic of the gas ionization avalanche and induced charge distribution on the cathode strips. Figure (c), Schematic view of a generic barrel RPC with 2 roll partitions. All figures are from Ref[88].

good timing and spatial performance. Each CSC consists of 6 anode wire planes interleaved among seven cathode panels. Each cathode panel contains 80 cathode strips arranged like a radial structure with a constant φ width and projected to the beamline. Among these layers, six gas gaps correspond to 6 anode wire planes, each of which is filled by a mixture of the CO_2 (50%), Ar (40%), and CF_4 (10%) gas. This structure makes the CSCs as standard multi-wire proportional counters, but with a cathode strip readout that precisely measures the position of a muon when the muon transverses across the gas volume. It gives a spatial resolution from 40-150 μm[88]. A schematic of a CSC gap is shown in Figure 3.17 (b).

In addition to the DTs and CSCs, the RPCs mounted in the barrel and endcaps provide excellent time resolution for fast, independent triggering. Each RPC has two gaps, each consisting of two 2-mm-thick Bakelite plates, and the 2-mm-thick air gap is filled with a mixture of $C_2H_2F_4$ (95.2%), i-$C_4H_1$0 (4.5%), and SF_6 (0.3%). A high voltage of 9.6 kV is applied to the thin conductive graphite layer on the outer surface of the resistive plate, which generates an avalanche when a charged particle passes through the RPC and ionizes the gas. The avalanche is quickly sent to the readout strip and forms a signal. Figure 3.17 (c) shows the schematic view of a generic barrel RPC. Time resolution of 3 ns or better can be achieved for each chamber of all 3 systems[88].

3.2.7 The Trigger System

Given that the maximum bunch crossing rate for the LHC pp collisions is about 40 MHz, while for each bunch crossing, the average PU during Run-2 is about 30, and the frequency of proton collisions is around 1 GHz. Considering the design value of the event size of CMS is about 2 MB, this would require a storage throughput of 800 TB/s. Due to the limitations of CPU time consumption, buffer size, and disk storage during data collection, it is impossible and unneeded to record all the information since most collisions are not physical phenomena of interest. The maximum capacity of the computational farm is 1 kHz. Therefore, the event rate must require a drastic rate reduction. This task is performed by the trigger system[18,89-90], which is the start of the physical event selection process. The CMS experiment serves a Level-1 (L1) trigger system that uses custom-designed, primarily programmable electronics to filter non-interesting physical analysis events at a maximum rate of 100 kHz. Adopted events are then sent to the High-Level Trigger (HLT), which uses the CMS offline reconstruction software in commercial PCs to reduce the rate to 1 kHz further. Finally, these events are sent to the CERN Tier system for reconstruction, calibration, and storage. Finally, these events are sent to the CERN Tier system for reconstruction, calibration, and storage.

3.2.7.1 The L1 Trigger

The Level-1 trigger system[90] in the CMS experiment uses only information from the muon system and calorimeter with coarse granularity to immediately but roughly reconstruct physical objects such as photons, electrons, muons, jets, etc. The triggering algorithm then uses simple criteria such as the lateral energy of the physical object E_{T} or η to select events. The L1 architecture is shown in Figure 3.18 and consists of three subsystems:

- The L1 calorimeter trigger, which is responsible for processing ECAL and HCAL information. The calorimeter trigger consists of two layers. Layer-1 receives, calibrates, and sorts the local energy deposits (Trigger Primitives, or TPs); Layer-2 uses these calibrated TPs to reconstruct and calibrate physics objects such as electrons, tau leptons, jets, and energy sums. A demultiplexer (DeMux) board then reorders, reserializes, and formats the events for the global trigger[90].
- All three subdetectors of the muon system, i.e. DT, CSC and RPC, are involved in triggering and their signals are combined together into TPs to reconstruct the muon and measure its p_{T}. The TPs provide information on coordinates, timing, and quality information from detector hits. The muon trigger system consists of three muon track finders (MTFs), which reconstruct muons in the barrel (BMTF), overlap (OMTF), and endcap (EMTF) regions of the detector, and the global muon trigger (μGMT) for final muon selection[90].
- The L1 global trigger finally collects muons and calorimeter objects and executes each algorithm in the menu in parallel to make the final trigger decision. It checks if at least one of the thresholds in the L1 Trigger menu is passed.

3.2.7.2 The HLT trigger

Events that pass through the Level 1 trigger are sent to the HLT system. The hardware of the HLT comprises a single processor field of commodity computers, the Event Filter Field (EVF), which performs a more complete and precise object reconstruction using the complete detector information. Therefore, not only simple physical quantities like E_{T} or η but more

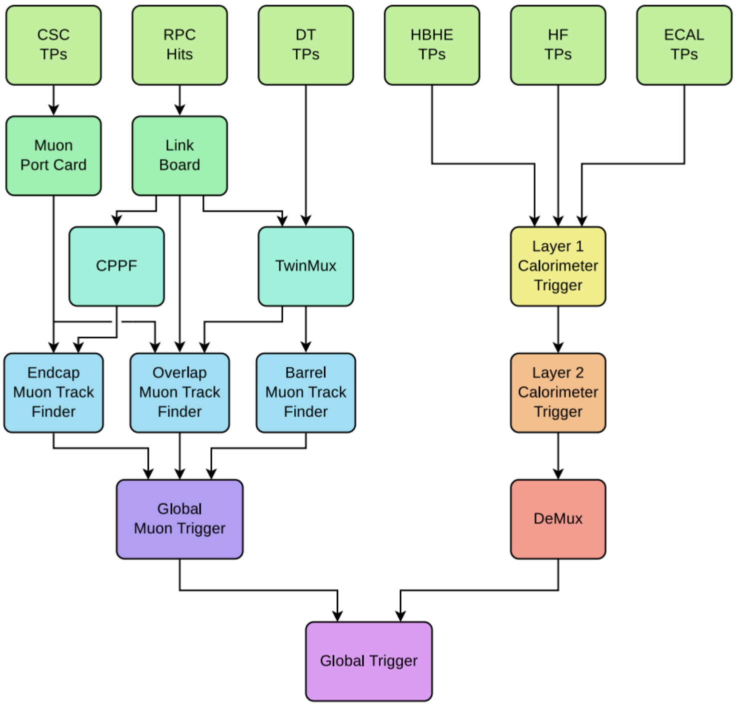

(a)

Figure 3.18 Schematic of the upgraded CMS Level-1 trigger system during Run 2[90].

sophisticated variables like shower shape, isolation and track-vertex related variables are considered as criteria in the menu. Since HLT is completely software-based, improvements to the HLT algorithm are easy to implement and do not require any hardware involvement. With a maximum processing time of about 320 ms per event, HLT provides higher performance to identify the most interesting events and reduces the rate given by the L1 trigger from 100 kHz to 1 kHz. Once events are accepted by HLT, they are divided into different data sets corresponding to the selection criteria of HLT. In this way, a dataset groups events with a set of common trigger selections, e.g., a muon dataset would include all events with muon triggers. These datasets are then sent to the LHC grid.

3.2.8 The CMS software

To process the digital detector signals from the readout electronics and convert them into physics objects, the CMS collaboration develops its C++ based software framework called CMSSW[91]. CMSSW provides a collection of all the CMS detector classes and things needed to handle the simulation, calibration, alignment, and reconstruction modules of the event data so that physicists can perform their analysis. Reconstruction of physics objects is performed in steps, where information from each subsystem is combined to form the complete reconstructed event. All systems are connected through a Python configuration module that can perform an entire software loop. After the CMSSW framework processes the data, the information is stored in ROOT[92] compatible objects that allow the user to perform data analysis.

Chapter 4

Reconstruction of physics objects

In the CMS experiment, the reconstruction of physics objects relies on a so-called Particle-Flow (PF) algorithm[93], developed by the CMS collaboration and used in almost all the physics analysis. In this chapter, the techniques to perform the reconstruction and identification of the physics objects needed in this thesis are introduced. The studies of polarized same-sign WW scattering and searches for Majorana neutrinos and Weinberg operator in pp → $\mu^{\pm}\mu^{\pm}jj$ use the identical framework developed for H→WW[94] analysis. The measurement of Wγ production cross section and constraints on EFT coefficients uses another analysis framework with different physics objects definitions. Thus, for the identification of physics objects, the illustrations in the first two analyses are described first, followed by the description in the last one.

4.1 The Particle-Flow algorithm

The PF algorithm aims at reconstructing and identifying all stable particles i.e. muons, electrons, photon, charged hadrons and neutron hadrons from collisions by combining the information from all subdetectors, as illustrated in Figure 4.1.

The algorithm starts from tracks and clusters. Hits reconstruct the tracks of charged particles on sensitive layers from either the inner tracker system or the muon detector. The position and energy deposited of electromagnetic and hadronic showers from the ECAL and HCAL are reconstructed by dedicated clustering algorithms. According to the reconstructed tracks, the positions of vertices associated with these tracks are further built to reconstruct interaction points of pp collisions. These tracks and clusters are finally collected to assemble a set of PF elements.

Once the PF elements are reconstructed, the PF algorithm executes a dedicated linking algorithm corresponding to the target stable particles to determine the relationship between the different PF elements. The linking algorithm spatially connects vertices, tracks, and showers to some stable particles. Each stable particle's corresponding energy and propagation direction

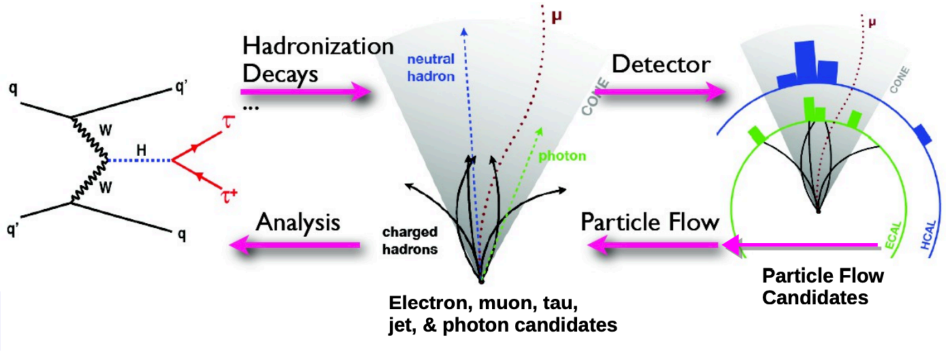

(a)

Figure 4.1 Concept of the CMS Particle-Flow (PF) algorithm. The top half of the figure shows how collisions lead to particle decays and final states of particles that leave tracks and deposits in the CMS detector. The bottom half shows that PF candidates are derived from the detector information. Then those candidates become the input to the PF algorithm, which uses them to construct high-level physics objects such as leptons and jets that are used to reconstruct the collision events[95].

can be optimally determined. Once the target particles are reconstructed, the associated PF elements are blocked from the PF element list, they are not used for the construction of other objects. For the PF algorithm in the CMS experiment, the priority of the reconstruction procedure depends on the level of essential features of the particular object. It starts with the muon reconstruction, which has vital features for other stable particles. The algorithm then targets isolated photons and electrons, and finally reconstructs the remaining non-isolated photons, charged and neutron hadrons. These physical objects are eventually collected as a set of PF candidates. Particle-based physical objects, such as jets and missing transverse energies, can be further reconstructed with these PF candidates.

4.2 Tracks and vertices

Inner tracks and clusters are the most basic elements in the Particle-Flow algorithm.

In the CMS experiment, there are several iterations for the tracking process, each of which has different configuration and targeted tracks. The first iteration aims at the prompt tracks with $p_T > 0.8$ GeV and three (four) pixel hits which are the dominant source in all reconstructed tracks. The next iteration recovers the prompt tracks with only two (three) pixel hits. The later iterations will search for lower pT tracks or tracks not originating from interaction points or not found in the previous iterations. Each tracking iteration is composed of four steps: seed generation, track finding, track fitting and track selection described in Ref[96].

The track reconstruction in the CMS experiment uses a specialized tracking algorithm called Combinatorial Track Finder (CTF), which runs several iterations of the Combinatorial Kalman Filter (KF)[97] that integrates pattern recognition and track fitting, as opposed to the standard KF algorithm. The most significant tracks with relatively high p_{T} or close to the interaction point are found at the beginning of the iteration. At the end of the iteration, the hits associated with these reconstructed tracks are masked out from the general hit list, requiring searching for lower importance tracks. The tracking process has several iterations in the CMS experiment, each with a different configuration and target tracks. The first iteration targeted prompt tracks with $p_{\mathrm{T}} > 0.8$ GeV and three (four) pixel hits, the primary source of all reconstructed tracks. The next iteration recovers the prompt tracks with only two (three) pixel hits. Subsequent iterations search for lower p_{T} tracks or tracks that do not originate from interaction points or tracks not found previous. Each tracking iteration consists of four steps: seed generation, track finding, track fitting, and track selection, as described in Ref[96].

- **Seed generation**: The seeds are defined by 2 or 3 hits that fit the spiral trajectory assumption from an origin. These seeds determine the initial trajectory parameters and their uncertainties.
- **Track finding**: The KF algorithm starts with those track parameters provided by track seeds with rough estimates. It builds track candidates by including more hits from successive tracker layers, updating the track parameters at each layer. This process is repeated layer by layer until the termination conditions are satisfied and the track candidates eventually form.
- **Track fitting**: The KF and smoother are refitted for each track candidate to give the best track parameters, including the innermost and outermost hits on the track, which are used to infer the track to the interaction point and outermost sub-detector, respectively. The refitting process iterates through all the hits from the inside outwards. It also updates the track estimations at each hit in turn. A large factor expands the covariance matrix at each iteration to avoid bias due to beam spot constraint.
- **Track selection**: These refitted trajectories are chosen based on qualitative requirements such as good χ^2/d.o.f and the number of layers of reconstructed trajectories not associated with charged particles.

Finally, the tracks found are combined into a single set. Then the algorithm can further reconstruct the vertices associated with these tracks. Vertex reconstruction aims to measure the location and associated uncertainty of the interacting points from the pp collisions, including the primary vertex from which the physics of interest comes and the vertices from PU collisions. These vertices are pretty vital information for further physics object reconstruction and identification.

In vertex reconstruction, there are three steps. The first step is the selection of the tracks originating from the interaction region. Some requirements are applied, such as impact factors related to the spot region and simple track qualities. The next step is to group tracks originating from the same interaction vertex. This step performs a deterministic annealing (DA) algorithm[98] and uses the z-coordinates of the chosen tracks and the beamspot positions. Finally, each vertex is reconstructed by performing a grouping fit with at least two tracks to obtain the best-estimated vertex parameters, e.g., their x, y, and z positions. The vertex with the largest summed squared transverse momenta ($\sum p_{\mathrm{T}}^2$) is chosen as the event primary vertex.

4.3 Calorimeter clusters

The calorimeter clusters are important to estimate energies and directions of physics objects using the information from the ECAL and HCAL. A specific clustering algorithm was developed for the PF event reconstruction[93]. The clustering algorithm detects and measures the energy and direction of stable neutral particles, such as photons and neutral hadrons. These neutral particles are then separated from the energy deposition of charged hadrons. In addition, the algorithm reconstructs and identifies electrons and all accompanying bremsstrahlung photons. Finally, it helps to measure the energy of charged hadrons whose track parameters are not accurately determined, such as charged hadrons in low-quality and high-p_{T} tracks.

Clustering is performed individually in each subdetector, the ECAL barrel and endcaps, the HCAL barrel and endcaps, and the two preshower layers. The clustering algorithm is a three-step process:

1. Clustering seeds are identified as cells with energy greater than a given seed threshold.
2. Topological clusters are created from the seeds by adjacent aggregating cells whose energy exceeds a unit threshold set to twice the noise level.
3. An expectation maximization algorithm of Gaussian mixture model based is used to reconstruct the clusters within the topological cluster.

The Gaussian mixture model assumes that the energy deposition in M individual cells of the topological cluster comes from N Gaussian energy deposits, with N being the number of seeds. The expectation-maximization algorithm is an iterative algorithm with two steps per iteration. For the first step, the parameters of the model are kept constant and the expected fraction f_{ji} of the energy E_j measured in the cells generated from the ith Gaussian energy deposition, calculated as

$$f_{ji} = \frac{A_i \mathrm{e}^{-\left(\vec{c}_j - \vec{\mu}_i\right)^2 / \left(2\sigma^2\right)}}{\sum_{k=1}^{N} A_k \mathrm{e}^{-\left(\vec{c}_j - \vec{\mu}_k\right)^2 / \left(2\sigma^2\right)}}, \tag{4.1}$$

where A_i is the amplitude of the ith Gaussian, $\vec{\mu}_i$ the mean in the (η, ϕ) plane of ith Gaussian, and σ is the width fixed to different values depending on the considered calorimeter. The second step determines the parameters of the model in an analytical maximum-likelihood fit yielding

$$A_i = \sum_{j=1}^{M} f_{ji} E_j, \vec{\mu}_i = \sum_{j=1}^{M} f_{ji} E_j \vec{c}_j. \tag{4.2}$$

The position and energy of the converged Gaussian function are used as cluster parameters.

4.4 Muon

The following sections introduce the muon reconstruction, identification, momentum scale corrections used in this thesis.

4.4.1 Muon reconstruction

Muons are first reconstructed under the PF algorithm. Since muons can pass through the whole detector and leave hits in all sub-detectors, the muon reconstructions are based on muon track reconstructions. The CMS experiment considers three approaches[99] for reconstructing muons.

- **Standalone muon**: Muon tracks rely on the muon system by combining hits from the CSC, DT, and RPC. The reconstruction starts from the seed generation of the DT or CSC segments and then uses the KF technique to build the muon trajectories.
- **Tracker muon**: The muon tracks are built ”inside-out,” i.e., muon systems with $p_{\mathrm{T}} > 0.5$ GeV and total momentum $p > 2.5$ GeV are extrapolated from the internal tracking system 3.2.2 and loosely matched with DT or CSC segments. If at least one of them is a match, then the inner track is believed to be the tracker muon track.
- **Global muon**: Matching the standalone muon tracks and the inner tracking tracks to build the muon tracks are in an ”outside-in” way. Once some mutual surface is found by comparing the parameters of these two tracks, a global muon track can be constructed from the information of the independent muon track and the internal tracker track by performing an integrated fit with the KF technique.

The global muon momentum can be extracted from the combination of tracker plus standalone tracks. Additional particles from the ECAL showers can create reconstructed hits and segments in the muon system. When reconstructing muons at high p_{T}, e.g., $p_{\mathrm{T}} > 200$ GeV, the trajectory building algorithm can identify these extra segments instead of the right muon track segments. Therefore, the information from the muon system needs to be handled carefully in the high p_{T} case. A set of high p_{T} muon track refits has been developed to solve this issue: the ”tracker-plus-first-muon-station” (TPFMS) fit, the ”Picky” fit, and the ”dynamic truncation” (DYT) fit. A so-called ”TuneP” algorithm chooses the best muon reconstruction among the four fits and performs the momentum assignment[100].

4.4.2 Muon identification and isolation

Depending on the physics analyses, several muon definitions can be used by modifying the selections based on the muon identification variables. For muons, all studies in this thesis use customized identifications based on the ”Tight” working point developed by the Muon Physics Object Group (POG)[101], noted as ”Muon Tight-WP”. The Muon Tight-WP selects a subset of the PF muons, which requires a set of muon identification variables. The selection criteria include the track fit χ^2 during the muon reconstruction, number of valid hits in the muon chambers, pixel detector and tracker layers, number of segments in the muon stations, and impact parameters with regards to the primary vertex. The summary about the criteria is shown in Table 4.1.

Table 4.1 Selection criteria at Tight working point in the Muon POG identification

Variable	**Requirement**
The candidate is reconstructed as a Global Muon	Yes
The candidate is a PF Muon	Yes
χ^2/ndof	< 10
Number of valid hits in the muon DTs	> 0
Number of valid segments in the muon CSCs	> 1
Matched muon stations	> 1
The transverse distance of the tracker track w.r.t. the primary vertex (d_{xy})	< 2 mm
The longitudinal distance of the tracker track w.r.t. the primary vertex (d_z)	< 5 mm
Number of valid pixel hits	> 0
Number of tracker layers with valid hits	> 5

The H→WW analysis framework adds several customized selections to the Muon Tight-WP to improve the quality of muons, noted as Muon HWW-ID. The additional variables are shown in Table 4.2.

Table 4.2 Additional selections required in Muon HWW-ID.

Variable	**Requirement**
p_{T}	10 GeV
$\lvert\eta\rvert$	2.4
d_{xy}	< 0.1 mm for $p_{\mathrm{T}} < 20$ GeV; < 0.2 mm for $p_{\mathrm{T}} > 20$ GeV
d_z	< 1 mm

In addition, to distinguish between prompt muons from W and Z boson decays and muons from heavy flavor decay within jets (also called non-prompt muons), an isolation criterion is applied in Muon HWW-ID. A relative isolation variable, I^{μ}_{rel}, is defined as the sum of the energy scale of all other particles within a geometric cone ($\Delta R = 0.4$) around the muon

$$I^{\mu}_{rel} = \frac{1}{p^{\mu}_{\mathrm{T}}}\left[\sum p_{\mathrm{T}}^{\text{ch.had.}} + \text{Max.}\left(0, \sum p_{\mathrm{T}}^{\text{neu.had.}} + \sum p_{\mathrm{T}}^{\gamma} - \Delta\beta \sum p_{\mathrm{T}}^{\text{ch.had.PU}}\right)\right], \tag{4.3}$$

where p^{μ}_{T}, $p_{\mathrm{T}}^{\text{ch.had.}}$, $p_{\mathrm{T}}^{\text{neu.had.}}$, p_{T}^{γ} represent the transverse momentum of the muon, charged hadrons, neutral hadrons and photons, respectively. The energy of neutral particles in the cone is overestimated because neutral particles at the PU vertices cannot be eliminated within the acceptance range of the tracker. The ratio of neutral particles to charged hadrons in inelastic proton-proton collisions, according to the simulation results, is about 0.5. Therefore, the PU correction is applied to the energy scale sum of the charged hadrons from PU vertices ($\sum p_{\mathrm{T}}^{\mathrm{ch.had.PU}}$) with $\Delta\beta = 0.5$[102].

Two muon selections are considered. A muon is labeled as *tight-HWW* if it passes Muon HWW-ID and $I^{\mu}_{rel} < 0.15$. A muon is labeled as *loose-HWW* if it passes Muon HWW-ID and $I^{\mu}_{rel} < 0.40$. The *loose-HWW* is used in the fake lepton background estimation procedure, described in Section 5. which involves extrapolation from the loose-but-not-tight lepton selection to the *tight-HWW* selection. The *loose-HWW* muon selection is also used to reject events with muons more than the required in the final states.

By applying the Tag and Probe(T&P)[103] technique to the $Z/\gamma^* \longrightarrow \mu^+\mu^-$ event, the efficiency of identification and isolation selections applied to the muons is determined as a function of muon p_{T} and η. The identification efficiency, $\epsilon_{tight-HWW}$, is evaluated assuming muons passing through the tracker muon requirement. In contrast, the isolation efficiency, ϵ_{ISO}, is calculated assuming muons passing through the *tight-HWW* requirement. The final muon identification and isolation efficiency is > 85% for muons with $p_{\mathrm{T}} > 20\,\mathrm{GeV}$ and > 98% for muons with $p_{\mathrm{T}} > 40$ GeV. To correct for small effects not considered in the simulation, the simulated events are corrected for the efficiencies of muon identification and isolation observed in the actual data with scale factors (SFs). The scale factors are defined as the ratio between the efficiencies in data (ϵ_{DATA}) and in simulation (ϵ_{MC}).

$$SF\left(p_{\mathrm{T}}, \eta\right) = \frac{\epsilon_{DATA}\left(p_{\mathrm{T}}, \eta\right)}{\epsilon_{MC}\left(p_{\mathrm{T}}, \eta\right)}. \tag{4.4}$$

The SF values for the muons and their systematic errors are calculated in the H→WW[94] framework.

4.4.3 Muon momentum corrections

There is a possible bias in the muons momentum measurement in the LHC, which can originate from a variety of sources such as as detector misalignment, software reconstruction bias, and uncertainties in the magnetic field. The Rochester group developed a method to extract corrections for the possible bias[104-105]. These corrections are derived from a sample of $Z/\gamma^* \longrightarrow \mu\mu$ events, in bins of charge, η, and ϕ of the muons. They are based on the comparison of the position of the peak in the dimuon invariant mass ($m_{\mu\mu}$) distributions with the nominal Z boson mass. Both data and MC samples are corrected with this method, which also provides a estimation of the associated systematic uncertainty. Figure 4.2 shows the data and MC comparison in 2017 before and after the Rochester corrections. The uncertainty in the muon momentum for all three years is considered to be 0.2% for both data and Monte Carlo (MC) simulated events.

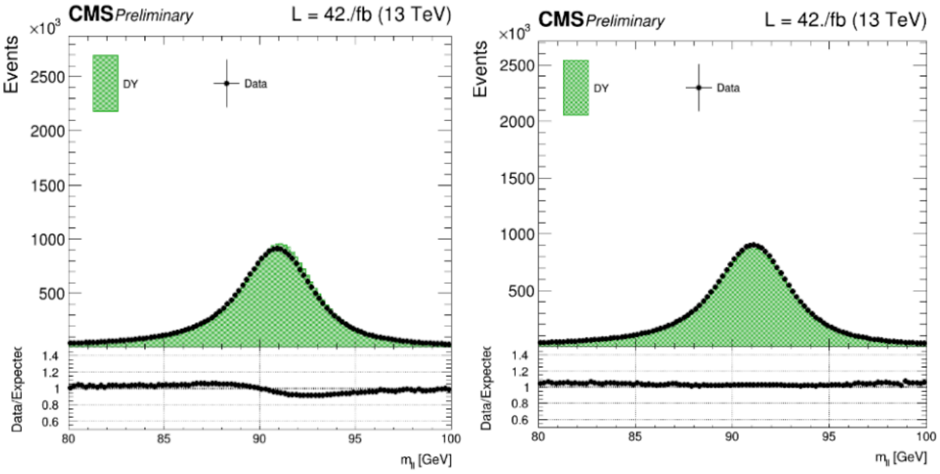

(a) (b)

Figure 4.2 Example data and MC comparison in 2017, (a) before the correction, (b) after the correction.

4.5 Electron and Photon

The following sections introduce the electron and photon reconstruction, identification, momentum scale and resolution used in this thesis. The electrons are used in all three analyses, the photons are only used in the measurements of Wγ.

4.5.1 Electron and Photon reconstruction

Due to the similar response of the ECAL detector, the reconstruction of electrons and photons share the same algorithm[106]. The difference is that the electron reconstruction performs an additional algorithm to reconstruct the electron trajectory. The electron tracks provide a more accurate measurement from the electron momentum and identify electrons and photons during the reconstruction. However, when photons or electrons arrive at the ECAL from the interaction point, they may interact with the internal tracker material and produce many different scenarios such as bremsstrahlung and conversion, making it a challenge to recover the original electron or photon, as shown in Figure 4.3.

The reconstruction of electrons and photons starts from PF clusters in the ECAL, which can overlap and share the same ECAL energy deposition. In addition, bremsstrahlung and photon transitions occur mainly in the material before hitting the ECAL. Hence, one ECAL cluster is not sufficient to recover the energy of the initial electron or photon. Instead, these associated ECAL clusters must be combined into a cluster called ”supercluster” (SC). To collect cluster energy deposits spread along ϕ direction due to the strong magnetic field, CMS uses a so-called mustache algorithm, as shown in 4.4, which includes information from the ECAL and preshower detectors. The algorithm starts from a seed cluster above a given threshold. The

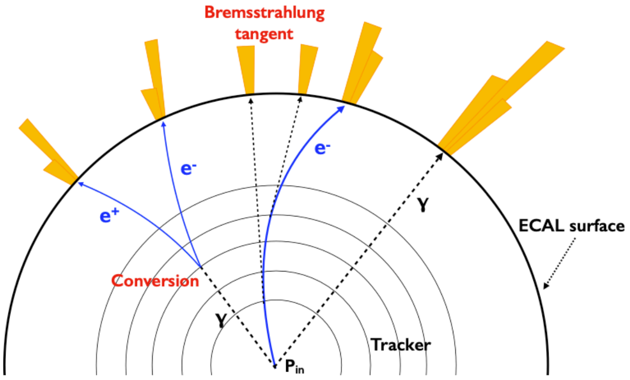

Figure 4.3 Event overview with a converted, an unconverted photons, and an electron including bremsstrahlung tangents.

additional clusters located in the mustache-like region in the $\eta - \phi$ plane concerning this seed cluster are added to form a SC.

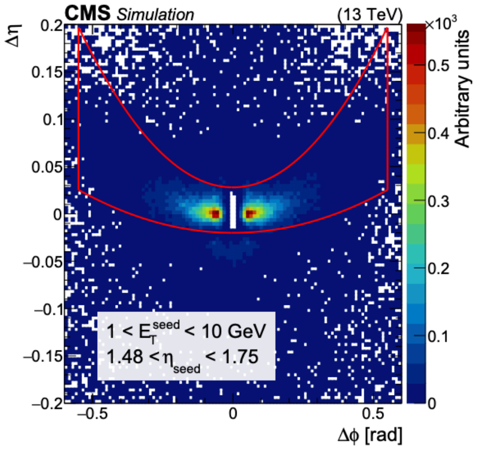

Figure 4.4 Distribution of $\Delta\eta = \eta_{\text{seed-cluster}} - \eta_{\text{cluster}}$ versus $\Delta\phi = \phi_{\text{seed-cluster}} - \phi_{\text{cluster}}$ for simulated electrons with $1 < E_{\text{T}}^{\text{seed}} < 10\,\text{GeV}$ and $1.48 < \eta_{\text{seed}} < 1.75$. The z-axis shows the occupation of the number of PF clusters that match the simulation (requiring at least 1% of the simulated electron energy to be shared) around the seed. The red line contains roughly the set of clusters selected by the mustache algorithm. The white area in the center of the figure represents the $\eta - \phi$ footprint of the seeded clusters.

The CMS also reconstructs electrons by track. Electron energy loss mainly originates from bremsstrahlung instead of ionization in the inner tracker layers. The distribution of fractional energy loss can be described by the Bethe-Heitler formula, which is non-Gaussian distribution. The standard KF algorithm is no longer applicable. Instead, a Gaussian-sum filter (GSF) algorithm is used, which uses a sum of multi-Gaussian functions to approximate the Bethe-Heitler formula and estimates the parameters of the electron trajectories under the assumption of a homogeneous magnetic field.

GSF track reconstruction starts with ECAL-driven or tracker-driven electron track seeding. ECAL-driven seeding approach selects SCs with the transverse energy greater than 4 GeV ($E_{\mathrm{T}}^{\mathrm{SC}} > 4\,\mathrm{GeV}$) and the ratio of HCAL tower energy deposited in a cone size of $\Delta R < 0.15$ centered on the SC position (H) to the total SC energy (E^{SC}) smaller than 0.15 ($H/E^{\mathrm{SC}} < 0.15$). Each selected SC, its energy-weighted position, transverse energy, and magnetic field are used to infer the trajectory toward the collision vertex (outside-in), assuming a spiral trajectory and no radiative emission. On the other hand, the tracker-driven seeding method is specific to all inner tracks. A given internal track is considered a GSF track seed if it is compatible with ECAL clusters by using some criteria of track mass and track cluster matching variables. The ECAL-driven method is more suited for isolated or high-p_{T} electrons, while the tracker-driven method is suited for low-p_{T} electrons. The electron track seeds from those two methods are then grouped as the start of the electron track reconstruction. Once the electron track candidates and their hits are collected, a GSF fit is applied to obtain the track parameters. The combination of the measured energy by the ECAL and the tracker greatly improves the energy resolution, as described in Figure 4.5.

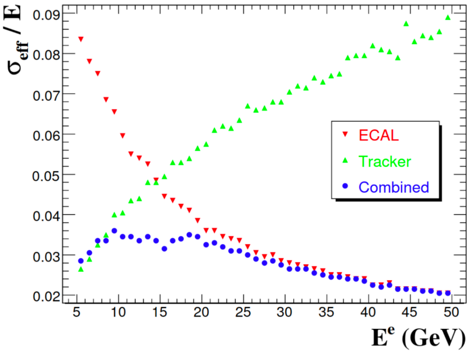

Figure 4.5 Resolution measured with ECAL superclusters (red), tracker tracks (green), and tracker-supercluster combinations (blue) as a function of the generated electron energy[107].

Once the SCs and GSF tracks are reconstructed, all ECAL clusters, inner tracks, SCs, and GSF tracks will be connected and integrated. Then, the transitions and bremsstrahlung are reconstructed to recover the missing parts, forming refined SCs. After that, all ECAL clusters, general tracks, refined SCs, and GSF tracks are grouped to form the e/γ hypothesis. Some loose choices based on the BDT classifier are applied to the e/γ objects. Finally, each electron candidate is defined as an e/γ object with GSF tracks and refined SCs, while the photon candidate is an object with refined SCs only.

4.5.2 Electron identification and isolation

Several strategies are used in CMS to identify prompt electrons[106] and to reduce the background from photon conversion, jets misidentified as electrons, and electrons from heavy quark decays. The identification of electrons is based on several tracking quality and calorimeter variables:

- H/E_{SC}: ratio of energy deposited in the HCAL tower behind the ECAL seed to the SC energy in the ECAL.
- $\left|\frac{1}{E_{\mathrm{SC}}} - \frac{1}{p}\right|$: the difference of the inverse of the SC energy E_{SC} in ECAL, and the inverse momentum p in the tracker.
- $\Delta\eta$: difference between SC and position of inner track extrapolated from interaction vertex.
- $\Delta\phi$: difference between SC and position of inner track extrapolated from interaction vertex.
- $\sigma_{i\eta i\eta}$: a variable corresponding to the ECAL shower shape, which is the weighted cluster RMS along η-direction inside 5x5 block of crystals of SC.
- $\sigma_{\phi\phi}$: a variable corresponding to the ECAL shower shape, which is the weighted cluster RMS along ϕ-direction inside 5x5 block of crystals of SC.
- $1 - E^{1\times5}/E^{5\times5}$: circularity, where $E^{n\times m}$ is the sum of cluster energies of n cells in ϕ and m cells η region.
- $R9$: defined as $1 - E^{3\times3}/E_{SC}$.
- $\Delta\eta^{\mathrm{SC}}_{trk}$ spatial matching between the track and SC in the η direction.
- $\Delta\phi^{\mathrm{SC}}_{trk}$ spatial matching between the track and SC in the ϕ direction.
- GSF track $\chi^2/$ ndof: calculated from the reconstructed track and corresponding hits.
- Missing inner hits: missing hits are calculated in the inner tracker of electron candidates, because for timely electrons there are no missing hits because their trajectory starts from the beampipe.
- Photon conversion veto: the track pairs that fit well with the common vertex of the converted photon $\gamma \longrightarrow e^+e^-$ are rejected.
- d_{xy} and d_z: the transverse and longitudinal impact parameters with respect to the primary vertex.

The other critical part of the background comes from non-prompt electrons caused by misidentified jets or real electrons from the decay of semileptonic quarks. In both cases, the candidate electrons have significant energy deposited in the vicinity of their trajectories. Therefore, electrons need to be isolated from such nearby activity, which can significantly reduce this background. Like the muon, the electron isolation variable is defined as

$$I^e_{\mathrm{rel}} = \frac{1}{p^e_{\mathrm{T}}}\left[\sum p^{\mathrm{ch.had.}}_{\mathrm{T}} + \max\left(0, \sum E^{\mathrm{neu.had.}}_{\mathrm{T}} + \sum E^{\gamma}_{\mathrm{T}} - \rho\cdot A_{\mathrm{eff}}\right)\right], \tag{4.5}$$

where $p^{\mathrm{ch.had.}}_{\mathrm{T}}$, $p^{\mathrm{neu.had.}}_{\mathrm{T}}$, and p^{γ}_{T} are the transverse momenta of charged hadrons, photons, and neutral hadrons inside an isolation cone of $\Delta R = 0.3$ with respect to the electron direction. To correct the isolation to mitigate the effect of PU, the quantity $\rho \cdot A_{\mathrm{eff}}$ is therefore subtracted from the relative isolation, where ρ is the median transverse energy density per unit area in the event. A_{eff} is the area of the isolation region, weighted by a factor that takes into account the dependence of the PU transverse energy density on the object η.

The CMS EGamma POG provides two sets of electron identification. One is known as the cut-based ID, which is based on the selections of the aforementioned electron identification and isolation variables. The other one is based on a Multivariate analysis (MVA) approach, a single discriminator variable is computed based on the electron identification and isolation variables which provides separation between the signal and backgrounds on the basis of Boosted Decision Tree (BDT) algorithm. In the H→WW analysis framework, several working points of the electron IDs are considered, a *loose-HWW* electron ID and a *tight-HWW* electron ID are defined. The *tight-HWW* selection is used to select the events in the signal regions and control regions. The *loose-HWW* selection is used in the fake lepton background estimation procedure, described in Section 5.3.1, which involves extrapolation from the loose-but-not-tight lepton selection to the tight selection.

For 2016, *loose-HWW* electron corresponds with the EGamma POG cut-based ”HLT Safe” electron selection, along with the additional requirements on the impact parameter variables and the expected missing inner hits listed in Table 4.3. The *tight-HWW* electron corresponds with EGamma POG cut-based Tight WP with same requirements in Table 4.3.

Table 4.3 Additional requirements for *loose-HWW* electron in 2016.

Variable	**Cut (EB)**	**Cut (EE)**
Expected missing inner hits ≤	1	1
abs(d0) <	0.05	0.1
abs(dz) <	0.1	0.2

Different from 2016, for 2017 and 2018, *looseHWW* electron uses the EGamma POG cut-based ”Medium” electron selection, while *tight-HWW* considers MVA identification ”Fall17-V1-MVA-WP90” with the 90% signal efficiency working point. Both IDs applied additional impact parameters and calorimetric selections in Table 4.4. The efficiencies of the IDs used in this thesis, are calculated as a function of the electron p_{T} and η by using the T&P technique on $\mathrm{Z}/\gamma^{*} \rightarrow e^{+}e^{-}$ events. the simulated events are corrected for the efficiencies of electron identification and isolation observed in the actual data with SFs. Figure 4.6 shows the electron *tight-HWW* efficiency and SFs as a function of the electron p_{T} and the electron η in 2018 separately. Figure 4.7 shows the electron *tight-HWW* efficiency and SFs as a function of the electron p_{T} and η in 2018.

4.5.3 Electron momentum scale and resolution

Specialized algorithms are used to correct the measured energies in the ECAL and estimate the electron p_{T} by combining independent measurements in the ECAL and the tracker. The ECAL energy response in individual crystals is calibrated before clustering. A correction factor is applied to account for radiation-induced changes in crystal transparency, which the laser

Table 4.4 Additional cuts in our 2017/2018 *loose-HWW* electron.

Variable	**Cut (EB)**	**Cut (EE)**
sigmaIetaIeta ($\sigma_{i\eta i\eta}$) <	–	0.03
ooEmoop ($\frac{1}{E_{SC}} - \frac{1}{p}$) <	–	0.014
abs(dxy) <	0.05	0.1
abs(dz) <	0.1	0.2

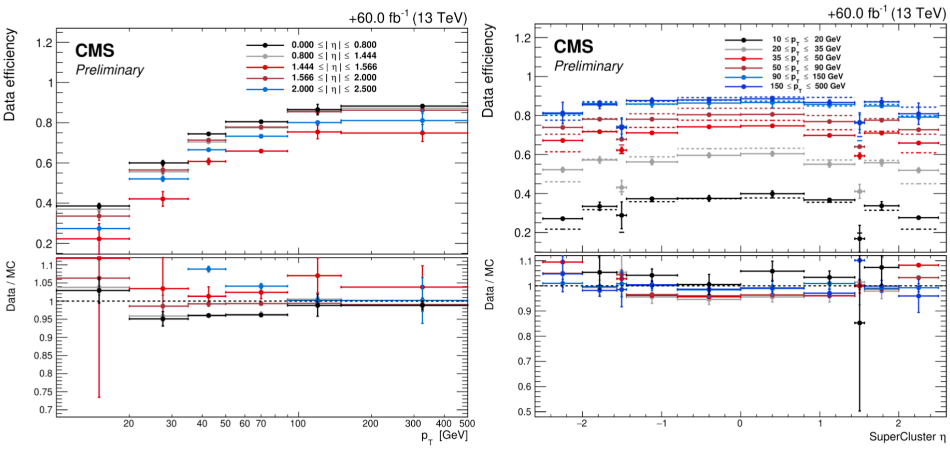

Figure 4.6 Efficiencies for *tight-HWW* for the 2018 dataset as a function of electron p_T (left) and electron η (right) are shown in the upper half of the plots and scale factors in the lower half.

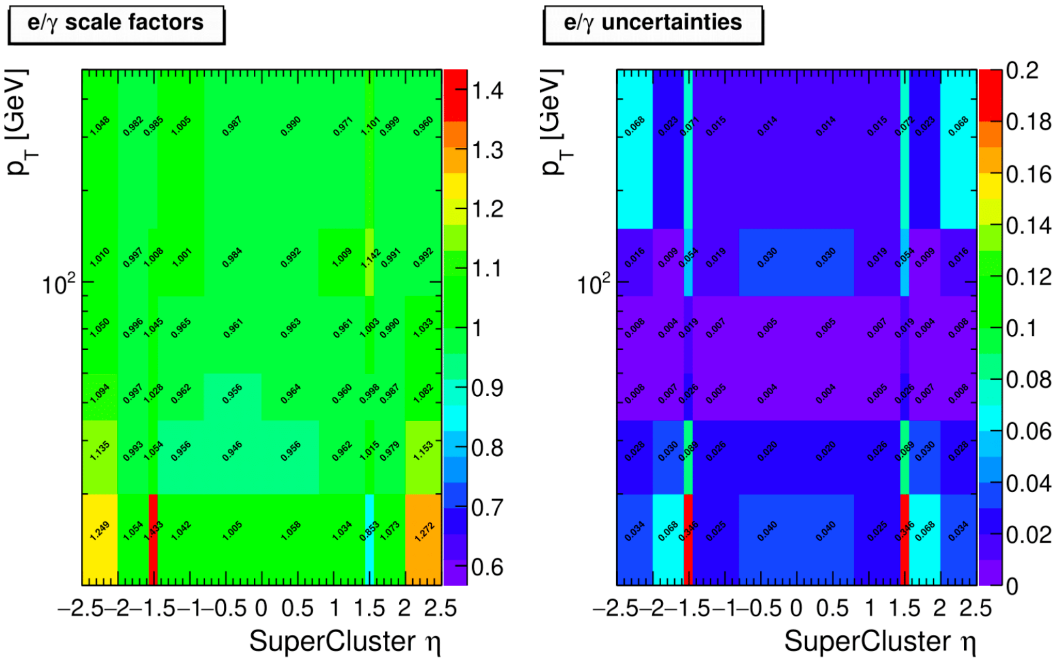

Figure 4.7 Scale factors (left) and corresponding uncertainties (right) for *tight-HWW* for the 2018 dataset as a function of electron p_T and η are shown.

monitoring system checks. On this basis, the SC energies are also corrected using the T&P technique for $Z/\gamma^* \to e^+e^-$ events. A detailed description of the measurement of the electron momentum scale and resolution and the associated uncertainties are given in Ref[108].

4.6 Jet

In QCD hard scattering, quarks or gluons can be produced in various ways, such as the decay of W and Z bosons or initial/final state radiation. These quarks or gluons can emit soft gluons, further producing quark and antiquark pairs or gluons. Due to the color confinement in QCD, these particles form colorless hadrons. At the LHC energy scale, these stable particles are boosted to an orientation similar to the initial quarks or gluons. The resulting experimental signatures, i.e., jets, are collimated spray structures of stable particles. In the measurements of polarization $W^\pm W^\pm$ and searches for Majorana neutrinos and Weinberg operator, jets are used to indicate VBF/VBS topology. Jets don't enter the $W\gamma$ analysis's event selections but help estimate backgrounds.

4.6.1 Jet reconstruction

In CMS, jets are reconstructed by clustering PF candidates. The standard method used by the CMS Collaboration is the anti-k_t algorithm[109]. In this thesis, the fastjet package[110] is used to apply the jet clustering with a cone size of $R = 0.4$ (AK4). The anti-k_t algorithm defines entities as either particles or pseudo-jets, which are intermediate jets during the clustering. The distances between entities i and j and between entity i and the beamline (B) are as follows:

$$d_{ij} = \min\left(\frac{1}{p_{\mathrm{T}i}^2}, \frac{1}{p_{\mathrm{T}j}^2}\right)\frac{\Delta\phi_{ij}^2 + \Delta\eta_{ij}^2}{R^2}, \tag{4.6}$$

$$d_{iB} = \frac{1}{p_{\mathrm{T}i}^2}. \tag{4.7}$$

The method first creates a set $\left\{d_{ij}, d_{iB}\right\}$ from all PF candidates. If the dij is the minimum, i and j particles are merged as a pseudo-jet in a list of entities; if the diB is the minimum, the i-th entity will be considered as a final jet and is removed from the list. This procedure is repeated until no entity is left in the list. The method first creates a $\left\{d_{ij}, d_{iB}\right\}$ set from all PF candidates. If d_{ij} is the minimum, the i and j particles are merged into a pseudo-jet in the entity list; if d_{iB} is the smallest value, the ith entity is considered the final jet and removed from the list. This process is repeated until there are no entities left. Since the weighting of the distances is proportional to $1/p_{\mathrm{T}}^2$, which ensures that hard particles are merged firstly, thus jets grow around particles with the highest p_{T} and have a smooth border.

However, a part of PF candidates from PU vertices leads to inaccurate energy reconstruction of jets. The charged-hadron subtraction (CHS) algorithm[111] is applied to eliminate the PU effect. The CHS algorithm takes the track information to remove the charged particles used to reconstruct the PU vertices and keep those not associated with any PU vertex or are neutral particles. Finally, the so-called AK4CHS jets are reconstructed and used.

4.6.2 Jet identification

Noises originating from calorimeters or electronics can build fake jets. To reduce these jets, dedicated jet identification criteria based on the hadron and electromagnetic component of the jet is applied, illustrated in Table 4.5. The efficiency is more than 99% for all η regions, whereas the background rejection is more than 98% for $|\eta| < 3$.

Table 4.5 Jet identification criteria in different $|\eta|$ for PF jets.

Variable	**Requirement**			
	$|\eta| \leq 2.6$	$2.6 < |\eta| \leq 2.7$	$2.7 < |\eta| \leq 3.0$	$3.0 < |\eta| \leq 5.0$
Constituents	> 1	–	–	–
Neutral Particles	–	–	> 2	> 10
Neutral Hadron Fraction	< 0.90	< 0.90	–	> 0.2
Neutral EM Fraction	< 0.90	< 0.99	0.99	< 0.9
Charged Multiplicity	> 0	> 0	–	–
Charged Hadron Fraction	> 0	–	–	–
Charged EM Fraction	< 0.80	< 0.80	–	–
Charged Hadron Fraction	< 0.80	< 0.80	–	–

Although the CHS algorithm has removed most of the charged PF candidates from PU vertices, a BDT classifier called PU jets ID[111] is used to maximize the rejection of PU jets. The PU jet classifier is trained with vertex information and jet shape information. It's observed that most of the trajectories within the PU jet are not from the primary vertex. Also, the shape of the PU jets constructed from particles coming from PU vertices is broader than that from the primary vertex. In this thesis, jets with $p_{\mathrm{T}} < 50$ GeV are required to pass the loose PU jet ID.

4.6.2.1 *b* quark jet identification

Hadrons containing *b* quarks have a relatively long lifetime of $O(10^{-12})$ s, leading to a distance of a few mm to a cm over which these *b* hadrons can travel. This displacement relative to the primary vertex yields a secondary vertex (SV) reconstructed from the displaced orbits of these b hadron decays, as shown in Figure 4.8.

Compare to light quarks, the *b* quarks are heavier and have harder fragmentation. Thus, decay products from *b* hadrons are expected to have relatively larger p_{T}. Additionally, around 20% *b* hadrons eventually decay to muons or electrons. Taking these features as input, a deep neural network (DNN) combined with secondary vertex (CSV) is performed to maximize the

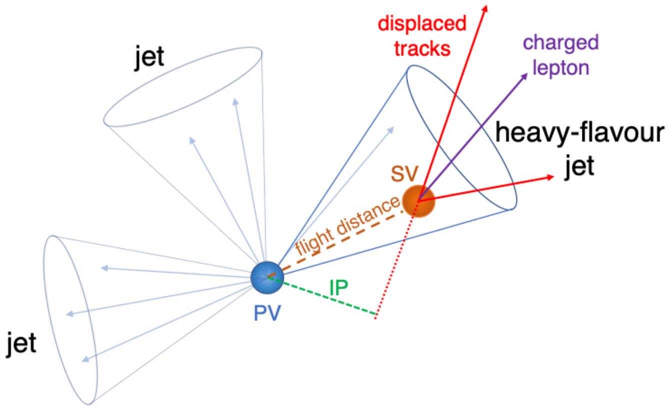

Figure 4.8 Figure of a heavy-flavour jet with a secondary vertex (SV) that are displaced with respect to the PV, and hence with a large impact parameter value[112].

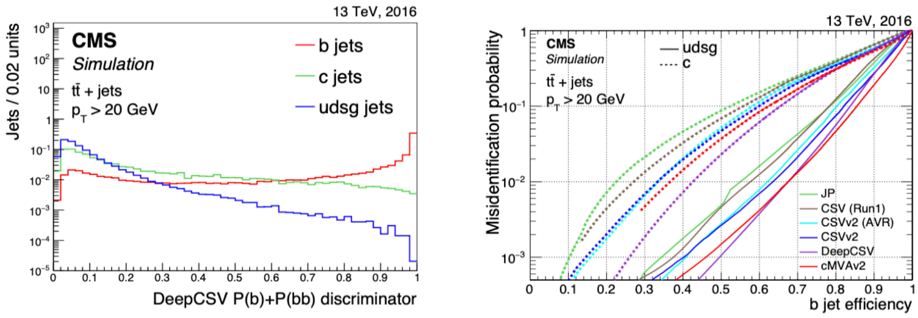

Figure 4.9 The left figure is distribution of the deepCSV discriminator values for the jets from different flavours in the $t\bar{t}$ events. The right figure shows the misidentification probability for c and light-flavour jets versus b jet identification efficiency for various algorithms applied to jets[112].

ability to separate the b jets from the charmed jets and light jets. The normalized distribution of output score and performance of the deepCSV for the b-jet discriminator are shown in Figure 4.9. The *medium* deepCSV working point, corresponding to a mistag rate of 1%[112], is used in polarized W$^\pm$W$^\pm$ and neutrinos in $\mu^\pm\mu^\pm jj$ analyses.

4.6.3 Jet energy correction

Due to the non-uniform and non-linear response of the CMS calorimeters, electronic noise and pileup, several corrections to the jet energy measured in the detector are required to recover the true energy of the corresponding final state jet. This is achieved by a sequential procedure which is referred as jet energy correction (JEC) method[113]. The JEC is applied to each component of the raw jet four-momentum as

$$p_\mu^{\text{cor}} = C \cdot p_\mu^{\text{raw}}, \tag{4.8}$$

where p_μ^{cor} is the corrected jet four-momentum and C is the JEC multiplicative factor, which consists of the following parts:

- C_{offset}: offset correction to eliminate the average extra energy of in-time PU and out-of-time neutral particle PU. A Jet Area Method[114] is performed, where ρ (p_{T}-density per unit area) is estimated in simulation to describe the combination of underlying events, electronics noise and pileup effects. In $\eta - \phi$ space, the region occupied by the aggregation of particles in each jet is defined as the active jet region A_j. The quantity ρ is estimated using $R = 0.6$ and is the median of the distribution of the variable p_{T}^{j}/A_j for all jets in each event and is therefore insensitive to the presence of hard jets. This jet-by-jet offset correction can be defined as $C_{\text{offset}}\left(p_{\text{T}}^{\text{raw}}, A_j, \rho\right) = 1 - \frac{(\rho - \langle\rho_{\text{UE}}\rangle \cdot A_j)}{p_{\text{T}}^{\text{raw}}}$, where $\langle\rho_{\text{UE}}\rangle$ is the average p_{T}-density of the underlying events and electronic noise.
- C_{MC}: the MC calibration factor takes into account the nonlinearity of the pT. The jet reconstructions applied to the data are also used to evaluate this correction for the simulated QCD events. Each reconstructed jet is spatially matched to the generated jet, requiring a $\Delta R < 0.25$. The average correction in each p_{T} bin is defined as: $C_{\text{MC}}\left(p_{\text{T}}^{\text{reco}}\right) = \left\langle \frac{p_{\text{T}}^{\text{gen}}}{p_{\text{T}}^{\text{reco}}} \right\rangle$.
- C_{rel}: the residual calibration of the relative energy scales is used to correct the jet response with respect to the η distribution by considering the differences between the data and the simulated events.
- C_{abs}: Residual calibration of the absolute energy scales was performed to correct the jet response regarding the p_{T} distribution, taking into account the differences between the data and the simulated events.

It is observed that the jet energy resolution (JER) in the data is not as good as in the simulation, the four-momentum of the simulated jet is corrected to give a better description of the data by the factor of $1 + (SF_{JER} - 1)\,\frac{p_{\text{T}}^{\text{reco}} - p_{\text{T}}^{\text{gen}}}{p_{\text{T}}^{\text{reco}}}$, in which SF_{JER} is the resolution scale factor. This method is only applicable to reconstructed jets that are well matched to the jets at generator level.

During the data acquisition in 2016 and 2017, an issue known as prefiring occurred and was induced by an early bunch crossing triggering in the ECAL endcaps. As a result, events with interesting physical properties are lost in the data, while this problem is not reproduced in MC. A weight is applied to all events in MC, i.e. (1-x), where x is the probability that an event is prefired. As shown in Figure 4.10, this pre-ignition correction leads to better data/MC consistency.

4.7 Missing transverse momentum

The particle flow algorithm in the CMS experiment attempts to reconstruct all objects in each event. But some particles such as neutrinos or other weakly interacting objects do not leave a signal in the detector. In particular, neutrinos are essential for processes with W boson decay leptonically. According to momentum conservation, the sum of momentum in the transverse plane is zero. Therefore, these missing objects create a momentum imbalance in the transverse

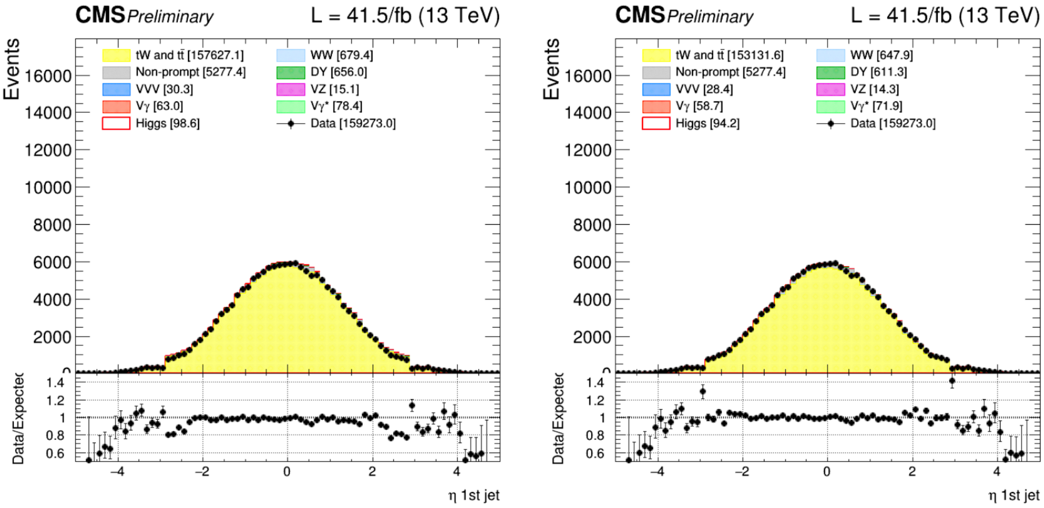

Figure 4.10 Impact on the Top control region with two jets in 2017 induced by the prefiring issue. The distribution on the left shows the data/MC agreement without prefiring correction, and the distribution on the right shows the data/MC agreement after applying the correction.

plane and require an offsetting transverse momentum to balance, known as missing transverse energy. It's calculated from the negative vector sum of all reconstructed particle flow candidates as

$$\vec{p}_{\mathrm{T}}^{\text{miss, raw}} = -\sum_{i=1}^{N_{\text{particles}}} \vec{p}_{\mathrm{T},i}, \tag{4.9}$$

where $\vec{p}_{\mathrm{T},i}$ is the transverse momentum of the i-th reconstructed PF candidate. To get $\vec{p}_{\mathrm{T}}^{miss}$ more precisely, corrections of these visible objects also have to propagate to the $\vec{p}_{\mathrm{T}}^{miss}$, which is dominant by jet energy correction. Therefore, a so-called Type-1 correction[115] is applied to propagate the difference between the corrected and uncorrected transverse momentum of the jets to the $\vec{p}_{\mathrm{T}}^{miss}$. Better agreement between data and simulation is found after correction.

To further suppress the dependence on the PU, an alternative algorithm, Pileup Per Particle Identification (PUPPI) of $p_{\mathrm{T}}^{\text{miss}}$ values (PUPPI)[116], is used in the Wγ measurements instead of the standard PF to reconstruct the $p_{\mathrm{T}}^{\text{miss}}$. The PUPPI algorithm uses information about the neighboring particles, tracking information, and the PU's properties to reduce the effect of the PU on clustering hadrons. Taking these inputs, a weight from 0 to 1 is computed event-by-event based on the local shape for a charged PU, where a value is 1 for the particle from the primary vertex. The weights are used to rescale the 4-momenta of the particles depending on their PU likeliness and then reduces the contribution of PU. The $p_{\mathrm{T}}^{\text{miss}}$ is computed with the PUPPI algorithm by scaling the PF candidates by their PUPPI weight and then applying the Type-I correction using jets corrected by PUPPI.

Meanwhile, various reconstruction failures and detector failures led to unexpected energy deposition and thus unexpected reconstruction of anomalous $p_{\mathrm{T}}^{\text{miss}}$, especially in the high-$p_{\mathrm{T}}^{\text{miss}}$ region. Some dead cells or channels in the sub-detector may occur due to non-functioning elec-

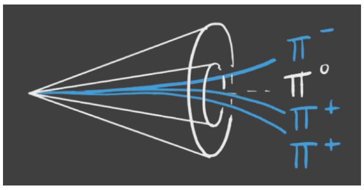

Figure 4.11 Schematic diagram of hadronic tau lepton decays.

tronics, which would lead to an underestimation of energy deposition. Spurious signals also come from noise in the readout electronics or photodetectors and direct particle interactions with signal transition fibers or amplifiers. In addition, those beam halo particles that propagate almost along the z-axis may hit the calorimeter and generate unexpected signals. Dedicated algorithms have removed these random signals based on topological and temporal information during the CMS's trigger system and event reconstruction phases. The rest will be removed by a series of reliable noise filters, as shown in Table 4.6.

Table 4.6 The noise filters to $p_{\mathrm{T}}^{\mathrm{miss}}$ that are applied each year.

Filter	**2016**	**2017**	**2018**
Primary vertex filter	Yes	Yes	Yes
Global super-tight	Yes	Yes	Yes
HBHE noise filter	Yes	Yes	Yes
HBHE iso noise filter	Yes	Yes	Yes
Ecal dead cell trigger primitive filter	Yes	Yes	Yes
Bad PF muon filter	Yes	Yes	Yes
EE bad SC noise filter (only for data)	Yes	Yes	Yes
ECAL bad calibration filter	No	Yes	Yes

4.8 Hadronic Taus

In the measurement of polarization $\mathrm{W}^{\pm}\mathrm{W}^{\pm}$ and studies of Majorana neutrinos and Weinberg operator, events with hadronic tau lepton decays are identified and suppress electroweak background. Hadronic tau lepton decays typically contain one or three highly collimated tracks without surrounding tracks, as illustrated in Figure 4.11. Following the recommendations from the CMS TAU POG[117], the selection for taus is done using the ”VLoose” working point of the ”old MVA2017v2” discriminator in combination with the decay mode based ID ”decayModeFindingOldDMs”. In order for the event to be vetoed, it must contain a tau lepton that satisfies these IDs, has $p_{\mathrm{T}} > 18(20)$ GeV for the former (latter) analysis, $|\eta| < 2.3$, and is separated by $\Delta R > 0.4$ from all *loose-HWW* or *tight-HWW* muons and electrons in the event.

4.9 Object definitions in the measurements of Wγ

4.9.1 Muon Selection

Three muon object selections are used in this analysis: the Muon Tight-WP mentioned in Section 4.4.2, combined with I^{μ}_{rel} (defined in Equation 4.3) less than 0.15 (the *tight-Wγ* muon selection), the Muon Tight-WP combined with I^{μ}_{rel} less than 0.4 (the *veto-Wγ* muon selection), and Muon Tight-WP combined with I^{μ}_{rel} between 0.2 and 0.4 (the *fakeable-Wγ* muon selection). In addition, for all three selections the muons are required to satisfy the kinematic cuts $p_{\mathrm{T}} > 30\,\mathrm{GeV}$ and $|\eta| < 2.4$ when analyzing 2017 samples and $p_{\mathrm{T}} > 26\,\mathrm{GeV}$ and $|\eta| < 2.4$ when analyzing 2016 or 2018 samples (the p_{T} cut follows the p_{T} in the single muon HLT).

4.9.2 Electron Selection

Three electron object selections are used in this analysis: the EGamma POG cut-based medium electron selection, discussed in Section 4.5.2 (the *tight-Wγ* electron selection) and the EGamma POG cut-based veto electron selection (the *veto-Wγ* electron selection), and the EGamma POG cut-based veto electron selection combined with the inverse of the EGamma POG cut-based loose electron (the *fakeable-Wγ* electron selection). In all three cases cases the primary vertex cuts cuts $0.1 > |d_z|$ and $0.05 > |d_{xy}|$ for electrons in the barrel and $0.2 > |d_z|$ and $0.1 > |d_{xy}|$ for electrons in the endcaps are applied. In addition, for both selections, the electrons are required to satisfy the kinematic cuts $p_{\mathrm{T}} > 30\,\mathrm{GeV}$ and $|\eta| < 2.4$ when analyzing 2016 samples and $p_{\mathrm{T}} > 35\,\mathrm{GeV}$ and $|\eta| < 2.4$ when analyzing 2017 or 2018 samples (the p_{T} cut follows the p_{T} in the single electron HLT).

4.9.3 Photon Selection

The EGamma cut-based medium photon working point selection, whose definition is similar as electron selections Section 4.5.2, is used along with the pixel-seed veto (the *tight-Wγ* photon selection). In addition, the photons are required to satisfy the kinematic cuts $p_{\mathrm{T}} > 25\,\mathrm{GeV}$ GeV and $|\eta_{sc}| < 1.4442$ or $1.566 < |\eta_{sc}| < 2.5$ where η_{sc} is the η associated with the super-cluster associated with the photon. For nonprompt photon estimation, a *fakeable-Wγ* photon selection is defined as the EGamma cut-based medium photon working point selection (with the pixel-seed) except that the $\sigma_{i\eta i\eta}$ cut is inverted and an upper bound on $\sigma_{i\eta i\eta}$ is set at 1.75 times the nominal cut value. Also a *charged-isolation-sideband-Wγ* selection is defined as the *tight-Wγ* photon selection with the charged isolation cut changed to $\sum$ (charged particle p_{T}) between 4 and 10 GeV.

4.9.4 Object Cleaning

The order of object selection is selection of the muons, then selection of the electrons, then selection of the photons. The selected electrons are cleaned (i.e. required to be separated based on a $\Delta R = 0.5$ cut) from the selected muons, and the selected photons are cleaned from both the selected muons and the selected electrons.

4.9.5 Jets and $p_{\mathrm{T}}^{\mathrm{miss}}$

While the jets are not used in the signal region selection, but are selected in some of background estimation methods. The AK4CHS jets with the JEC applied are used. For the $p_{\mathrm{T}}^{\mathrm{miss}}$ cut in the signal region, the Puppi $p_{\mathrm{T}}^{\mathrm{miss}}$ with the JEC applied is used due to its lower pileup dependence[116].

Chapter 5

Measurements of Polarized Same-Sign WW Scattering

This chapter describes the detail in the measurements of polarized $W^{\pm}W^{\pm}$ scattering. Data samples, Relevant studies on the signals with Monte-Carlo (MC) generators, and simulated backgrounds are given in Section 5.1. According to the final state topology of the signals, the event selections are built in Section 5.2. Section 5.3 discusses the estimations of the backgrounds. Next, a dedicated study of the uncertainties is shown in Section 5.4. The results are included in Section 5.7. Finally, this analysis is summarized in Section 5.8.

5.1 Data Samples and Monte-Carlo Simulations

The data format used in this analysis is NanoAOD[118], which is newly developed by the CMS collaboration. It is a compact event data format that only contains high-level information on physics objects, such as jets and leptons, thus significantly reducing data. It's only one-twentieth of the parent MiniAOD format. Additionally, NanoAOD is designed to be a flat ROOT[92] TTree, which is very efficient for analysis. In this analysis, the version of NanoAOD is v5, which is centrally produced of "02Apr2020-v1" production campaign. Several Monte Carlo (MC) event generators are used to simulate background processes for each year. The interactions of all final-state particles with the CMS detector are simulated using GEANT4[119]. For all years, event reconstruction is performed using the same algorithms as those used for data. Additionally, Monte Carlo samples are created with additional interactions per bunch crossing (pileup). Simulated events are weighted so that the pileup distributions match the data.

5.1.1 Data

This analysis is performed with the full Run-2 dataset including pp collisions collected in 2016, 2017 and 2018 with the CMS experiment at $\sqrt{s} = 13\,\text{TeV}$. The used data samples are double lepton (electron and muon) datasets and our main triggers are the lowest un-prescaled double lepton triggers. To recover inefficiency, single lepton datasets and single lepton triggers are also considered. All data analyzed is selected using only centrally approved luminosity sections using the following certification files provided by the CMS collaboration:

- **2016 (35.9 fb^{-1})**:
  Cert_271036-284044_13TeV_23Sep2016ReReco_Collisions16_JSON.txt
- **2017 (41.5 fb^{-1})**:
  Cert_294927-306462_13TeV_EOY2017ReReco_Collisions17_JSON.txt
- **2018 (59.7 fb^{-1})**:
  Cert_314472-325175_13TeV_17SeptEarlyReReco2018ABC_PromptEraD_Collisions18_JSON.txt

The full list of data samples and HLT paths for 2016, 2017, and 2018 is given in Table 5.1. Events firing at least one of the listed triggers are used in the analysis. Events may be present in multiple datasets and an overlap removal procedure is performed in order to avoids double-counting of these events.

Table 5.1 Primary data samples and HLT paths used in the analysis

Year	Dataset name	HLT paths
2016	SingleMuon	HLT_IsoMu24 HLT_IsoTkMu24
	SingleElectron	HLT_Ele27_WPTight_Gsf HLT_Ele25_eta2p1_WPTight_Gsf
	DoubleMuon	HLT_Mu17_TrkIsoVVL_Mu8_TrkIsoVVL HLT_Mu17_TrkIsoVVL_TkMu8_TrkIsoVVL
	DoubleEG	HLT_Ele23_Ele12_CaloIdL_TrackIdL_IsoVL_DZ
	MuonEG	HLT_Mu8_TrkIsoVVL_Ele23_CaloIdL_TrackIdL_IsoVL HLT_Mu23_TrkIsoVVL_Ele12_CaloIdL_TrackIdL_IsoVL_DZ HLT_Mu12_TrkIsoVVL_Ele23_CaloIdL_TrackIdL_IsoVL_DZ
2017	SingleMuon	HLT_IsoMu27
	SingleElectron	HLT_Ele35_WPTight_Gsf
	DoubleMuon	HLT_Mu17_TrkIsoVVL_Mu8_TrkIsoVVL_DZ HLT_Mu17_TrkIsoVVL_Mu8_TrkIsoVVL_DZ_Mass8
	DoubleElectron	HLT_Ele23_Ele12_CaloIdLTrackIdL_IsoVL_DZ
	MuonEG	HLT_Mu12_TrkIsoVVL_Ele23_CaloIdL_TrackIdL_IsoVL_DZ HLT_Mu23_TrkIsoVVL_Ele12_CaloIdL_TrackIdL_IsoVL_DZ
2018	SingleMuon	HLT_IsoMu24
	DoubleMuon	HLT_Mu17_TrkIsoVVL_Mu8_TrkIsoVVL_DZ_Mass3p8
	EGamma	HLT_Ele32_WPTight_Gsf HLT_Ele35_WPTight_Gsf HLT_Ele23_Ele12_CaloIdL_TrackIdL_IsoVL_DZ
	MuonEG	HLT_Mu12_TrkIsoVVL_Ele23_CaloIdL_TrackIdL_IsoVL_DZ HLT_Mu23_TrkIsoVVL_Ele12_CaloIdL_TrackIdL_IsoVL_DZ

5.1.2 Simulation of polarized $W^{\pm}W^{\pm}jj$ samples

There are two Monte-Carlo (MC) generator tools capable of generating processes with final state particles in specific polarization states in the market: MadGraph5_aMC@NLO[120] and PHANTOM[121]. Since version 2.7.0, MadGraph5_aMC@NLO supports a syntax to handle the polarization state from initial and final particles. It can perform scattering and decay simulations involving polarization, asymptotic states, and preservation of spin correlation and off-shell effects. The new syntax is validated with PHANTOM in Ref[122]. The MadGraph5_aMC@NLO version 2.7.2 is adopted to generate the polarized WW samples in this analysis.

The following shows an example of the bracket polarization syntax in v2.7.2 of MadGraph5_aMC@NLO at leading order (LO):

```
generate p p > t t~{R}
generate e+{L} e- > w+{0} w-{T}
```

for spin 1/2 particles, ”L” or ”+” for the left handed helicity, ”R” or ”-” for the right handed helicity.

For EW $W^{\pm}W^{\pm}jj$, three polarized components are generated: the fully longitudinally polarized ($W^{\pm}_{L}W^{\pm}_{L}$), fully transverse polarized ($W^{\pm}_{T}W^{\pm}_{T}$) components are performed, and partially longitudinally polarized ($W^{\pm}_{L}W^{\pm}_{T}$). Following is the example to generate $W^{\pm}_{L}W^{\pm}_{T}$ with the W bosons leptonically decay:

```
define l- = e- mu- ta-
define l+ = e+ mu+ ta+
define vl  = ve  vm  ta
define vl = ve vm ta
generate p p > w+{L} w+{T} j j QED=4 QCD=0, w+ > l+ vl
add process p p > w-{L} w-{T} j j QED=4 QCD=0, w- > l- vl̃
```

where, `L` and `T` indicate longitudinal helicity and transverse helicity.

In MadGraph5_aMC@NLO, a new configuration parameter ”me_frame” is introduced along with the polarization syntax, which allows the user to select the reference frame in which the polarizations matrix-element is evaluated. The default is the partonic center of mass. As the polarization vector is not Lorentz invariant for massive particles, longitudinally and transversely polarized vectors require a choice of reference frame. In this analysis, both signal processes with the helicity eigenstates defined in the $W^{\pm}W^{\pm}$ center-of-mass reference frame (WW-frame) and in the initial parton-parton reference frame (pp-frame) are Simulated. The simulated samples were generated with the above syntax for jet p_{T} greater than 10 GeV and dijet mass greater than 200 GeV. For each data taking period, samples of $W^{\pm}_{L}W^{\pm}_{L}$, $W^{\pm}_{L}W^{\pm}_{T}$, and $W^{\pm}_{T}W^{\pm}_{T}$ scattering in the pp-frame and WW-frame were generated. Table 5.2 shows the cross sections of simulated sample. The $W^{\pm}_{L}W^{\pm}_{L}$ part only accounts for 7.3% and 10.9% of the total process in the pp-frame and WW-frame respectively.

Kinematic distributions have been studied for both polarized samples and inclusive sample.

Table 5.2 Cross sections (σ) for polarized components and inclusive process of EW $W^{\pm}W^{\pm}jj$ defined in pp-frame and WW-frame

Component	σ in pp-frame (fb)	σ in WW-frame (fb)
$W^{\pm}_{L}W^{\pm}_{L}$	2.189	3.286
$W^{\pm}_{L}W^{\pm}_{T}$	11.18	9.553
$W^{\pm}_{T}W^{\pm}_{T}$	16.87	17.39
Inclusive $W^{\pm}W^{\pm}$	30.05	30.05

Figure 5.1 compares $\Delta\phi_{jj}$ and $\Delta\phi_{\ell\ell}$ distributions, good agreement is found between incoherent sum of the polarized samples and inclusive sample. Figure 5.2 shows the normalized shapes of the $\Delta\phi_{jj}$ and $\Delta\phi_{\ell\ell}$ the polarized samples in both frames, which indicate the discriminating power of those kinematic variables.

The WW-frame seems to be the best choice, due to the fact that:

1. it is the natural choice for vector boson scattering processes, where 2-2 scattering appears.
2. the interference effects among polarization states are the smallest, compared with other choices such as the partonic or di-lepton center of mass frames.

Figure 5.3 shows a preview of the comparison on the diboson mass M_{WW}, for $W^{\pm}W^{\pm}$ scattering at the $\sqrt{s} = 13$ TeV in the LHC, in the pp-frame (12) or WW-frame (34). The solid lines are for the SM case, while the dashed lines for the simple BSM case with HWW coupling scaled by a factor of 0.8. One can clearly see that the production rates in the WW-frame are larger than in the pp-frame at lower mass region, while agree with each other at high mass bins. Thus one would expect both frames can be used to probe unitarity restoration mechanism, while higher significance can be achieved for the WW-frame.

5.1.3 Overview of simulated background samples

Simulated samples are used to model all backgrounds other than the nonprompt lepton background, mentioned in Section 5.3.1, which can lead to two same sign muons, two or more reconstructed jets. The WZ processes, where two bosons decay leptonically, are simulated using MadGraph5_amc@nlo 2.4.2[120] at leading order (LO) accuracy with six electroweak ($\mathcal{O}(\alpha^6)$) and zero quantum chromodynamics (QCD) vertices. The QCD-induced $W^{\pm}W^{\pm}$ process is also simulated with MadGraph5_amc@nlo 2.4.2. Contributions with an initial-state b quark are excluded from the electroweak WZ simulation because they are included in the simulation of the production of a Zboson in association with a single top quark (tZq), which is simulated at NLO using MadGraph5_amc@nlo 2.3.3. The ZZ $\to 4\ell$ and $gg \to$ ZZ processes are simulated with the powheg v2[123] and mcfm 7.0.1[124] generators, respectively. Production of $t\bar{t}$W, $t\bar{t}$Z, and triple vector boson (WWW, WWZ, WZZ, ZZZ) background events is simulated at NLO accuracy in QCD using the MadGraph5_amc@nlo 2.2.2 (2.4.2) generator[120,125-126] for the 2016 (2017 and 2018) samples. The production of $W^{\pm}W^{\pm}$ events through double-parton

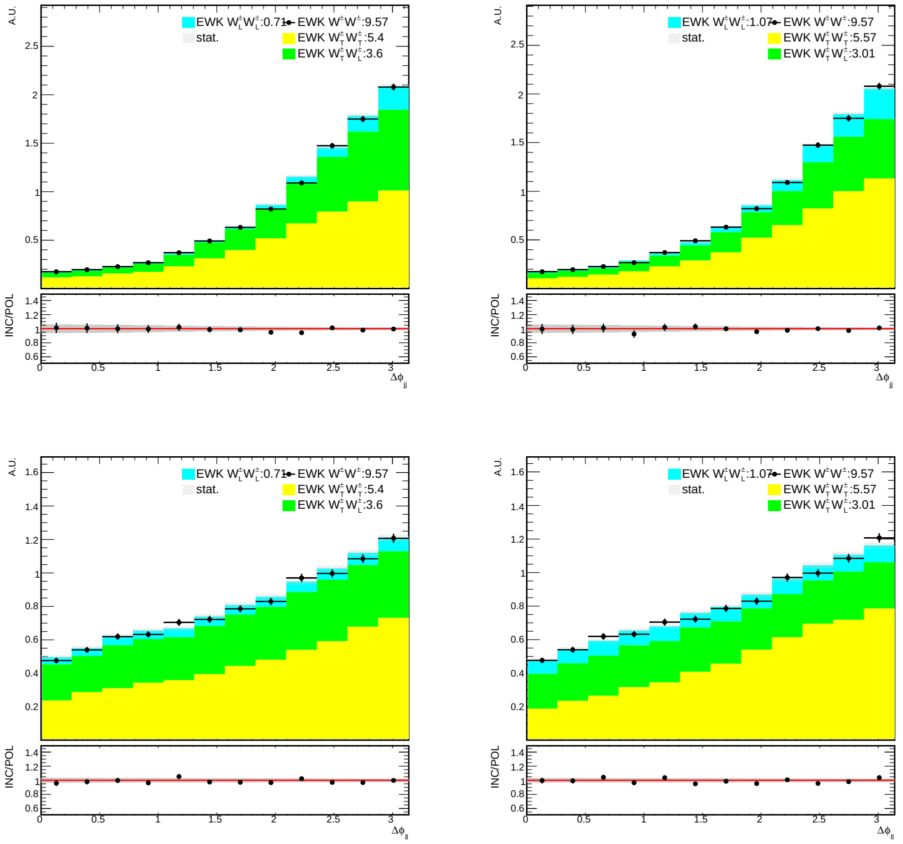

Figure 5.1 $\Delta\phi_{jj}$ (top) and $\Delta\phi_{\ell\ell}$ (bottom) distributions in pp-frame (left) and WW-frame (right). Here, the reference frames are the frames in which the polarization vectors are defined. The kinematics are still measured in the laboratory frame.

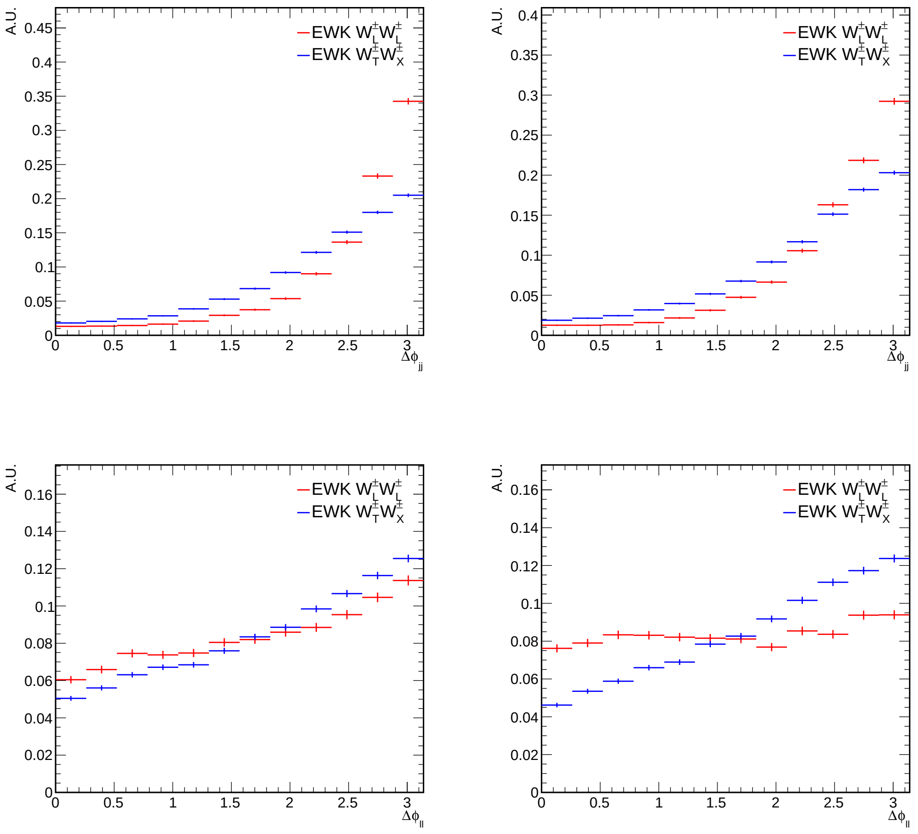

Figure 5.2 Normalized distributions of $\Delta\phi_{jj}$ (top) and $\Delta\phi_{\ell\ell}$ (bottom) in pp-frame (left) and WW-frame (right). Here, the reference frames are the frames in which the polarization vectors are defined. The kinematics are still measured in the laboratory frame.

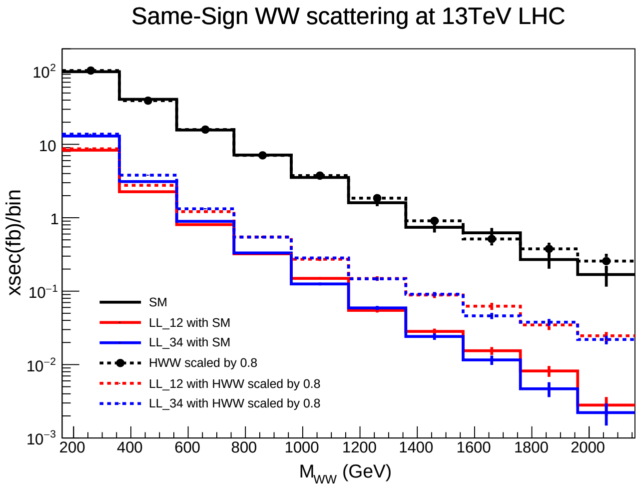

Figure 5.3 Comparing WW invariant mass distributions in the WW-frame and pp-frame, with the SM or HWW coupling scaled by 0.8.The solid curve is for the SM case, while the dashed curve is for the simple BSM case with HWW coupling scaled by a factor of 0.8. The blue line is for $W_L^\pm W_L^\pm$ in WW-frame, the red line is for $W_L^\pm W_L^\pm$ in pp-frame, and the black line is for the unpolarized $W^\pm W^\pm$.

scattering is generated at LO using PYTHIA 8.226 (8.230)[127] in 2016 (2017 and 2018).

Simulated events are then interfaced with PYTHIA to model the fragmentation and hadronization of partons in the initial and final states, along with the underlying event. The CUETP8M1 (CP5) tune[128-129] is used in the simulation for the 2016 (2017 and 2018) data-taking period. In LO (NLO) simulations performed with MADGRAPH5_AMC@NLO, jets are matched to the parton shower produced by PYTHIA 8.2 following the MLM[130] (FxFx[126]) prescription. The simulated samples for the 2016 (2017 and 2018) data-taking period use the NNPDF 3.0 (3.1) parton distribution functions[131-132]. The interactions of all final-state particles with the CMS detector are simulated using GEANT4[133]. Simulated events include the contribution of particles from additional pp interactions within the same or nearby bunch crossings (PU); the PU distribution in the simulated samples matches that observed in data.

5.2 Event Selection

The signal region is intended to isolate the unpolarized EW-induced $\mathrm{W^\pm W^\pm} jj$ process. Two deep neural networks (DNNs) are trained, in Section 5.5, in order to separate the polarization components of EW-induced $\mathrm{W^\pm W^\pm} jj$ within the signal region.

To construct the signal region (SR), first require exactly two same-sign tight electrons or muons, as defined in Chapter 4, each of which is required to have p_T larger than 30 GeV. Selections for VBS topology are considered, which requires dijet mass (m_jj) greater than 500, the pseudo-rapidity separation of the jets ($|\Delta\eta_\mathrm{jj}|$) greater than 2.5. A so-called Zeppenfeld variable[134] is considered in the signal region, which is defined in Equation 5.1. To reduce the background due to $\mathrm{t\bar{t}}$ production, reject events which contain at least one jet that passes b-tagging selection, as described in Section 4.6. In order to reduce the background due to Z+jets events, reject $eejj$ events where the mass of the electron pair is within 15 GeV of the nominal Z boson mass. In order to reduce the background due to WZ production, veto events containing a hadronically decaying tau leptons.

$$\mathcal{Z}(\ell) = \left|\eta_\ell - \frac{\eta_{j1} + \eta_{j2}}{2}\right| / \left|\Delta\eta_{jj}\right|. \tag{5.1}$$

In addition to the SR, three background-dominated control regions (CRs)are defined to validate background estimate procedures and constrain uncertainties on the backgrounds. A b-tagged control region is defined with the exact selection requirements as the SR, except with the b-jet veto is inverted. This region is dominated by events that contain nonprompt leptons. A WZ control region is constructed by selecting three leptons instead of two and requiring one pair of same flavor and opposite charge leptons, whose invariant mass is within 15 GeV of the nominal Z mass. A WZb control region is defined similarly to the WZ control region but with the b-jet veto inverted, such that the region is dominated by nonprompt and $\mathrm{t\bar{t}V}$. The SR and CRs definitions are summarized in Table 5.3.

Table 5.3 Signal region and control region definitions.

Variable	**Signal region**	**WZ**	**WZb**	***b*-tagged**
Lepton p_{T}	> 30/30 GeV	>25/10/25 GeV	>25/10/25 GeV	> 30/30 GeV
$m_{\ell\ell}$	> 20 GeV	> 20 GeV	-	-
$\lvert m_{\ell\ell} - m_{\mathrm{Z}}\rvert$	> 15 GeV (ee)	< 15 GeV	< 15 GeV	> 15 GeV (ee)
$m_{\ell\ell\ell}$	-	> 100 GeV	> 100 GeV	-
$\mathcal{Z}(\ell)$	< 0.75	< 1.0	< 1.0	< 0.75
Jet p_{T}	> 30/30 GeV	> 30/30 GeV	> 30/30 GeV	> 30 GeV
$\Delta\eta_{\mathrm{jj}}$	> 2.5	> 2.5	> 2.5	> 2.5
m_{jj}	> 500 GeV	> 500 GeV	> 500 GeV	> 500 GeV
$p_{\mathrm{T}}^{\mathrm{miss}}$	> 30 GeV	> 30 GeV	> 30 GeV	> 30 GeV
b-jet veto	Yes	Yes	Inverted	Inverted
Hadronically decay tau veto	Yes	Yes	Yes	Yes

5.3 Background estimation

We use a data-driven method to estimate the background due to events containing nonprompt (fake) leptons and a mixed data-driven and MC-driven method to estimate the background due to events containing an electron that is assigned the wrong electric charge.

5.3.1 Nonpromt lepton background estimation

The so-called nonprompt leptons are one of the dominant backgrounds in the analysis. A variety of sources contribute to this backgrounds. For example, charged pions whose shower shape resembles an electron can be reconstructed as electrons, charged pions that ”punch-through” the calorimeters and the magnets can be reconstructed as muons, jet induced fake leptons. The processes that produce nonprompt (or fake) electrons and muons are potentially badly mismodeled in our simulations because they involve non-perturbative QCD and detector material interactions. Therefore, a data-driven method is used to estimate this background category. In this analysis, the main source of fake leptons at the final selection level are from $\mathrm{t\bar{t}}$ events, where at least one of the jets or a constituent is misidentified as an isolated lepton. A data-driven approach, based on the ”fakeable object” technique, is pursued to estimate this background. It provides a measurement of the yield and kinematic distributions of the nonprompt background.

The fundamental idea of the fakeable object method is to select a control sample of events enriched in the background being estimated, and then use an extrapolation factor to relate these events to the background in the signal region. The method is data-driven since the control sample is selected in data, and the extrapolation factor is measured with the data as well. For non-prompt leptons, the extrapolation is done in the (p_{T}, η) phase space of the lepton. The control sample is defined using the *loose-HWW* lepton definition in Chapter 4, chosen such that the rate of mis-identification is increased. The extrapolation factor relates the background misidentified with this criteria, to the background misidentified as passing the full particle selection of the signal region.

A set of *loose-HWW* leptons, referred to as the ”denominator” from here on, is defined in a sample of events dominated by dijet production, which is accessed by using a set of prescaled trigger paths to data. The efficiency for these denominator objects to pass the *tight-HWW* lepton selection criteria is measured. This background efficiency, typically referred to as the ”fake rate”, is gotten in the (p_{T}, η) phase space of the denominator object in order to capture any dependence on kinematic and geometric quantities. These fake rates are then used as weights to extrapolate the background yield from a sample of *loose-HWW* denominator objects to the sample of *tight-HWW* selected leptons.

The dijet control region requires one *loose-HWW* lepton, lepton candidates are required to be well separated from the highest-p_{T} jet of the event, with $\Delta R(\ell, j) > 1$. In addition, to reduce the contamination from real leptons in that sample, the events are required to have at least one additional jet, the jet of highest-p_{T} is called the recoiling jet, no additional loose leptons, $p_{\mathrm{T}}^{\mathrm{miss}} < 20$ GeV, and $m_{\mathrm{T}} < 20$ GeV, where the variable m_{T} is the transverse mass variable constructed with the lepton p_{T} and the $p_{\mathrm{T}}^{\mathrm{miss}}$,

$$m_{\mathrm{T}} = \sqrt{2 p_{\mathrm{T}}^{\ell} p_{\mathrm{T}}^{\mathrm{miss}} (1 - cos(\phi_{\ell} - \phi_{p_{\mathrm{T}}^{\mathrm{miss}}}))} \tag{5.2}$$

The data-driven extrapolation is based on the following system of equations:

$$\begin{pmatrix} m_{20} \\ m_{11} \\ m_{02} \end{pmatrix} = \frac{p_2 - p_1}{-(p_1 - p_2)^3} \begin{pmatrix} p_2^2 & -p_2(1 - p_2) & (1 - p_2)^2 \\ -2p_2p_1 & p_1(1 - p_2) + p_2(1 - p_1) & -2(1 - p)(1 - p_2) \\ p^2 & -p_1(1 - p_1) & (1 - p_1)^2 \end{pmatrix} \begin{pmatrix} n_{20} \\ n_{11} \\ n_{02} \end{pmatrix}$$

where

- n_{20} is the number of events in our signal region containing two tight leptons
- n_{11} is the number of events in our signal region containing one loose-but-not-tight leptons
- n_{02} is the number of events in our signal region containing two loose-but-not-tight leptons
- m_{20} is the number of events in our signal region containing two real leptons
- m_{11} is the number of events in our signal region containing one real and one fake lepton
- m_{02} is the number of events containing two fake leptons
- p_1 is the probability for a real lepton that passes the loose selection to also pass the tight selection
- p_2 is the probability for a fake lepton that passes the loose selection to also pass the tight selection

n_{20}, n_{11}, and n_{02} are observable quantities, and p_1 and p_2 are probabilities that can be measured in control regions that are enriched in real and fake leptons. Therefore, the system of equations above can be inverted in order to obtain m_{20}, m_{11}, and m_{02} as a function of the known or measured quantities n_{20}, n_{11}, n_{02}, p_1, and p_2. The background estimate due to events containing one or two fake leptons is $m_{11} + m_{02}$. This method is applied to electrons and muons separately.

This method is described in more detail in Ref[135].

5.3.2 Electron charge mis-identification background estimation

Charge mis-identification can happen for leptons, which then can contribute to the SR. Previous studies by the muon POG have shown that the charge mis-identification rate for muons is negligible. So only electron charge mis-identification is considered.

The charge mis-identification scale factor is defined as the charge mis-identification rate in data, ϵ_{data}, divided by the charge mis-identification rate in simulation, ϵ_{sim}. For MC, DY samples are used. Two electrons events with $p_{\mathrm{T}} > 20$ GeV and $|m_{\ell\ell} - m_Z| < 15$ GeV. Electrons should pass object selection discussed in Section 4.5.2.

The charge mis-identification rate is measured in 3 $|\eta|$ bins taking into account all combinations, there are 9 different $|\eta_1| - |\eta_2|$ regions. A simultaneous fit is performed to extract mis-identification rate in 3 $|\eta|$ bins. Same studies also done on data. The background is fitted by an exponential function. The charge flip rate in data and simulations are shown in Table 5.4.

Table 5.4 Charge flip rate of data, MC and their scale factors for each year.

$\vert\eta\vert$-range	**Data**	**MC**	**Scale factor**
2016			
0.0-1.0	0.0054 ± 0.0005	0.0063 ± 0.0004	0.85 ± 0.10
1.0-1.5	0.0517 ± 0.0023	0.0644 ± 0.0024	0.80 ± 0.05
1.5-2.0	0.2298 ± 0.0058	0.2009 ± 0.0052	1.14 ± 0.04
2017			
0.0-1.0	0.0050 ± 0.0004	0.0048 ± 0.0003	1.05 ± 0.11
1.0-1.5	0.0349 ± 0.0017	0.0247 ± 0.0010	1.41 ± 0.09
1.5-2.0	0.1170 ± 0.0030	0.0837 ± 0.0022	1.40 ± 0.05
2018			
0.0-1.0	0.0055 ± 0.0004	0.0047 ± 0.0003	1.19 ± 0.11
1.0-1.5	0.0373 ± 0.0014	0.0245 ± 0.0010	1.52 ± 0.09
1.5-2.0	0.1146 ± 0.0023	0.0932 ± 0.0017	1.23 ± 0.03

5.3.3 WZ

The signal regions still receive some contribution from WZ process. The fraction of EW WZjj is small, same as EW $\mathrm{W}^{\pm}\mathrm{W}^{\pm}jj$. Refer to analysis[65], the NLO QCD and EW corrections are considered in EW WZjj. The QCD WZ process is the main component of WZ process. The normalization of the WZ process is a free parameter measured from data.

5.3.4 ZZ, TVX, Vγ, WW DPS and tribosons

The background from the ZZ production is completely dominated by ZZ $\rightarrow 4\ell$ events where one or two leptons are not identified or outside the acceptance region. The estimation of ZZ is from simulation, after selection, the contribution is very tiny.

The $t\bar{t}V$ processes are also estimated from simulation, a WZb CR is used to assess the normalization of tZq process. Although after selection, the TVX contributions are tiny.

The Vγ, WW DPS and all tribosons processes (WWW, WWZ, WZZ, ZZZ and also WWG) are taken into account with simulated samples. They are tiny backgrounds.

5.4 Systematic Uncertainties

In the following the systematic uncertainties which are taken into account in the fit are listed, the uncertainties indicated as correlated between three years are represented by a single common nuisance parameter, while ones indicated as uncorrelated are given as three independent parameters.

5.4.1 Uncertainties affecting all MC-based backgrounds and signal modeling

This category mostly consists of uncertainties in MC modeling of reality. All uncertainties under this category are uncorrelated among the three years unless otherwise stated.

Integrated luminosity Follow the recommendation from the LUM POG[16-17,136], the values of the uncertainties are used in Table 5.5. Each column represents one year, and each line represents one correlated uncertainty, with the uncorrelated uncertainties represented simply as lines containing nonzero entries only for one year.

Table 5.5 Uncertainties in the integrated luminosity measurements.

Uncertainty source	**size in 2016 (%)**	**size in 2017 (%)**	**size in 2018 (%)**
Uncorrelated 2016	2.2	0.0	0.0
Uncorrelated 2017	0.0	2.0	0.0
Uncorrelated 2018	0.0	0.0	1.5
X-Y factorization	0.9	0.8	2.0
Length scale 17-18	0.0	0.3	0.2
Beam-beam deflection 16-17	0.4	0.4	0.0
Dynamic beta 16-17	0.5	0.5	0.0
Beam current calibration 17-18	0.0	0.3	0.2
Ghosts and satellites 16-17	0.4	0.1	0.0

Trigger efficiency Trigger efficiency uncertainties are of the order of less than 1%. These uncertainties are computed by varying the tag selection as well as the Z mass window in the tag and probe method used to compute the corresponding scale factors.

Prefiring correction The uncertainty due to prefiring is obtained by creating a new prefiring map with the prefiring probabilities increased or decreased by the maximum of their statistical uncertainty. Overall, the recommended uncertainty is about 2%. Present only in 2016 and 2017. Uncorrelated between years.

Lepton reconstruction and identification efficiency The lepton reconstruction and identification efficiencies are measured with the tag and probe method in data. To correct for the difference in the lepton identification efficiencies between data and MC, data/MC scale factors dependent on p_{T} and η are applied to the MC. The resulting uncertainty in the signal region is about 1% for electrons and about 2% for muons.

Muon momentum scale and resolution These uncertainties arise due to different detector effects and are p_{T} and η-dependent. Uncertainties on both the scale and resolution individually amount to about 0.2% for muons. The uncertainty values for the muons are provided by Muon POG following Ref[104].

Jet energy scale (JES) uncertainties A variety of sources of systematic uncertainty affect the jet energy scale, which affects our signal region and control regions explicitly through jet selection and also implicitly through the $p_{\mathrm{T}}^{\mathrm{miss}}$ selection. We estimate the effect of this uncertainty by shifting the jet energy scale, and thereby the type-1 corrected $p_{\mathrm{T}}^{\mathrm{miss}}$, by $\pm 1\sigma$ variations provided by the JetMET group. The fit templates are modified both in shape and normalization as a result of this variation. The combination of all sources of the jet energy scale is used to define a single jet energy scale variation, which is the sum of all uncertainties in quadrature. The uncertainty is uncorrelated across years. JES uncertainty affects the rates in the signal region at the level of around 10%.

Jet energy resolution (JER) uncertainties This uncertainty is estimated by smearing the jet energy scale, by $\pm 1\sigma$ variations provided by the CMS JetMET POG. The total JER uncertainty is uncorrelated between all the years.

$p_{\mathrm{T}}^{\mathrm{miss}}$ unclustered component Uncertainties on $p_{\mathrm{T}}^{\mathrm{miss}}$ that are not due to lepton and jet momentum scales are assessed by varying the momentum of each PF candidate that is not associated to a lepton or a jet according to the reconstructed particle type. This procedure follows the official JetMET POG recommendations. The effect on the rates is of the order of 1% to 10% depending on the process.

Jet PU ID SF Uncertainty on the loose Jet PU ID scale factor applied on all the jets of the analysis ($p_{\mathrm{T}} < 50$ GeV). The recipe is provided centrally by CMS JetMET POG. Uncorrelated between the years.

b-tagging scale factor The uncertainty due to the b-tagging data/MC scale factor is divided into the following sources: contamination of the light/heavy flavor region, where the scale factors are derived by heavy/light flavor jets, linear and quadratic shape variations of the b-tagging distribution within statistical uncertainties, and the effect of the jet energy scale on the jet selection. Uncertainties on the b-tagging scale factor are evaluated by shifting the per-jet scale factors by ranges provided by the BTV POG.

Pileup reweighting The uncertainty due to pileup is obtained by creating new pileup reweighting histograms with the minimum bias cross-section scaled up and down by 4.6%.

5.4.2 Theoretical uncertainties

The renormalization and factorization scale (QCD) and parton distribution function (PDF) uncertainties are considered for the EW and QCD $\mathrm{W}^{\pm}\mathrm{W}^{\pm}jj$ processes. The PDF uncertainty is taken as the standard deviation of the 32 PDF variations of the PDF4LHC15_nnlo_30_pdfas PDF set. The QCD scale uncertainty is taken as the maximum from the central value of the 6 variations that are not 2.0/0.5 or 0.5/2.0.

Following[65], an uncertainty related to the QCD+EW corrections for the EW-induced $\mathrm{W}^{\pm}\mathrm{W}^{\pm}jj$ processes have been considered. These corrections are applied to all polarization modes by default in the analysis. The differences between the QCD+EW and the QCD only corrections is taken as a systematic uncertainty.

5.4.3 Uncertainties of nonprompt lepton background

Nonprompt background is modeled by applying weights to a superset of signal candidate events identified by leptons passing the *loose-HWW* selection criteria. Systematic uncertainties on the non-prompt background prediction arise from the limited size of the samples used to measure the fake rates and the difference in the flavor composition of the jets faking the leptons between the measurement sample and the signal region. The latter is assessed by varying the p_{T} of the jet that recoils against the lepton object in the dijet control sample used to measure the fake rate. Assuming that the control sample is dominated by events with two back-to-back jets, varying the p_{T} of the ”away-side” jet for a fixed lepton object p_{T} corresponds to varying the fraction of the lepton object p_{T} to the total p_{T} of the jet that contains it, which in turn has an effect of probing different jet flavor compositions. The statistical uncertainty of the control samples affects the non-prompt background prediction by at most 10% and 5% for the samples electron and muon fakes.

The effect of jet p_T variation is at most 8% and 7% from electron and muon fake rate measurements, respectively. The jet p_T variation is, however, expected to not fully cover the uncertainty due to flavor variation. The uncertainty in these methods have extensively been studied over the last 10 years, and a conservative value of 30% is assumed. Therefore, a conservative 30% normalization uncertainty is additionally assigned to the non-prompt lepton background prediction.

Uncertainties on the non-prompt background from the statistical uncertainty in the measurement and the jet p_T variation are uncorrelated among three years. The additional 30% normalization uncertainties are correlated within each observable.

5.4.4 Sample normalization

As mentioned in Section 5.3, the normalization of QCD WZ, EW-induced WZjj, and tZq are free parameters measured from data.

5.4.5 Sample statistical uncertainties

Statistical uncertainties on the background estimates and the signal estimate are handled with the Barlow-Beeston-lite[137] option of the Higgs Combination tool[138] with the threshold parameter set to 10.

5.5 DNN training

The $\mathrm{W}^\pm_\mathrm{L}\mathrm{W}^\pm_\mathrm{L}$ just represents a small fraction of the total cross section of the unpolarized EW $\mathrm{W}^\pm\mathrm{W}^\pm jj$ and has observables that are largely similar to the unpolarized process. Therefore, machine learning techniques are essential to harness correlations between variables and extract as much information as possible from the finite dataset.

Two DNN training are used, they are built with the KERAS python library[139] and the TENSORFLOW[140] backend. One is trained to discriminate the $\mathrm{W}^\pm_\mathrm{L}\mathrm{W}^\pm_\mathrm{L}$ ($\mathrm{W}^\pm_\mathrm{L}\mathrm{W}^\pm_\mathrm{T}$ or $\mathrm{W}^\pm_\mathrm{T}\mathrm{W}^\pm_\mathrm{T}$) process from other polarization modes of EW-induced $\mathrm{W}^\pm\mathrm{W}^\pm$ process, denoted as DNN^WW. To get signal strength of $\mathrm{W}^\pm_\mathrm{L}\mathrm{W}^\pm_\mathrm{L}$, DNN^WW is performed considering $\mathrm{W}^\pm_\mathrm{L}\mathrm{W}^\pm_\mathrm{L}$ as signal, while $\mathrm{W}^\pm_\mathrm{T}\mathrm{W}^\pm_\mathrm{L}$, $\mathrm{W}^\pm_\mathrm{L}\mathrm{W}^\pm_\mathrm{T}$, and $\mathrm{W}^\pm_\mathrm{T}\mathrm{W}^\pm_\mathrm{T}$ processes as background. DNN^{WW} has the structure and training parameters in Table 5.6. The inputs to the DNN^WW are in 5.7. The same is true for $\mathrm{W}^\pm_\mathrm{T}\mathrm{W}^\pm_\mathrm{T}$ processes.

Table 5.6 Structure and training parameters of the DNN^WW.

layer	**number of nodes**	**activation function**	**dropout rate**
layer 1	64	relu	0.414
layer 2	128	sigmoid	0.092
layer 3	64	relu	0.209
layer 4	1	sigmoid	-

Table 5.7 Input variables of the $\mathrm{DNN}^{\mathrm{WW}}$.

Variables	**Definitions**
$\Delta\phi_{jj}$	Azimuth angle between the the leading and trailing jets
p_{T}^{j1}	Leading jet transverse momentum
p_{T}^{j2}	Trailing jet transverse momentum
$p_{\mathrm{T}}^{\ell 1}$	Leading lepton transverse momentum
$p_{\mathrm{T}}^{\ell 2}$	Trailing lepton transverse momentum
$\Delta\phi_{\ell\ell}$	Azimuth angle between the two leptons
$m_{\ell\ell}$	Dilepton mass
$p_{\mathrm{T}}^{\mathrm{miss}}$	Missing transverse momentum
p_{T}^{ll}	Dilepton mass
m_{WW}	WW diboson mass
$\mathcal{Z}(\ell 1)$	Zeppenfeld variable of the leading lepton
$\mathcal{Z}(\ell 2)$	Zeppenfeld variable of the trailing lepton
$\Delta R_{j1,\ell\ell}$	The ΔR between the leading jet and the dilepton system
$\Delta R_{j2,\ell\ell}$	The ΔR between the trailing jet and the dilepton system
$p_{\mathrm{T}}^{\ell 1} p_{\mathrm{T}}^{\ell 2} / p_{\mathrm{T}}^{j1} p_{\mathrm{T}}^{j2}$	Ratio of scalar transverse momentum products between leptons and jets

Another one is $\mathrm{DNN}^{\mathrm{nonVBS}}$, which is used to seperate EW-induced $\mathrm{W}^{\pm}\mathrm{W}^{\pm}jj$ from non-VBS events, which is completely dominated by the nonprompt lepton background. In this analysis, the nonprompt lepton background is studied by data-driven method whose statistics is limited. Since main nonprompt lepton same-sign background comes from top-quark production, it's reasonable to use oppositely charged dilepton simulated events to obtain a very large training sample. Thus, the training is performed by considering the sum of all polarization modes of $\mathrm{W}_{\mathrm{L}}^{\pm}\mathrm{W}_{\mathrm{L}}^{\pm}$ as the signal, while $\mathrm{t\bar{t}}$ and tW processes as backgrounds. Selections are same as 5.2 except oppsite sign are required for $\mathrm{t\bar{t}}$ and tW processes. $\mathrm{DNN}^{\mathrm{nonVBS}}$ has the structure and training parameters in Table 5.8. The inputs to the $\mathrm{DNN}^{\mathrm{WW}}$ are in 5.9.

Table 5.8 Structure and training parameters of the $\mathrm{DNN}^{\mathrm{nonVBS}}$.

layer	**number of nodes**	**activation function**	**dropout rate**
layer 1	32	softmax	0.448
layer 2	32	softmax	0.017
layer 3	16	sigmoid	0.044
layer 4	64	softmax	0.117
layer 5	1	sigmoid	-

The DNN trainings are performed on events which pass the signal region selection cuts. The receiver operating characteristic (ROC) curves and normalized testing sample DNN output distributions are in Figure 5.4.

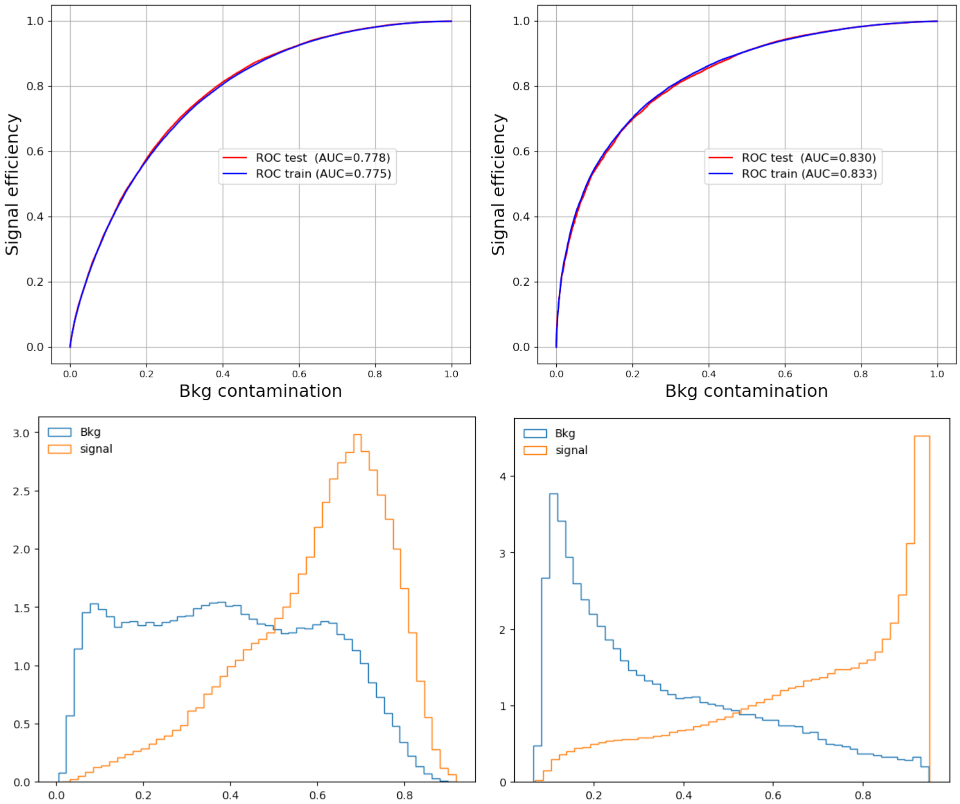

Figure 5.4 ROC curves (top) and normalized testing sample DNN output distributions (bottom) for DNN$^{\mathrm{WW}}$ (left) and ROC curve for DNN$^{\mathrm{nonVBS}}$ (right).

Table 5.9 Input variables of the $\mathrm{DNN}^{\mathrm{nonVBS}}$.

Variables	**Definitions**
m_{jj}	Dijet mass
$\Delta\phi_{jj}$	Azimuth angle between the the leading and trailing jets
$\|\Delta\eta_{jj}\|$	Different in eta angles of the leading and trailing jets
p_{T}^{j1}	Leading jet transverse momentum
p_{T}^{j2}	Trailing jet transverse momentum
$p_{\mathrm{T}}^{\ell 1}$	Leading lepton transverse momentum
$p_{\mathrm{T}}^{\ell 2}$	Trailing lepton transverse momentum
$p_{\mathrm{T}}^{\ell\ell}$	Dilepton mass
$p_{\mathrm{T}}^{\mathrm{miss}}$	Missing transverse momentum
$\mathcal{Z}(\ell 1)$	Zeppenfeld variable of the leading lepton
$\mathcal{Z}(\ell 2)$	Zeppenfeld variable of the trailing lepton

5.6 Statistical methods

This section describes the statistical methods used in the analysis. The main reference is Ref[141].

5.6.1 Limit setting procedure

This section summarizes the procedure for computing exclusion limits, which is based on the modified frequentist method, usually referred to as $\mathrm{CL_s}$[141-146]. The selection of the test statistic and how to handle the nuisance parameters when constructing the test statistic and generating pseudo-data are explained below.

In this analysis, the expected SM $\mathrm{W_L^\pm W_L^\pm}$ event yields are denoted as s, backgrounds as b. These stand for event counts in one or multiple bins. It has become customary to express null results of the SM-like searches as a limit on a *signal strength modifier* μ (also refer to as r) that is taken to change the SM $\mathrm{W_L^\pm W_L^\pm}$ prodcution cross sections by exactly the same scale μ.

Predictions for both signal and background yields, prior to the review of the *observed data entering the statistical analysis*, are subject to multiple uncertainties that are handled by introducing nuisance parameters θ, so that signal and background expectations become functions of the nuisance parameters: $s(\theta)$ and $b(\theta)$. The systematic error probability density functions (pdf)s can be written as $\rho(\theta \mid \tilde{\theta})$, where $\tilde{\theta}$ is the default value of the nuisance parameter, reflecting the degree of belief on the possible true value of θ.

According to the Bayes' theorem, a conceptual step to re-interpret systematic error pdfs $\rho(\theta \mid \tilde{\theta})$ as posteriors arising from some real or imaginary measurements $\tilde{\theta}$ is taken to be:

$$\rho(\theta \mid \tilde{\theta}) \sim p(\tilde{\theta} \mid \theta) \cdot \pi_\theta(\theta), \tag{5.3}$$

in which $\pi_\theta(\theta)$ functions are hyper-priors for those ”measurements”.

Observed limits The following steps illustrate how to compute the observed limits on μ:

1 Construct the likelihood function $\mathcal{L}(\text{ data } \mid \mu, \theta)$

$$\mathcal{L}(\text{ data } \mid \mu, \theta) = \text{ Poisson } (\text{ data } \mid \mu \cdot s(\theta) + b(\theta)) \cdot p(\tilde{\theta} \mid \theta). \tag{5.4}$$

Here ”data” can be either the actual experimental observation or pseudo-data for constructing sampling distributions. The parameter μ is the signal strength modifier and θ stands for the full set of nuisance parameters. Poisson $(data \mid \mu s + b)$ represents a product of Poisson probabilities to observe n_i events in bins i:

$$\prod_i \frac{(\mu s_i + b_i)^{n_i}}{n_i!} e^{-\mu s_i - b_i}. \tag{5.5}$$

2 To compare the compatibility of the ”data” with the *background-only* and *signal+background* hypotheses, where the signal is allowed to be scaled by some factor μ, the test statistic $\tilde{q}_\mu$[147] is built based on the negative profile log-likelihood ratio:

$$\tilde{q}_\mu = -2 \ln \frac{\mathcal{L}\left(\text{ data } \mid \mu, \hat{\theta}_\mu\right)}{\mathcal{L}(\text{ data } \mid \hat{\mu}, \hat{\theta})}, \quad \text{with a constraint } 0 \leq \hat{\mu} \leq \mu \tag{5.6}$$

here $\hat{\theta}_\mu$ refers to the conditional maximum likelihood estimators of θ, given the signal strength parameter μ and ”data” that may refer to the actual experimental observation or pseudo-data (toys). The pair of parameter estimators $\hat{\mu}$ and $\hat{\theta}$ correspond to the global maximum of the likelihood.

3 Find the *observed* value of $\tilde{q}_\mu^{obs}$ for the given μ under test.

4 Find values of the nuisance parameters $\hat{\theta}_0^{obs}$ and $\hat{\theta}_\mu^{obs}$ best describing the experimentally *observed* data, i.e. maximising the likelihood as given in Equation 5.4, for the *background-only* and *signal+background* hypotheses, respectively.

5 Generate toy Monte Carlo pseudo-data to construct pdfs $f\left(\tilde{q}_\mu \mid \mu, \hat{\theta}_\mu^{\text{obs}}\right)$ and $f\left(\tilde{q}_\mu \mid 0, \hat{\theta}_0^{\text{obs}}\right)$ assuming a signal with strength μ in the *signal+background* hypothesis and for the *background-only* hypothesis ($\mu = \theta$). When generating a $pseudo - dataset$, the nuisance parameters are fixed to the values obtained by fitting the *observed* data, but are allowed to float in fits needed to evaluate the test statistic. So that the nuisance parameters are fixed to their maximum likelihood estimates, which gives good coverage properties[148].

6 Having constructed $f\left(\tilde{q}_\mu \mid \mu, \hat{\theta}_\mu^{\text{obs}}\right)$ and $f\left(\tilde{q}_\mu \mid 0, \hat{\theta}_0^{\text{obs}}\right)$ distributions, two p-values are defined to be associated with the actual observation for the *signal+background* and *background-only* hypotheses, p_μ and p_b:

$$p_\mu = P\left(\tilde{q}_\mu \geq \tilde{q}_\mu^{\text{obs}} \mid \text{signal+background}\right) = \int_{\tilde{q}_\mu^{\text{oss}}}^{\infty} f\left(\tilde{q}_\mu \mid \mu, \hat{\theta}_\mu^{\text{obs}}\right) d\tilde{q}_\mu, \tag{5.7}$$

$$1 - p_b = P\left(\tilde{q}_\mu \geq \tilde{q}_\mu^{\text{obs}} \mid \text{background-only}\right) = \int_{q_0^{\text{obs}}}^{\infty} f\left(\tilde{q}_\mu \mid 0, \hat{\theta}_0^{\text{obs}}\right) d\tilde{q}_\mu, \tag{5.8}$$

and calculate $\text{CL}_\text{s}(\mu)$ as a ratio of both probabilities:

$$CL_s(\mu) = \frac{p_\mu}{1 - p_b}. \tag{5.9}$$

7 If, for $\mu = 1, \text{CL}_\text{s} \leq \alpha$, one could state that the SM $\text{W}_\text{L}^\pm \text{W}_\text{L}^\pm$ is excluded with (1-α) CL_s confidence level (C.L.).

8 To quote the 95% Confidence Level upper limit on μ, to be further denoted as $\mu^{95\%\text{CL}}$ by adjusting μ until $\text{CL}_\text{s} = 0.05$.

Expected limits To define the expected median upper-limit and $\pm 1\sigma$ and $\pm 2\sigma$ bands for the *background-only* hypothesis, one can generate a large set of *background-only* pseudo-data and calculate CL_s and $\mu^{95\%\text{CL}}$ for each of them, as if they were real data. Then, a cumulative probability distribution of results by starting integration from the side corresponding to low event yields could be constructed. The point at which the cumulative probability distribution crosses the quantile of 50% is the median expected value. The $\pm 1\sigma$ (68%) band is defined by the crossings of the 16% and 84% quantiles. Crossings at 2.5% and 97.5% define the $\pm 2\sigma$ (95%) band. However, this prescription is very computationally intensive and in order to save computational resources, the fact that the distributions of the test statistic for a given μ do not depend on the pseudo-data is used, so they can be computed only once. The computation of the p-values for each pseudo-data then requires the test statistic to be evaluated only once for each trial value of μ, and the total number of evaluations is proportional to $N + M$ instead of $N \cdot M$.

5.6.2 Significance

The presence of the signal is quantified by the *background-only* p-value, i.e. the probability for the background to fluctuate and give an excess of events as large or larger than the observed one. As before, this requires defining a test statistic and the construction of its sampling distribution. For a given cross section hypothesis of $\text{W}_\text{L}^\pm \text{W}_\text{L}^\pm$, the test statistic used is q_0:

$$q_0 = -2 \ln \frac{\mathcal{L}\left(\text{ data } \mid 0, \hat{\theta}_0 \right)}{\mathcal{L}(\text{ data } \mid \hat{\mu}, \hat{\theta})} \quad \text{and } \hat{\mu} \geq 0. \tag{5.10}$$

The constraint $\hat{\mu} \geq 0$ gives an accumulation of the test statistic at zero for events with downward fluctuations. Following the discussion in **??**, the distribution $f\left(q_0 \mid 0, \hat{\theta}_0^{\text{obs}}\right)$ is built by generating pseudo-data for nuisance parameters around $\hat{\theta}_0^{\text{obs}}$ and event counts following Poisson probabilities under the *background-only* hypotheses. The p-value corresponding to a given experimental observation q_0^{obs} is evaluated as follows:

$$p_0 = P\left(q_0 \geq q_0^{\text{obs}}\right) = \int_{q_0^{obs}}^{\infty} f\left(q_0 \mid 0, \hat{\theta}_0^{\text{obs}}\right) dq_0. \tag{5.11}$$

The p-value is coverting into a significance Z following the convention of a ”one-sided Gaussian tail”:

$$p = \int_Z^{\infty} \frac{1}{\sqrt{2\pi}} \exp\left(-x^2/2\right) dx = \frac{1}{2} P_{\chi_1^2}\left(Z^2\right). \tag{5.12}$$

where, $P_{\chi_1^2}$ stands for survival function of χ^2 for one degree of freedom. The 5σ significance (Z = 5) corresponds to $p_b = 2.8 \times 10^{-7}$.

5.7 Signal Extraction

5.7.1 Fit Strategy

The signal extraction is performed in a simultaneous fit of the SR and the three CRs with the Higgs Combination tool[138]. The fitted variables and the binnings in each region are given in Table 5.10.

Table 5.10 The fitted distribution in the signal region and the control regions.

region	**variable** 1	**variable** 1 **binning**	**variable** 2	**variable** 2 **binning**
SR	$\text{DNN}^{\text{nonVBS}}$	(0,0.454,0.588,0.669,0.740,1)	DNN^{WW}	(0,0.417,0.618,0.767,0.890,1)
b-tagged CR	m_{jj}	(500,800,1200,1800,inf)		
WZ CR	m_{jj}	(500,1000,1500,2000,inf)	$\lvert\Delta\eta_{jj}\rvert$	(2.5,4.0,5.0,inf)
WZb CR	m_{jj}	(500,800,1200,1800,inf)		

The signal ($\text{W}_\text{L}^\pm\text{W}_\text{L}^\pm$ or $\text{W}_\text{T}^\pm\text{W}_\text{T}^\pm$) is freely floating in the fit, while all background processes are fixed based on their SM cross sections, except the WZ and tZq backgrounds which are allowed to freely float because it is heavily constrained from the data in the control regions. The effect of the systematic uncertainties on normalization is modeled with log-normal constraining functions. The effect of systematic uncertainties on shapes is modeled by vertical interpolation of 1 σ up, central, and 1 σ down templates with quadratic interpolation within $\pm 1\sigma$ and a linear extrapolation beyond $\pm 1\sigma$.

5.7.2 Results

This analysis was accomplished by several groups. The published results are in the Ref[14], in which the statistical interpretations are given by fitting to the two-dimensional (2D) distributions of boosted decision trees (BDTs), details are in the Appendix A.4.2 in the SR and kinematic distributions in the CRs, denoted as the BDT-fit. The statistical analysis by fitting to the 2D distributions of DNNs in the SR and kinematic distributions in the CRs, denoted as the DNN-fit, is performed independently and serves as a cross-check, which gives consistent results with the published ones. In this section, the expected results of the DNN-fit are given in sub section 5.7.2.1. Then the published results from the BDT-fit are reported in sub section 5.7.2.2.

5.7.2.1 The expected results in the DNN-fit

Good agreement between the data and the prediction is found in Figure 5.5, 5.6 and 5.7 containing the m_{jj} distributions or unrolled 2D distributions in the b-tagged, WZ CR, and WZb control regions, respectively. Figure 5.8 shows the unrolled 2D distributions of DNN$^{\mathrm{WW}}$:DNN$^{\mathrm{nonVBS}}$ distribution in the signal region.

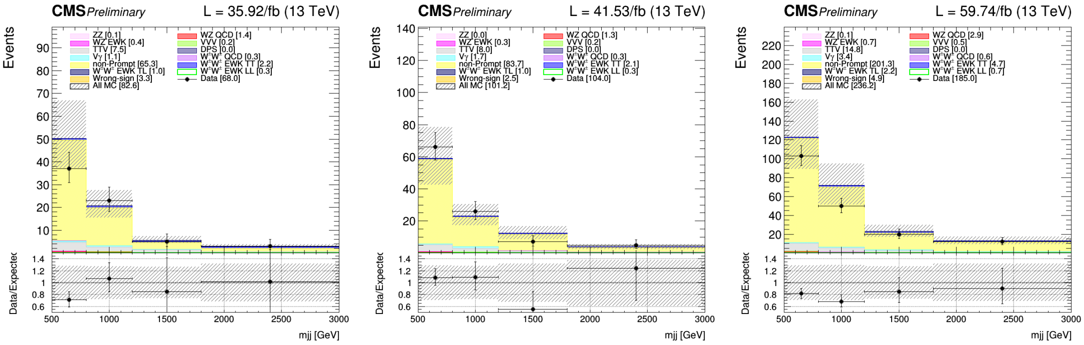

Figure 5.5 The m_{jj} distribution of data and pre-fit prediction in the b-tagged control region. Distributions are used in signal extraction for 2016 (left), 2017 (middle), and 2018 (right).

The expected values in the statistical analysis are obtained by performing the simultaneous fit with the strategy mentioned in Section 5.7.1.

Following the discussion in Section 5.6.2, the expected significances for different polarized components are evaluated with the combine tool[138]. Table 5.11 lists the expected significance for the three years individuals and the expected for the statistical combination of the three years for $\mathrm{W}_{\mathrm{L}}^{\pm}\mathrm{W}_{\mathrm{L}}^{\pm}$, $\mathrm{W}_{\mathrm{T}}^{\pm}\mathrm{W}_{\mathrm{T}}^{\pm}$, singly longitudinal component $\mathrm{W}_{\mathrm{L}}^{\pm}\mathrm{W}_{\mathrm{X}}^{\pm}$, where X = L or T, and singly transverse component $\mathrm{W}_{\mathrm{T}}^{\pm}\mathrm{W}_{\mathrm{X}}^{\pm}$ in the WW-frame. In the WW-frame, the expected significance of

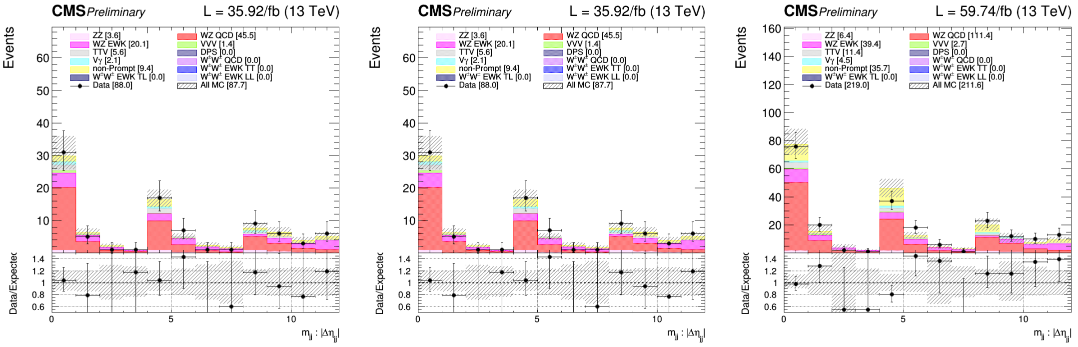

Figure 5.6 Unrolled 2D distributions of m_{jj}:$|\Delta\eta|$ of data and pre-fit prediction in the WZ control region. Distributions are used in signal extraction for 2016 (left), 2017 (middle), and 2018 (right).

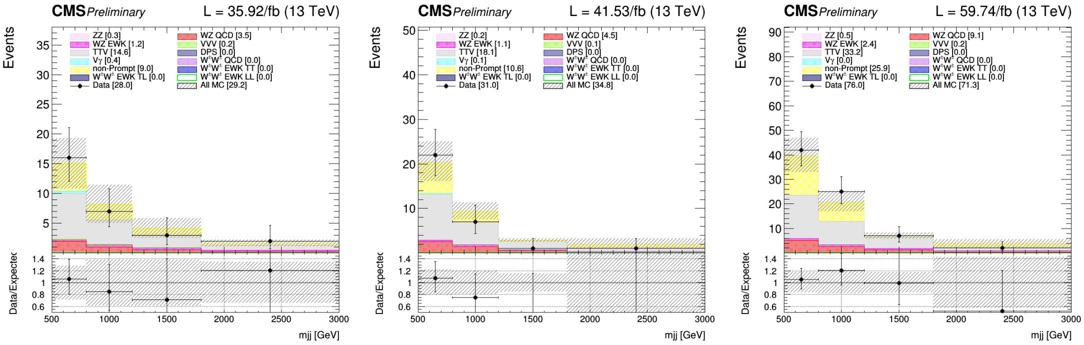

Figure 5.7 The m_{jj} distribution of data and pre-fit prediction in the b-tagged WZ control region. Distributions are used in signal extraction for 2016 (left), 2017 (middle), and 2018 (right).

$\mathrm{W}^{\pm}_{\mathrm{L}}\mathrm{W}^{\pm}_{\mathrm{L}}$ is 0.9 standard deviations, the expected significance of the singly polarized component $\mathrm{W}^{\pm}_{\mathrm{L}}\mathrm{W}^{\pm}_{\mathrm{X}}$ is 2.2 standard deviations. A comparison with significance measurements in the pp-frame are in Appendix A.4.1.

Table 5.11 Expected significance for different polarized component for each data-taking period and the combined.

Signal process	**2016**	**2017**	**2018**	**2016-2018 Combined**
$\mathrm{W}^{\pm}_{\mathrm{L}}\mathrm{W}^{\pm}_{\mathrm{L}}$	0.5	0.4	0.6	0.9
$\mathrm{W}^{\pm}_{\mathrm{T}}\mathrm{W}^{\pm}_{\mathrm{T}}$	1.7	1.7	2.4	3.4
$\mathrm{W}^{\pm}_{\mathrm{L}}\mathrm{W}^{\pm}_{\mathrm{X}}$	1.2	1.0	1.6	2.2
$\mathrm{W}^{\pm}_{\mathrm{T}}\mathrm{W}^{\pm}_{\mathrm{X}}$	3.8	4.2	4.9	7.2

Following the Section 5.6.1. Table 5.12 lists the expected signal strength for the three years individually and the expectation for the statistical combination of the three years for different polarized components in the WW-frame.

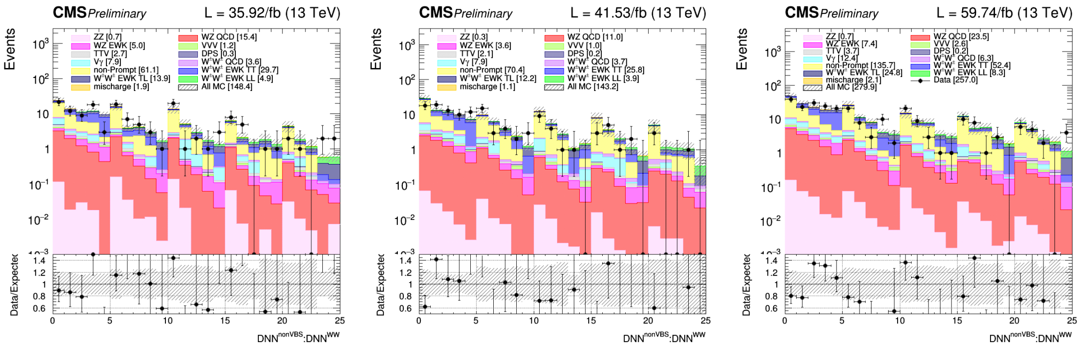

Figure 5.8 Unrolled 2D distributions of $\mathrm{DNN}^{\mathrm{WW}}$:$\mathrm{DNN}^{\mathrm{nonVBS}}$ of data and pre-fit prediction in the signal region. Distributions are used in signal extraction for 2016 (left), 2017 (middle), and 2018 (right).

Table 5.12 Signal strength for the different polarized components.

Polarization mode	Expected signal strength
$\mathrm{W}^\pm_\mathrm{L}\mathrm{W}^\pm_\mathrm{L}$	$1^{+1.27}_{-1.11}$
$\mathrm{W}^\pm_\mathrm{T}\mathrm{W}^\pm_\mathrm{T}$	$1^{+0.40}_{-0.33}$
$\mathrm{W}^\pm_\mathrm{L}\mathrm{W}^\pm_\mathrm{X}$	$1^{+0.58}_{-0.48}$
$\mathrm{W}^\pm_\mathrm{T}\mathrm{W}^\pm_\mathrm{X}$	$1^{+0.28}_{-0.22}$

5.7.2.2 The results in the BDT-fit

The BDT-fit strategy is similar to the DNN-fit. Simultaneous fits are performed using the SR and the WZ, b-tagged, WZb, and ZZ CRs. The ZZ CR is added in the Ref[14], which selects events with four leptons with the exact VBS requirements as the SR. Two separate fits are performed, one for the simultaneous measurements of the $\mathrm{W}^\pm_\mathrm{L}\mathrm{W}^\pm_\mathrm{L}$ and $\mathrm{W}^\pm_\mathrm{T}\mathrm{W}^\pm_\mathrm{X}$ cross sections and a second for the simultaneous measurements of the $\mathrm{W}^\pm_\mathrm{L}\mathrm{W}^\pm_\mathrm{X}$ and $\mathrm{W}^\pm_\mathrm{T}\mathrm{W}^\pm_\mathrm{T}$ cross sections. A 2D distribution is used in the simultaneous fits for the $\mathrm{W}^\pm\mathrm{W}^\pm$ SR with five bins in the $\mathrm{BDT}^{\mathrm{nonVBS}}$ and five bins in the corresponding $\mathrm{BDT}^{\mathrm{WW}}$. In the SR, the choosing bin boundaries make the contributions of $\mathrm{W}^\pm_\mathrm{L}\mathrm{W}^\pm_\mathrm{L}$ and $\mathrm{W}^\pm_\mathrm{L}\mathrm{W}^\pm_\mathrm{X}$ similar across the bins. For the CRs, the m_{jj} distribution is used with four bins [500, 800, 1200, 1800, ∞] GeV.

The distributions of the $\mathrm{BDT}^{\mathrm{nonVBS}}$ and the two $\mathrm{BDT}^{\mathrm{WW}}$ output scores are shown in Fig. 5.9. The predicted yields are shown with their best fit normalizations from the simultaneous fit for the $\mathrm{W}^\pm_\mathrm{L}\mathrm{W}^\pm_\mathrm{L}$ and $\mathrm{W}^\pm_\mathrm{T}\mathrm{W}^\pm_\mathrm{X}$ cross sections. The data yields are given in the Table 5.13, along with the SM expectation with best-fit normalization. The resulting background yields from the fit for the $\mathrm{W}^\pm_\mathrm{L}\mathrm{W}^\pm_\mathrm{X}$ and $\mathrm{W}^\pm_\mathrm{T}\mathrm{W}^\pm_\mathrm{T}$ cross sections are consistent with the yields shown in Table 5.13 within a few percent.

To measure the cross section, a fiducial region is defined by a set of generator level cuts, which requires two same-sign leptons with $p_\mathrm{T} > 20\,\mathrm{GeV}$, $|\eta| < 2.5$, and $m_{\ell\ell} > 20\,\mathrm{GeV}$, and two jets with $m_{\mathrm{jj}} > 500\,\mathrm{GeV}$ and $\Delta\eta_{\mathrm{jj}} > 2.5$. The generator level leptons are selected at the so-called dressed level by combining with photons found within a cone of $\Delta R = 0.1$

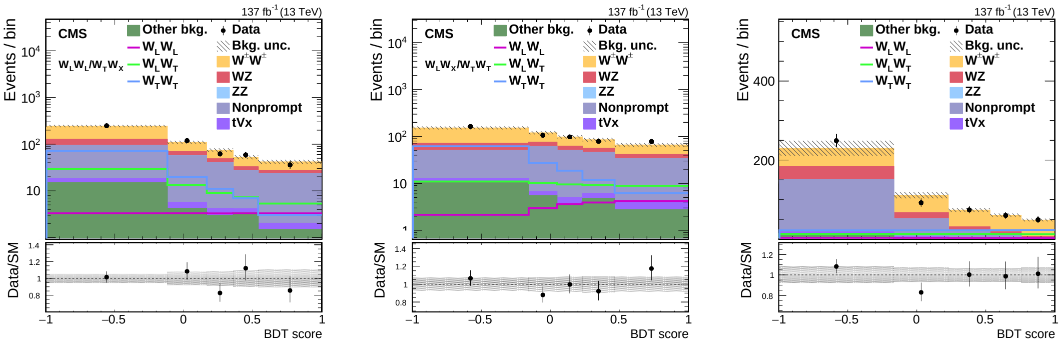

Figure 5.9 Distributions of the output score of the BDT$^{\mathrm{WW}}$ used for the $\mathrm{W}^{\pm}_{\mathrm{L}}\mathrm{W}^{\pm}_{\mathrm{L}}$ and $\mathrm{W}^{\pm}_{\mathrm{T}}\mathrm{W}^{\pm}_{\mathrm{X}}$ cross section measurements (left) and of the output score of the signal BDT used for the $\mathrm{W}^{\pm}_{\mathrm{L}}\mathrm{W}^{\pm}_{\mathrm{X}}$ and $\mathrm{W}^{\pm}_{\mathrm{T}}\mathrm{W}^{\pm}_{\mathrm{T}}$ cross section measurements (middle) in the $\mathrm{W}^{\pm}\mathrm{W}^{\pm}$ SR. The right one is the distribution of the BDT$^{\mathrm{nonVBS}}$ score in the $\mathrm{W}^{\pm}\mathrm{W}^{\pm}$ SR. The histograms for the $\mathrm{W}^{\pm}\mathrm{W}^{\pm}$ process include the contributions from the $\mathrm{W}^{\pm}_{\mathrm{L}}\mathrm{W}^{\pm}_{\mathrm{L}}$, $\mathrm{W}^{\pm}_{\mathrm{L}}\mathrm{W}^{\pm}_{\mathrm{T}}$, and $\mathrm{W}^{\pm}_{\mathrm{T}}\mathrm{W}^{\pm}_{\mathrm{T}}$ processes (shown separately as solid lines), QCD $\mathrm{W}^{\pm}\mathrm{W}^{\pm}$, and the interference.

Table 5.13 Expected yields from each SM process and observed data events in $\mathrm{W}^{\pm}\mathrm{W}^{\pm}$ SR. The combination of the statistical and systematic uncertainties is presented. The expected yields are shown with their best fit normalizations from the simultaneous fit for the $\mathrm{W}^{\pm}_{\mathrm{L}}\mathrm{W}^{\pm}_{\mathrm{L}}$ and $\mathrm{W}^{\pm}_{\mathrm{T}}\mathrm{W}^{\pm}_{\mathrm{X}}$ cross sections. The tVx background yield includes the contributions from $\mathrm{t\bar{t}V}$ and tZq processes.

Process	**Yields in $\mathrm{W}^{\pm}\mathrm{W}^{\pm}$ SR**
$\mathrm{W}^{\pm}_{\mathrm{L}}\mathrm{W}^{\pm}_{\mathrm{L}}$	16.0 ± 18.3
$\mathrm{W}^{\pm}_{\mathrm{L}}\mathrm{W}^{\pm}_{\mathrm{T}}$	63.1 ± 10.7
$\mathrm{W}^{\pm}_{\mathrm{T}}\mathrm{W}^{\pm}_{\mathrm{T}}$	110.1 ± 18.1
QCD $\mathrm{W}^{\pm}\mathrm{W}^{\pm}$	13.8 ± 1.6
Interference $\mathrm{W}^{\pm}\mathrm{W}^{\pm}$	8.4 ± 0.6
WZ	63.3 ± 7.8
ZZ	0.7 ± 0.2
Nonprompt	213.7 ± 52.3
tVx	7.1 ± 2.2
Other background	26.9 ± 9.9
Total SM	522.9 ± 60.7
Data	524

around the lepton. The overall efficiency of the signal selection within the fiducial region is around 40%. Electrons and muons that are products of decaying τ leptons are excluded in the definition of the fiducial region. Signal events selected at the reconstructed level but do not satisfy the fiducial requirements are called nonfiducial events, which are treated as background events. Those events are scaled together with the fiducial signal events in the simultaneous fit. The relative contribution of the nonfiducial events is approximately 20%. The fiducial cross section σ^{fid} can be translated from the measured signal strength $\hat{\mu}$, discussed in Section 5.6.1 as follows:

$$\sigma^{\text{fid}} = \hat{\mu}\sigma^{\text{gen}} \times \mathcal{A}, \tag{5.13}$$

where σ^{gen} is the cross section given by the MC generator, $\mathcal{A}$ is the acceptance of the fiducial region, which can be calculated by the following formula:

$$\mathcal{A} = \frac{N_{pass}}{N_{pass} + N_{fail}}, \tag{5.14}$$

in which N_{pass} is the number of events passing the fiducial selection, and N_{fail} is the number of events failing the fiducial selection.

Figure 5.10 shows the fit results for the $\mathrm{W}^{\pm}_{\mathrm{L}}\mathrm{W}^{\pm}_{\mathrm{L}}$ and $\mathrm{W}^{\pm}_{\mathrm{T}}\mathrm{W}^{\pm}_{\mathrm{X}}$ cross sections. The results are scans of the negative profile log-likelihood, $-2\Delta\ln\mathcal{L}$, i.e. the $\tilde{q}_{\mu}$ mentioned in Section 5.6.1, as a function of the $\mathrm{W}^{\pm}_{\mathrm{L}}\mathrm{W}^{\pm}_{\mathrm{L}}$ cross section. The corresponding observed (expected) upper limit at 95% confidence level (CL) is 1.17 (0.88) fb. The fiducial cross section measurements for the $\mathrm{W}^{\pm}_{\mathrm{L}}\mathrm{W}^{\pm}_{\mathrm{L}}$ and $\mathrm{W}^{\pm}_{\mathrm{T}}\mathrm{W}^{\pm}_{\mathrm{X}}$ processes and the theoretical predictions are demonstrated in Table 5.14, which agree with the theoretical predictions within uncertainties.

The fiducial cross section measurements for the $\mathrm{W}^{\pm}_{\mathrm{L}}\mathrm{W}^{\pm}_{\mathrm{X}}$ and $\mathrm{W}^{\pm}_{\mathrm{T}}\mathrm{W}^{\pm}_{\mathrm{T}}$ processes are extracted from a separate fit including a re-trained $\mathrm{BDT}^{\mathrm{WW}}$. The measurements and the expectations are listed in Table 5.14. The measured (expected) significance of the $\mathrm{W}^{\pm}_{\mathrm{L}}\mathrm{W}^{\pm}_{\mathrm{X}}$ corresponds to 2.3 (3.1) standard deviations.

Table 5.14 Measured fiducial cross sections for the $\mathrm{W}^{\pm}_{\mathrm{L}}\mathrm{W}^{\pm}_{\mathrm{L}}$ and $\mathrm{W}^{\pm}_{\mathrm{T}}\mathrm{W}^{\pm}_{\mathrm{X}}$ processes, and for the $\mathrm{W}^{\pm}_{\mathrm{L}}\mathrm{W}^{\pm}_{\mathrm{X}}$ and $\mathrm{W}^{\pm}_{\mathrm{T}}\mathrm{W}^{\pm}_{\mathrm{T}}$ processes for the helicity eigenstates defined in the WW-frame. The combination of the statistical and systematic uncertainties is presented. $\mathcal{B}$ is the branching fraction for WW → $\ell\nu\ell'\nu$[49].

Process	**$\sigma^{\text{fid}}\mathcal{B}$ (fb)**	**Theoretical prediction (fb)**
$\mathrm{W}^{\pm}_{\mathrm{L}}\mathrm{W}^{\pm}_{\mathrm{L}}$	$0.32^{+0.42}_{-0.40}$	0.44 ± 0.05
$\mathrm{W}^{\pm}_{\mathrm{T}}\mathrm{W}^{\pm}_{\mathrm{X}}$	$3.06^{+0.51}_{-0.48}$	3.13 ± 0.35
$\mathrm{W}^{\pm}_{\mathrm{L}}\mathrm{W}^{\pm}_{\mathrm{X}}$	$1.20^{+0.56}_{-0.53}$	1.63 ± 0.18
$\mathrm{W}^{\pm}_{\mathrm{T}}\mathrm{W}^{\pm}_{\mathrm{T}}$	$2.11^{+0.49}_{-0.47}$	1.94 ± 0.21

The measurements are also performed for the polarized observables defined using the he-

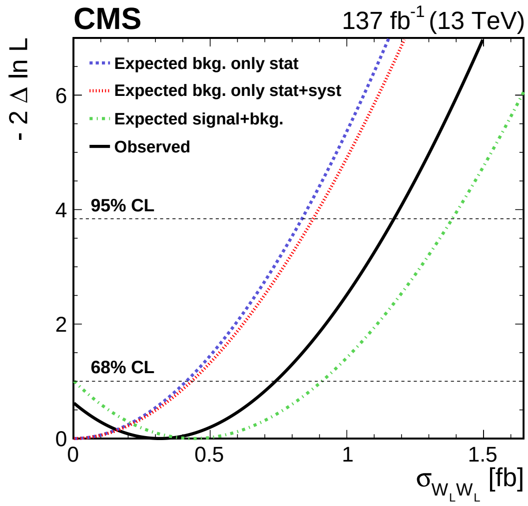

Figure 5.10 Profile likelihood scan as a function of the $\mathrm{W}^{\pm}_{\mathrm{L}}\mathrm{W}^{\pm}_{\mathrm{L}}$ cross section. The red (blue) line represents the expected values in the background-only hypothesis, i.e., assuming no contribution from the $\mathrm{W}^{\pm}_{\mathrm{L}}\mathrm{W}^{\pm}_{\mathrm{L}}$ process, considering all systematic uncertainties (only statistical ones). The green line shows the expected values for the signal-plus-background hypothesis. The observed values are represented by the black line.

licity eigenstates in the initial state pp-frame. Defining the polarization vectors in the pp-frame changes the respective contributions of $\mathrm{W}^{\pm}_{\mathrm{L}}\mathrm{W}^{\pm}_{\mathrm{L}}$, $\mathrm{W}^{\pm}_{\mathrm{L}}\mathrm{W}^{\pm}_{\mathrm{X}}$ and $\mathrm{W}^{\pm}_{\mathrm{T}}\mathrm{W}^{\pm}_{\mathrm{X}}$, and the distributions of the input observables sensitive to the polarization[149]. The fiducial cross section measurements and the theoretical predictions are summarized in Table 5.15. The observed (expected) 95% CL upper limit of the production cross section is 1.06 (0.85) fb for the $\mathrm{W}^{\pm}_{\mathrm{L}}\mathrm{W}^{\pm}_{\mathrm{L}}$ process. The observed (expected) significance of the $\mathrm{W}^{\pm}_{\mathrm{L}}\mathrm{W}^{\pm}_{\mathrm{X}}$ process is 2.6 (2.9) standard deviations.

Table 5.15 Measured fiducial cross sections for the $\mathrm{W}^{\pm}_{\mathrm{L}}\mathrm{W}^{\pm}_{\mathrm{L}}$ and $\mathrm{W}^{\pm}_{\mathrm{T}}\mathrm{W}^{\pm}_{\mathrm{X}}$ processes, and for the $\mathrm{W}^{\pm}_{\mathrm{L}}\mathrm{W}^{\pm}_{\mathrm{X}}$ and $\mathrm{W}^{\pm}_{\mathrm{T}}\mathrm{W}^{\pm}_{\mathrm{T}}$ processes for the helicity eigenstates defined in the pp-frame. The combination of the statistical and systematic uncertainties is shown. $\mathcal{B}$ is the branching fraction for WW → $\ell\nu\ell'\nu$[49].

Process	$\sigma^{\mathrm{fid}}\,\mathcal{B}$ **(fb)**	**Theoretical prediction (fb)**
$\mathrm{W}^{\pm}_{\mathrm{L}}\mathrm{W}^{\pm}_{\mathrm{L}}$	$0.24^{+0.40}_{-0.37}$	0.28 ± 0.03
$\mathrm{W}^{\pm}_{\mathrm{T}}\mathrm{W}^{\pm}_{\mathrm{X}}$	$3.25^{+0.50}_{-0.48}$	3.32 ± 0.37
$\mathrm{W}^{\pm}_{\mathrm{L}}\mathrm{W}^{\pm}_{\mathrm{X}}$	$1.40^{+0.60}_{-0.57}$	1.71 ± 0.19
$\mathrm{W}^{\pm}_{\mathrm{T}}\mathrm{W}^{\pm}_{\mathrm{T}}$	$2.03^{+0.51}_{-0.50}$	1.89 ± 0.21

5.8 Summary

A study of the polarized electroweak-induced production of $\mathrm{W}^{\pm}\mathrm{W}^{\pm}jj$ using the fully leptonic final states has been presented. The data set used is the 137 fb^{-1} in proton-proton collisions at $\sqrt{s} = 13\,\text{TeV}$. The dependence of the signal on the reference frame was studied and the conclusion is that the $\mathrm{W^{\pm}W^{\pm}}$ center-of-mass frame is both the most physically meaningful and also the most signal-rich reference frame. Two boosted decision trees are trained in the signal region, one is to separate the $\mathrm{W^{\pm}W^{\pm}}jj$ polarization states. Another is to separate $\mathrm{W^{\pm}W^{\pm}}jj$ from nonprompt background. A binned maximum likelihood fit of the signal region along with control regions is performed to extract the signal significance. In the $\mathrm{W^{\pm}W^{\pm}}$ center-of-mass reference frame, the observed (expected) signal significance of $\mathrm{W^{\pm}_{L}W^{\pm}_{L}}$ is 1.17 (0.88) σ. The observed (expected) 95%CL upper limit on the signal strength of $\mathrm{W^{\pm}_{L}W^{\pm}_{L}}$ is 2.3 (3.1) standard deviations. In the parton-parton center-of-mass reference frame, the observed (expected) 95% CL upper limit of the production cross section is 1.06 (0.85) fb for the $\mathrm{W^{\pm}_{L}W^{\pm}_{L}}$ process. The observed (expected) significance of the singly longitudinal component process is 2.6 (2.9) standard deviations. This author made a significant contribution to signal modeling and did an independent study of the polarization of same-sign WW pairs production, obtaining the results as a cross-check with published results. In this analysis, the author acted as the co-speaker of the approval talk.

Chapter 6

Probing Majorana Neutrinos and Weinberg Operator in pp → $\mu^{\pm}\mu^{\pm}jj$

This chapter shows the detail in probing Majorana neutrinos and Weinberg operator in pp → $\mu^{\pm}\mu^{\pm}jj$, which uses the same analysis framework as Chapter 5. Due to similar signal signature as polarization studies of $\mathrm{W}^{\pm}\mathrm{W}^{\pm}jj$, those two analyses share many common settings. For such common parts, this chapter focuses on the differences. The data and signal samples are given in Section 6.1. Understanding high-p_{T} muon performance is important for this analysis, which is discussed in 6.2. Then event selections are described in Section 6.3. Section 6.4 discusses the estimations of the backgrounds. Next the systematic uncertainties are shown in Section 6.5. The results are given in Section 6.6. In Section 6.8, this analysis is summarized.

6.1 Data Samples and Monte-Carlo Simulations

This analysis is later than the polarized $\mathrm{W}^{\pm}\mathrm{W}^{\pm}jj$ measurement. So a newer version of NanoAOD, version v7, was used. The simulated backgrounds are same as the polarized $\mathrm{W}^{\pm}\mathrm{W}^{\pm}jj$ measurement, which are already described in Section 5.1.3.

6.1.1 Data

This analysis is also based on the full Run-2 dataset in pp collisions at $\sqrt{s} = 13\,\mathrm{TeV}$. Since only dimuon channel is considered, so **SingleMuon** and **DoubleMuon** primary datasets are considered. All data analyzed is selected using same approved luminosity certification files as shown in Section 5.1.

The full list of data samples and HLT paths for each year is given in Table 6.1.

6.1.2 Simulation of signal samples

In this analysis, two types of signals are generated, one from the heavy Majorana neutrino type-I seesaw model, the other is from the Weinberg operator. The signal sample productions

Table 6.1 Primary data samples and HLT paths used in the analysis

Year	Dataset name	HLT paths
2016	SingleMuon	HLT_IsoMu24 HLT_IsoTkMu24
	DoubleMuon	HLT_Mu17_TrkIsoVVL_Mu8_TrkIsoVVL HLT_Mu17_TrkIsoVVL_TkMu8_TrkIsoVVL
2017	SingleMuon	HLT_IsoMu27
	DoubleMuon	HLT_Mu17_TrkIsoVVL_Mu8_TrkIsoVVL_DZ HLT_Mu17_TrkIsoVVL_Mu8_TrkIsoVVL_DZ_Mass8
2018	SingleMuon	HLT_IsoMu24
	DoubleMuon	HLT_Mu17_TrkIsoVVL_Mu8_TrkIsoVVL_DZ_Mass3p8

are documented in the following sections.

6.1.2.1 The heavy Majorana neutrino in $W^{\pm}W^{\pm}$ scattering

The heavy Majorana neutrino in $W^{\pm}W^{\pm}$ processes are simulated at Next-to-Leading order (NLO) with the NLO event generator MadGraph5_amc@nlo version 2.6.5[120]. The parton showering and hadronization are performed using pythia8 version 8.226[127], and the detector simulation is performed using Geant4[119]. To match data-taking conditions, three sets of signal samples are generated corresponding to 2016, 2017, and 2018. The samples are generated with 4-flavours schema, so the pythia8 CUETP8M1[150] tune with the NNPDF30_nlo_nf_4_pdfas[151] parton distribution functions (PDFs) are used for the 2016 simulation, and the pythia8 CP5[152] tune with the NNPDF31_nnlo_as_0118_nf_4_mc_hessian[153] PDFs are used for the 2017 and 2018 simulations.

The UFO model implementing heavy Majorana neutrino hypothesis can be found at Ref[154], in which three Majorana neutrinos are introduced in addition to the common SM setups. According to paper[37].The process definition is shown below

```
import model SM_HeavyN_NLO
define p = g u c d s ũc̃d̃s̃
define j = p
generate p p > mu+ mu+ j j QED=4 QCD=0 $$ w+ w- / n2 n3 [QCD]
add process p p > mu- mu- j j QED=4 QCD=0 $$ w+ w- / n2 n3 [QCD]
```

For simplicity, only the lightest heavy Majorana neutrino n1, denoted as N, is considered, all n2, n3 contributions are forbidden. Only dimuon channel is generated. Due to the mass dependence, a scan over the hypothesis heavy Majorana neutrino mass from 50 GeV to 20000 GeV is performed. The configurations for mixing parameters are as following

$$|V_{eN}|^2 = 0,\ \ |V_{\tau N}|^2 = 0,\ \ \left|V_{\mu N}\right|^2 = 1.0. \tag{6.1}$$

A check was made with the literature[37]. The obtained cross sections are shown in the

Table 6.2 and Figure 6.1. A good agreement with the literature was found. Note that the PDF sets and tunes are different in 2016 than in 2017 and 2018, so the cross sections are different in 2016 than in 2017 and 2018.

Table 6.2 Cross section of heavy Majorana neutrino in $W^{\pm}W^{\pm}$ processes with different masses

m_N **(GeV)**	50	150	300	450	600	750	900	1000	1250
σ^{2016} **(fb)**	4.725	13.66	17.06	17.66	16.26	15.05	13.48	12.36	10.12
$\sigma^{2017/2018}$ **(fb)**	4.606	13.57	17.99	18.20	16.91	15.47	13.86	12.84	10.67
m_N **(GeV)**	1500	1750	2000	2500	5000	7500	10000	15000	20000
σ^{2016} **(fb)**	8.598	7.303	6.264	4.602	1.536	0.7521	0.3977	0.2018	0.1089
$\sigma^{2017/2018}$ **(fb)**	8.918	7.612	6.425	4.811	1.598	0.7736	0.4480	0.2052	0.1165

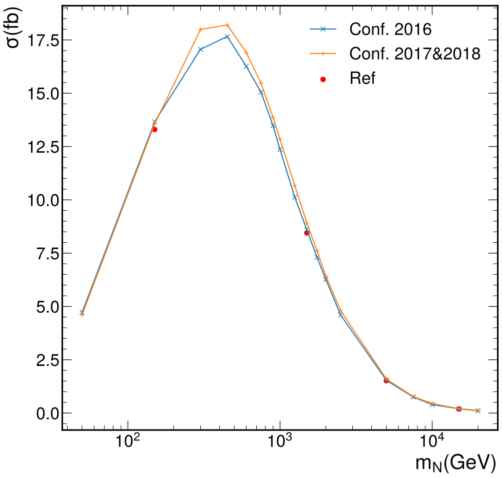

Figure 6.1 Cross sections for heavy Majorana neutrino with different masses. The blue line is the 2016 simulation, the orange line is the 2017/2018 simulation. The red dots are from Ref[37]. Good agreement with the literature was found.

To check the kinematics distributions of the samples at the generator level, similar selections as the Ref[37] are applied:

- $p_T^{\mu_1}\ (\mu_2) > 27(10)$ GeV, $\quad |\eta^{\mu}| < 2.7, \quad n_{\mu} = 2$
- $p_T^{j} > 25$GeV, $\quad \left|\eta^{j}\right| < 4.5, \quad n_j \geq 2$
- $Q_{\mu_1} \times Q_{\mu_2} = 1$

Several important signal kinematic distributions are plotted. For better illustration, only plot for $m_N = 750, 1500, 5000$ GeV as representative processes, which is the same choice as in Ref[37]. In Figure 6.2, the leading lepton p_T, azimuthal separation of the leading lepton pair $\Delta\phi_{\ell\ell}$, missing transverse momentum p_T^{miss}, invariant mass of the leading dijet system m_{jj}, pseudorapidity difference of the leading dijet system $\Delta\eta_{jj}$, ratio of scalar sum of all jet p_T (H_T) to leading lepton p_{T}, i.e. $H_{\mathrm{T}}/p_{\mathrm{T}}(\ell 1)$, where $H_{\mathrm{T}} = \sum_{k\in\{\text{ jets }\}} \left|\vec{p}_T^{\,k}\right|$, here only jets with $p_{\mathrm{T}} > 30\,\mathrm{GeV}$ are considered. There are several notable features. In the Figure 6.2 (d), a narrow collection of events at $m_{\mathrm{jj}} \ll 500\,\mathrm{GeV}$ is also observed. These events occur because one forward jet possesses relatively low p_{T} while another jet undergoes a hard $q* \longrightarrow qg$ splitting. In this case, the (qg) pair can be identified as the leading jet pair but still return a small m_{jj}. In the Figure 6.2 (e), here the $\Delta\eta_{\mathrm{jj}}$ is $\left(\eta_{j1} - \eta_{j2}\right)$, the collection of events with $|\Delta\eta_{\mathrm{jj}}| \lesssim 1$, are consistent with the low m_{jj} distribution in the Figure 6.2 (d) originating from $q* \longrightarrow qg$ with relatively small opening angles. But most of the phase space populates the region where $|\Delta\eta_{\mathrm{jj}}| \gtrsim 2$ and doesn't depend on the heavy Majorana neutrino masses.

In the production of the heavy Majorana neutrino processes, the bulk of the leading lepton is with high-p_{T}. It's also found that the leptons exhibit a strong back-to-back trajectory with the separation peaking (curtailing) at $\Delta\phi_{\ell\ell} \approx \pi$ (0). For increasing heavy neutrino masses, there is a higher tendency for back-to-back trajectories. Thus the $\Delta\phi_{\ell\ell}$ variable is helpful for the signal region (SR) and control region (CR) definition for the heavy Majorana neutrino processes. Due to no outgoing light neutrinos in the final state, $p_{\mathrm{T}}^{\mathrm{miss}}$ strongly peaks at $p_{\mathrm{T}}^{\mathrm{miss}} < 10\,\mathrm{GeV}$, no substantial dependence of $p_{\mathrm{T}}^{\mathrm{miss}}$ on the heavy neutrino mass observed. The large m_{jj} and $\Delta\eta_{\mathrm{jj}}$ are two typical characteristics of VBS/VBF process. It's observed that a majority of the phase space sits well below $H_{\mathrm{T}}/p_{\mathrm{T}} = 1$. This indicates that on an event-by-event basis more transverse momentum is carried by the leading muon than in all jets combined.

6.1.2.2 The Weinberg operator in $\mathrm{W}^{\pm}\mathrm{W}^{\pm}$ scattering

The Weinberg operator in $\mathrm{W}^{\pm}\mathrm{W}^{\pm}$ samples are also simulated at Next-to-Leading order (NLO) with MadGraph5_amc@nlo. The samples are generated with 5-flavours schema, the pythia8 CUETP8M1 tune with the NNPDF30_nlo_nf_5_pdfas[155] PDFs are used for the 2016 simulation, and the pythia8 CP5 tune with the NNPDF31_nnlo_as_0118_mc_hessian_pdfas[153] PDFs are used for the 2017 and 2018 simulations. The UFO model implementing the Majorana approximation of the Weinberg operator can be found in SMWeinberg[156], in which the effective mass is an internal parameter determined by both Weinberg operator inputs and SM ones. As the double electron channel has been well studied in the nuclear $0\nu\beta\beta$ experiments and the $e\mu$ channel requires mixing two generations, the analysis only studies the dimuon channel. Under this consideration, the parameters settings of the Weinberg operator process are as follows

- EFT scale Λ: 10 TeV, 100 TeV, 200 TeV and 400 TeV for check, and 200 TeV only for sample production;
- Wilson Coefficients $C^{\ell\ell'}$: $C^{\ell\ell'} = \delta_{\ell\mu}\delta_{\ell'\mu}$.

The samples are generated with the following syntax:

```
import model SMWeinbergNLO
generate p p > mu+ mu+ j j QED=4 QCD=0 $$ w+ w- [QCD]
add process p p > mu- mu- j j QED=4 QCD=0 $$ w+ w- [QCD]
```

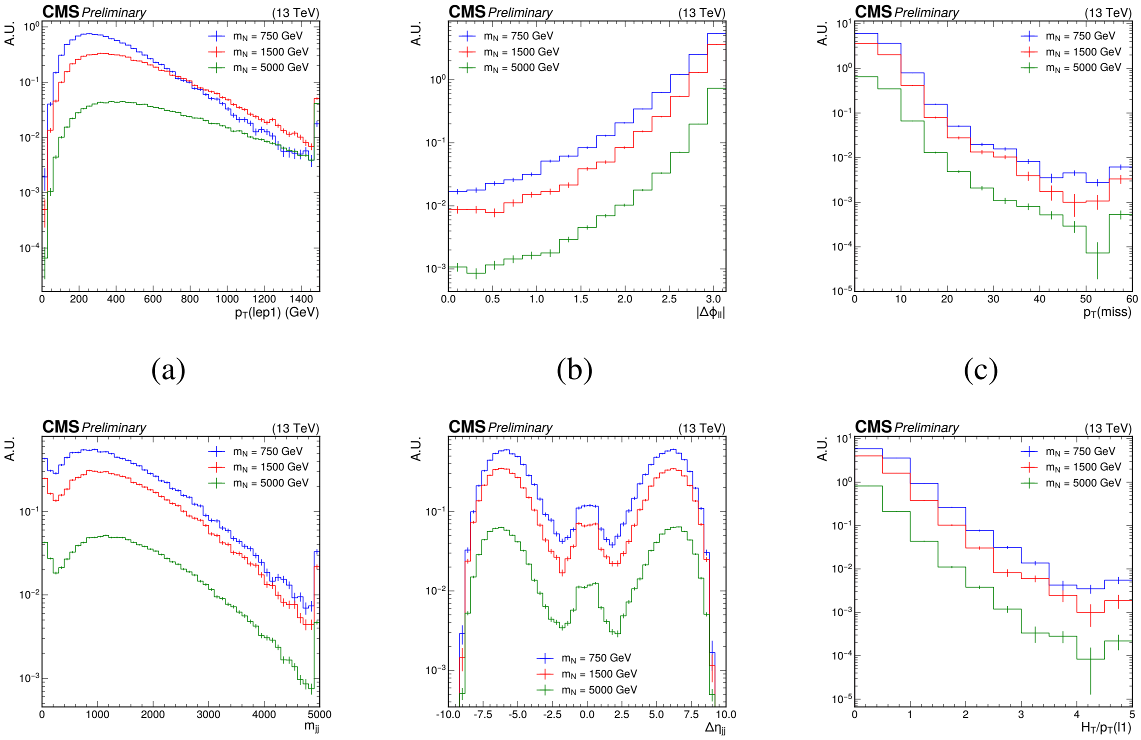

(a) (b) (c)

(d) (e) (f)

Figure 6.2 Kinematic distributions for the heavy Majorana neutrino processes with $\mathrm{m_N}$ = 750 GeV (blue), 1.5 TeV (red), and 5 TeV (green), of the (a) leading lepton transverse momentum p_{T}, (b) azimuthal separation of the leading lepton pair $\Delta\phi_{\ell\ell}$, (c) missing transverse momentum $p_{\mathrm{T}}^{\mathrm{miss}}$, (d) invariant mass of the leading dijet system m_{jj}, (e) pseudorapidity difference of the leading dijet system $\Delta\eta_{\mathrm{jj}}$, (f) ratio of scalar sum of all jet p_{T} (H_{T}) to leading lepton p_{T}, i.e. $H_{\mathrm{T}}/p_{\mathrm{T}}(\ell 1)$.

Table 6.3 compares the cross sections with the Ref[74], a great agreement is found.

Table 6.3 Cross section of the Weinberg operator in $W^{\pm}W^{\pm}$ processes

EFT scale Λ(TeV)	10	100	200	400
Effective Majorana mass (GeV)	6	0.6	0.3	0.15
Cross Sec. Ref (pb)	1.33×10^{-4}	1.42×10^{-6}	3.61×10^{-7}	9.04×10^{-8}
Cross Sec. MG, 2018 config. (pb)	1.33×10^{-4}	1.498×10^{-6}	3.738×10^{-7}	9.346×10^{-8}

After applying the same selections in 6.1.2.1, kinematic distributions are shown in Figure 6.3. For those plots, the Weinberg operator process with EFT scale $\Lambda = 200\text{TeV}$ are superimposed on the heavy Majorana neutrino processes in the same kinematics as Figure 6.2 for illustration and better comparison. From Fig 6.3, cut on large lepton p_{T} is no longer a good selection rule because of the small mass of the effective Majorana neutrino in Weinberg operator case. Instead, it's found that the $H_{\mathrm{T}}/p_{\mathrm{T}}(\ell 1)$ differs a bit. Using this $H_{\mathrm{T}}/p_{\mathrm{T}}(\ell 1)$ alone is not enough for this study, additionally considering the $p_{\mathrm{T}}^{\mathrm{miss}}$ can gain more.

6.2 Study of high-p_{T} muons

Majority of events in the Majorana neutrinos signal processes have muons with high p_{T} (>200 GeV). The author checked that if it is safe to use PF algorithm for high-p_{T} muons in this section.

The compatibility of the PF and TuneP algorithms Studies of high-p_{T} muons are well documented in Ref[100], as mentioned in Section 4.4, TuneP algorithm is preferred for high-p_{T} assignment. In this analysis, muons are reconstructed by the PF algorithm. Both algorithms are compared by using DoubleMuon datasets for each year, the selections are in Table 6.4.

Table 6.4 Opposite sign control regions to compare PF algorithm and TuneP algorithm.

Variable	**Control region**
Number of leptons	2 opposite sign muons
Lepton p_{T}	$> 30/30$ GeV
$m_{\ell\ell}$	> 20 GeV
$\mathcal{Z}(\ell)$	< 0.75
Jet p_{T}	> 30 GeV
$\Delta\eta_{jj}$	> 2.5
m_{jj}	> 500 GeV
b-jet veto	Yes
tau veto	Yes

in above table $\mathcal{Z}(\ell)$ is the Zeppenfeld variable defined in Equation 5.1.

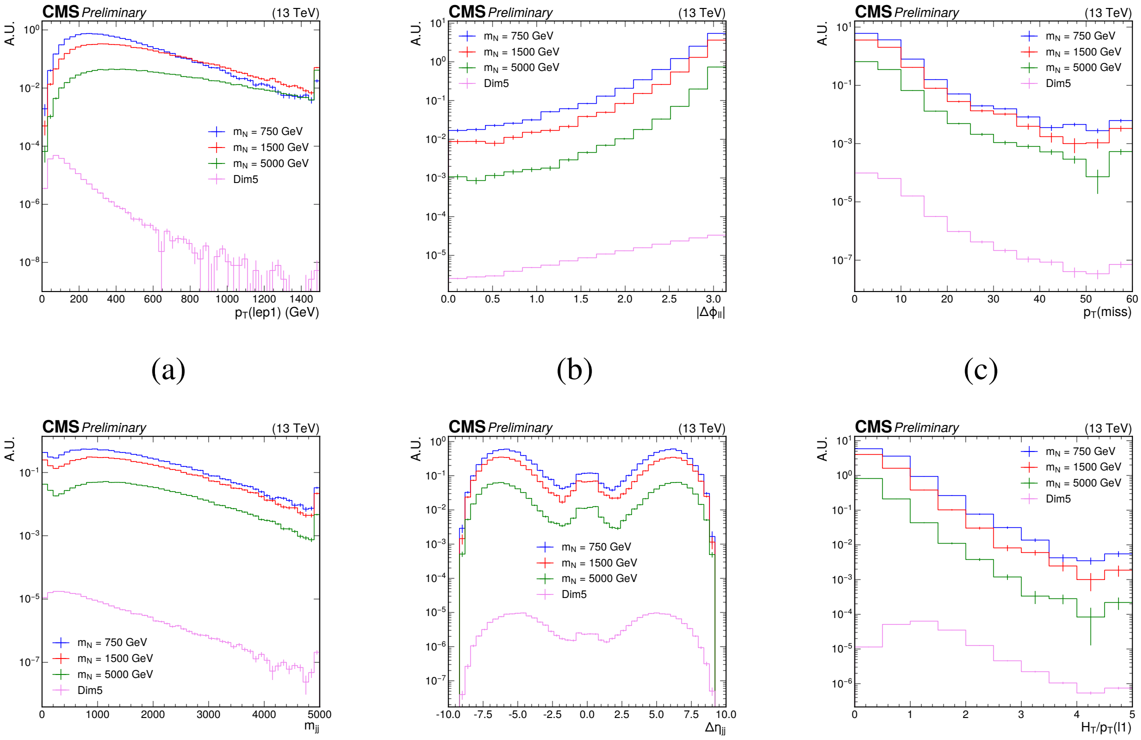

(a) (b) (c)

(d) (e) (f)

Figure 6.3 Kinematic distributions for Weinberg operator process (magenta) and the heavy Majorana neutrino processes with m_N = 750 GeV (blue), 1.5 TeV (red), and 5 TeV (green), of the (a) leading lepton transverse momentum p_T, (b) azimuthal separation of the leading lepton pair $\Delta\phi_{\ell\ell}$, (c) missing transverse momentum p_T^{miss}, (d) invariant mass of the leading dijet system m_{jj}, (e) pseudorapidity difference of the leading dijet system $\Delta\eta_{jj}$, (f) ratio of scalar sum of all jet p_T (H_T) to leading lepton p_T, i.e. $H_T/p_T(\ell 1)$.

The comparison plots are in Figure 6.4, which shows that both algorithms are equivalent in the analysis.

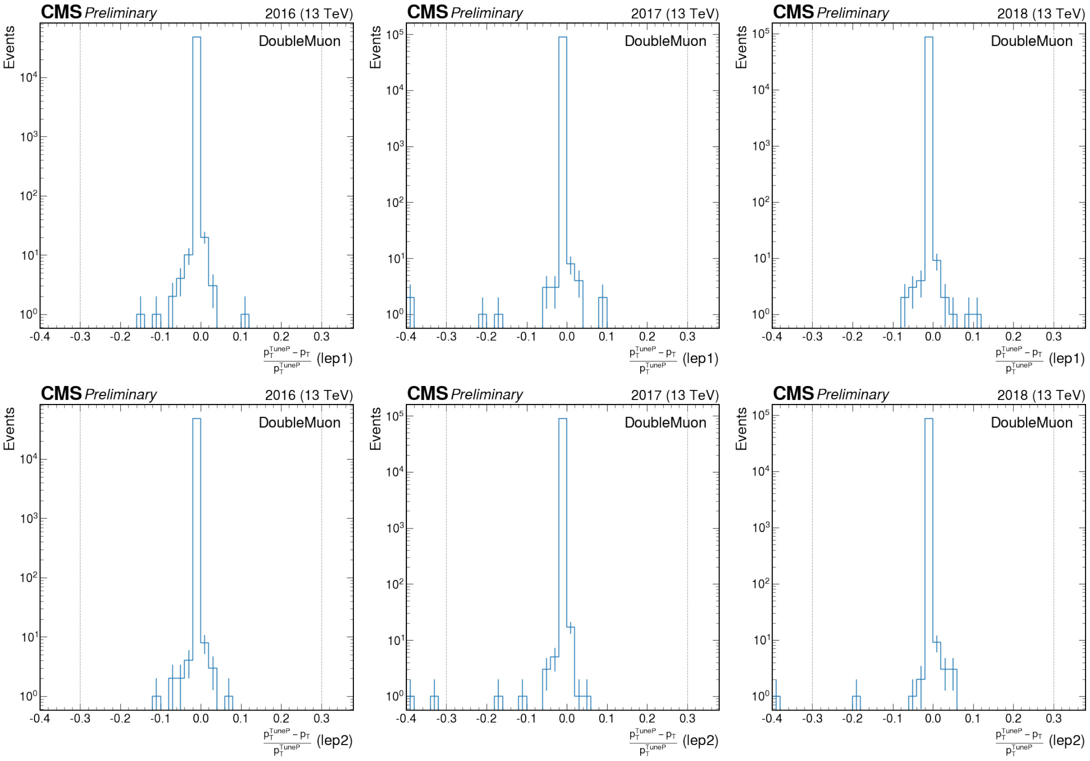

Figure 6.4 Comparison between PF p_{T} and TuneP p_{T} of leading muon p_{T} (top) and trailing muon p_{T} (bottom) for 2016 (left), 2017 (middle) and 2018 (right). The variable is $\frac{p_{\mathrm{T}}^{TuneP} - p_{\mathrm{T}}}{p_{\mathrm{T}}^{TuneP}}$, $|\frac{p_{\mathrm{T}}^{TuneP} - p_{\mathrm{T}}}{p_{\mathrm{T}}^{TuneP}}| > 0.3$ indicates large discrepancies between two algorithms. Only very rate events are observed to have large discrepancies, so we can still use PF algorithm in our analysis.

The events which have large discrepancies are in Table 6.5. Since the signal regions of this analysis require same-sign muons, events which are similar as Table 6.5 should be negligible in the analysis.

Table 6.5 Events have large discrepancies $|\frac{p_{\mathrm{T}}^{TuneP} - p_{\mathrm{T}}}{p_{\mathrm{T}}^{TuneP}}| > 0.3$ between Particle-Flow algorithm and TuneP algorithm.

Year	**Run**	**luminosityBlock**	**Event**	**Muon idx**	**PF p_{T}(GeV)**	**TuneP p_{T}(GeV)**	η	ϕ	**PF $m_{\ell\ell}$(GeV)**	**TuneP $m_{\ell\ell}$ (GeV)**	**PF pT^{miss}(GeV)**	**TuneP $\mathbf{p}_T^{miss}$ (GeV)**
2017	305814	456	716396397	1	84.62	42.31	-2.16	-2.05	132.86	93.95	27.13	48.71
2017	300517	231	284632362	1	378.73	195.28	-1.39	0.54	93.14	66.88	29.39	170.88
2017	304738	333	567406354	2	37.47	24.88	1.12	1.27	91.27	74.38	20.36	32.60
2017	301567	50	37964664	2	37.28	27.96	-0.82	-2.45	89.39	77.41	52.92	62.03
2018	324878	891	1626972627	2	36.27	25.50	-2.13	-2.80	107.26	89.94	23.29	31.41

Tight Muon ID scale factor for high-p_{T} muons For the *tight-HWW* scale factors, Ref[157] only considered muons with p_{T} up to 200 GeV. For high-p_{T} muons, *tight-HWW* corrections are derived and applied in the analysis. The SingleMuon and DY_madgraph datasets are used, which are post-processed by Muon POG. The selections are in Table 6.6, passing probes need to pass Tight-WP muon selections, except PF relative isolation cut mentioned in Section 4.4.

Table 6.6 Selections for high p_{T} scale factor calculation.

Object	**Selections**
Tag_muon	p_{T} >53 GeV, $\lvert\eta\rvert$ <2.4 pass POG Tight id, particle-flow relative isolation < 0.15 pass trigger requirement in Sec 6.1.1
Probe_muon	p_{T} >53 GeV, $\lvert\eta\rvert$ <2.4 is global muon, pass tight tracker isolation
Tag_probe pair	m$_{ll}$ <120 GeV, opposite sign, $p_{\mathrm{T}}^{Tag}/p_{\mathrm{T}}^{Probe}$ <3, $\chi^2/ndof$ < 20, $dR(tag, probe) > 0.4$

There are three bins in p_{T} : (53,120,200,1000) GeV, three bins in $\lvert\eta\rvert$: (0,0.9,1.2,2.4). The plots of the scale factors are in Figure 6.5. The scale factors for $p_{\mathrm{T}} > 200$ GeV are used on high-p_{T} muons, the values are in Table 6.7.

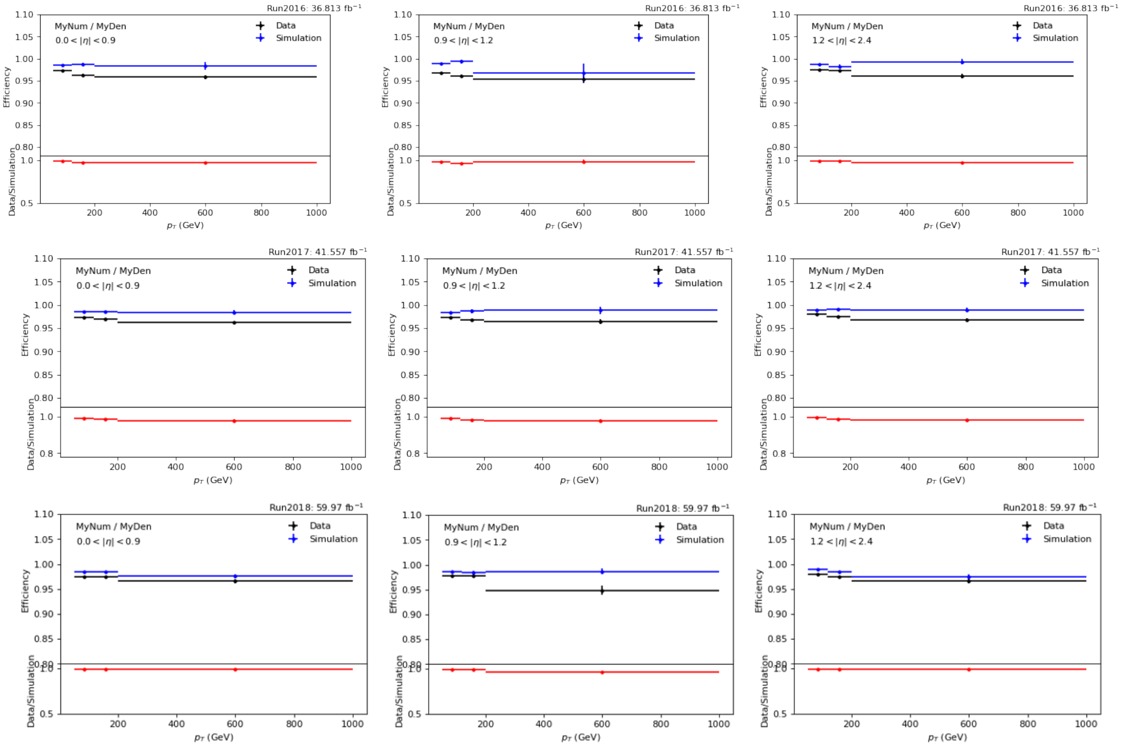

Figure 6.5 The ”Tight Muon” scale factors for 2016 (top), 2017 (middle) and 2018 (bottom).

6.3 Event Selection

Similar as the polarized W$^{\pm}$W$^{\pm}jj$ analysis in Chapter 5, a same-sign dimuon SR is defined, which requires two same-charge muons passed the *tight-HWW* have p_{T} greater than 30 GeV.

Table 6.7 The Tight-WP scale factors for muons with $p_{\mathrm{T}} > 200\,\mathrm{GeV}$

Year	$\lvert\eta\rvert < 0.9$	$0.9 < \lvert\eta\rvert < 1.2$	$1.2 < \lvert\eta\rvert < 2.4$
2016	0.974665 ± 0.009893	0.984908 ± 0.023332	0.966947 ± 0.008291
2017	0.977282 ± 0.005489	0.974852 ± 0.009392	0.978643 ± 0.005678
2018	0.989867 ± 0.005886	0.961165 ± 0.010920	0.991457 ± 0.007223

Events with additional leptons (additional $loose - HWW$ muons or electrons pass as defined in Chapter 4) or hadronic decay τ leptons are rejected, such requirements affect the events with real additional leptons in the final state, i.e. the WZ $\to 3\ell\nu$ events. Higher dijet mass is required than the polarized $\mathrm{W}^{\pm}\mathrm{W}^{\pm}jj$ analysis, which can give higher sensitivity, detail study is in Appendix A.5.1. Large pseudo-rapidity separation of the jets, and a cut on the Zeppenfeld variable[134] of each muon, $\mathcal{Z}(\ell)$, defined in Equation 5.1 are required. One of the main backgrounds is the large contribution from semi-leptonic decay $\mathrm{t\bar{t}}$ events, in which leptons come from the mis-identified jets. Those nonprompt leptons are estimated by the same method as described in Section 5.3.1. To reduce the nonprompt background, events contain a jet that passes the b-tagging selection in Section 4.6 are rejected.

Control regions (CRs) disjoint from one another and SR are built. A WZ CR is used to select event samples enriched with WZ background events by selecting three muons instead of two, and requiring two muons are opposite charge, and with invariant mass within 15 GeV of the nominal Z mass. The $\mathrm{W}^{\pm}\mathrm{W}^{\pm}$ SR and WZ CR definitions used in this analysis are summarized in Table 6.8. To select event samples enriched with nonprompt leptons, a b-tagged CR is defined by requiring the same selection as for the $\mathrm{W}^{\pm}\mathrm{W}^{\pm}$ SR, with the b jet veto requirement inverted. Similarly, a WZb CR is defined by requiring the same selection as for the WZ CR, but with the b quark veto requirement inverted. The dominate backgrounds in $\mathrm{W}^{\pm}\mathrm{W}^{\pm}$ SR are the VBS $\mathrm{W}^{\pm}\mathrm{W}^{\pm}$ and nonprompt leptons.

To optimize the signal regions for the heavy Majorana neutrino analysis and the Weinberg operator analysis respectively, according to the discussion about the signal kinematics in Section 6.1.2, different selections on $p_{\mathrm{T}}^{\mathrm{miss}}$ and $|\Delta\phi_{\ell\ell}|$ are applied based on $\mathrm{W}^{\pm}\mathrm{W}^{\pm}$ SR. For the heavy Majorana neutrino, $|\Delta\phi_{\ell\ell}| > 2$ is required, this region is called high-$\Delta\phi_{\ell\ell}$ bin. And a low-$\Delta\phi_{\ell\ell}$ bin, with $|\Delta\phi_{\ell\ell}| > 2$ is defined. For the Weinberg operator, $p_{\mathrm{T}}^{\mathrm{miss}} < 50$ is required, this region is called low-$p_{\mathrm{T}}^{\mathrm{miss}}$ bin. And a high-$p_{\mathrm{T}}^{\mathrm{miss}}$ bin region, with $p_{\mathrm{T}}^{\mathrm{miss}} > 50$ is defined. The threshold of the $p_{\mathrm{T}}^{\mathrm{miss}}$ is studied In Appendix A.5.2.

For the heavy Majorana neutrino process, the efficiency after passing high-$\Delta\phi_{\ell\ell}$ bin selection is in Figure 6.6, the efficiency starts from around 15% to around 38% as a function of $\mathrm{m_N}$. For the Weinberg operator process, the efficiency after passing low-$p_{\mathrm{T}}^{\mathrm{miss}}$ bin selection is about 10.3%.

Table 6.8 Signal region and WZ control region definitions.

Variable	SR	WZ CR
Number of leptons	2 same sign muons	3 muons
Lepton p_{T}	$> 30/30$ GeV	$> 25/10/25$ GeV
Di-lepton mass $m_{\ell\ell}$	-	> 20 GeV
$\lvert m_{\ell\ell} - m_{\mathrm{Z}}\rvert$	-	< 15 GeV (for one $\mu^{+}\mu^{-}$ pair)
Tri-lepton mass $m_{\ell\ell\ell}$	-	> 100 GeV
$\mathcal{Z}(\ell)$	< 0.75	< 1.0
Jet p_{T}	> 30 GeV	> 30 GeV
$\lvert\Delta\eta_{\mathrm{jj}}\rvert$	> 2.5	> 2.5
m_{jj}	> 750 GeV	> 750 GeV
$p_{\mathrm{T}}^{\mathrm{miss}}$	-	> 30 GeV
Additional lepton veto	Yes	Yes
Tau lepton veto	Yes	Yes
b-jet veto	Yes	Yes

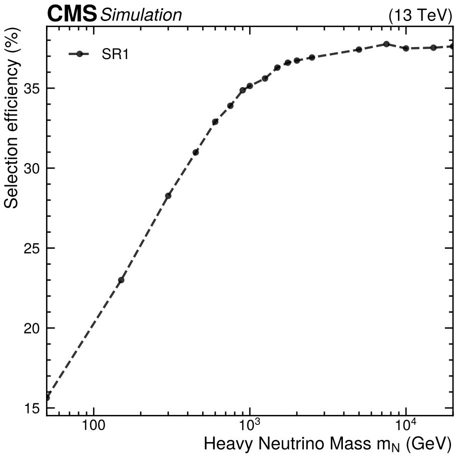

Figure 6.6 The signal efficiency for heavy Majorana neutrino process as a function of $\mathrm{m_N}$, the efficiency starts from $\sim$ 15% to $\sim$ 38% .

6.4 Background estimation

The estimations of background processes are almost same as the polarized $W^{\pm}W^{\pm}$ scattering in Section 5.3. This section only focuses on the differences. Backgrounds in signal extraction is estimated from simulation except nonprompt lepton contributions. The estimation of the nonprompt (fake). Since the analysis focuses on the same sign dimuon channel, the charge flip of muons is studied in Appendix A.5.3. Not like the charge flip of electrons, it's found that the charge flip of muons can be neglected.

6.4.1 $W^{\pm}W^{\pm}jj$

The SM $W^{\pm}W^{\pm}jj$ is one of the dominant backgrounds in our analysis, since except larger p_{T}^{miss}, the EWK and QCD $W^{\pm}W^{\pm}jj$ have the same final state as our signals. The fraction of QCD induced events after selection is very small, the main contribution is from EWK $W^{\pm}W^{\pm}jj$. By following Ref[65], the NLO QCD and EW corrections to EWK $W^{\pm}W^{\pm}jj$ are considered, which give the most accurate prediction of the kinematic distribution shapes. To better estimate the contribution from $W^{\pm}W^{\pm}jj$, the normalization is a free parameter measured from data.

6.4.2 WZ

The signal regions still receive some contribution from WZ process. The fraction of EWK $WZjj$ is small, same as EWK $WZjj$, the NLO QCD and EW corrections are considered in EWK $WZjj$. The QCD WZ process is the main competent of WZ process. The normalization of the whole WZ process is a free parameter measured from data.

6.4.3 ZZ, TVX, $V\gamma$, WW DPS and tribosons

The background from the ZZ production is completely dominated by $ZZ \rightarrow 4\ell$ events where one or two leptons are not identified or outside the acceptance region. The estimation of ZZ is from simulation, after selection, the contribution is very tiny.

The $t\bar{t}V$ processes are also estimated from simulation, a WZb CR is used to assess the normalization of tZq process. Although after selection, the TVX contributions are tiny.

The $V\gamma$, WW DPS and all tribosons processes (WWW, WWZ, WZZ, ZZZ and also WWG) are taken into account with simulated samples. They are tiny backgrounds.

6.4.4 Non-prompt lepton background estimation

As mentioned, the nonprompt estimation described in 5.3.1. An additional closure test of the nonprompt muon is done in a low m_{jj} region close to the signal region, the selections are list in Table 6.9. The comparison of m_{jj} and $H_{T}/p_{T}^{\ell 1}$ between data and prediction is shown in Figure 6.7. Within the uncertainty, the agreement between data and prediction is good.

Table 6.9 Low m_{jj} region definition for closure test of nonprompt lepton estimation.

Variable	Low m_{jj} control region
# leptons	2 same sign muons
Lepton p_{T}	$> 30/30$ GeV
$m_{\ell\ell}$	> 20 GeV
Jet pt	> 30 GeV
m_{jj}	$\in (150, 750)$ GeV
Additional lepton veto	Yes
hadronic τ lepton veto	Yes
b-jet veto	Yes

6.5 Systematic Uncertainties

The systematic uncertainties are almost same as that introduced in Section 5.4, so only differences are mentioned in this section.

Integrated luminosity Follow the latest recommendation from the LUM POG, the full three year correlation matrix is updated. The values are shown in Table 6.10. Each column represents one year, and each line represents one correlated uncertainty, with the uncorrelated uncertainties represented simply as lines containing nonzero entries only for one year.

Table 6.10 The full three year correlation matrix of luminosity uncertainty

Uncertainty source	**size in 2016 (%)**	**size in 2017 (%)**	**size in 2018 (%)**
Uncorrelated 2016	1.0	0.0	0.0
Uncorrelated 2017	0.0	2.0	0.0
Uncorrelated 2018	0.0	0.0	1.5
Correlated 2016, 2017, 2018	0.6	0.9	2.0
Correlated 2017, 2018	0.0	0.6	0.2

Muon momentum scale and resolution These uncertainties arise due to different detector effects and are p_{T} and η-dependent. Uncertainties on both the scale and resolution individually amount to about 0.2% for muons. The uncertainty values for the muons are taken from Ref[158]. Special treatments of the uncertainties for high-p_{T} muons are suggested by the CMS Muon POG. For high-p_{T} muons, the systematic for momentum scale and resolution are different from medium p_{T} muons. Figure 6.8 shows the ways to consider the systematic of events with high-p_{T} muons. As mentioned in the last Section 6.2, new scale factors for muon with $p_{\mathrm{T}} > 200$ GeV are used, the uncertainty should also be considered. Following the recommendations in Ref[100], dedicated momentum scale measurement for high-p_{T} muons, namely, Generalized Endpoint (GE) method, has been performed to access the uncertainty as mentioned in Figure 6.8. The differences between nominal and GE momentum scale are treated as

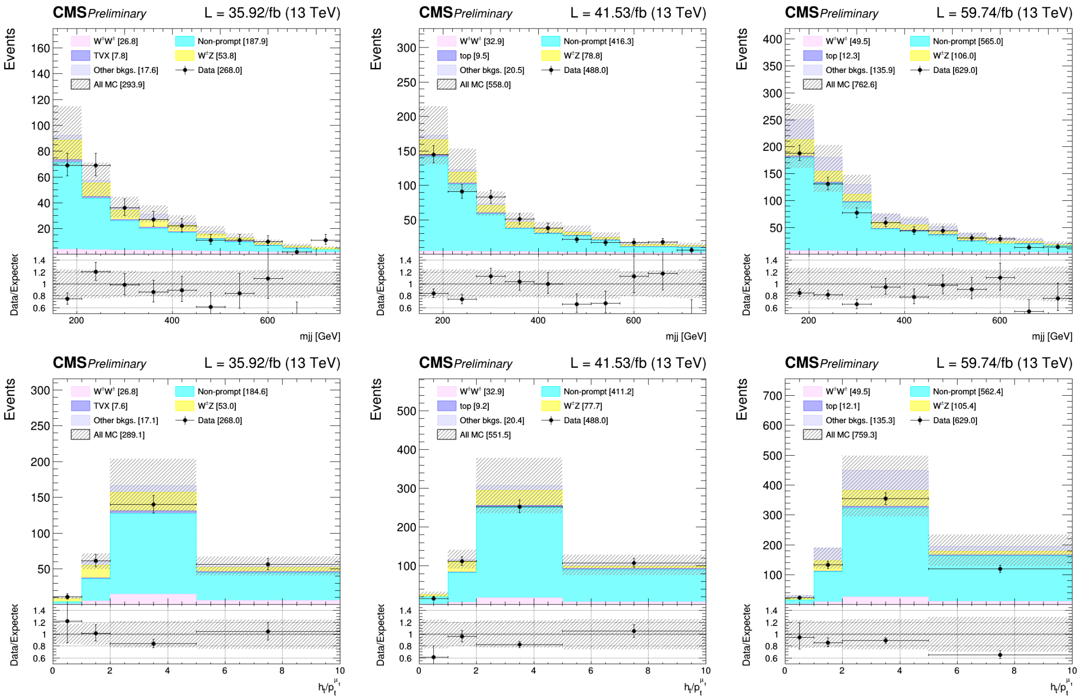

Figure 6.7 Closure test of non-prompt lepton estimation. The m_{jj} (top) and $H_{\mathrm{T}}/p_{\mathrm{T}}^{\mu 1}$ (bottom) are shown for 2016 (left), 2017 (middle) and 2018 (right). The agreement between data and predictions is good.

the uncertainty. The uncertainty of momentum resolution is considered in a similar way to the momentum scale.

6.5.1 Theoretical uncertainties

The re-normalization and factorization scale (QCD) and parton distribution function (PDF) uncertainties are considered for the heavy Majorana neutrino samples, the Weinberg operator sample and EW $\mathrm{W}^{\pm}\mathrm{W}^{\pm}jj$ processes. The PDF uncertainty is taken as the standard deviation of the PDF variations of the PDF set used in the sample production. The QCD scale uncertainty is taken as the maximum of the central value of the 6 variations that are not 2.0/0.5 or 0.5/2.0. By following[65], NLO electro-weak corrections are considered in SM $\mathrm{W}^{\pm}\mathrm{W}^{\pm}jj$ and $\mathrm{WZ}jj$ processes, described in Section 6.4.

6.5.2 Sample normalization

As mentioned in Section 6.4, the normalization of $\mathrm{W}^{\pm}\mathrm{W}^{\pm}jj$, WZ and tZq are free parameters measured from data.

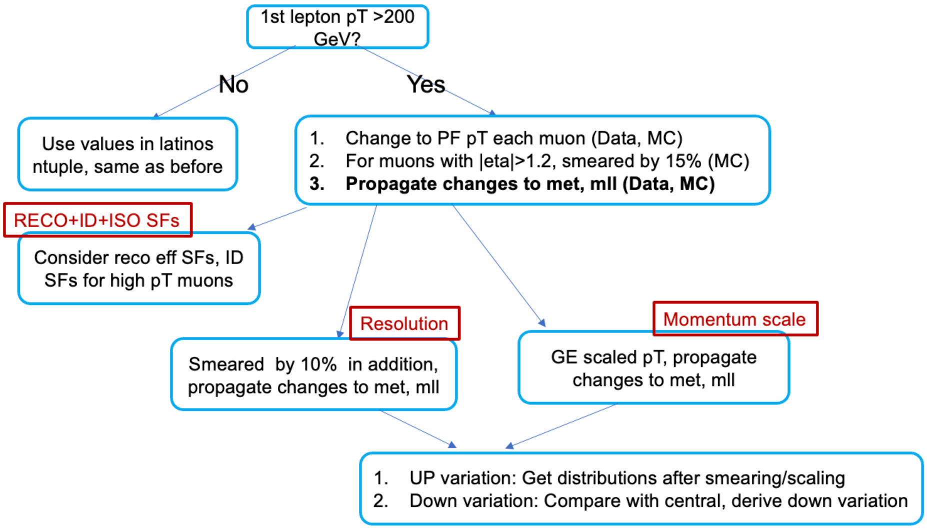

Figure 6.8 There are three kinds of uncertainty considered for events with high-p_{T} muons, they are new scale factor uncertainty, momentum scale uncertainty and resolution uncertainty.

6.6 Limits Extraction

The signal extraction is performed in a simultaneous fit of the signal regions and control regions. The fitted distribution in each region is defined in Table 6.11 for the heavy Majorana neutrino processes and Table 6.12 for the Weinberg operator process.

Table 6.11 The fitted distributions for the heavy Majorana neutrino processes.

Region	**Variable**	**variable binning**
high-$\Delta\phi_{\ell\ell}$ bin in SR	$H_{\mathrm{T}}/p_{\mathrm{T}}^{\ell 1}$	$(0, 1, 2, 5, \infty)$
low-$\Delta\phi_{\ell\ell}$ bin in SR	$H_{\mathrm{T}}/p_{\mathrm{T}}^{\ell 1}$	$(0, 2, 5, \infty)$
b-tagged CR	$H_{\mathrm{T}}/p_{\mathrm{T}}^{\ell 1}$	$(0, 2, 3, 5, \infty)$
WZ CR	$H_{\mathrm{T}}/p_{\mathrm{T}}^{\ell 1}$	$(0, 2, 3, 5, \infty)$
WZb CR	$H_{\mathrm{T}}/p_{\mathrm{T}}^{\ell 1}$	$(0, 2, 5, \infty)$

Table 6.12 The fitted distributions for Weinberg Operator.

Region	**Variable**	**variable binning**
low $p_{\mathrm{T}}^{\mathrm{miss}}$ bin in SR	$H_{\mathrm{T}}/p_{\mathrm{T}}^{\ell 1}$	$(0, 1.5, 3, 6, \infty)$
high $p_{\mathrm{T}}^{\mathrm{miss}}$ bin in SR	$H_{\mathrm{T}}/p_{\mathrm{T}}^{\ell 1}$	$(0, 2, 3, 5, \infty)$
b-tagged CR	$H_{\mathrm{T}}/p_{\mathrm{T}}^{\ell 1}$	$(0, 2, 3, 5, \infty)$
WZ CR	$H_{\mathrm{T}}/p_{\mathrm{T}}^{\ell 1}$	$(0, 2, 3, 5, \infty)$
WZb CR	$H_{\mathrm{T}}/p_{\mathrm{T}}^{\ell 1}$	$(0, 2, 5, \infty)$

The heavy Majorana neutrino signals and the Weinberg operator signal are freely floating in the fit, the normalization of $\mathrm{W}^{\pm}\mathrm{W}^{\pm}jj$ (EW and QCD are considered together), WZ (EW and QCD are considered together) and tZq are allowed to freely float because it is heavily constrained from the data in our control regions. All other background processes are fixed based on their SM cross sections. The effect of the systematic uncertainties on normalization is modeled with log-normal constraining functions. The effect of systematic uncertainties on shapes is modeled by vertical interpolation of 1 σ up, central, and 1 σ down templates with quadratic interpolation within $\pm 1\sigma$ and a linear extrapolation beyond $\pm 1\sigma$.

6.7 Results

6.7.1 Prefit plots for each year

Good agreement between the data and the prediction can be seen in Figure 6.9, 6.10, and 6.11 for WZ, WZb, and b-tagged control regions, respectively. Figure 6.12 and 6.13 contains the m_{jj} and $H_{\mathrm{T}}/p_{\mathrm{T}}^{\ell 1}$ distributions in the low-$\Delta\phi_{\ell\ell}$ bin and high-$\Delta\phi_{\ell\ell}$ bin. Figure 6.14 and 6.15 contains the m_{jj} and $H_{\mathrm{T}}/p_{\mathrm{T}}^{\ell 1}$ distributions in the high-$p_{\mathrm{T}}^{\mathrm{miss}}$ bin and low-$p_{\mathrm{T}}^{\mathrm{miss}}$ bin respectively.

6.7.2 Prefit and postfit plots for Run-2

Combine three years together, we get full Run-2 prefit plots. As mentioned in Section 6.6, the postfit plots are generated by fitting to signal regions and control regions simultaneously. Figure 6.16 shows prefit $H_{\mathrm{T}}/p_{\mathrm{T}}^{\mu 1}$ for $\mathrm{W}^{\pm}\mathrm{W}^{\pm}$ SR, b-tagged CR, WZ CR and WZb CR, Figure 6.17 shows postfit $H_{\mathrm{T}}/p_{\mathrm{T}}^{\mu 1}$ for $\mathrm{W}^{\pm}\mathrm{W}^{\pm}$ SR, b-tagged CR, WZ CR and WZb CR.

The prefit and postfit yields of each sample in different regions are in Table 6.13, 6.14, 6.15 and 6.16

Table 6.13 Prefit yields of each process in signal and control regions for studies of the heavy Majorana neutrino processes.

Process	**high-$\Delta\phi_{\ell\ell}$ bin**	**low-$\Delta\phi_{\ell\ell}$ bin**	**b-tagged CR**	**WZ CR**	**WZb CR**
Non-prompt	55.74 ± 13.32	38.40 ± 9.43	90.73 ± 21.87	16.96 ± 5.10	12.42 ± 4.46
$\mathrm{W}^{\pm}\mathrm{W}^{\pm}$	26.95 ± 2.02	28.51 ± 2.17	3.49 ± 0.43	-	-
WZ	11.21 ± 2.54	12.65 ± 2.68	2.12 ± 0.55	86.33 ± 12.68	5.73 ± 1.91
Top	1.07 ± 0.05	1.07 ± 0.06	6.34 ± 0.19	5.85 ± 0.22	13.95 ± 0.37
Others	1.66 ± 0.19	2.32 ± 0.31	0.55 ± 0.04	3.31 ± 0.34	0.30 ± 0.05
Total bkg.	96.62 ± 13.71	82.94 ± 10.04	103.23 ± 21.88	112.45 ± 13.67	32.39 ± 4.87
Data	82.0 ± 9.06	110.0 ± 10.49	92.0 ± 9.59	117.0 ± 10.82	28.0 ± 5.29
m_N = 750 GeV (Exp.)	681.18 ± 30.92	31.45 ± 1.10	16.96 ± 1.45	-	-
m_N = 1500 GeV (Exp.)	424.55 ± 20.72	13.43 ± 0.47	10.49 ± 0.83	-	-
m_N = 5000 GeV (Exp.)	75.85 ± 4.34	1.66 ± 0.08	1.65 ± 0.14	-	-

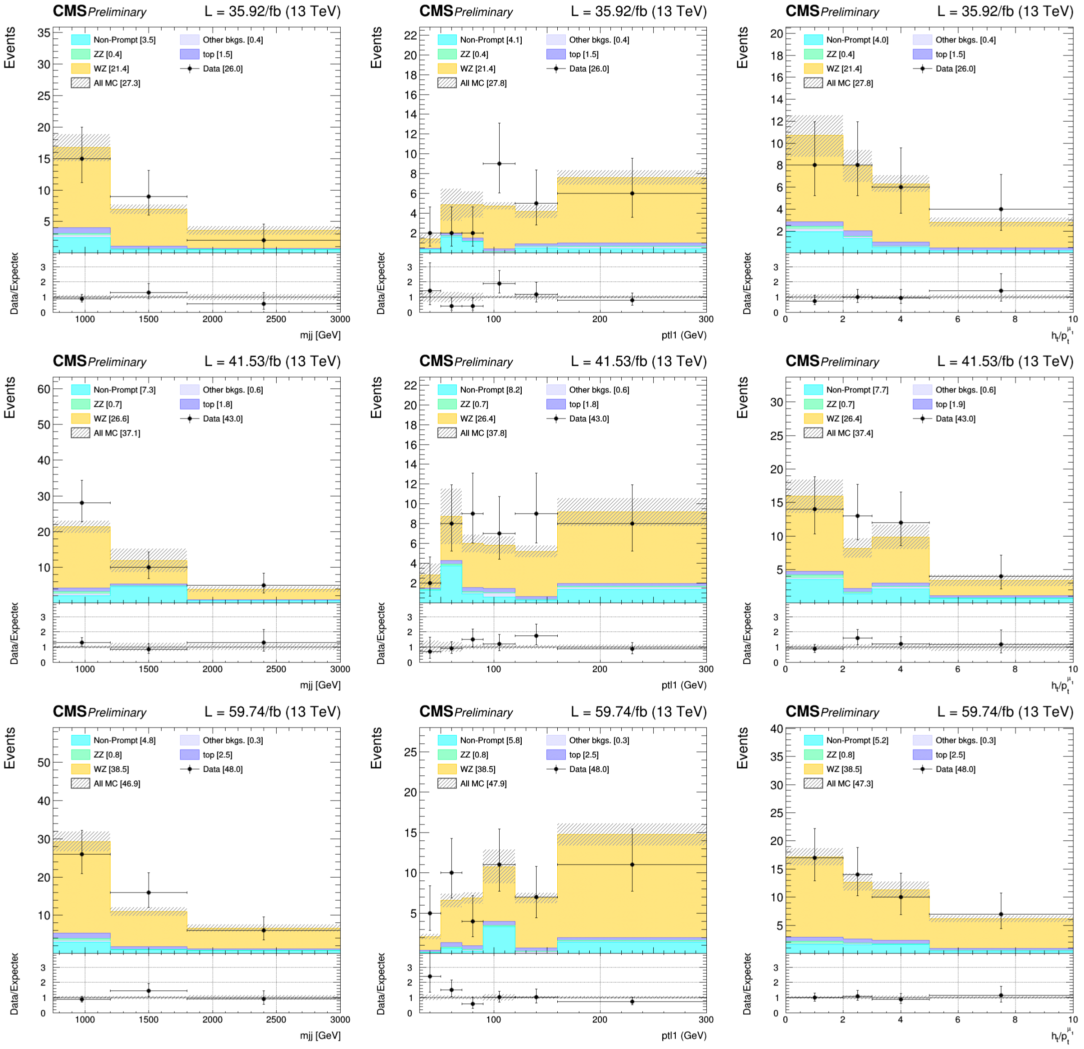

Figure 6.9 Observed data and pre-fit prediction $m_{\rm jj}$ (left), $p_{\rm T}^{\ell 1}$ (middle) and $H_{\rm T}/p_{\rm T}^{\ell 1}$ (right) distributions in the WZ control region for 2016 (top), 2017 (middle) and 2018 (bottom). The $H_{\rm T}/p_{\rm T}^{\ell 1}$ distributions are used in the simultaneous fit.

Table 6.14 Postfit yields of each process in signal and control regions for studies of heavy Majorana neutrino processes.

Process	**high-$\Delta\phi_{\ell\ell}$ bin**	**low-$\Delta\phi_{\ell\ell}$ bin**	**BTagged CR**	**WZ CR**	**WZb CR**
Non-prompt	45.07 ± 6.54	36.73 ± 5.40	78.23 ± 8.02	14.54 ± 3.18	8.62 ± 2.53
$W^{\pm}W^{\pm}$	40.89 ± 5.89	43.40 ± 6.36	5.29 ± 0.94	-	-
WZ	11.56 ± 1.22	13.80 ± 1.61	2.32 ± 0.34	96.26 ± 8.35	5.84 ± 0.96
Top	0.95 ± 0.15	0.94 ± 0.18	5.89 ± 0.65	4.63 ± 1.62	11.40 ± 3.52
Others	1.66 ± 0.16	2.36 ± 0.23	0.54 ± 0.04	3.34 ± 0.27	0.30 ± 0.05
Total bkg.	100.14 ± 8.89	97.23 ± 8.51	92.28 ± 8.11	118.77 ± 9.08	26.16 ± 4.44
Data	82.0 ± 9.06	110.0 ± 10.49	92.0 ± 9.59	117.0 ± 10.82	28.0 ± 5.29
m_N = 750 GeV (Exp.)	681.18 ± 30.92	31.45 ± 1.10	16.96 ± 1.45	-	-
m_N = 1500 GeV (Exp.)	424.55 ± 20.72	13.43 ± 0.47	10.49 ± 0.83	-	-
m_N = 5000 GeV (Exp.)	75.85 ± 4.34	1.66 ± 0.08	1.65 ± 0.14	-	-

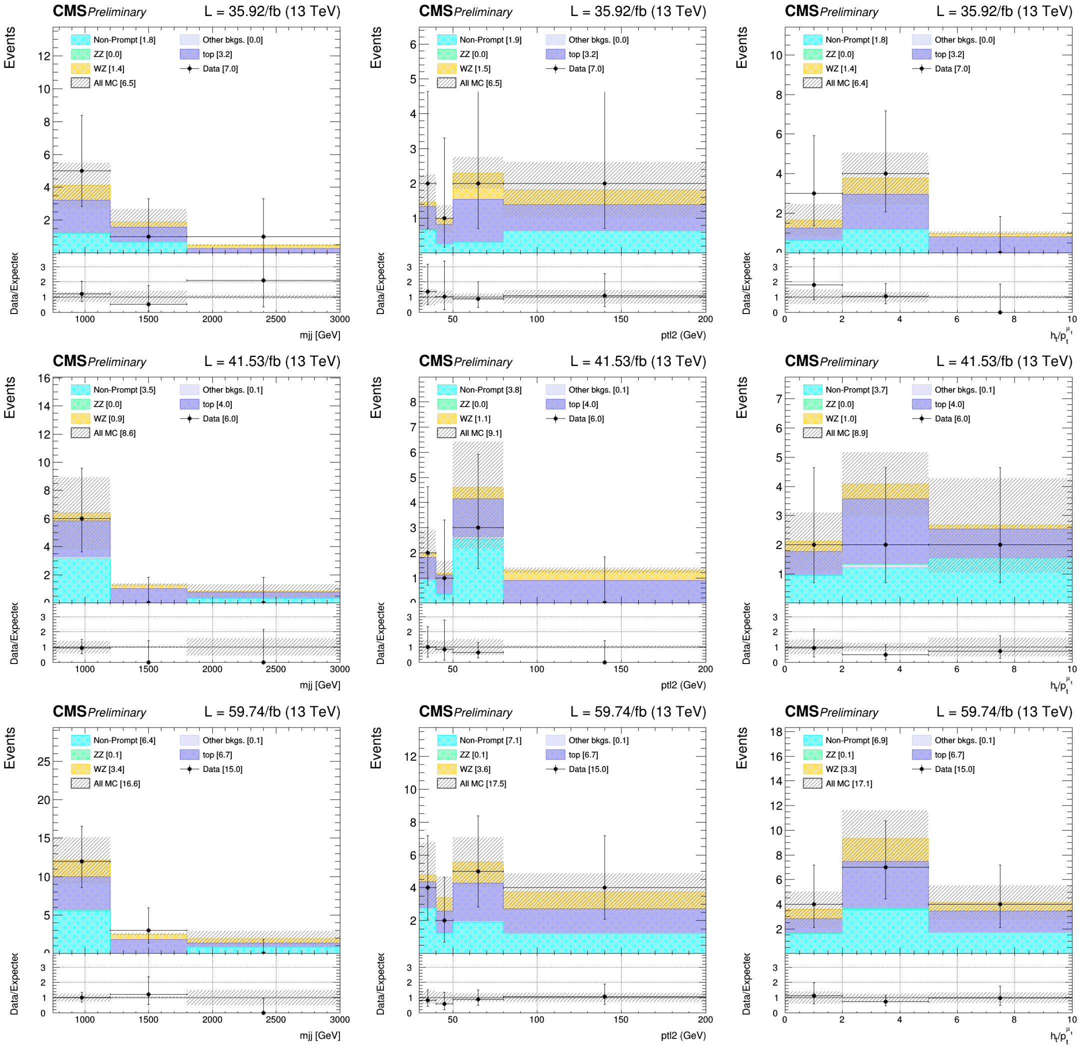

Figure 6.10 Observed data and pre-fit prediction m_{jj} (left), $p_T^{\ell 2}$ (middle) and $H_{\mathrm{T}}/p_{\mathrm{T}}^{\ell 1}$ (right) distributions in the WZb control region for 2016 (top), 2017 (middle) and 2018 (bottom). The $H_{\mathrm{T}}/p_{\mathrm{T}}^{\ell 1}$ distributions are used in the simultaneous fit.

Table 6.15 Prefit yields of each process in signal and control regions for studies of the Weinberg operator process.

Process	**high-$p_{\mathrm{T}}^{\mathrm{miss}}$ bin**	**low-$p_{\mathrm{T}}^{\mathrm{miss}}$ bin**	**BTagged CR**	**WZ CR**	**WZb CR**
Non-prompt	38.98 ± 9.92	58.03 ± 13.69	90.73 ± 21.38	16.96 ± 5.40	12.42 ± 4.47
$\mathrm{W}^{\pm}\mathrm{W}^{\pm}$	13.46 ± 0.91	41.99 ± 3.17	3.49 ± 0.41	-	-
WZ	7.58 ± 2.20	16.40 ± 2.81	2.12 ± 0.47	86.33 ± 12.34	5.73 ± 1.62
Top	0.48 ± 0.05	1.62 ± 0.09	6.34 ± 0.19	5.85 ± 0.23	13.95 ± 0.37
Others	1.88 ± 0.20	2.11 ± 0.20	0.55 ± 0.10	3.31 ± 0.33	0.30 ± 0.06
Total bkg.	62.39 ± 10.21	120.14 ± 14.33	103.23 ± 21.39	112.45 ± 13.47	32.39 ± 4.77
Data	53.0 ± 7.28	139.0 ± 11.79	92.0 ± 9.59	117.0 ± 10.82	28.0 ± 5.29
Signal (Exp.)	0.0057 ± 0.0002	0.0013 ± 0.0001	-	-	-

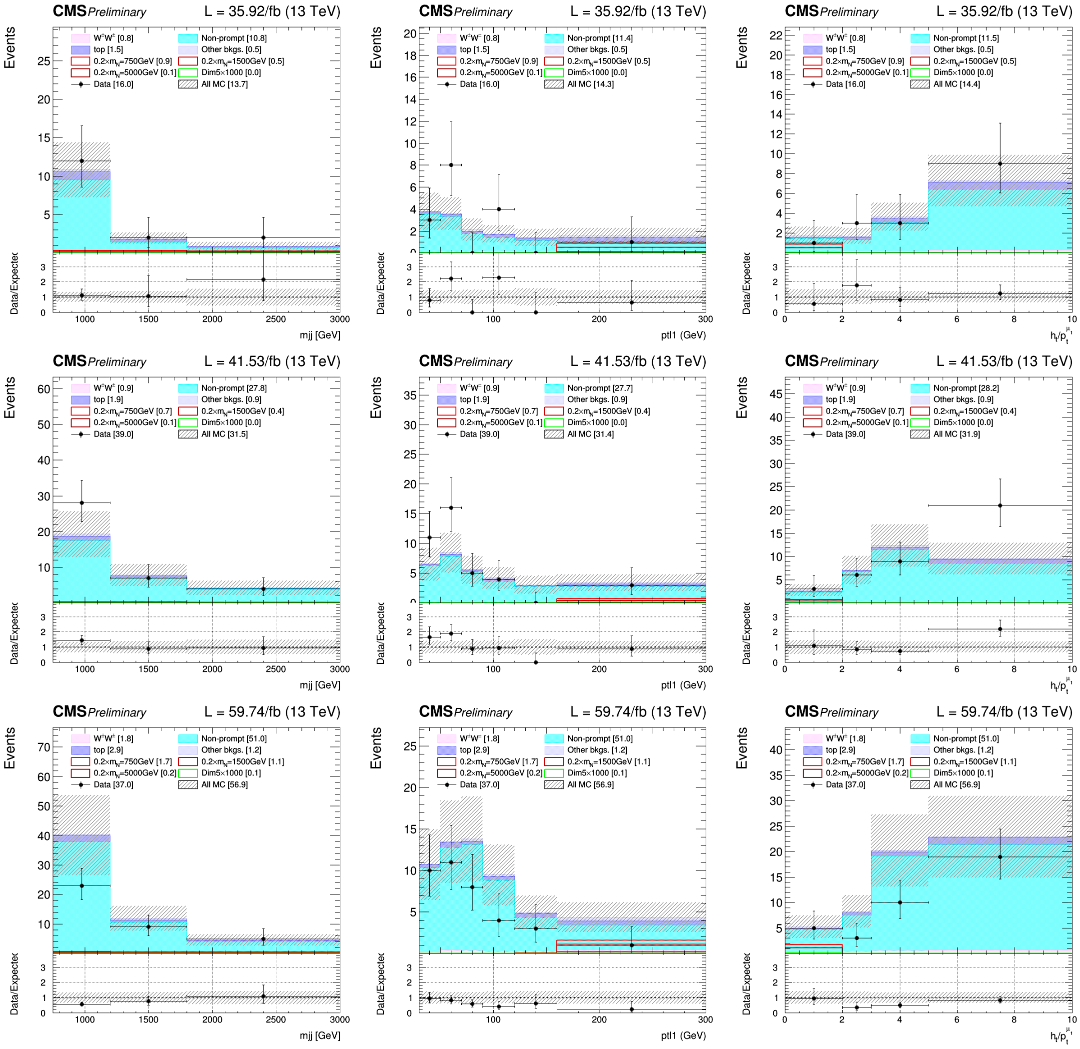

Figure 6.11 Observed data and pre-fit prediction m_{jj} (left), p_T^{l1} (middle) and $H_{\mathrm{T}}/p_{\mathrm{T}}^{\ell 1}$ (right) distributions in the btagged control region for 2016 (top), 2017 (middle) and 2018 (bottom). The $H_{\mathrm{T}}/p_{\mathrm{T}}^{\ell 1}$ distributions are used in the simultaneous fit.

Table 6.16 Postfit yields of each process in signal and control regions for studies of Weinberg operator process.

Process	**high-$p_{\mathrm{T}}^{\mathrm{miss}}$ bin**	**low-$p_{\mathrm{T}}^{\mathrm{miss}}$ bin**	**BTagged CR**	**WZ CR**	**WZb CR**
Non-prompt	34.90 ± 4.94	55.51 ± 7.03	80.73 ± 7.51	15.16 ± 3.38	9.04 ± 2.68
$W^{\pm}W^{\pm}$	18.74 ± 2.82	58.49 ± 8.83	4.87 ± 0.93	-	-
WZ	8.04 ± 1.22	17.93 ± 1.86	2.29 ± 0.39	95.13 ± 8.71	6.08 ± 0.98
Top	0.36 ± 0.11	1.41 ± 0.22	5.74 ± 0.66	4.20 ± 1.67	10.55 ± 3.58
Others	1.85 ± 0.18	2.12 ± 0.16	0.54 ± 0.06	3.35 ± 0.25	0.30 ± 0.05
Total bkg.	63.90 ± 5.82	135.45 ± 11.44	94.16 ± 7.60	117.84 ± 9.49	25.98 ± 4.58
Data	53.0 ± 7.28	139.0 ± 11.79	92.0 ± 9.59	117.0 ± 10.82	28.0 ± 5.29
Signal (Exp.)	0.0057 ± 0.0002	0.0013 ± 0.0001	-	-	-

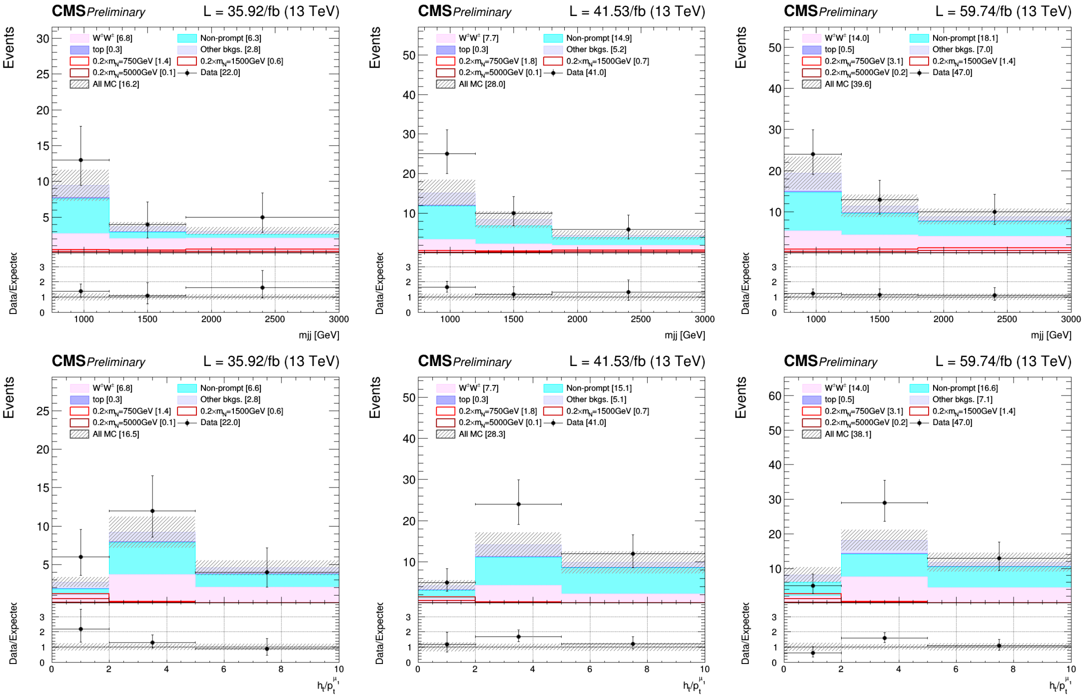

Figure 6.12 Observed data and pre-fit prediction $m_{\rm jj}$ (top) and $H_{\rm T}/p_{\rm T}^{\ell 1}$ (bottom) distributions for 2016 (left), 2017 (middle) and 2018 (right) in low-$\Delta\phi_{\ell\ell}$ bin, the $H_{\rm T}/p_{\rm T}^{\ell 1}$ distributions are used for the heavy Majorana neutrino limits extraction.

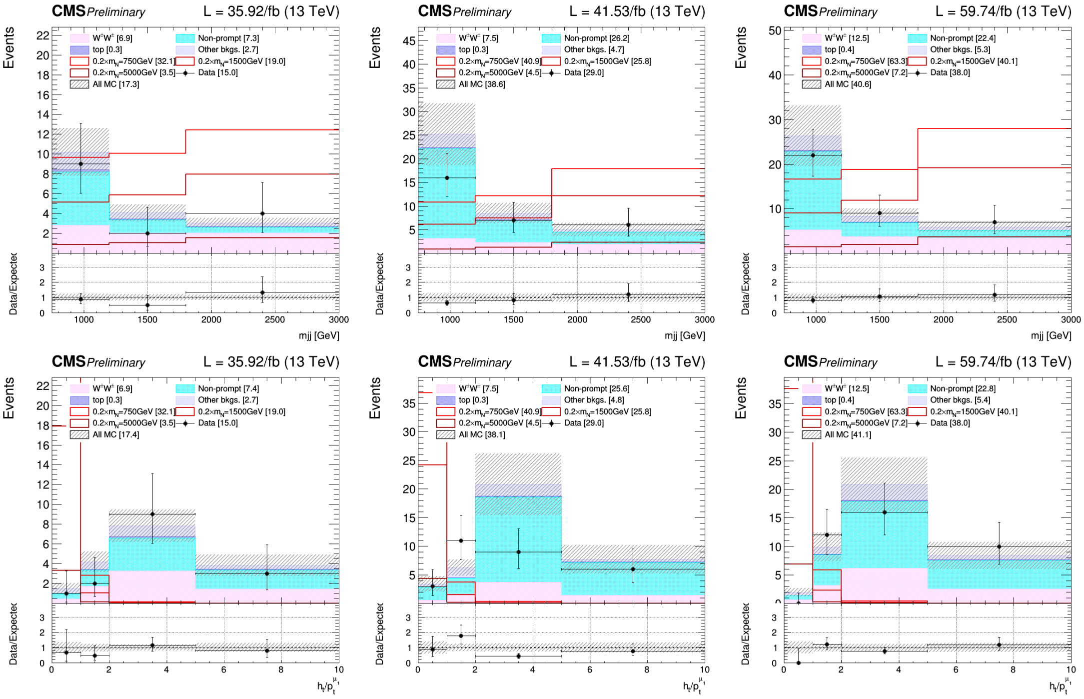

Figure 6.13 Observed data and pre-fit prediction $m_{\rm jj}$ (top) and $H_{\rm T}/p_{\rm T}^{\ell 1}$ (bottom) distributions for 2016 (left), 2017 (middle) and 2018 (right) in high-$\Delta\phi_{\ell\ell}$ bin, the $H_{\rm T}/p_{\rm T}^{\ell 1}$ distributions are used for heavy Majorana neutrino limits extraction.

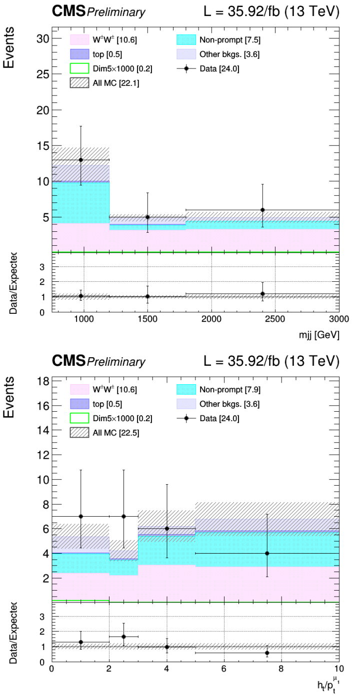

Figure 6.14 Observed data and pre-fit prediction m_{jj} (top) and $H_{\mathrm{T}}/p_{\mathrm{T}}^{\ell 1}$ (bottom) distributions for 2016 (left), 2017 (middle) and 2018 (right) in high $p_{\mathrm{T}}^{\mathrm{miss}}$ bin, the $H_{\mathrm{T}}/p_{\mathrm{T}}^{\ell 1}$ distributions are used for Weinberg operator limits extraction.

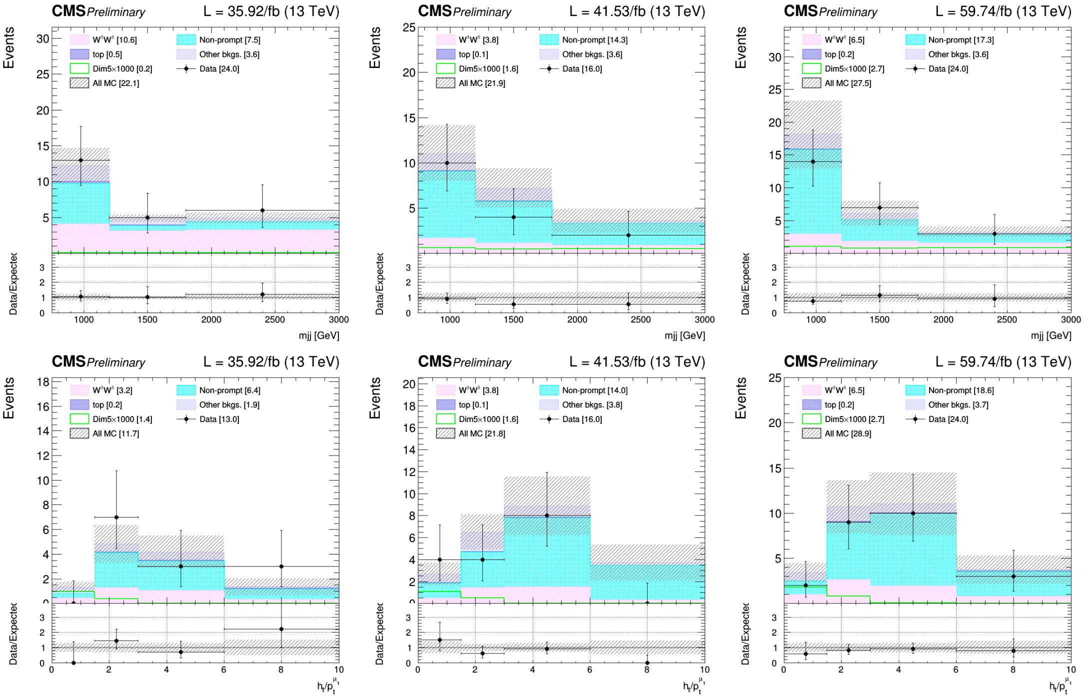

Figure 6.15 Observed data and pre-fit prediction m_{jj} (top) and $H_{\mathrm{T}}/p_{\mathrm{T}}^{\ell 1}$ (bottom) distributions for 2016 (left), 2017 (middle) and 2018 (right) in low $p_{\mathrm{T}}^{\mathrm{miss}}$ bin, the $H_{\mathrm{T}}/p_{\mathrm{T}}^{\ell 1}$ distributions are used for Weinberg operator limits extraction.

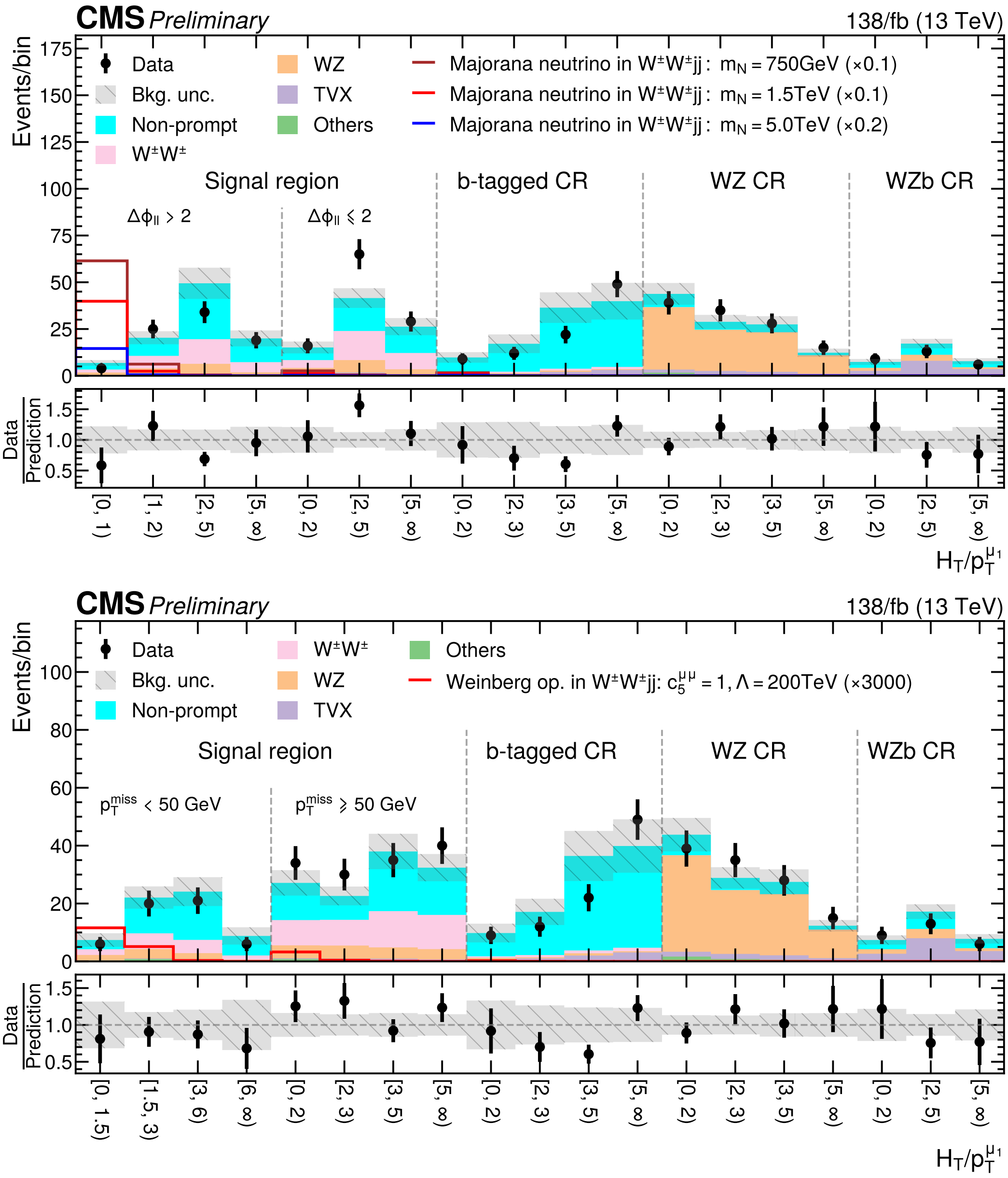

Figure 6.16 Prefit distributions of $H_{\mathrm{T}}/p_{\mathrm{T}}^{\mu 1}$ in the W±W± SR, b-tagged CR, WZ CR and WZb CR for the heavy Majorana neutrino process (top) and the Weinberg operator process (bottom). The solid lines in the top plot are the scaled expected distribution of the heavy Majorana neutrino process with m_N = 750 (brown), 1500 (red) and 5000 (blue) GeV. The solid red line in the bottom plot is the expected Weinberg operator process scaled by a factor 3000.

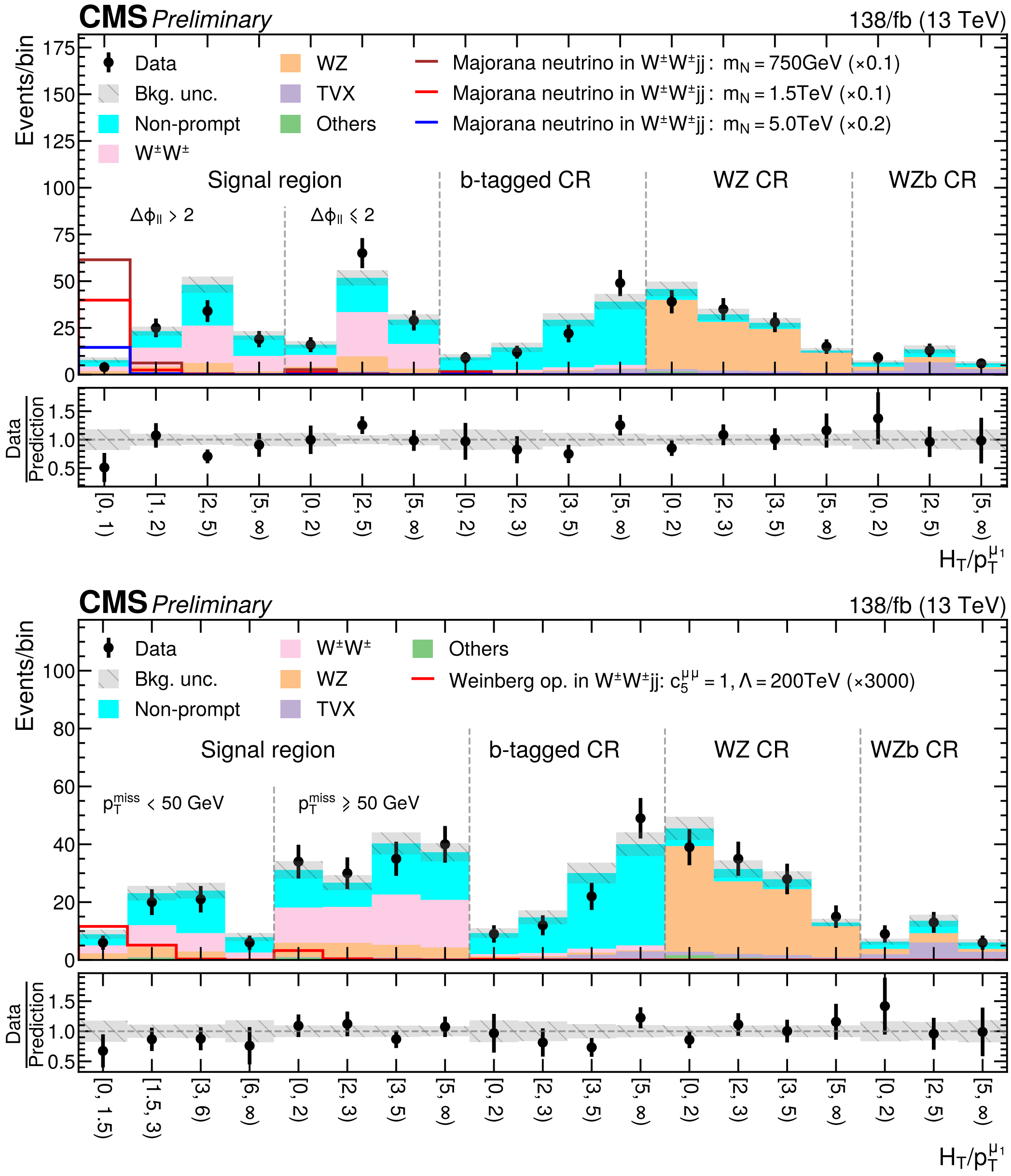

Figure 6.17 Postfit distributions of $H_\mathrm{T}/p_\mathrm{T}^{\mu1}$ in the W±W± SR, b-tagged CR, WZ CR and WZb CR for the heavy Majorana neutrino process (top) and the Weinberg operator process (bottom). The solid lines in the top plot are the scaled expected distribution of the heavy Majorana neutrino process with m_N = 750 (brown), 1500 (red) and 5000 (blue) GeV. The solid red line in the bottom plot is the expected Weinberg operator process scaled by a factor 3000.

6.7.3 Limits

For heavy Majorana neutrino processes, the upper limits are measured based on the procedure described in Chapter 2. From the fitting, the limits of the signal strength r (discussed in Section 5.6.1), can be translated to the limits of $|V_{\mu N}|^2$, the limits equal to $\sqrt{r}$, and the limits on the $\sigma \times \mathcal{B}$ is $r \times (\sigma \times \mathcal{B})_{theory}$. Table 6.17 lists the expected upper limits of $|V_{\mu N}|^2$ for all heavy Majorana neutrino process and $\pm 1\sigma$ and $\pm 2\sigma$ around the limits. Figure 6.18 shows the upper limits in Table 6.17. The red dashed line is observed upper limits in Ref[29], the blue dashed line is observed upper limits in Ref[34]. When $\mathrm{m_N}$ is greater than around 1 TeV, this analysis shows better constraints.

Table 6.17 Observed and expected 95% CL upper limits of $|V_{\mu N}|^2$, and $\pm 1\sigma$ and $\pm 2\sigma$ around the limits for different m_N.

m_N (GeV)	Observed	Expected	$\pm 1\sigma$ Expected	$\pm 2\sigma$ Expected
50	0.251	0.313	[0.258,0.382]	[0.220,0.458]
150	0.112	0.141	[0.119,0.175]	[0.100,0.210]
300	0.084	0.106	[0.087,0.132]	[0.077,0.160]
450	0.078	0.101	[0.085,0.123]	[0.069,0.150]
600	0.077	0.101	[0.082,0.123]	[0.069,0.150]
750	0.081	0.103	[0.087,0.129]	[0.071,0.155]
900	0.081	0.106	[0.084,0.129]	[0.073,0.156]
1000	0.087	0.110	[0.093,0.137]	[0.075,0.166]
1250	0.093	0.119	[0.101,0.148]	[0.084,0.179]
1500	0.099	0.127	[0.106,0.158]	[0.090,0.192]
1750	0.108	0.138	[0.115,0.172]	[0.096,0.208]
2000	0.117	0.151	[0.123,0.185]	[0.105,0.224]
2500	0.137	0.178	[0.146,0.218]	[0.124,0.265]
5000	0.232	0.300	[0.247,0.370]	[0.209,0.449]
7500	0.329	0.426	[0.349,0.525]	[0.296,0.637]
10000	0.437	0.566	[0.465,0.697]	[0.394,0.847]
15000	0.634	0.821	[0.674,1.013]	[0.571,1.229]
20000	0.862	1.118	[0.918,1.379]	[0.778,1.673]
25000	1.064	1.378	[1.131,1.698]	[0.959,2.061]

To probe the Weinberg Operator, in signal regions and control regions, $H_{\mathrm{T}}/p_{\mathrm{T}}^{\mu 1}$ is fitted as described in Chapter 2. Since only the di-muon channel is considered in this analysis, so the effective Majorana mass $|m_{\mu\mu}|$ is,

$$|m_{\mu\mu}| = |C_5^{\mu\mu}|\frac{v^2}{\Lambda}. \tag{6.2}$$

The limits on $|m_{\mu\mu}|$ is $\frac{v^2 \times |C_5^{\mu\mu}| \times \sqrt{r}}{\Lambda}$. The observed (expected) scales is as heavy as $\Lambda = 5.63$ (4.74) TeV, which can be translated to effective $\mu\mu$ Majorana mass of $|m_{\mu\mu}|$= 10.84 (12.84) GeV. The $\pm 1\sigma$ and $\pm 2\sigma$ expected of $|m_{\mu\mu}|$ are [10.59,15.57] and [9.03,18.61] GeV.

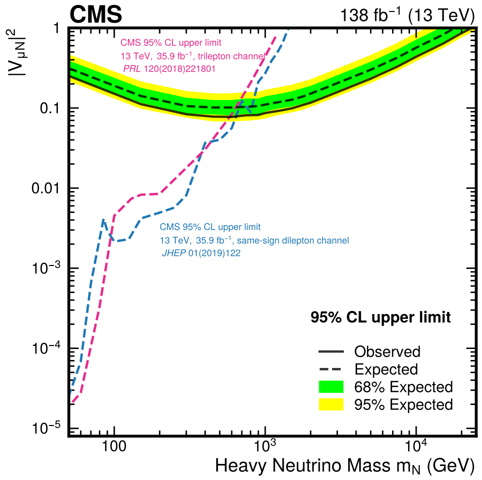

Figure 6.18 Upper limits on $|V_{\mu N}|^2$ at the 95% CL as a function of $\mathrm{m_N}$. The black dashed line represents the expected upper limit, where one and two standard deviation bands are indicated in lime green and light yellow, respectively. The solid black line is the observed upper limit. The red dashed line indicates observed upper limits from Ref[159], while the blue dashed curve shows the observed upper limits from Ref[160]. For $\mathrm{m_N} > 650\,\mathrm{GeV}$, this analysis shows improvements upon the upper limits from those references.

6.8 Summary

In summary, this analysis presents the first search for Majorana neutrinos at several TeV and a first probe of the Weinberg operator at the LHC, using vector boson fusion processes resulting in the same-sign dimuon final state. The results are consistent with the predictions from the standard model. For heavy Majorana neutrinos, upper limits on the mixing element $|V_{\mu\mathrm{N}}|^2$ are set for the mass range $50\,\mathrm{GeV} < \mathrm{m_N} < 25\,\mathrm{TeV}$ and the best sensitivity is reached for $\mathrm{m_N} \gtrsim 650\,\mathrm{GeV}$. The phase space explored exceeds the center-of-mass energy of the LHC, breaking the limit of direct production for Majorana neutrinos with masses above several TeV in previous searches. The highest mass for which $|V_{\mu\mathrm{N}}|^2 = 1$ is excluded is around 23 TeV. Concerning the Weinberg operator, the observed (expected) 95% confidence level upper limit on the effective $\mu\mu$ Majorana mass is 10.8 (12.8) GeV. The authors served as the analysis contact person for this study and contributed to many aspects of this analysis, such as signal modeling, selection optimization, statistical interpretation, and paper writing. Also, the authors gave the pre-approval report of the study.

Chapter 7

Measurement of Wγ Production Cross Section and Constraints on EFT Coefficients

This chapter shows the detail in the measurement of Wγ production cross section and constraints on EFT coefficients. This analysis used a different analysis framework as the previous two in Chapter 5 and 6. The identifications of physics objects have been changed accordingly, as mentioned in Section 4.9. This chapter is structured so that Section 7.1 describes Data and MC sample simulations. Section 7.2, 7.3, and 7.4 introduce the event selections, background estimation, and systematic uncertainties, respectively. Section 7.5 explains the fitting procedure and results. At last, this analysis is summarized in Section 7.6.

7.1 Data Samples and Monte-Carlo Simulations

Same as the previous two analyses, this analysis is performed with the full Run-2 dataset, the used NanoAOD version is v5.

7.1.1 Data

All data analyzed is selected using same approved luminosity certification files as shown in Section 5.1. The full list of data samples and HLT paths for each year is given in Table 7.1.

7.1.2 Simulated Samples

7.1.2.1 MADGRAPH5_AMC@NLO 0+1 Jet NLO-QCD FxFx Wγ Sample

Inclusive Wγ production can be generated at NLO-QCD by MADGRAPH5_AMC@NLO[120]. The sample is generated using the following process definition:

```
    p p > lep nu a [QCD] @0
    p p > lep nu j a [QCD] @1
```

Table 7.1 Primary data samples and HLT paths used in the analysis

Year	**Dataset name**	**HLT paths**
2016	SingleMuon	HLT_IsoMu24 HLT_IsoTkMu24
	SingleElectron	HLT_Ele27_WPTight_GsfHLT
2017	SingleMuon	HLT_IsoMu27
	SingleElectron	HLT_Ele32_WPTight_Gsf_L1DoubleEG
2018	SingleMuon	HLT_IsoMu24
	EGamma	HLT_Ele32_WPTight_Gsf

with the FxFx jet multiplicity merging method, the PDF set NNPDF30_nlo_nf_5_pdfas for 2016 conditions and NNPDF31_nnlo_as_0118_mc_hessian_pdfas for 2017/2018 conditions, and the default dynamical renormalization and factorization scale were used. The following generator-level cuts were applied

- minimum lepton p_{T} = 15 GeV
- minimum photon p_{T} = 15 GeV
- maximum photon $|\eta|$ = 2.6
- Frixione isolation[161] with $n = 1.0$, $\epsilon_{\gamma} = 1.0$, $\delta_0 = 0.05$

7.1.2.2 POWHEG NLO-QCD Wγ Sample

Inclusive Wγ production can be generated at NLO-QCD by POWHEG, followed the Ref[162]. POWHEG actually generates Wγ+jets and W+jets production at the same time in order to improve the modeling of photons radiated from jets. Several schemes are available for combining the W+jets and Wγ+jets processes. The so-called *C-NLO* option was used. The *C* stands for competition and indicates that competition occurs between the radiation of a photon and the radiation of a jet from the Wj Born events. The -NLO indicates that the Wj process is generated at NLO-QCD. Because the sample includes W+jets, the total cross-section of the sample is 2–3 orders of magnitude larger than the MadGraph5_amc@nlo Wγ sample, and the selection efficiency is correspondingly smaller, this is also reported in the Ref[162]. The percentage of events with negative weights in the sample can be reduced by increasing the folding parameters (foldcsi, foldy, foldphi) which at the expense of computing time. Folding parameters such that 5.6% of the events have negative weights were used. The sample is parton showered and hadronized with special emission veto settings that properly veto QED radiation in addition to QCD radiation.

7.1.2.3 Wγ Samples Comparison

Figure 7.1 shows a comparison of the quantity of the MadGraph5_amc@nlo Wγ sample discussed in Section 7.1.2.1 and the POWHEG Wγ sample discussed in Section 7.1.2.2.

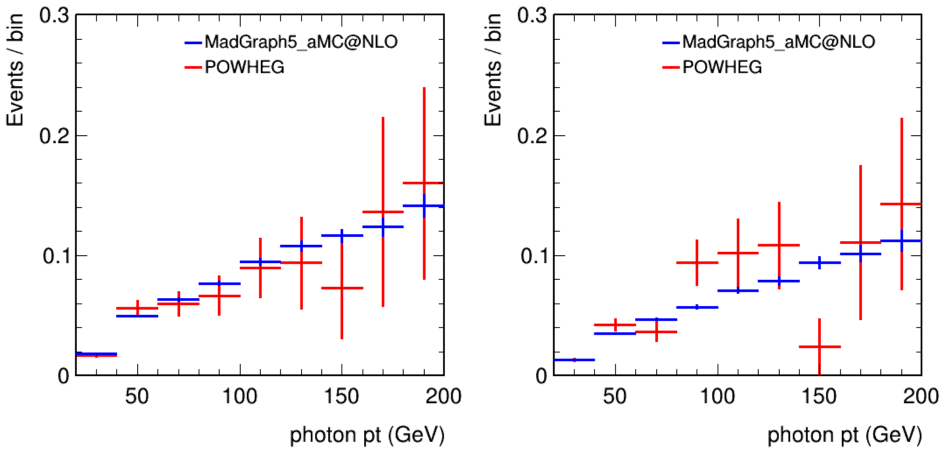

(a) muon channel (b) electron channel

Figure 7.1 Comparison of the selection efficiency of the two Wγ samples. The uncertainties are statistical only.

Within the limited statistical power of the POWHEG sample, this efficiency is consistent between the two samples are consistent.

7.1.2.4 MadGraph5_amc@nlo 0+1 Jet NLO-QCD FxFx $Z\gamma$ Sample

The MadGraph5_amc@nlo Zγ sample is generated similarly to the MadGraph5_amc@nlo Wγ using the process definition

```
p p > lep lep a [QCD] @0
p p > lep lep j a [QCD] @1
```

Zγ production contributes to the Wγ signal region when one of the leptons is low p_{T}, so the $m_{\ell\ell}$ cut was set to 4 and the lepton p_{T} cut was set to 0 when generating this sample.

7.1.2.5 Overlap Removal

Because final state radiation (FSR) photons are added by the parton showering and hadronization step of the simulation, care must be taken to avoid double-counting when running samples containing hard processes X and $X + \gamma$, and also prevent double-counting between MC simulated samples and data-driven methods to estimate the fake photon and fake lepton backgrounds in Sections 7.3.2, 7.3.3, 7.3.5, and 7.3.6. Generator-level FSR photons are identified by requiring the CMS isPrompt flag and requiring that the mother is a charged lepton. Similary, generator-level non-FSR are identified by requiring the CMS isPrompt flag and requiring that the mother is not a charged lepton. These prompt FSR and prompt non-FSR generator-level photons are then matched to reconstructed photons based on the NanoAOD matching. The Photon_genPartIdx leaf in the NanoAOD content is used to match reconstructed photons to generator level photons. Results obtained using the Photon_genPartIdx leaf in the NanoAOD were found to be consistent with results obtained by performing the matching based on the generator particle collection in the NanoAOD using a simple $p_{\mathrm{T}} > 5\,\mathrm{GeV}$ and $\Delta R < 0.3$ criteria.

Reconstructed photons can also be caused by physical electrons or by jets. A fit to an analytic function is performed to estimate the resonant electron to photon fake background (see Section 7.5), simulated samples are used to estimate the non-resonant electron to photon fake background. Reconstructed photons that are within $\Delta R = 0.3$ of a CMS isPrompt generator-level electron are considered $e \to \gamma$ matched.

The photon generator matching requirements for each of the samples are shown in Table 7.2.

Table 7.2 Generator matching of the Monte Carlo samples. Note that the Z+jets sample is only used for the subtraction from the data-driven fake photon and fake lepton estimates.

	FSR	**non–FSR**	$e \to \gamma$
$\mathrm{t\bar{t}} \to 2\ell 2\nu$	✓	×	✓
$\mathrm{t\bar{t}} \to 2j\ell\nu$	✓	×	✓
$\mathrm{t\bar{t}}\gamma$+jets	✓	✓	✓
Wγ+jets	✓	✓	×
Zγ+jets	✓	✓	×
Z+jets	×	×	✓

7.1.2.6 MADGRAPH5_AMC@NLO Dimension-six Effective Field Theory Sample

In order to interpret Wγ production measurement in the context of BSM physics consider a dimension-six effective field theory model. The model is described in detail in Chapter 2. Five continuous real-number parameters are scanned of the model, the coefficients of the operators c_{WWW}, c_W, c_B, $c_{W\tilde{W}W}$, and $c_{\tilde{W}}$. A reweighted Wγ sample i.e. a sample which has n per-event weight corresponding to n model parameter settings was generated. The NLO reweighting feature of MADGRAPH5_AMC@NLO[163-164] is used. First an unweighted (weight = 1 or -1 because it is NLO) Wγ sample is generated for the coefficient c_{WWW} set to 25. Then a per-event weight is calculated and stored for each of the coefficient values shown in the Table 7.3.

Table 7.3 The dimension–six operator coefficient values that are reweighted to. All but one of the coefficients is set to 0 at a time.

c_{WWW}	c_{W}	c_{B}	$c_{\mathrm{W\tilde{W}W}}$	$c_{\mathrm{\tilde{W}}}$
0	0	0	0	0
±1	±17	±17	±0.5	±8
±2	±34	±34	±1.0	±16
±3	±51	±51	±1.5	±24

7.1.2.7 MadGraph5_amc@nlo 0-3 Jets MLM γ+jets Samples

A γ+jets sample is used in order to perform a closure test of the method used to estimate the background due to fake leptons. This sample was generated using the process definition

```
p p > a j
p p > a j j
p p > a j j j
p p > a j j j j
```

and divided into 5 H_T bins: 40-100 GeV, 100-200 GeV, 200-400 GeV, 400-600 GeV, and > 600 GeV.

7.2 Event Selection

In this analysis, events should first pass the year-dependent HLT path in Section 7.1.1. The final state requires exact one lepton (muon or electron), moderate p_T^{miss}, and an energetic photon (γ), the set of selection requirements are summarized in Table 7.4.

Table 7.4 The event selection.

Variable	Requirement
Number of *tight-Wγ* or *fakeable-Wγ* lepton	= 1
Number of *tight-Wγ* photon	= 1
Photon p_T	> 25 GeV
p_T^{miss} (Puppi)	> 40 GeV
Lepton p_T	For muon, > 25 (30) GeV for 2016 and 2018 (2017) For electron, > 30 (35) GeV for 2016 (2017 and 2018)

7.3 Background overview

Three types of nonprompt events make non-negligible contributions to the region where the number of Wγ events is extracted: nonprompt muon events, nonprompt electron events, and nonprompt photon backgrounds events. The size and shape of these backgrounds is estimated using data-driven methods which all involve applying weights calculated from a control region in data to data events with a muon, electron, or photon which passes a control selection.

7.3.1 Electron-induced photon background Estimation

Despite the use of the powerful pixel seed veto, a background due to events containing a reconstructed photon caused by a physical electron still contributes to the signal region. This contribution is dominant in the electron channel (due to the Z $\rightarrow$ ee process) and small in the muon channel. This background is estimated using an MC template with floating normalization that is constrained by the $Z \rightarrow ee$ resonance in the electron channel, as described more in Section 7.5

7.3.2 Fake Muon Background Estimation

Muon fake rates are measured using the following region in data:

- Event passes the year-dependent single muon HLT selection detailed in Section 7.1.1
- Exactly one muon that passes the *tight-Wγ* selection or the *fakeable-Wγ* selection
- No additional muons or electrons that pass the *veto-Wγ* selection
- $m_T < 20$ GeV
- $p_T^{\text{miss}}(\text{Puppi}) < 20\,\text{GeV}$
- One jet with $p_T > 30\,\text{GeV}$ and $\Delta R(\text{muon,jet}) > 0.3$

where the variable m_T is the transverse mass, defined in Equation 5.2. These cuts are intended to select dijet events in which one of the jets fakes a muon and to reduce contamination from real muons. The muon fake rate is defined as the ratio of the number of events in this region in which the muon passes the tight selection (the numerator) to the total number of events in this region (the denominator). In order to further remove contamination from prompt muons, the W+jets and Z+jets samples are subtracted from both the numerator and denominator. The fake rates are binned in $|\eta|$,p_T, and year and are shown in Table 7.5. The size of the subtracted contamination is shown in Figure 7.2.

Table 7.5 Muon fake rates.

Year	$\lvert\eta\rvert < 0.5$	$0.5 < \lvert\eta\rvert < 1$	$1 < \lvert\eta\rvert < 1.5$	$1.5 < \lvert\eta\rvert < 2$	$2 < \lvert\eta\rvert$
			$20 < p_T^{\mu} < 30\,\text{GeV}$		
2016	0.58	0.60	0.64	0.71	0.75
2017	-	-	-	-	-
2018	0.62	0.64	0.67	0.78	0.84
			$30 < p_T^{\mu} < 40\,\text{GeV}$		
2016	0.62	0.64	0.67	0.74	0.78
2017	0.67	0.67	0.69	0.79	0.83
2018	0.65	0.67	0.70	0.81	0.86
			$p_T^{\mu} > 40\,\text{GeV}$		
2016	0.72	0.74	0.74	0.80	0.81
2017	0.76	0.77	0.77	0.85	0.87
2018	0.73	0.76	0.76	0.86	0.90

The muon fake rates are then applied to data events that pass the full event selection except that the muon fails the tight selection and passes the loose selection. The weight applied to these events is

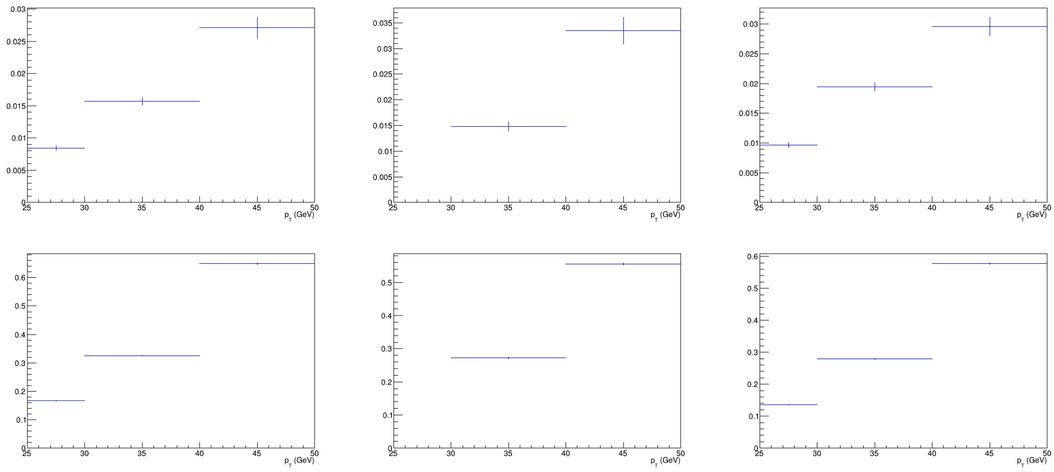

Figure 7.2 Electroweak contamination rate (i.e. electroweak divided data) in the *fakeable-Wγ* object (top) and *tight-Wγ* (bottom) muon selections for 2016 (left), 2017 (middle), and 2018 (right).

$$\frac{\text{muon fake rate}}{1 - \text{muon fake rate}}, \tag{7.1}$$

which can be thought of as the transfer factor for transfering from the *fakeable-Wγ* object selection to the *tight-Wγ* selection.

The region where these weights are applied can be contaminated by real muons, and this contamination is estimated using simulated samples with generator matching. For each simulated event which contains a matched reconstructed muon that passes the *fakeable-Wγ* object muon selection, the weight above is subtracted from the fake muon estimate.

7.3.3 Fake Electron Background Estimation

Electron fake rates are obtained similarly to muon fake rates, based on the following region in data:

- Event passes the year-dependent single electron HLT selection detailed in Section 7.5
- Exactly one electron that passes either the *tight-Wγ* selection or the *fakeable-Wγ* object selection
- No additional muons or electrons that pass either the *veto-Wγ* selection
- $m_{\mathrm{T}} < 20$ GeV
- $p_{\mathrm{T}}^{\mathrm{miss}}$(Puppi) $< 20\,\mathrm{GeV}$
- One jet with $p_{\mathrm{T}} > 20\,\mathrm{GeV}$ and $\Delta R(\text{electron,jet}) > 0.3$

These cuts are intended to select dijet events in which one of the jets fakes a electron and to reduce contamination from real electrons. The electron fake rate is defined as the ratio of the number of events in this region in which the electron passes the tight selection (the numerator) to the total number of events in this region (the denominator). In order to remove contamination from prompt electrons and prompt photon conversions, the W+jets, Z+jets, and γ+jets samples are subtracted from both the numerator and denominator. The fake rates are binned in $|\eta|$, p_T and year are shown in Table 7.6. The size of the subtracted contamination is shown in Figure 7.3.

Table 7.6 Electron fake rates.

Year	$\|\eta\| < 0.5$	$0.5 < \|\eta\| < 1$	$1 < \|\eta\| < 1.5$	$1.5 < \|\eta\| < 2$	$2 < \|\eta\|$
$30 < p_\mathrm{T}^{\mu} < 40\,\mathrm{GeV}$					
2016	0.76	0.77	0.78	0.81	0.80
2017	0.74	0.74	0.74	0.78	0.80
2018	0.71	0.71	0.72	0.80	0.85
$p_\mathrm{T}^{\mu} > 40\,\mathrm{GeV}$					
2016	0.81	0.80	0.77	0.79	0.77
2017	0.82	0.82	0.81	0.85	0.85
2018	0.80	0.80	0.78	0.83	0.87

The electron fake rates are then applied to data events that pass the full event selection except that the electron fails the *tight-Wγ* selection and passes the *fakeable-Wγ* selection. The weight applied to these events is

$$\frac{\text{electron fake rate}}{1-\text{electron fake rate}}, \tag{7.2}$$

which can be thought of as the transfer factor for transferring from the *fakeable-Wγ* object selection to the *tight-Wγ* selection.

The region where we apply these weights can be contaminated by real electrons, and this contamination is estimated using simulated samples with generator matching. For each simulated event which contains a matched reconstructed electron that passes the control electron selection, the weight above is subtracted from the fake electron estimate.

7.3.4 Prompt Pileup Photons

The background due to prompt photons from PU interactions (i.e. a W event from the primary vertex combined with a γ+jet event from a pileup vertex) is estimated using the W+jets simulation. In order to access the promptness information for the minimum bias events that are mixed into the primary vertex event, the following workflow is used.

- Record the event and luminosity block numbers of the selected events in the NANOAODSIM W+jets sample
- Using a DAS query, find the MINIAODSIM W+jets file that contains each of the events from the previous step

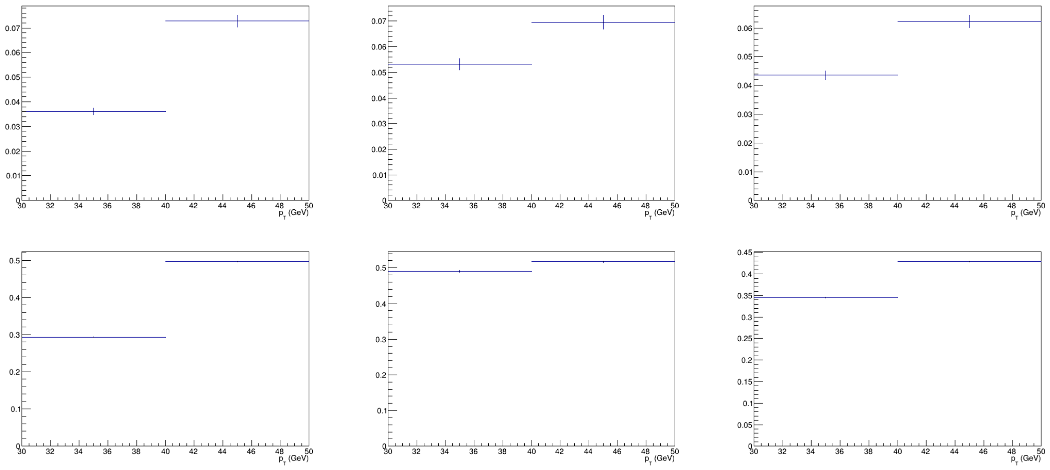

Figure 7.3 Electroweak contamination rate (i.e. electroweak divided data) in the *fakeable-Wγ* object (top) and *tight-Wγ* (bottom) electron selections for 2016 (left), 2017 (middle), and 2018 (right).

- Access each of the MINIAODSIM files from the previous step, and record the event and luminosity block numbers of the minimum bias events that are mixed into the 0th bunch crossing of the W+jets event
- Using a Data Aggregation System (DAS) query, find the GENSIM minimum bias file that contains each of the minimum bias events from the previous step
- Match the generator photons in the minimum bias files to the selected reconstructed photons in the W+jets events
- If there is a matched generator photon, determine whether it is prompt based on its parents

7.3.5 Fake Photon Background Estimation

The background due to fake photons is estimated using a method similar to that used in the electroweak Zγ analysis[165]. The extrapolation factor from the fakeable object photon selection to the tight photon selection for fake photons is measured in data and applied to data. In order to measure it in data, we use the following selection:

- Exactly one *tight-Wγ* electron or muon and no *veto-Wγ* electrons or mouns.
- Exactly one *tight-Wγ* photon or *fakeable-Wγ* object photons.
- Event is required to pass the year-dependent single lepton HLT selection detailed in Section 7.1.1
- In the electron channel, the electron photon mass m_{eg} is required to be satisfy $|m_{eg} - m_Z| >$ 10 GeV (to reduce contamination from Z $\rightarrow e^+e^-$ events in which one electron causse a photon to be reconstructed).
- The event is required to fail the main event selection (Section 7.2)

This region is expected to contain a mixture of real photons and fake photons. In order to extract the fake photon component, a fit to the photon's $\sigma_{i\eta i\eta}$ (mentioned in Section 4.5.2) distribution is considered. A real photon $\sigma_{i\eta i\eta}$ template is easily constructed from simulated Wγ events in which the reconstructed photon is matched to a generator photon. The fake photon $\sigma_{i\eta i\eta}$ template is constructed from data by replacing the tight photon selection with the charged isolation sideband photon selection in the above list of cuts. Based on these templates, the fake photon fraction is extracted in four photon p_{T} bins separately for the barrel and endcap and separately for the electron channel and muon channel. Figure 7.4 shows fake photon fraction calculation in $|\eta| < 1$ range and p_{T} bin 20 to 30 GeV, (a) is the real photon template, (b) is the fake photon template, (c) is the comparison between data and total fit result, and (d) is the true and fake components after fitting. Tables 7.7 shows the resulting fake photon fractions for 2016.

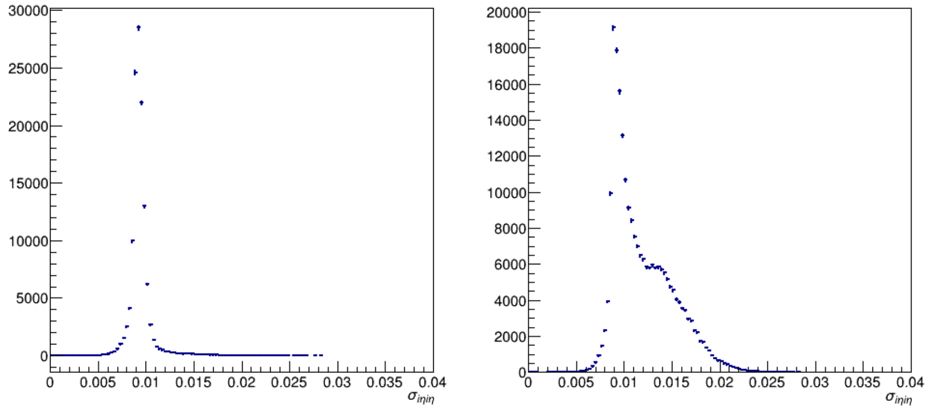

(a) Real photon template (b) Fake photon template

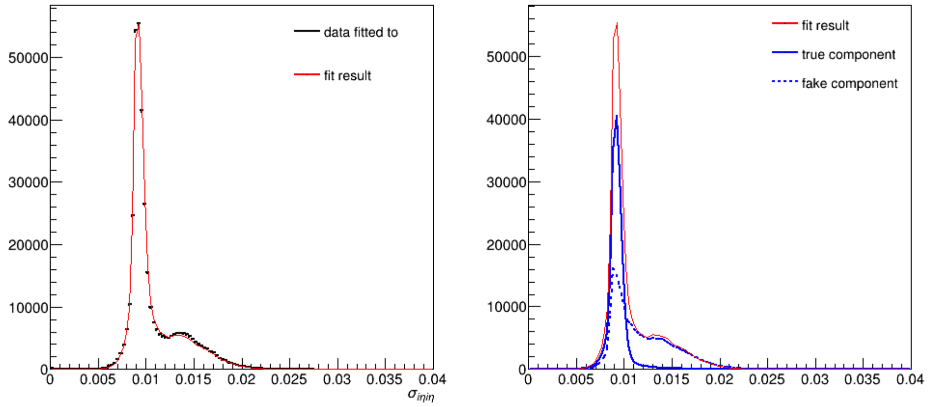

(c) Comparison between data and total fit (d) True and fake component after fitting

Figure 7.4 Figures related to the fake photon fraction calculation in $|\eta| < 1$ range and p_{T} bin 20 to 30 GeV.

Table 7.8 shows the extrapolation factors from the *fakeable-Wγ* object photon selection to the *tight-Wγ* photon selection, which are calculated from the formula

Table 7.7 Fake photon fractions calculated from data for 2016.

η **range**	$20 < p_\mathrm{T} < 30\,\mathbf{GeV}$	$30 < p_\mathrm{T} < 40\,\mathbf{GeV}$	$40 < p_\mathrm{T} < 50\,\mathbf{GeV}$	$50\,\mathbf{GeV} < p_\mathrm{T}$
$\lvert\eta\rvert < 1$	0.330	0.129	0.096	0.075
$1 < \lvert\eta\rvert < 1.5$	0.368	0.178	0.156	0.120
$1.5 < \lvert\eta\rvert < 2$	0.428	0.232	0.189	0.164
$2 < \lvert\eta\rvert < 2.5$	0.365	0.186	0.136	0.095

$$\text{(fake photon event weight)} = \frac{\text{(fake photon fraction)} \cdot \text{(number of } \textit{tight-W}\gamma \text{ photons)}}{\text{(number of } \textit{fakeable-W}\gamma \text{ object photons)}}. \quad (7.3)$$

Table 7.8 Fake photon weights calculated from data for 2016.

η **range**	$20 < p_\mathrm{T} < 30\,\mathbf{GeV}$	$30 < p_\mathrm{T} < 40\,\mathbf{GeV}$	$40 < p_\mathrm{T} < 50\,\mathbf{GeV}$	$50\,\mathbf{GeV} < p_\mathrm{T}$
$\lvert\eta\rvert < 1$	0.69	0.66	0.55	0.39
$1 < \lvert\eta\rvert < 1.5$	0.85	0.84	0.75	0.53
$1.5 < \lvert\eta\rvert < 2$	1.13	1.13	1.02	0.97
$2 < \lvert\eta\rvert < 2.5$	0.68	0.74	0.79	0.88

For other bins, the fake photon fraction and weights calculation can be found in Appendix A.6.1. The prompt photon contamination of the fakeable object selection is estimated based on simulated samples and subtracted (Figure 7.5).

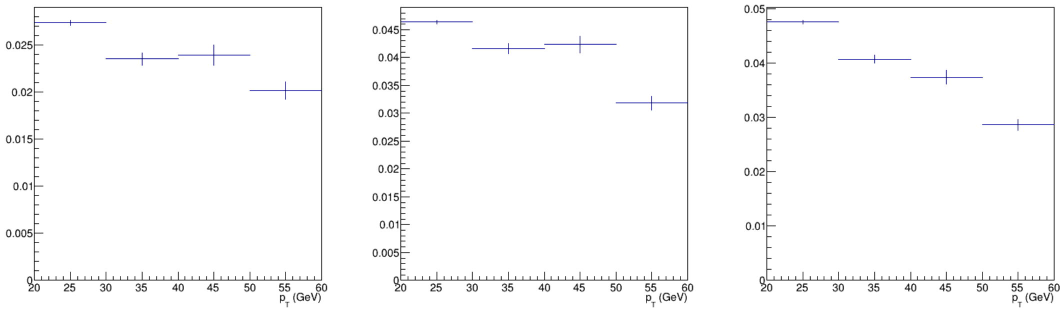

Figure 7.5 Electroweak contamination rate (i.e. electroweak divided data) in the fakeable object photon selections for 2016 (top), 2017 (middle), and 2018 (bottom).

7.3.6 Double Fake Background Estimation

Events that contain both a fake photon and a fake lepton are estimated by combining the two methods described above. For each event that contains both a photon that passes the fakeable object photon selection and an electron or muon that passes the fakeable object lepton selection, a weight of

$$(\text{fake photon weight}) \cdot (\text{fake lepton weight}), \tag{7.4}$$

is applied and the event is added to a new category called *double fake*. In addition, this event is subtracted from the fake photon and the fake lepton estimate in order to avoid double counting.

7.3.7 Prompt contamination in the fake photon, fake lepton estimates

The signal process can also contribute to the fake photon and fake lepton estimates. Those contaminations are subtracted from the fake photon and fake lepton estimates and added back to the signal estimate. The contaminations in the fake photon and fake lepton estimates are shown in Figure 7.6.

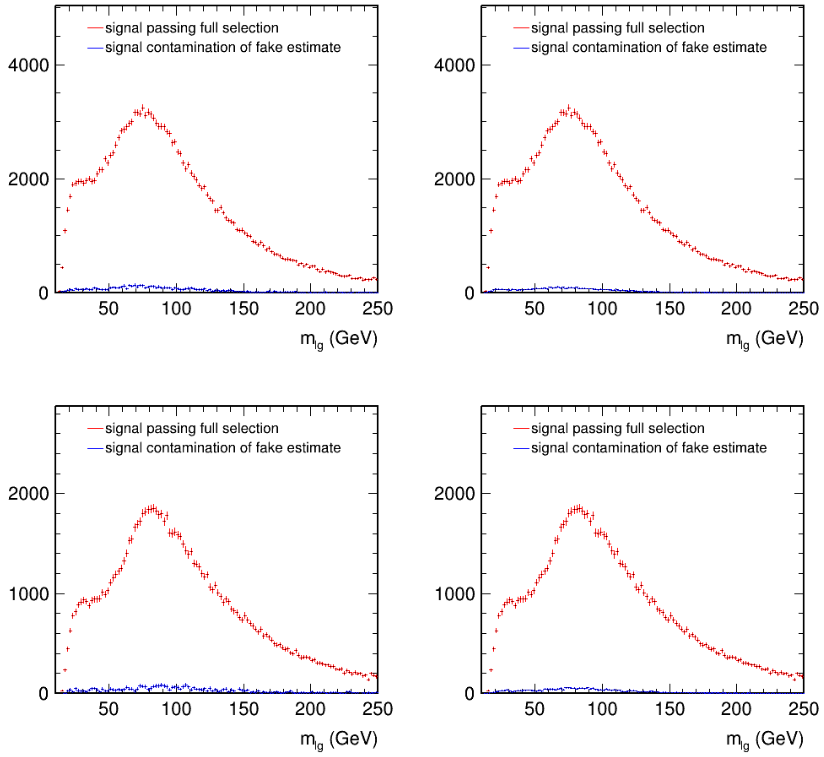

Figure 7.6 Contamination of the fake lepton and photon background estimates due to the signal process. Upper left: muon channel, fake muon estimate contamination. Upper right: muon channel, fake photon estimate contamination. Lower left: electron channel, fake electron contamination. Lower right: electron channel, fake photon contamination.

Simulated processes rather than the signal process can also contribute to the fake photon and fake lepton estimates. Those contaminations are removed from the fake photon and fake lepton estimates. The contaminations in the fake photon and fake lepton estimates caused by those processes are shown in Figure 7.7.

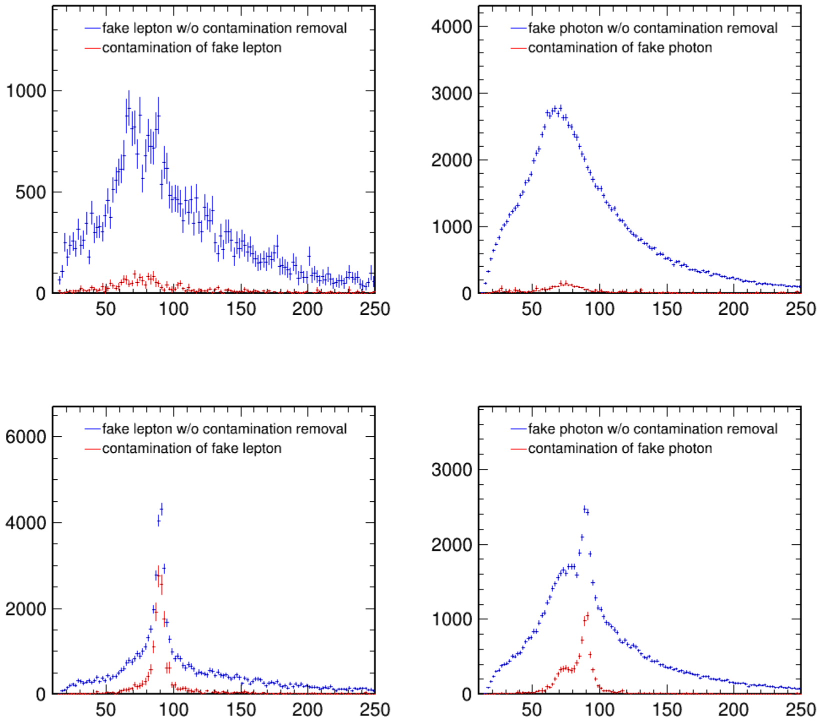

Figure 7.7 Contamination of the fake lepton and photon background estimates due to processes other than the signal process. Upper left: muon channel, fake muon estimate contamination. Upper right: muon channel, fake photon estimate contamination. Lower left: electron channel, fake electron contamination. Lower right: electron channel, fake photon contamination.

7.4 Uncertainties

Uncertainty on the JES and the JER The JES and the JER affect the $p_{\mathrm{T}}^{\mathrm{miss}}$ through the type 1 correction. A single uncertainty for the JES and a single uncertainty for the JER are obtained by replacing the cut $p_{\mathrm{T}}^{\mathrm{miss}}$ (Puppi) $>$ 40 GeV with $p_{\mathrm{T}}^{\mathrm{miss}}$ (Puppi,JESUp) $>$ 40 GeV and $p_{\mathrm{T}}^{\mathrm{miss}}$ (Puppi,JERUp) $>$ 40 GeV, respectively. This uncertainty is applied to all simulated samples.

QCD scale and PDF uncertainties The QCD and PDF uncertainties are considered for the signal and the QCD $Z\gamma$ background. The PDF uncertainty is taken as the standard deviation of the 32 PDF variations of the PDF4LHC15_nnlo_30_pdfas PDF set[151,166-168]. The QCD scale uncertainty is taken as the maximum from the central value of the 6 variations that are not 2.0/0.5 or 0.5/2.0.

Efficiency scale factor uncertainties The scale factor uncertainties are obtained using the scale factor errors provided by the EGamma and the Muon POG and applying the updated scale factors event-by-event.

Uncertainty on the integrated luminosity The uncertainty on the full Run 2 integrated luminosity is 1.8% from LUM POG.

Uncertainty on pileup modeling The uncertainty due to pileup is obtained by creating a new pileup reweighting histogram with the minimum bias cross-section scaled up by 4.6%.

Uncertainty on L1 ECAL prefiring correction The uncertainty due to the prefiring correction is obtained by computing new prefiring weights based on object prefiring probabilities that are adjusted upwards by

$$\sqrt{(0.2 \times \text{prefiring probability})^2 + (\text{statistical uncertainty on prefiring probability})}. \tag{7.5}$$

Statistical uncertainties Bin-by-bin ”Monte Carlo stat” and ”data-driven stat” systematic uncertainties are considered due to the finite statistical power of the simulated samples and the control regions in data.

Uncertainty due to the data-driven fake photon estimation method The systematic uncertainty on the data-driven fake photon estimate is divided into three components. The first component covers for the bias in the procedure to calculate the fake photon weights. The second component covers for the contamination of the data-driven fake photon procedure by prompt photons from the $W\gamma$ signal. The third component covers for the dependence of the fake photon weights on properties of the event other than the photon p_{T} and η. The first and third components are obtained by applying the method to simulated samples and comparing with the correct result i.e. by performing a MC closure test. The second component is obtained as the difference between including the Wγ signal in the data-driven fake photon weight procedure and not including it. The first and second components are considered in our statistical analysis by adding one variation of the fake photon estimate for each fake photon weight. The third component is considered in the statistical analysis by applying a bin-by-bin uncertainty based on the size of the non-closure around that bin.

The per-fake photon weight variations for the first component are obtained as follows. The W+jets and Wγ+jets Monte Carlo samples are combined using generator photon matching and then the $\sigma_{i\eta i\eta}$ fits are performed using this combined sample to create the fake photon template and the data that is fitted to (the real photon template is already made using the Wγ+jets Monte Carlo sample). The results of these $\sigma_{i\eta i\eta}$ are used to create the fake photon event weights.

These fake photon event weights are compared to the true fake photon event weights, and then the difference is added to the original fake photon event weights from the real data to create the alternative fake photon event weights. In other words, the non-closure are added from a closure test to the nominal weights, the calculations are in Appendix A.6.2.

The bin-by-bin uncertainties for the third component of the systematic uncertainty on the fake photon background estimate are obtained as follows. The true fake photon weights is applied to W+jets MC events containing a reconstructed photon that does not match to a prompt photon that pass the signal region cuts with the tight photon selection replaced by the control photon selection. This sample is compared bin-by-bin with W+jets MC events containing a reconstructed photon that does not match to a prompt photon that pass the signal region cuts to obtain the non-closure plots shown in Figure 7.8 for m_{lg} with several different binnings and for the difference in ϕ between the lepton and photon.

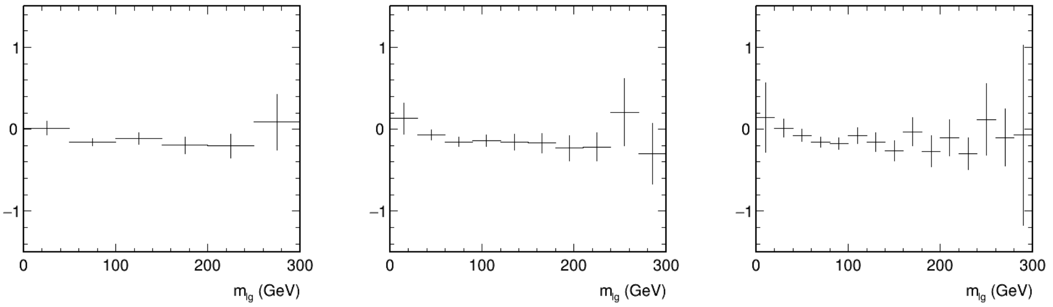

Figure 7.8 Fake photon closure test results.

The m_{lg} plots in the figure indicate that there is no sufficient MC statistical power to calculate the non-closure with 2 GeV m_{lg} bins. In order to reduce statistical uncertainties, the 22 GeV smoothing is performed to the m_{lg} distribution meaning that, for example, the content of the bin 40 to 42 is calculated based on the range 30 to 52 GeV. It's believed that this smoothing procedure is valid because it would be unphysical for the non-closure of the fake photon background estimate of m_{lg} to have structures smaller than 22 GeV. The choice of 22 GeV is a mostly arbitrary choice, other than it is the same order as the width or resolution of the Z peak. The result of the smoothing is shown in Figure 7.9

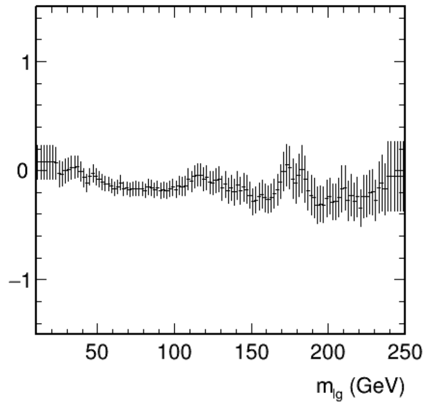

Figure 7.9 Fake photon closure test results.

The systematic uncertainty on each bin is the absolute value of the central value in that bin plus the error bar in that bin.

Uncertainty due to the data-driven fake lepton estimation method The simulated γ+jets samples described in Section 7.1.2.7 are used to perform a closure test for the electron channel and a closure test for the muon channel. The closure test compares the yield from the γ+jets sample to the yield from the γ+jets samples based on applying the lepton fake rates applied to fakeable object lepton events. The selection that is used is the same as the main event selection, except that the m_{T} and $p_{\mathrm{T}}^{\mathrm{miss}}$ (Puppi) cuts are removed in order to increase statistical power.

The integrated non-closure factor is 1.288 ± 0.197 for the electron channel 0.839 ± 0.145 for the muon channel. Based on these factors and previous studies of non-closure, a bin-by-bin 30% uncertainty to the electron and muon fake estimates is applied.

Uncertainty due to the data-driven double fake estimation method As the double fake estimate is based on multiplying a fake lepton weight and a fake photon weight, the uncertainties applied to the double fake estimate are the same as those applied to the fake lepton and fake photon estimates, and they are correlated with the corresponding uncertainty applied to the fake lepton and fake photon estimate. This includes the 30% systematic uncertainty described in Section 7.4 and the first two components of the fake photon uncertainty described

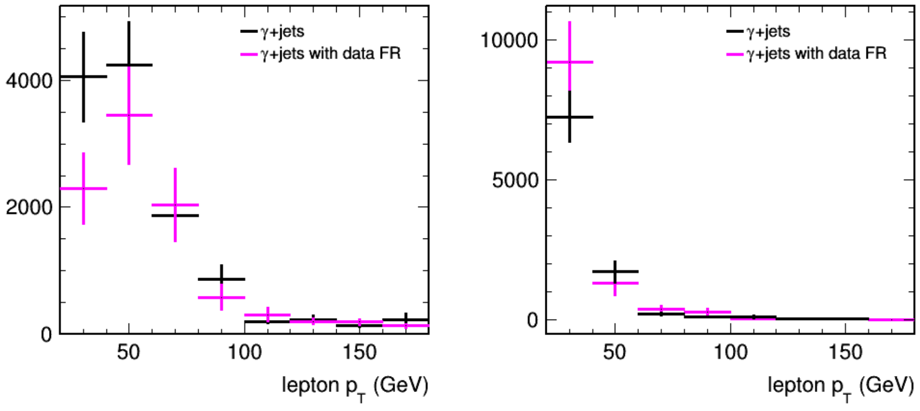

Figure 7.10 The results of the fake electron (left) and muon (right) closure test as a function of lepton p_{T}.

in Section 7.4. The last component of the fake photon uncertainty is not applied to the double fake estimate because it is specific to the W+jets process, and there isn't a large enough dijet MC sample to calculate this uncertainty for the double fake estimate. But because the double fake estimate is much smaller than the fake photon estimate, it's believed the last component of the fake photon uncertainty (dependence of the fake photon weights on properties of the event other than the p_{T} and η of the photon) can be reasonably neglected.

7.5 Limits Extraction

The signal strength is extracted in a simultaneous fit of the electron and muon channels. A private version of the Higgs Combination Tool is used, which contains a TensorFlow based minimizer[169]. This version of the Higgs Combination Tool was also used in the W rapidity, helicity, and differential cross section measurement[170]. It is preferred over the standard Higgs Combination Tool because it can fit hundreds of nuisance parameters in seconds or thousands of nuisance parmaeters in minutes, and therefore increases the flexibility of our fitting strategy. The fitting strategy we chose is a binned fit of the m_{lg} distribution with 2 GeV bins the range 10 to 250 GeV. The binning is the same in the electron and muon channel. In the muon channel fit, the Wγ signal strength is the only freely floating parameter. In the electron channel and the simultaneous fit, the normalization of the electron-induced photon background is allowed to float in addition to the Wγ normalization, while in the muon channel, the normalization of the electron-induced photon background is constrained by a 100% log-normal uncertainty.

The signal in the fit is the Wγ process that originates from the following fiducial region:

- photon $|\eta| < 2.5$
- lepton $|\eta| < 2.5$
- photon $p_{\mathrm{T}} > 25\,\mathrm{GeV}$

- lepton $p_{\mathrm{T}} > 25\,\mathrm{GeV}$
- photon is prompt and isolated, where isolated means isolation sum divided by photon p_{T} is less than 0.5, where the isolation sum equals the sum of the p_{T} of all status 1 particles within $\Delta R = 0.4$ of the photon, excluding the photon itself and all neutrinos
- lepton is isolated and either prompt itself or a direct decay product of a prompt tau lepton, where isolated means isolation sum divided by lepton p_{T} is less than 0.5, where the isolation sum equals the sum of the p_{T} of all status 1 particles within $\Delta R = 0.4$ of the lepton, excluding the lepton itself and all neutrinos
- $\Delta R(\text{lepton,photon}) > 0.5$

The signal includes a component that passes the full event selection and a much smaller component that contaminates the fake lepton and fake photon background estimate (Figures 7.6).

The Wγ events that originate from outside of this fiducial region are considered as a background in the fit, with normalization constrained to its simulated prediction.

The expected number of signal and background events in the signal region are shown in Tables 7.9 and 7.10:

Table 7.9 Number of background expected events per category in the muon channel. The uncertainty is statistical. The uncertainty is statistical. Wγ and Wγ out are the contributions to the signal region from the Wγ process originating from inside and outside the fiducial region, respectively.

Process	**Expected number of events**
Wγ	164438 ± 419
Wγ out	2863 ± 50
$Z\gamma$	45227 ± 187
top	23103 ± 70
VV	2414 ± 34
fake photon	96022 ± 351
fake lepton	23324 ± 414
double fake	14039 ± 175
electron–induced photon	8175 ± 75
pileup	11085 ± 628
conversion	0 ± 0
sum	390691 ± 956

The observed number of events in the muon channel is 395818 and the observed number of events in the electron channel is 385224. The pre-fit and the observed distributions used in the fit are shown in Figure 7.11. The normalization of the electron-induced photon background is floating in the fit, so there is no meaningful pre-fit normalization, so for the pre-fit plot, a chosen normalization that for the electron-induced photon background which is roughly correct.

Table 7.10 Number of background expected events per category in the electron channel. The uncertainty is statistical. Wγ and Wγ out are the contributions to the signal region from the Wγ process originating from inside and outside the fiducial region, respectively.

Process	**Expected number of events**
Wγ	95953 ± 321
Wγ out	1530 ± 37
Zγ	22164 ± 128
top	15000 ± 55
VV	1501 ± 26
fake photon	47146 ± 357
fake lepton	27485 ± 796
double fake	16254 ± 239
electron-induced photon	152947 ± 858
pileup	4892 ± 401
conversion	8318 ± 93
sum	393190 ± 1338

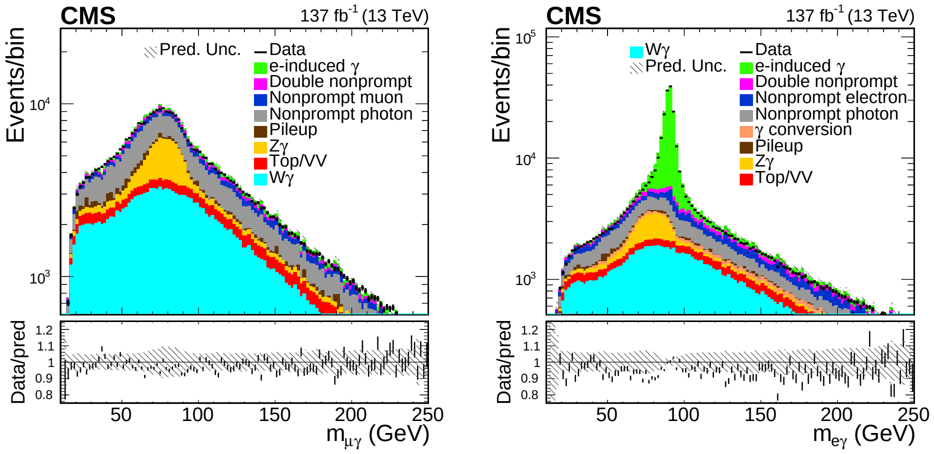

Figure 7.11 The pre-fit $m_{l\gamma}$ distributions. The electron-induced photon estimate is scaled by a factor of 1.8 for the electron channel. The uncertainty on the expected yield is the sum of the systematic uncertainties added in quadrature.

7.5.1 Experimentally Measured Cross Section

7.5.1.1 Measured cross-section

The measured cross section is obtained by multiplying the signal strength fit result by the theoretically predicted fiducial cross section. The cross sections are observed (expected) cross sections in electron channel only and muon channel only, and the cross sections combining the electron and muon channels are listed in Table 7.11. Table 7.11 shows shows the total uncertainty, but also the statistical, experimental and theoretical uncertainties. The observed cross sections have a pretty good agreement with the expected ones.

Table 7.11 The observed (expected) cross-sections (σ) in the electron channel, muon channel, and both channels.

Channel		**σ (pb)**	**Total uncertainty (pb)**	**Split uncertainties (pb)** **Statistical**	 **Experimental**	 **Theoretical**
Electron	Observed	15.09	±1.07	±0.09	±1.02	±0.32
	Expected	15.44	±1.03	±0.09	±0.97	±0.32
Muon	Observed	15.77	±0.89	±0.06	±0.88	±0.12
	Expected	15.44	±0.82	±0.06	±0.81	±0.12
Combined	Observed	15.58	±0.75	±0.05	±0.73	±0.15
	Expected	15.44	±0.70	±0.05	±0.68	±0.14

7.5.1.2 Theoretically Predicted Cross Section

The theoretically predicted fiducial cross-section can be calculated based on the MadGraph5_amc@nlo sample described in Section 7.1.2.1 or the powheg sample described in Section 7.1.2.2.

- MadGraph5_amc@nlo: 15.4 ± 1.2 (scale) ± 0.1 (PDF) pb
- powheg: 22.5 ± 3.2 (scale) ± 0.1 (PDF) pb

The measured fiducial cross section is $\sigma = 15.58 \pm 0.75$ pb $= 15.58 \pm 0.05$ (stat) $\pm$ 0.73 (syst) ± 0.15 (theo) pb, which is consistent with the MadGraph5_amc@nlo NLO QCD prediction of $\sigma = 15.4 \pm 1.2$ (scale)± 0.1 (PDF) pb and less than the powheg NLO QCD prediction of $\sigma = 22.4 \pm 3.2$ (scale) $\pm$ 0.1 (PDF) pb. The discrepancy between the two cross-sections is expected based on the previous studies by the powheg authors[162]. It's also discussed in the Section 7.1.2.2.

7.5.1.3 Limit-setting Method

Expected and observed limits on the coefficients of the dimension 6 operators are calculated based on the negative profile log-likelihood, $-2\Delta\ln\mathcal{L}$ (or $\tilde{q}_{\mu}$), discussed in Section 5.6.1. The steps taken to determine the upper and lower limit for each operator are:

1. Using the reweighted sample, construct the yield scaling distributions for each operator and for each photon p_{T} bin (Figure 7.13)

2. Perform a quadratic fit to each of these histograms (Figure 7.13)
3. For each operator, find the coefficient value such that $-2\Delta\ln\mathcal{L}$ is minimized.
4. For each operator, calculate $-2\Delta\ln\mathcal{L}$ with respect to the coefficient value found in the previous step.
5. For each operator, find the positive and negative coefficient value such that $-2\Delta\ln\mathcal{L} = 3.84$ ①.

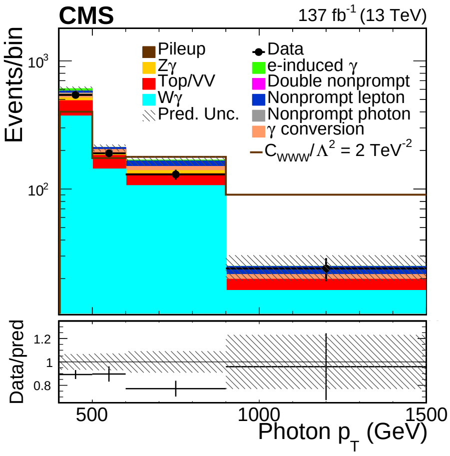

Figure 7.12 The photon p_{T} distribution used for the extraction of limits on dimension 6 effective field theory operators. The last bin includes overflow.

7.5.2 Results

The observed and expected 95% confidence limits on the coefficients of the 5 dimension 6 operators c_{WWW}, c_W, c_B, $c_{\overline{W}WW}$, and $c_{\overline{W}}$ are shown in Table 7.12.

Table 7.12 Observed and expected 95% confidence limits on five dimension 6 operators. The units are TeV^{-2}.

Operator coefficient	Exp Lower	Exp Upper	Obs Lower	Obs Upper
c_{WWW}/Λ^2	−0.85	0.87	−0.90	0.91
c_W/Λ^2	−45.5	44.6	−39.7	40.7
c_B/Λ^2	−45.5	44.6	−39.7	40.7
$c_{\overline{W}WW}/\Lambda^2$	−0.43	0.43	−0.45	0.45
$c_{\overline{W}}/\Lambda^2$	−22.8	22.3	−20.3	20.0

7.6 Summary

In conclusion, the first measurement of the inclusive Wγ production cross-section with proton-proton collisions at $\sqrt{s} = 13\,\text{TeV}$ is reported. The measured fiducial cross section is $\sigma =$

---

① 3.84 is the value of x such that $\int_0^x \chi^2(x', r)\, dx'$ equals 95%.

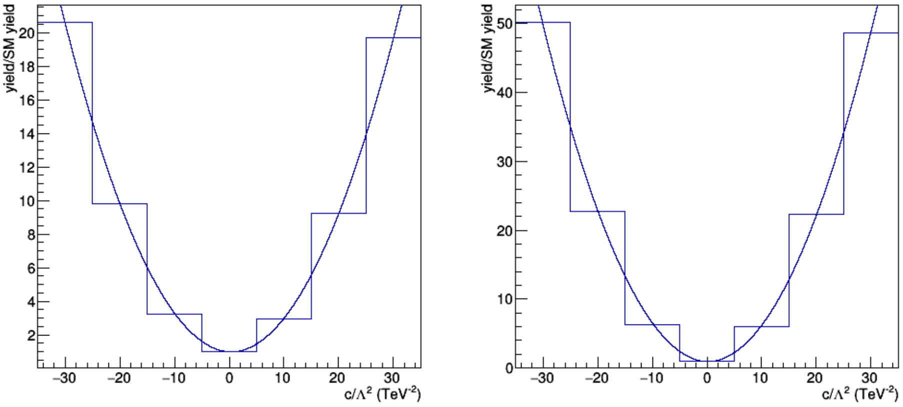

(a) $p_{\mathrm{T}}^{\gamma} \in (400, 500)$ GeV (b) $p_{\mathrm{T}}^{\gamma} \in (500, 600)$ GeV

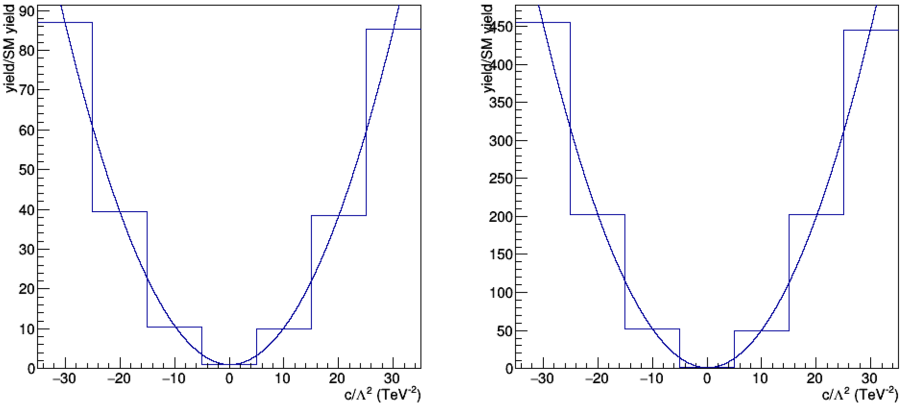

(c) $p_{\mathrm{T}}^{\gamma} \in (600, 900)$ GeV (d) $p_{\mathrm{T}}^{\gamma} > 900$ GeV

Figure 7.13 Yield scaling histograms for the c_{WWW} operator.

Table 7.13 Observed and expected 95% confidence limits on anomalous coupling parameters in the LEP parametrization.

Operator coefficient	**Exp Lower**	**Exp Upper**	**Obs Lower**	**Obs Upper**
g_1^Z	0.81	1.19	0.83	1.17
λ_γ	−0.0033	0.0033	−0.0035	0.0035
λ_Z	−0.0033	0.0033	−0.0035	0.0035
$\tilde{\kappa}_\gamma$	−0.074	0.072	−0.066	0.065
$\tilde{\kappa}_Z$	−0.021	0.022	−0.019	0.020
$\tilde{\lambda}_\gamma$	−0.0016	0.0016	−0.0017	0.0017
$\tilde{\lambda}_Z$	−0.0016	0.0016	−0.0017	0.0017

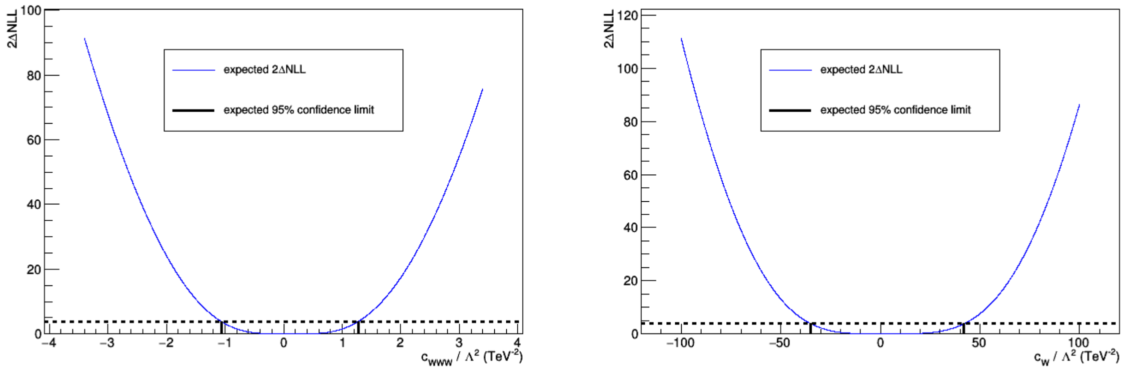

(a) 2ΔNLL distribution for c_{WWW} (b) 2ΔNLL distribution for c_W

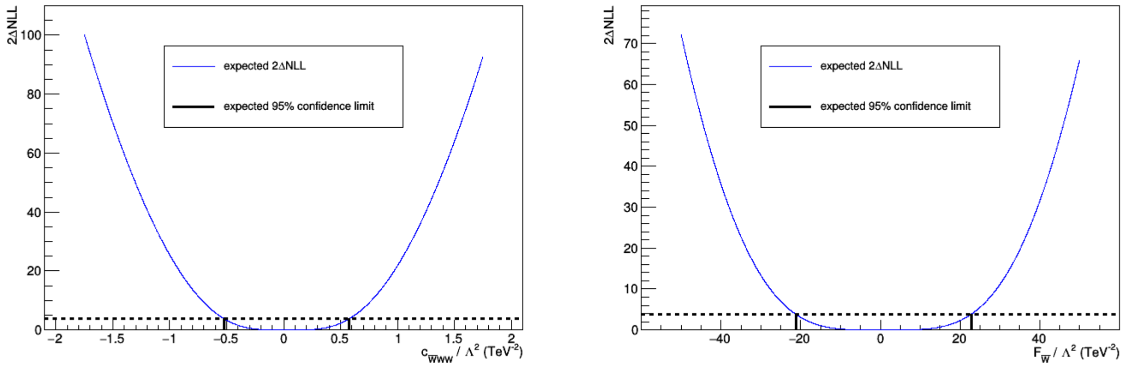

(c) 2ΔNLL distribution for $c_{\overline{W}WW}$ (d) 2ΔNLL distribution for $c_{\overline{W}}$

Figure 7.14 2ΔNLL (negative log likelihood) distributions.

15.58 ± 0.75 pb = 15.58 ± 0.05 (stat) ± 0.73 (syst) ± 0.15 (theo) pb, which is consistent with the MadGraph5_amc@nlo NLO QCD prediction of $\sigma = 15.4 \pm 1.2$ (scale) ± 0.1 (PDF) pb and less than the powheg NLO QCD prediction of $\sigma = 22.4 \pm 3.2$ (scale) ± 0.1 (PDF) pb. The cross-sections measured in the electron channel and the muon channel separately are consistent with each other. The high photon p_{T} part of the photon p_{T} distribution was used to set 95% confidence level limits on dimension-six effective field theory parameters, including the most stringent limit to date on the coefficient of O_{WWW}, the lowest dimension CP-even operator that directly alters the WWγ triple gauge coupling. In this analysis, the author contributed to the signal simulation and gave the approval talk.

Chapter 8

Summary and Outlook

Three analyses based on the data set in proton-proton collisions at $\sqrt{s} = 13\,\text{TeV}$ collected by the CMS experiment, corresponding to around 137 fb^{-1}, are introduced in this thesis.

The first one studies the polarized $\text{W}^{\pm}\text{W}^{\pm}$ scattering, and the second one searches Majorana neutrino and constrains dimension-five Weinberg operator coefficient via dimuon final state for production in $\text{W}^{\pm}\text{W}^{\pm}$ fusion. The physics objects and background estimation methods of those two analyses follow closely those used in the H→WW differential cross section analysis. In the former analysis, detailed signal sample simulations were carried out, the dependence of the signal on the reference frame was studied and the conclusion is that the $\text{W}^{\pm}\text{W}^{\pm}$ center-of-mass frame is both the most physically meaningful and also the most signal-rich reference frame. The expected signal significance of $\text{W}^{\pm}_{\text{L}}\text{W}^{\pm}_{\text{L}}$ in the $\text{W}^{\pm}\text{W}^{\pm}$ the $\text{W}^{\pm}\text{W}^{\pm}$ center-of-mass frame is 0.895 σ. The expected 95%CL upper limit on the signal strength of $\text{W}^{\pm}_{\text{L}}\text{W}^{\pm}_{\text{L}}$ is 2.418. The final observed (expected) 95% CL upper limit of the production cross section is 1.06 (0.85) fb for the $\text{W}^{\pm}_{\text{L}}\text{W}^{\pm}_{\text{L}}$ component. The observed (expected) significance of the singly longitudinal component process is 2.6 (2.9) standard deviations. The author was also involved in the approval talk of this study, and contributed to the generator study in the published paper.

The latter analysis performs the first search for heavy Majorana neutrinos at the TeV-mass-scale. The upper limits on $|V_{\mu N}|^2$ are set for the significantly extended mass range $750\,\text{GeV} < m_N < 25\,\text{TeV}$. This analysis also serves as the first test at colliders of the Weinberg operator, which is the only gauge invariant operator at dimension-five in the effective field theory approach. The observed (expected) 95% confidence level upper limit on the effective $\mu\mu$ Majorana mass is $|m_{\mu\mu}| = 10.84\ (12.84)$ GeV. The results agree with the predictions from the standard model. The author is the contact person for the analysis, and gave the pre-approval talk for the analysis.

In addition, the third analysis precisely measured inclusive Wγ production cross-section at $\sqrt{s} = 13\,\text{TeV}$, which is 15.58 ± 0.75 pb, and is consistent with the MadGraph5_amc@nlo NLO-QCD prediction of $\sigma = 15.44 \pm 1.24$ (scale) pb but slightly below the powheg NLO-QCD prediction of $\sigma = 22.45 \pm 3.21$ (scale) pb. The high photon p_{T} part of the photon p_{T}

distribution was found to be useful for setting limits on dimension-six effective field theory parameters. The author gave the approval talk for the analysis.

These three analyses involve precise measurements of the standard model, searching directly or indirectly for new physics beyond the Standard Model, which indicates that multiboson processes harbor a wealth of physics. With the Run-3 data taking at the LHC about to begin, many opportunities for possible physics analysis are on the horizon. On the one hand, the study of longitudinally polarized vector boson scattering processes will undoubtedly benefit from more experimental data. Currently, such analyses are limited by the statistics, and longitudinally polarized same-sign WW scattering would have a much higher expected significance. We can also extend to other diboson scattering processes, e.g., longitudinally polarized WZ scattering. On the other hand, due to the lack of signals explicitly beyond the Standard Model at the LHC, the indirect search for new physics beyond the Standard Model through the effective field theory approach will become increasingly popular. The study of the Weinberg operator lays the foundation for subsequent studies of higher dimension operators. Exploring dimension-seven and dimension-nine operators becomes possible at the LHC. By applying the effective field theory method, we can investigate more dimension-six operators that are sensitive in specific channels with the help of multiboson processes.

Bibliography

[1] CMS Collaboration. Observation of a New Boson at a Mass of 125 GeV with the CMS Experiment at the LHC. Phys. Lett. B, 2012, 716: 30-61. arXiv: 1207.7235 `[hep-ex]`.

[2] ATLAS Collaboration. Observation of a new particle in the search for the Standard Model Higgs boson with the ATLAS detector at the LHC. Phys. Lett. B, 2012, 716: 1-29. arXiv: 1207.7214 `[hep-ex]`.

[3] F. Englert, R. Brout. Broken Symmetry and the Mass of Gauge Vector Mesons. Phys. Rev. Lett., 1964, 13: 321-323.

[4] Peter W. Higgs. Broken Symmetries and the Masses of Gauge Bosons. Phys. Rev. Lett., 1964, 13: 508-509.

[5] G. S. Guralnik, C. R. Hagen, T. W. B. Kibble. Global Conservation Laws and Massless Particles. Phys. Rev. Lett., 1964, 13: 585-587.

[6] J. T. Boyd. LHC Run-2 and Future Prospects//2019 European School of High-Energy Physics. 2020. arXiv: 2001.04370 `[hep-ex]`.

[7] LHC Machine. JINST, 2008, 3: S08001.

[8] CMS Collaboration. Observation of electroweak production of same-sign W boson pairs in the two jet and two same-sign lepton final state in proton-proton collisions at $\sqrt{s} = 13$ TeV. Phys. Rev. Lett., 2018, 120: 081801. arXiv: 1709.05822 `[hep-ex]`.

[9] ATLAS Collaboration. Observation of electroweak production of a same-sign W boson pair in association with two jets in pp collisions at $\sqrt{s} = 13$ TeV with the ATLAS detector. Phys. Rev. Lett., 2019, 123: 161801. arXiv: 1906.03203 `[hep-ex]`.

[10] Benjamin W. Lee, C. Quigg, H. B. Thacker. The Strength of Weak Interactions at Very High-Energies and the Higgs Boson Mass. Phys. Rev. Lett., 1977, 38: 883-885.

[11] Benjamin W. Lee, C. Quigg, H. B. Thacker. Weak Interactions at Very High-Energies: The Role of the Higgs Boson Mass. Phys. Rev. D, 1977, 16: 1519.

[12] Domènec Espriu, Brian Yencho. Longitudinal WW scattering in light of the “Higgs boson” discovery. Phys. Rev. D, 2013, 87(5): 055017. arXiv: 1212.4158 `[hep-ph]`.

[13] Jung Chang, Kingman Cheung, Chih-Ting Lu, et al. WW scattering in the era of post-Higgs-boson discovery. Phys. Rev. D, 2013, 87: 093005. arXiv: 1303.6335 `[hep-ph]`.

[14] CMS Collaboration. Measurements of production cross sections of polarized same-sign W boson pairs in association with two jets in proton-proton collisions at $\sqrt{s} = 13$ TeV. Phys. Lett. B, 2021, 812: 136018. arXiv: 2009.09429 `[hep-ex]`.

[15] CMS Collaboration. Precision luminosity measurement in proton-proton collisions at $\sqrt{s} = 13$ TeV in 2015 and 2016 at CMS. Eur. Phys. J. C, 2021, 81(9): 800. arXiv: 2104.01927 `[hep-ex]`.

[16] CMS Collaboration. CMS luminosity measurement for the 2017 data-taking period at $\sqrt{s} = 13$ TeV., 2018.

[17] CMS Collaboration. CMS luminosity measurement for the 2018 data-taking period at $\sqrt{s} = 13$ TeV., 2019.

[18] CMS Collaboration. The CMS Experiment at the CERN LHC. JINST, 2008, 3: S08004.

[19] Q. R. Ahmad, et al. Direct evidence for neutrino flavor transformation from neutral current interactions in the Sudbury Neutrino Observatory. Phys. Rev. Lett., 2002, 89: 011301. arXiv: nucl-ex/0204008.

[20] Y. Ashie, et al. A Measurement of atmospheric neutrino oscillation parameters by SUPER-KAMIOKANDE I. Phys. Rev. D, 2005, 71: 112005. arXiv: hep-ex/0501064.

[21] Ernest Ma. Pathways to naturally small neutrino masses. Phys. Rev. Lett., 1998, 81: 1171-1174. arXiv: hep-ph/9805219.

[22] Anupama Atre, Tao Han, Silvia Pascoli, et al. The Search for Heavy Majorana Neutrinos. JHEP, 2009, 05: 030. arXiv: 0901.3589 `[hep-ph]`.

[23] Frank F. Deppisch, P. S. Bhupal Dev, Apostolos Pilaftsis. Neutrinos and Collider Physics. New J. Phys., 2015, 17(7): 075019. arXiv: 1502.06541 `[hep-ph]`.

[24] Yi Cai, Juan Herrero-García, Michael A. Schmidt, et al. From the trees to the forest: a review of radiative neutrino mass models. Front. in Phys., 2017, 5: 63. arXiv: 1706.08524 `[hep-ph]`.

[25] Yi Cai, Tao Han, Tong Li, et al. Lepton Number Violation: Seesaw Models and Their Collider Tests. Front. in Phys., 2018, 6: 40. arXiv: 1711.02180 `[hep-ph]`.

[26] CMS Collaboration. Search for high mass dijet resonances with a new background prediction method in proton-proton collisions at $\sqrt{s} = 13$ TeV. JHEP, 2020, 05: 033. arXiv: 1911.03947 `[hep-ex]`.

[27] ATLAS Collaboration. Search for new resonances in mass distributions of jet pairs using 139 fb^{-1} of pp collisions at $\sqrt{s} = 13$ TeV with the ATLAS detector. JHEP, 2020, 03: 145. arXiv: 1910.08447 `[hep-ex]`.

[28] CMS Collaboration. A Search for a Doubly-Charged Higgs Boson in pp Collisions at $\sqrt{s} = 7$ TeV. Eur. Phys. J. C, 2012, 72: 2189. arXiv: 1207.2666 `[hep-ex]`.

[29] CMS Collaboration. Search for heavy neutral leptons in events with three charged leptons in proton-proton collisions at $\sqrt{s} = 13$ TeV. Phys. Rev. Lett., 2018, 120(22): 221801. arXiv: 1802.02965 `[hep-ex]`.

[30] ATLAS Collaboration. Search for doubly charged scalar bosons decaying into same-sign W boson pairs with the ATLAS detector. Eur. Phys. J. C, 2019, 79(1): 58. arXiv: 1808.01899 `[hep-ex]`.

[31] ATLAS Collaboration. Search for heavy neutral leptons in decays of W bosons produced in 13 TeV pp collisions using prompt and displaced signatures with the ATLAS detector. JHEP, 2019, 10: 265. arXiv: 1905.09787 `[hep-ex]`.

[32] CMS Collaboration. Search for physics beyond the standard model in multilepton final states in proton-proton collisions at $\sqrt{s} = 13$ TeV. JHEP, 2020, 03: 051. arXiv: 1911.04968 `[hep-ex]`.

[33] ATLAS Collaboration. Search for type-III seesaw heavy leptons in dilepton final states in pp collisions at $\sqrt{s} = 13$ TeV with the ATLAS detector. Eur. Phys. J. C, 2021, 81(3): 218. arXiv: 2008.07949 `[hep-ex]`.

[34] CMS Collaboration. Search for heavy Majorana neutrinos in same-sign dilepton channels in proton-proton collisions at $\sqrt{s} = 13$ TeV. JHEP, 2019, 01: 122. arXiv: 1806.10905 `[hep-ex]`.

[35] CMS Collaboration. Search for a heavy right-handed W boson and a heavy neutrino in events with two same-flavor leptons and two jets at $\sqrt{s} = 13$ TeV. JHEP, 2018, 05: 148. arXiv: 1803.11116 `[hep-ex]`.

[36] ATLAS Collaboration. Search for heavy Majorana or Dirac neutrinos and right-handed W gauge bosons in final states with two charged leptons and two jets at $\sqrt{s} = 13$ TeV with the ATLAS detector. JHEP, 2019, 01: 016. arXiv: 1809.11105 `[hep-ex]`.

[37] Benjamin Fuks, Jonas Neundorf, Krisztian Peters, et al. Majorana neutrinos in same-sign $W^{\pm}W^{\pm}$ scattering at the LHC: Breaking the TeV barrier. Phys. Rev. D, 2021, 103(5): 055005. arXiv: 2011.02547 `[hep-ph]`.

[38] B. Grzadkowski, M. Iskrzynski, M. Misiak, et al. Dimension-Six Terms in the Standard Model Lagrangian. JHEP, 2010, 10: 085. arXiv: 1008.4884 `[hep-ph]`.

[39] Steven Weinberg. Baryon and Lepton Nonconserving Processes. Phys. Rev. Lett., 1979, 43: 1566-1570.

[40] CMS Collaboration. Measurement of the Wγ Production Cross Section in Proton-Proton Collisions at $\sqrt{s}$=13 TeV and Constraints on Effective Field Theory Coefficients. Phys. Rev. Lett., 2021, 126(25): 252002. arXiv: 2102.02283 `[hep-ex]`.

[41] Kaoru Hagiwara, S. Ishihara, R. Szalapski, et al. Low-energy effects of new interactions in the electroweak boson sector. Phys. Rev. D, 1993, 48: 2182-2203.

[42] Celine Degrande, Nicolas Greiner, Wolfgang Kilian, et al. Effective Field Theory: A Modern Approach to Anomalous Couplings. Annals Phys., 2013, 335: 21-32. arXiv: 1205.4231 `[hep-ph]`.

[43] W. Buchmuller, D. Wyler. Effective Lagrangian Analysis of New Interactions and Flavor Conservation. Nucl. Phys. B, 1986, 268: 621-653.

[44] S. L. Glashow. Partial Symmetries of Weak Interactions. Nucl. Phys., 1961, 22: 579-588.

[45] Steven Weinberg. A Model of Leptons. Phys. Rev. Lett., 1967, 19: 1264-1266.

[46] Abdus Salam. Weak and Electromagnetic Interactions. Conf. Proc. C, 1968, 680519: 367-377.

[47] S. L. Glashow, J. Iliopoulos, L. Maiani. Weak Interactions with Lepton-Hadron Symmetry. Phys. Rev. D, 1970, 2: 1285-1292.

[48] Carsten Burgard. Elementary particles in the Standard Model. https://texample.net/tikz/examples/model-physics/.

[49] P. A. Zyla, et al. Review of Particle Physics. PTEP, 2020, 2020(8): 083C01.

[50] C. S. Wu, E. Ambler, R. W. Hayward, et al. Experimental Test of Parity Conservation in β Decay. Phys. Rev., 1957, 105: 1413-1414.

[51] Sheldon L. Glashow. The renormalizability of vector meson interactions. Nucl. Phys., 1959, 10: 107-117.

[52] Guido Altarelli. Collider Physics within the Standard Model: a Primer., 2013. arXiv: `1303.2842 [hep-ph]`.

[53] Oleg Kuprash. Multiboson production at the LHC (diboson, triboson). Geneva: CERN, 2021. https://cds.cern.ch/record/2790473.

[54] CMS Collaboration. Measurement of the $W\gamma$ and $Z\gamma$ Inclusive Cross Sections in pp Collisions at $\sqrt{s} = 7$ TeV and Limits on Anomalous Triple Gauge Boson Couplings. Phys. Rev. D, 2014, 89(9): 092005. arXiv: 1308.6832 `[hep-ex]`.

[55] ATLAS Collaboration. Measurements of $W\gamma$ and $Z\gamma$ production in pp collisions at $\sqrt{s}$=7 TeV with the ATLAS detector at the LHC. Phys. Rev. D, 2013, 87(11): 112003. arXiv: 1302.1283 `[hep-ex]`.

[56] Sally Dawson. The Effective W Approximation. Nucl. Phys. B, 1985, 249: 42-60.

[57] Malcolm J. Duncan, Gordon L. Kane, W. W. Repko. W W Physics at Future Colliders. Nucl. Phys. B, 1986, 272: 517-559.

[58] R. N. Cahn, Sally Dawson. Production of Very Massive Higgs Bosons. Phys. Lett. B, 1984, 136: 196.

[59] I. Kuss, H. Spiesberger. Luminosities for vector boson - vector boson scattering at high-energy colliders. Phys. Rev. D, 1996, 53: 6078-6093. arXiv: hep-ph/9507204.

[60] E. Accomando, Ansgar Denner, S. Pozzorini. Logarithmic electroweak corrections to e+ e- —> nu(e) anti-nu(e) W+ W-. JHEP, 2007, 03: 078. arXiv: hep-ph/0611289.

[61] T. Figy, C. Oleari, D. Zeppenfeld. Next-to-leading order jet distributions for Higgs boson production via weak boson fusion. Phys. Rev. D, 2003, 68: 073005. arXiv: hep-ph/0306109.

[62] Alessandro Ballestrero, et al. Precise predictions for same-sign W-boson scattering at the LHC. Eur. Phys. J. C, 2018, 78(8): 671. arXiv: 1803.07943 `[hep-ph]`.

[63] Roberto Covarelli, Mathieu Pellen, Marco Zaro. Vector-Boson scattering at the LHC: Unraveling the electroweak sector. Int. J. Mod. Phys. A, 2021, 36(16): 2130009. arXiv: 2102.10991 `[hep-ph]`.

[64] Benedikt Biedermann, Ansgar Denner, Mathieu Pellen. Complete NLO corrections to W^+W^+ scattering and its irreducible background at the LHC. JHEP, 2017, 10: 124. arXiv: 1708.00268 `[hep-ph]`.

[65] CMS Collaboration. Measurements of production cross sections of WZ and same-sign WW boson pairs in association with two jets in proton-proton collisions at $\sqrt{s} = 13$ TeV. Phys. Lett. B, 2020, 809: 135710. arXiv: 2005.01173 `[hep-ex]`.

[66] Michał Szleper. The Higgs boson and the physics of WW scattering before and after Higgs discovery. 2014. arXiv: 1412.8367 `[hep-ph]`.

[67] Y. Fukuda, et al. Evidence for oscillation of atmospheric neutrinos. Phys. Rev. Lett., 1998, 81: 1562-1567. arXiv: hep-ex/9807003.

[68] Ettore Majorana. Teoria simmetrica dell’ elettrone e del positrone. Nuovo Cim., 1937, 14: 171-184.

[69] Peter Minkowski. $\mu \rightarrow e\gamma$ At a Rate of One Out of 1-Billion Muon Decays? Phys. Lett. B, 1977, 67: 421.

[70] Murray Gell-Mann, Pierre Ramond, Richard Slansky. Complex Spinors and Unified Theories. Conf. Proc. C, 1979, 790927: 315-321. arXiv: 1306.4669 `[hep-th]`.

[71] Tsutomu Yanagida. Horizontal gauge symmetry and masses of neutrinos. Conf. Proc. C, 1979, 7902131: 95-99.

[72] Rabindra N. Mohapatra, Goran Senjanovi ć. Neutrino Mass and Spontaneous Parity Violation. Phys. Rev. Lett., 1980, 44: 912.

[73] Steven Weinberg. Baryon- and Lepton-Nonconserving Processes. Phys. Rev. Lett., 1979, 43: 1566.

[74] Benjamin Fuks, Jonas Neundorf, Krisztian Peters, et al. Probing the Weinberg operator at colliders. Phys. Rev. D, 2021, 103(11): 115014. arXiv: 2012.09882 `[hep-ph]`.

[75] Christophe Grojean, Witold Skiba, John Terning. Disguising the oblique parameters. Phys. Rev. D, 2006, 73: 075008. arXiv: hep-ph/0602154.

[76] COMSOL. Analyzing the LHC Magnet Quenches. https://spectrum.ieee.org/analyzing-the-lhc-magnet-quenches.

[77] R. Bruce, C. Bracco, R. De Maria, et al. Reaching record-low * at the CERN Large Hadron Collider using a novel scheme of collimator settings and optics. Nucl. Instrum. Meth. A, 2017, 848: 19-30.

[78] Paul Rincon. Collider halted until next year. http://news.bbc.co.uk/2/hi/science/nature/7632408.stm.

[79] Jorg Wenninger. Operation and Configuration of the LHC in Run 2., 2019. https://cds.cern.ch/record/2668326.

[80] CMS Collaboration. Tracking detectors. https://cms-docdb.cern.ch/cgi-bin/PublicDocDB/RetrieveFile?docid=4227&

[81] CMS Collaboration. The CMS Phase-1 Pixel Detector Upgrade. JINST, 2021, 16(02): P02027. arXiv: 2012.14304 `[physics.ins-det]`.

[82] CMS Collaboration. Electromagnetic calorimeter. https://cms-docdb.cern.ch/cgi-bin/PublicDocDB/RetrieveFile?doc

[83] CMS Collaboration. The CMS ECAL performance with examples. JINST, 2014, 9: C02008.

[84] P. Adzic, et al. Energy resolution of the barrel of the CMS electromagnetic calorimeter. JINST, 2007, 2: P04004.

[85] S. Abdullin, et al. The CMS barrel calorimeter response to particle beams from 2-GeV/c to 350-GeV/c. Eur. Phys. J. C, 2009, 60: 359-373.

[86] CMS Collaboration. Calibration of the CMS hadron calorimeters using proton-proton collision data at $\sqrt{s}$ = 13 TeV. JINST, 2020, 15(05): P05002. arXiv: 1910.00079 `[physics.ins-det]`.

[87] CMS Collaboration. Precise Mapping of the Magnetic Field in the CMS Barrel Yoke using Cosmic Rays. JINST, 2010, 5: T03021. arXiv: 0910.5530 `[physics.ins-det]`.

[88] CMS Collaboration. The Performance of the CMS Muon Detector in Proton-Proton Collisions at $\sqrt{s} = 7$ TeV at the LHC. JINST, 2013, 8: P11002. arXiv: 1306.6905 `[physics.ins-det]`.

[89] CMS Collaboration. The CMS trigger system. JINST, 2017, 12(01): P01020. arXiv: 1609.02366 `[physics.ins-det]`.

[90] CMS Collaboration. Performance of the CMS Level-1 trigger in proton-proton collisions at $\sqrt{s} =$ 13 TeV. JINST, 2020, 15(10): P10017. arXiv: 2006.10165 `[hep-ex]`.

[91] CMS Collaboration. CMSSW. http://cms-sw.github.io/.

[92] ROOT Group. ROOT: analyzing petabytes of data, scientifically. https://root.cern/.

[93] CMS Collaboration. Particle-flow reconstruction and global event description with the CMS detector. JINST, 2017, 12(10): P10003. arXiv: 1706.04965 `[physics.ins-det]`.

[94] CMS Collaboration. Measurement of the inclusive and differential Higgs boson production cross sections in the leptonic WW decay mode at $\sqrt{s} = 13$ TeV. JHEP, 2021, 03: 003. arXiv: 2007.01984 `[hep-ex]`.

[95] CMS Collaboration. Mini-AOD: A New Analysis Data Format for CMS. J. Phys. Conf. Ser., 2015, 664(7): 7. arXiv: 1702.04685 `[physics.ins-det]`.

[96] CMS Collaboration. Description and performance of track and primary-vertex reconstruction with the CMS tracker. JINST, 2014, 9(10): P10009. arXiv: 1405.6569 `[physics.ins-det]`.

[97] R. Fruhwirth. Application of Kalman filtering to track and vertex fitting. Nucl. Instrum. Meth. A, 1987, 262: 444-450.

[98] K. Rose. Deterministic annealing for clustering, compression, classification, regression, and related optimization problems. IEEE Proc., 1998, 86(11): 2210-2239.

[99] CMS Collaboration. Performance of the CMS muon detector and muon reconstruction with proton-proton collisions at $\sqrt{s} = 13$ TeV. JINST, 2018, 13(06): P06015. arXiv: 1804.04528 `[physics.ins-det]`.

[100] CMS Collaboration. Performance of the reconstruction and identification of high-momentum muons in proton-proton collisions at $\sqrt{s} = 13$ TeV. JINST, 2020, 15(02): P02027. arXiv: 1912.03516 `[physics.ins-det]`.

[101] CMS Collaboration. Performance of CMS Muon Reconstruction in pp Collision Events at $\sqrt{s} = 7$ TeV. JINST, 2012, 7: P10002. arXiv: 1206.4071 `[physics.ins-det]`.

[102] CMS Collaboration. Search for neutral Higgs bosons decaying to tau pairs in pp collisions at $\sqrt{s} = 7$ TeV. Phys. Lett. B, 2012, 713: 68-90. arXiv: 1202.4083 `[hep-ex]`.

[103] CMS Collaboration. Tag and Probe. https://twiki.cern.ch/twiki/bin/view/CMSPublic/TagAndProbe. 2014.

[104] A. Bodek, A. van Dyne, J. Y. Han, et al. Extracting Muon Momentum Scale Corrections for Hadron Collider Experiments. Eur. Phys. J. C, 2012, 72: 2194. arXiv: 1208.3710 `[hep-ex]`.

[105] Rochester Group. Rochester Correction for muon momentum scale and resolution. https://twiki.cern.ch/twiki/bin/view/CMS/RochcorMuon. 2021.

[106] CMS Collaboration. Electron and photon reconstruction and identification with the CMS experiment at the CERN LHC. JINST, 2021, 16(05): P05014. arXiv: 2012.06888 `[hep-ex]`.

[107] CMS Collaboration. CMS Physics: Technical Design Report Volume 1: Detector Performance and Software., 2006.

[108] CMS Collaboration. Performance of Electron Reconstruction and Selection with the CMS Detector in Proton-Proton Collisions at $\sqrt{s} = 8$ TeV. JINST, 2015, 10(06): P06005. arXiv: 1502.02701 `[physics.ins-det]`.

[109] Matteo Cacciari, Gavin P. Salam, Gregory Soyez. The anti-k_t jet clustering algorithm. JHEP, 2008, 04: 063. arXiv: 0802.1189 `[hep-ph]`.

[110] Matteo Cacciari, Gavin P. Salam, Gregory Soyez. FastJet User Manual. Eur. Phys. J. C, 2012, 72: 1896. arXiv: 1111.6097 `[hep-ph]`.

[111] CMS Collaboration. Pileup mitigation at CMS in 13 TeV data. JINST, 2020, 15(09): P09018. arXiv: 2003.00503 `[hep-ex]`.

[112] CMS Collaboration. Identification of heavy-flavour jets with the CMS detector in pp collisions at 13 TeV. JINST, 2018, 13(05): P05011. arXiv: 1712.07158 `[physics.ins-det]`.

[113] CMS Collaboration. Jet energy scale and resolution in the CMS experiment in pp collisions at 8 TeV. JINST, 2017, 12(02): P02014. arXiv: 1607.03663 `[hep-ex]`.

[114] Matteo Cacciari, Gavin P. Salam. Pileup subtraction using jet areas. Phys. Lett. B, 2008, 659: 119-126. arXiv: 0707.1378 `[hep-ph]`.

[115] CMS Collaboration. Performance of missing transverse momentum reconstruction in proton-proton collisions at $\sqrt{s} = 13$ TeV using the CMS detector. JINST, 2019, 14(07): P07004. arXiv: 1903.06078 `[hep-ex]`.

[116] CMS Collaboration. Performance of missing energy reconstruction in 13 TeV pp collision data using the CMS detector. CMS-PAS-JME-16-004. Geneva: CERN, 2016. http://cds.cern.ch/record/2205284.

[117] CMS Collaboration. Performance of reconstruction and identification of τ leptons decaying to hadrons and ν_τ in pp collisions at $\sqrt{s} = 13$ TeV. JINST, 2018, 13(10): P10005. arXiv: 1809.02816 `[hep-ex]`.

[118] CMS Collaboration. The NanoAOD event data format in CMS. J. Phys. Conf. Ser., 2020, 1525(1): 012038.

[119] S. Agostinelli, et al. GEANT4–a simulation toolkit. Nucl. Instrum. Meth. A, 2003, 506: 250-303.

[120] J. Alwall, R. Frederix, S. Frixione, et al. The automated computation of tree-level and next-to-leading order differential cross sections, and their matching to parton shower simulations. JHEP, 2014, 07: 079. arXiv: 1405.0301 `[hep-ph]`.

[121] Alessandro Ballestrero, Aissa Belhouari, Giuseppe Bevilacqua, et al. PHANTOM: A Monte Carlo event generator for six parton final states at high energy colliders. Comput. Phys. Commun., 2009, 180: 401-417. arXiv: 0801.3359 `[hep-ph]`.

[122] Diogo Buarque Franzosi, Olivier Mattelaer, Richard Ruiz, et al. Automated predictions from polarized matrix elements. JHEP, 2020, 04: 082. arXiv: 1912.01725 `[hep-ph]`.

[123] Paolo Nason, Giulia Zanderighi. W^+W^- , WZ and ZZ production in the POWHEG-BOX-V2. Eur. Phys. J. C, 2014, 74: 2702. arXiv: 1311.1365 `[hep-ph]`.

[124] John M. Campbell, R. Keith Ellis, Ciaran Williams. Vector boson pair production at the LHC. JHEP, 2011, 07: 018. arXiv: 1105.0020 `[hep-ph]`.

[125] Johan Alwall, Michel Herquet, Fabio Maltoni, et al. MadGraph 5 : Going Beyond. JHEP, 2011, 06: 128. arXiv: 1106.0522 `[hep-ph]`.

[126] Rikkert Frederix, Stefano Frixione. Merging meets matching in MCNLO. JHEP, 2012, 12: 061. arXiv: 1209.6215 `[hep-ph]`.

[127] Torbjörn Sjöstrand, Stefan Ask, Jesper R. Christiansen, et al. An introduction to PYTHIA 8.2. Comput. Phys. Commun., 2015, 191: 159-177. arXiv: 1410.3012 `[hep-ph]`.

[128] CMS Collaboration. Event generator tunes obtained from underlying event and multiparton scattering measurements. Eur. Phys. J. C, 2016, 76: 155. arXiv: 1512.00815 `[hep-ex]`.

[129] CMS Collaboration. Extraction and validation of a new set of CMS PYTHIA8 tunes from underlying-event measurements. Eur. Phys. J. C, 2020, 80: 4. arXiv: 1903.12179 `[hep-ex]`.

[130] Michelangelo L. Mangano, Mauro Moretti, Fulvio Piccinini, et al. Matching matrix elements and shower evolution for top-quark production in hadronic collisions. JHEP, 2007, 01: 013. arXiv: hep-ph/0611129 `[hep-ph]`.

[131] Richard D. Ball, et al. Parton distributions for the LHC Run II. JHEP, 2015, 04: 040. arXiv: 1410.8849 `[hep-ph]`.

[132] Richard D. Ball, et al. Parton distributions from high-precision collider data. Eur. Phys. J. C, 2017, 77: 663. arXiv: 1706.00428 `[hep-ph]`.

[133] S. Agostinelli, et al. GEANT4 —a simulation toolkit. Nucl. Instrum. Meth. A, 2003, 506: 250.

[134] David L. Rainwater, R. Szalapski, D. Zeppenfeld. Probing color singlet exchange in Z + two jet events at the CERN LHC. Phys. Rev. D, 1996, 54: 6680-6689. arXiv: hep-ph/9605444.

[135] Albert M. Sirunyan, et al. Measurements of properties of the Higgs boson decaying to a W boson pair in pp collisions at $\sqrt{s} = 13$ TeV. Phys. Lett. B, 2019, 791: 96. arXiv: 1806.05246 `[hep-ex]`.

[136] CMS Collaboration. CMS Luminosity Measurements for the 2016 Data Taking Period., 2017.

[137] J. S. Conway. Incorporating Nuisance Parameters in Likelihoods for Multisource Spectra//PHYSTAT 2011. 2011: 115-120. arXiv: 1103.0354 `[physics.data-an]`.

[138] CMS Collaboration. RooStats/RooFit - based software tools used for statistical analysis within the Higgs PAG - combine. https://cms-analysis.github.io/HiggsAnalysis-CombinedLimit/.

[139] François Chollet, et al. Keras. https://keras.io. 2015.

[140] Martín Abadi, et al. TensorFlow: large-scale machine learning on heterogeneous distributed systems. 2016. http://tensorflow.org/.

[141] Procedure for the LHC Higgs boson search combination in Summer 2011. Geneva: CERN, 2011. http://cds.cern.ch/record/1379837.

[142] Tom Junk. Sensitivity, Exclusion and Discovery with Small Signals, LargeBackgrounds, and Large Systematic Uncertainties., 2006.

[143] Wade Fisher. Systematics and limit calculations., 2006.

[144] Thomas Junk. Confidence level computation for combining searches with small statistics. Nucl. Instrum. Meth. A, 1999, 434: 435-443. arXiv: hep-ex/9902006.

[145] Alexander L. Read. Modified frequentist analysis of search results (The CL(s) method)//Workshop on Confidence Limits. 2000: 81-101.

[146] Alexander L. Read. Presentation of search results: The CL(s) technique. J. Phys. G, 2002, 28: 2693-2704.

[147] Glen Cowan, Kyle Cranmer, Eilam Gross, et al. Asymptotic formulae for likelihood-based tests of new physics. Eur. Phys. J. C, 2011, 71: 1554. arXiv: 1007.1727 `[physics]`.

[148] KYLE CRANMER. STATISTICAL CHALLENGES FOR SEARCHES FOR NEW PHYSICS AT THE LHC//Statistical Problems in Particle Physics, Astrophysics and Cosmology. PUBLISHED BY IMPERIAL COLLEGE PRESS AND DISTRIBUTED BY WORLD SCIENTIFIC PUBLISHING CO., 2006. https://doi.org/10.1142%2F9781860948985_0026.

[149] Alessandro Ballestrero, Ezio Maina, Giovanni Pelliccioli. Different polarization definitions in same-sign WW scattering at the LHC. Phys. Lett. B, 2020, 811: 135856. arXiv: 2007.07133 `[hep-ph]`.

[150] CMS Collaboration. Event generator tunes obtained from underlying event and multiparton scattering measurements. Eur. Phys. J. C, 2016, 76(3): 155. arXiv: 1512.00815 `[hep-ex]`.

[151] Richard D. Ball, et al. Parton distributions for the LHC Run II. JHEP, 2015, 04: 040. arXiv: 1410.8 849 `[hep-ph]`.

[152] CMS Collaboration. Extraction and validation of a new set of CMS PYTHIA8 tunes from underlying-event measurements. Eur. Phys. J. C, 2020, 80(1): 4. arXiv: 1903.12179 `[hep-ex]`.

[153] Richard D. Ball, et al. Parton distributions from high-precision collider data. Eur. Phys. J. C, 2017, 77(10): 663. arXiv: 1706.00428 `[hep-ph]`.

[154] Richard Ruiz. HeavyN: The Standard Model + Heavy Neutrinos at NLO in QCD.

[155] Parton distributions for the LHC run II., 2015, 04: 040. arXiv: 1410.8849 `[hep-ph]`.

[156] Richard Ruiz. SMWeinberg: The Standard Model + The Weinberg Operator at NLO in QCD. https ://feynrules.irmp.ucl.ac.be/wiki/SMWeinberg.

[157] Latinos working group. Common analysis object definitions and trigger efficiencies for the $H \rightarrow WW$ analysis with full Run-II data. CMS Analysis Note, 2019, 2019/105.

[158] CMS Collaboration. Rochester corrections.

[159] CMS Collaboration. Search for heavy neutral leptons in events with three charged leptons in proton-proton collisions at $\sqrt{s} = 13$ TeV. Phys. Rev. Lett., 2018, 120(22): 221801. arXiv: `1802.02965` `[physics.data-an]`.

[160] CMS Collaboration. Search for heavy Majorana neutrinos in same-sign dilepton channels in proton-proton collisions at $\sqrt{s} = 13$ TeV. JHEP, 2019, 01: 122. arXiv: 1806.10905 `[physics.data-an]`.

[161] Stefano Frixione. Isolated photons in perturbative QCD. Phys. Lett. B, 1998, 429: 369-374. arXiv: hep-ph/9801442.

[162] Luca Barze, Mauro Chiesa, Guido Montagna, et al. Wγ production in hadronic collisions using the POWHEG+MiNLO method. JHEP, 2014, 12: 039. arXiv: 1408.5766 `[hep-ph]`.

[163] Olivier Mattelaer. On the maximal use of Monte Carlo samples: re-weighting events at NLO accuracy. Eur. Phys. J. C, 2016, 76(12): 674. arXiv: 1607.00763 `[hep-ph]`.

[164] MadGraph5_aMC@NLO. Https://cp3.irmp.ucl.ac.be/projects/madgraph/wiki/Reweight,

[165] CMS Collaboration. Measurement of the cross section for electroweak production of a Z boson, a photon and two jets in proton-proton collisions at $\sqrt{s} = 13$ TeV and constraints on anomalous quartic couplings. JHEP, 2020, 06: 076. arXiv: 2002.09902 `[hep-ex]`.

[166] Jon Butterworth, et al. PDF4LHC recommendations for LHC Run II. J. Phys. G, 2016, 43: 023001. arXiv: 1510.03865 `[hep-ph]`.

[167] L. A. Harland-Lang, A. D. Martin, P. Motylinski, et al. Parton distributions in the LHC era: MMHT 2014 PDFs. Eur. Phys. J. C, 2015, 75(5): 204. arXiv: 1412.3989 `[hep-ph]`.

[168] Sayipjamal Dulat, Tie-Jiun Hou, Jun Gao, et al. New parton distribution functions from a global analysis of quantum chromodynamics. Phys. Rev. D, 2016, 93(3): 033006. arXiv: 1506.07443 `[hep-ph]`.

[169] CMS Collaboration. Higgs Combination Tool with a TensorFlow based minimizer. https://github.com/bendavid/HiggsAnalysis-CombinedLimit/tree/tensorflowfit.

[170] CMS Collaboration. Measurement of the W boson rapidity, helicity, and differential cross sections in pp collisions at $\sqrt{s} = 13$ TeV. CMS-PAS-SMP-18-012. Geneva: CERN, 2020. http://cds.cern.ch/record/2708491.

[171] K. Doroba, J. Kalinowski, J. Kuczmarski, et al. The $\mathrm{W_L W_L}$ scattering at the LHC: improving the selection criteria. Phys. Rev. D, 2012, 86: 036011. arXiv: 1201.2768 `[hep-ph]`.

[172] Helge Voss, Andreas Höcker, Jörg Stelzer, et al. TMVA, the Toolkit for Multivariate Data Analysis with ROOT//XIth International Workshop on Advanced Computing and Analysis Techniques in Physics Research (ACAT). 2007: 40. arXiv: physics/0703039.

Appendix A

Summary of work during doctoral studies and additional materials

A.1 Publication

- CMS Collaboration. Probing Majorana neutrinos and the Weinberg operator in the same-charge dimuon channel through vector boson fusion processes in proton-proton collisions at $\sqrt{s} = 13$ TeV. To be submitted to PRL. **Leading contributions, as the analysis contact gave the pre-approval talk**
- CMS Collaboration. (2021). Measurements of production cross sections of polarized same-sign W boson pairs in association with two jets in proton-proton collisions at $\sqrt{s} =$ 13 TeV. Physics Letters B, 812, 136018. arXiv: 2009.09429[hep-ex]. **Leading contributions, contributed to the approval talk**
- CMS Collaboration. (2021). Measurement of the Wγ Production Cross Section in Proton-Proton Collisions at $\sqrt{s} = 13$ TeV and Constraints on Effective Field Theory Coefficients. Physical Review Letters, 126(25), 252002. arXiv: 2102.02283[hep-ex]. **Crucial contributions, gave the approval talk**
- R. Bellan, G. Boldrini, D. Brambilla. et al. (2021). A sensitivity study of VBS and diboson WW to dimension-6 EFT operators at the LHC. To be submitted to JHEP. arXiv: 2108.03199 [hep-ph]. **Participated in the study of the same-sign WW scattering**
- S. Qian, C. Li, Q. Li. et al. (2021). Searching for heavy leptoquarks at a muon collider. J. High Energ. Phys. 2021, 47. arXiv: 2109.01265 [hep-ph]. **Participated in the study of the vector boson and leptoquark scattering**
- M. Lu, A.M. Levin, C. Li. et al. (2020). The Physics Case for an Electron-Muon Collider. Adv. High Energy Phys., vol. 2021, p. 6693618. arXiv:2010.15144 [hep-ph]. **Studied the property of Higgs at the electron-muon collider**.

A.2 Service work

- **Generator validation convener** (Sep 2021 – Present).
  - Participate in and lead the validation of the latest version v331 of MadGraph5 to prepare for Run3 CMS Monte-Carlo sample simulation.
  - Participate in the construction of the new generator validation framework genValidation using Rivet.
  - Lead the CPU and physics performance study of the new MadGraph5 settings for VBF/VBS processes.
- **Machine Learning Contact** (Sep 2020 – Present).
  - Maintain and reinforce the communication bridge between the CMS Standard Model Physics.

A.3 Meetings and workshops

- ”VBF production of same-sign muons through Majorana neutrinos or the Weinberg operator”, CMS Week Agenda, Sep. 2021.
- ”Searches for new physics in events with leptons in the final state in CMS”, Phenomenology 2021 Symposium, May 2021.
- ”Preapproval of EXO-21-003: Search for VBF production of same-sign muons through Majorana neutrinos or the Weinberg operator”, Exotica Jets+X Working Group Meeting, 14 Jun 2021.
- ”Approval for SMP-19-002 : Wgamma cross section”, Physics Plenary Meeting, 22 Oct 2020.
- ”Longitudinally polarised Same-Sign WW scattering searches with the CMS detector”, Effective Field Theory in Polarised VBS, 22 Sep 2020.
- ”Report on use of ML techniques in SMP”, Machine Learning Town Hall & Group Kick-Off, Jul 2020.
- ”Approval of SMP-20-006 : Measurements of the scattering of polarized same-sign WW bosons”, SMP General Meeting, 30 Jun 2020.

A.4 Additional materials for polarized $\mathrm{W}^{\pm}\mathrm{W}^{\pm}$

A.4.1 Expected significances in the pp-frame

Table A.1 reports the expected significances in the pp-frame and in the WW-frame calculated with the same DNN training and statistical analysis. Please be aware that these results are in very early stage. The NLO QCD and EW corrections are not applied. But the results indicate that $\mathrm{W}^{\pm}_{\mathrm{L}}\mathrm{W}^{\pm}_{\mathrm{L}}$ in WW-frame can get better significance.

Table A.1 Expected significance of $\mathrm{W}^{\pm}_{\mathrm{L}}\mathrm{W}^{\pm}_{\mathrm{L}}$ for each data-taking periods in the pp-frame and the WW-frame.

Signal process	**2016**	**2017**	**2018**	**2016-2018 Combined**
pp-frame	0.51	0.43	0.62	0.900
WW-frame	0.74	0.63	0.90	1.315

A.4.2 BDTs for extracting polarization information

Different polarization states of the W boson can lead to different kinematic distributions and influence the kinematical properties of the two leptons, the two jets, and $\vec{p}_{\mathrm{T}}^{\mathrm{miss}}$. The W_{L} bosons tend to be radiated at a smaller angle with respect to the incoming quark direction, resulting in a smaller W_{L} boson p_{T} compared to the radiated W_{T} boson p_{T}. In addition, there are differences in the behavior of the scattering amplitudes as a function of the $\mathrm{W}^{\pm}\mathrm{W}^{\pm}$ center-of-mass energy and the scattering angle[171].

Multivariate techniques are used to enhance the separation between the different processes. This section shows the boosted decision trees (BDTs) with gradient boosting using the TMVA package[172]. Two different BDTs, referred to as the BDT^{WW}s, are trained on simulated events to separate either the $\mathrm{W}^{\pm}_{\mathrm{L}}\mathrm{W}^{\pm}_{\mathrm{L}}$ and $\mathrm{W}^{\pm}_{\mathrm{T}}\mathrm{W}^{\pm}_{\mathrm{X}}$ processes or the $\mathrm{W}^{\pm}_{\mathrm{L}}\mathrm{W}^{\pm}_{\mathrm{X}}$ and $\mathrm{W}^{\pm}_{\mathrm{T}}\mathrm{W}^{\pm}_{\mathrm{T}}$ processes. Discriminating observables used as the inputs to the BDTs are listed in Table A.2. The distributions of these observables are taken from the SM predictions. Angular variables are included, such as the difference in the azimuthal angles between the leading two jets ($\Delta\phi_{\mathrm{jj}}$) and leptons ($\Delta\phi_{\ell\ell}$), and the ΔR between the leading (subleading) jet and the dilepton system $\Delta R_{\mathrm{j1},\ell\ell}$ ($\Delta R_{\mathrm{j2},\ell\ell}$). The dilepton $p_{\mathrm{T}}^{\ell\ell}$, $m_{\ell\ell}$, and the transverse diboson mass $m_{\mathrm{T}}^{\mathrm{WW}}$ as defined in Ref[65] are also considered. The kinematic variable $(p_{\mathrm{T}}^{\ell_1} p_{\mathrm{T}}^{\ell_2})/(p_{\mathrm{T}}^{\mathrm{j1}} p_{\mathrm{T}}^{\mathrm{j2}})$ proposed in Ref[171] is also included in the BDT inputs. Only variables that improve the sensitivity are kept in the training. The signal extraction was also compared with a deep neural network using the KERAS[139] deep learning library, interfaced with the TENSORFLOW[140] library, which led to a consistently good performance.

To distinguish EW $\mathrm{W}^{\pm}\mathrm{W}^{\pm}$ production from the SM background processes before extracting the individual polarizations, a BDT is trained using the TMVA. Input observables are listed in Table A.3, which is named as the $\mathrm{BDT}^{\mathrm{nonVBS}}$. The values of m_{jj} and $\Delta\eta_{\mathrm{jj}}$ are powerful because VBS topologies.

Table A.2 List and description of all the input variables for the signal BDT trainings.

Variables	**Definitions**
$\Delta\phi_{\mathrm{jj}}$	Difference in azimuthal angle between the leading and subleading jets
$p_{\mathrm{T}}^{\mathrm{j1}}$	p_{T} of the leading jet
$p_{\mathrm{T}}^{\mathrm{j2}}$	p_{T} of the subleading jet
$p_{\mathrm{T}}^{\ell_1}$	Leading lepton p_{T}
$p_{\mathrm{T}}^{\ell_2}$	Subleading lepton p_{T}
$\Delta\phi_{\ell\ell}$	Difference in azimuthal angle between the two leptons
$m_{\ell\ell}$	Dilepton mass
$p_{\mathrm{T}}^{\ell\ell}$	Dilepton p_{T}
$m_{\mathrm{T}}^{\mathrm{WW}}$	Transverse WW diboson mass
$\mathcal{Z}_{\ell_1}$	Zeppenfeld variable of the leading lepton
$\mathcal{Z}_{\ell_2}$	Zeppenfeld variable of the subleading lepton
$\Delta R_{\mathrm{j1},\ell\ell}$	ΔR between the leading jet and the dilepton system
$\Delta R_{\mathrm{j2},\ell\ell}$	ΔR between the subleading jet and the dilepton system
$(p_{\mathrm{T}}^{\ell_1} p_{\mathrm{T}}^{\ell_2})/(p_{\mathrm{T}}^{\mathrm{j1}} p_{\mathrm{T}}^{\mathrm{j2}})$	Ratio of p_{T} products between leptons and jets
$p_{\mathrm{T}}^{\mathrm{miss}}$	Missing transverse momentum

Table A.3 List and description of the input variables for the inclusive BDT training.

Variables	**Definitions**
m_{jj}	Dijet mass
$\Delta\eta_{\mathrm{jj}}$	Difference in pseudorapidity between the leading and subleading jets
$\Delta\phi_{\mathrm{jj}}$	Difference in azimuth angles between the leading and subleading jets
$p_{\mathrm{T}}^{\mathrm{j1}}$	p_{T} of the leading jet
$p_{\mathrm{T}}^{\mathrm{j2}}$	p_{T} of the subleading jet
$p_{\mathrm{T}}^{\ell_1}$	Leading lepton p_{T}
$p_{\mathrm{T}}^{\ell\ell}$	Dilepton p_{T}
$\mathcal{Z}_{\ell_1}$	Zeppenfeld variable of the leading lepton
$\mathcal{Z}_{\ell_2}$	Zeppenfeld variable of the subleading lepton
$p_{\mathrm{T}}^{\mathrm{miss}}$	Missing transverse momentum

A.5 Additional materials for probing Majorana neutrinos and Weinberg Operator in $\mathrm{pp} \to \mu^{\pm}\mu^{\pm}jj$

A.5.1 Selection optimization

In order to optimize the selections, punzi significance is calculated as follows:

$$Punzi\_significance = 0.7 \times n_{signal}/\sqrt{n_{background}+1}. \tag{A.1}$$

Scan 20 m_{jj} thresholds are scanned from 0 GeV to 900 GeV in signal region, the Punzi significance distributions are shown in Figure A.1. For most of the heavy Majorana neutrino processes, the Punzi significance gets larger when m_{jj} threshold gets larger. But for Weinberg Operator process, the Punzi significance is largest when $m_{\mathrm{jj}} > 750$ GeV. So the m_{jj} threshold is set to 750 GeV.

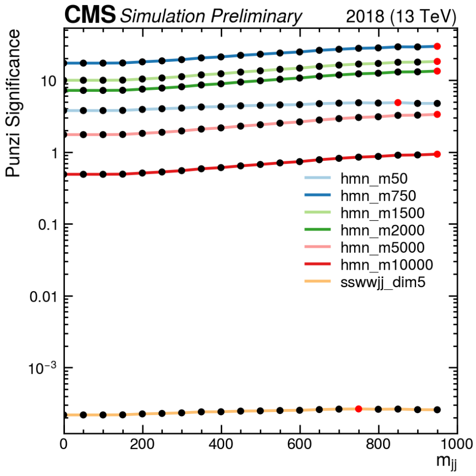

Figure A.1 Punzi significance for different m_{jj} thresholds.

A.5.2 Apply $p_{\mathrm{T}}^{\mathrm{miss}}$ cut in signal region

Unlike the SM W±W± VBS process, the Weinberg Operator process does not contain outgoing neutrinos. From the $p_{\mathrm{T}}^{\mathrm{miss}}$ distributions in Figure A.2, the Weinberg Operator signal events are most in low $p_{\mathrm{T}}^{\mathrm{miss}}$ region.

No $p_{\mathrm{T}}^{\mathrm{miss}}$ cut, $p_{\mathrm{T}}^{\mathrm{miss}} < 50$ GeV and $p_{\mathrm{T}}^{\mathrm{miss}} < 100$ GeV are tested in signal region. For $p_{\mathrm{T}}^{\mathrm{miss}} <$ 50 GeV, the $H_{\mathrm{T}}/p_{\mathrm{T}}^{\ell 1}$ distributions are in Figure A.3.

With m_{jj} in control regions, we got expected scales as heavy as Λ=4.5 (4.7) TeV, when no $p_{\mathrm{T}}^{\mathrm{miss}}$ cut ($p_{\mathrm{T}}^{\mathrm{miss}} < 100$ GeV). The related effective $\mu\mu$ Majorana masses of $|m_{\mu\mu}|$ are in Table A.4 and Figure A.4. We decide to use $p_{\mathrm{T}}^{\mathrm{miss}} < 50$ GeV in the final result as it gives stringent upper limits.

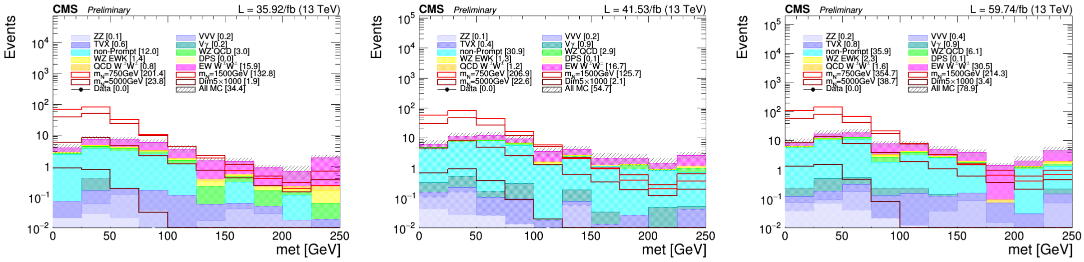

Figure A.2 $p_{\mathrm{T}}^{\mathrm{miss}}$ distributions in signal region for each year.

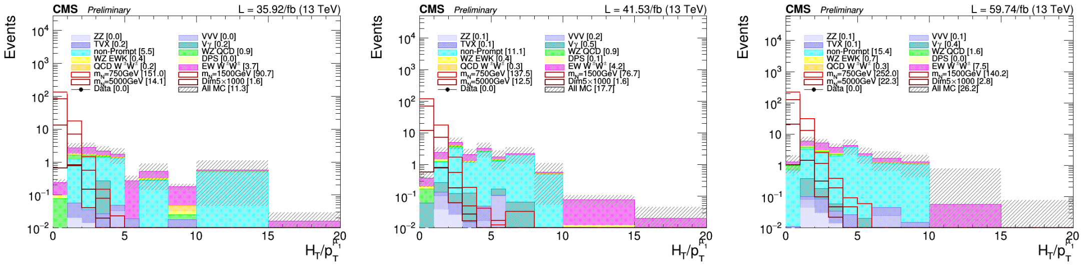

Figure A.3 $H_{\mathrm{T}}/p_{\mathrm{T}}^{\ell 1}$ distributions in signal region for each year.

Table A.4 Expected upper limits for effective $\mu\mu$ Majorana mass of $|m_{\mu\mu}|$ in GeV 5.3 with different $p_{\mathrm{T}}^{\mathrm{miss}}$ cuts.

$p_{\mathrm{T}}^{\mathrm{miss}}$ **cut in SR**	**Expected**	$\pm 1\sigma$	$\pm 2\sigma$
no $p_{\mathrm{T}}^{\mathrm{miss}}$ cut	13.48	[11.2,16.4]	[9.57,19.52]
$p_{\mathrm{T}}^{\mathrm{miss}} < 50$ GeV	12.2	[9.98,15.06]	[8.43,18.17]
$p_{\mathrm{T}}^{\mathrm{miss}} < 100$ GeV	12.92	[10.71,15.77]	[9.13,18.89]

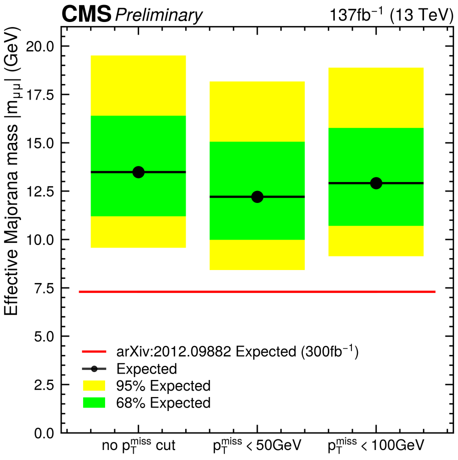

Figure A.4 Effective $\mu\mu$ Majorana mass of $|m_{\mu\mu}|$ with different $p_{\mathrm{T}}^{\mathrm{miss}}$ cuts.

A.5.3 Study of charge flip muons

Dedicated study of change flip of muons is preformed by selecting Z→ $\mu\mu$ events with cuts in Table A.5, the $m_{\ell\ell}$ is not necessary to be around m_Z, since the same sign events are not expected to have a peak around the m_Z. Anti-btagging is used to suppress $t\bar{t}$ contributions.

Table A.5 Selections for charge flip regions, the two muons can be OS or SS.

Variable	**Selections**
leptons	2 muons with p_{T} > 25/25 GeV
3rd lepton veto	applied
$m_{\ell\ell}$	> 60 GeV
Anti-btagging	applied

For the signals, we consider Drell-Yan process, t$\bar{\text{t}}$ $\rightarrow$ $ll\nu\nu$, tW and W$^+$W$^-$. The backgrounds are EW W$^\pm$W$^\pm$, VZ, VVV, Vγ, higgs processes (ggH, VBF H, VH), tZq, ttV and non-prompt. There are three muon p_{T} bins (25,100) GeV, (100,200) GeV, (200, inf) GeV, so there are 6 sub regions because of the combinations of leading and trailing leptons' p_{T}.

The non-prompt background is data-driven, but in opposite sign DY control regions, the data-driven non-prompt background is replaced by Wjets. Because data-driven non-prompt background doesn't perform well in such prompt lepton enhanced regions, it gives negative yields sometimes. The non-prompt is not important in OS regions, only very small effects on the charge flip rates of data and scale factors.

The $m_{\ell\ell}$ distributions of 2016 are shown for each sub region with opposite sign selection in Figure A.5 and with same sign selection in Figure A.6.

The $m_{\ell\ell}$ distributions of 2017 are shown for each sub region with opposite sign selection in Figure A.7 and with same sign selection in Figure A.8.

The $m_{\ell\ell}$ distributions of 2018 are shown for each sub region with opposite sign selection in Figure A.9 and with same sign selection in Figure A.10.

We count the number of opposite sign events n$_{OS}$ and the number of same sign events n$_{OS}$ in each sub region. We note charge flip rate as ϵ_{p_T}, which is as a function of lepton p_{T}. So for di-lepton events, the charge flip probability $prob_{p_T^{l1},p_T^{l2}}$ is:

$$prob_{p_T^{l1},p_T^{l2}} = \epsilon_{p_T^{l1}} \times (1 - \epsilon_{p_T^{l2}}) + (1 - \epsilon_{p_T^{l1}}) \times \epsilon_{p_T^{l2}} = \frac{n_{SS}}{n_{SS} + n_{OS}} \tag{A.2}$$

To calculate the ratio $\frac{n_{SS}}{n_{SS}+n_{OS}}$ of MC, the n_{SS} and n_{OS} are from simulations. For data, we get the yields scale factor in A.2 firstly, the statistical uncertainties for simulation samples are considered, for data-driven background non-prompt a flat 30% uncertainty is applied. We assume the signal events in data (n^{sig}_{Data}) is the product sf$_{\text{Yields}}$ $\times$ n^{sig}_{MC}. In this way, we get n_{SS} and n_{OS} for data.

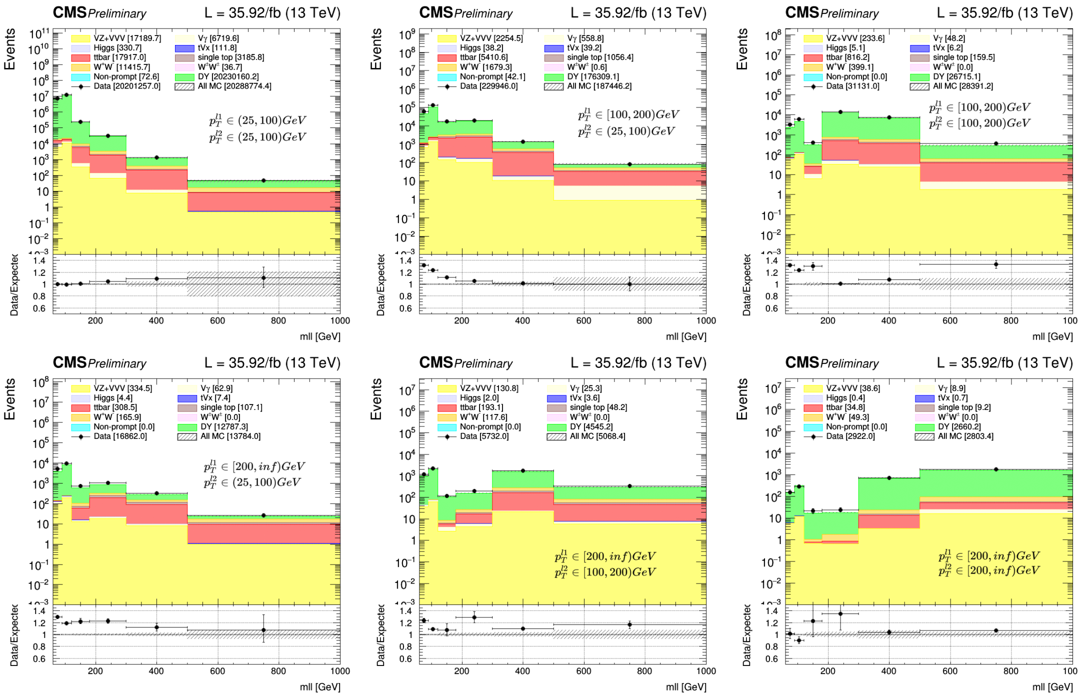

Figure A.5 $m_{\ell\ell}$ distributions of 2016 OS events for different lepton p_{T} selections in (25,100), (100,200),(200,inf) GeV.

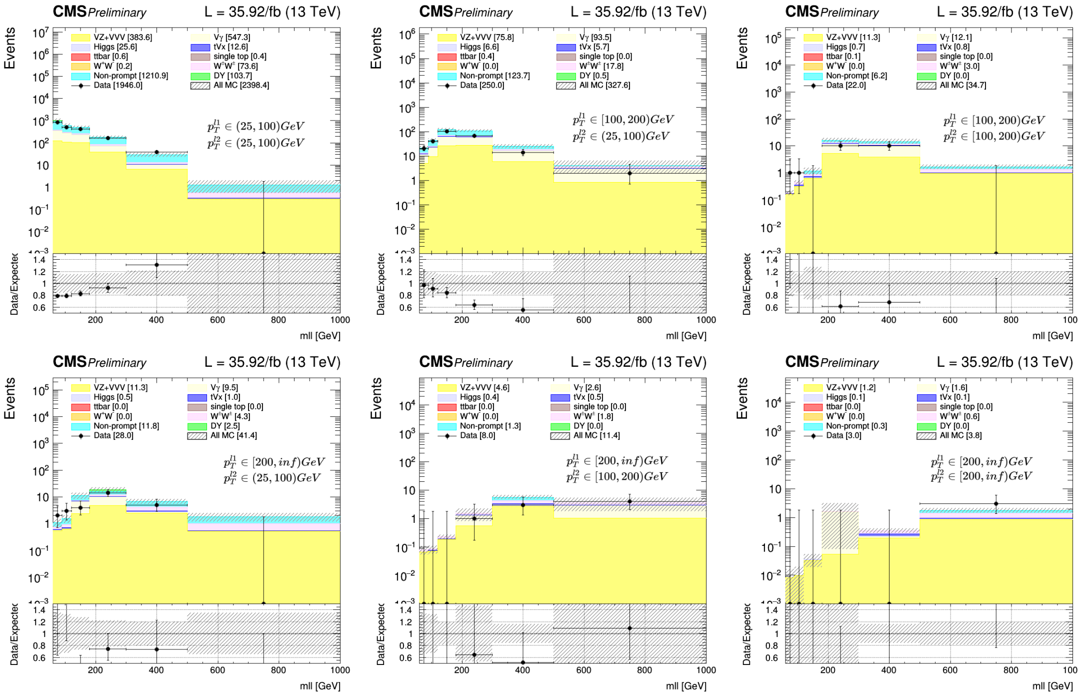

Figure A.6 $m_{\ell\ell}$ distributions of 2016 SS events for different lepton p_{T} selections in (25,100), (100,200),(200,inf) GeV.

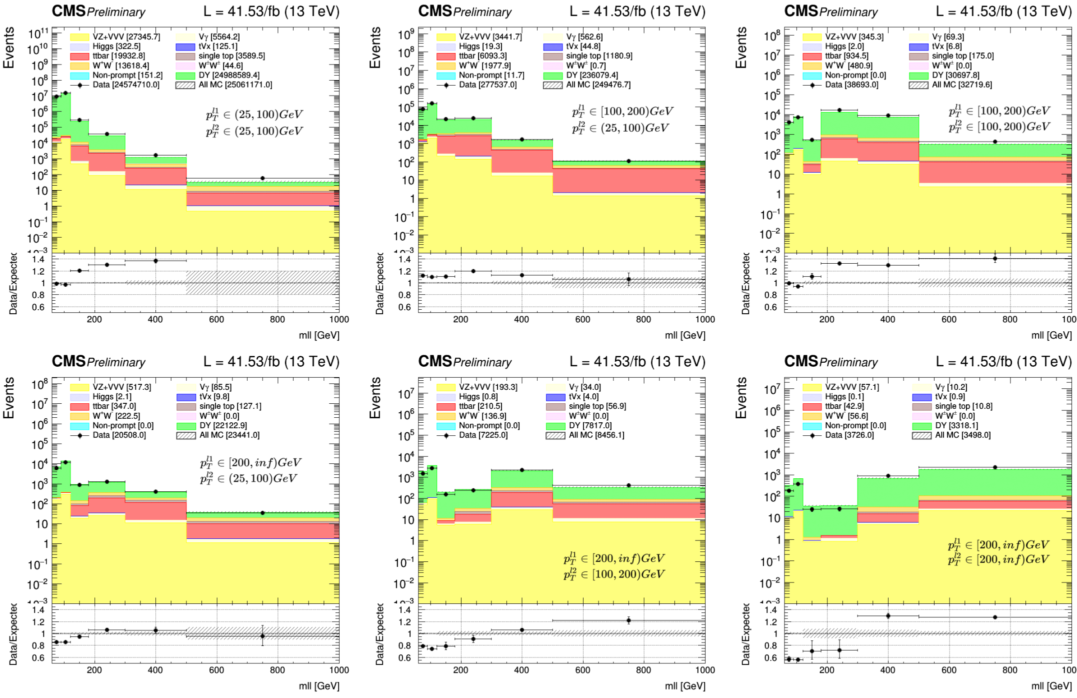

Figure A.7 $m_{\ell\ell}$ distributions of 2017 OS events for different lepton p_{T} selections in (25,100), (100,200), (200,inf) GeV.

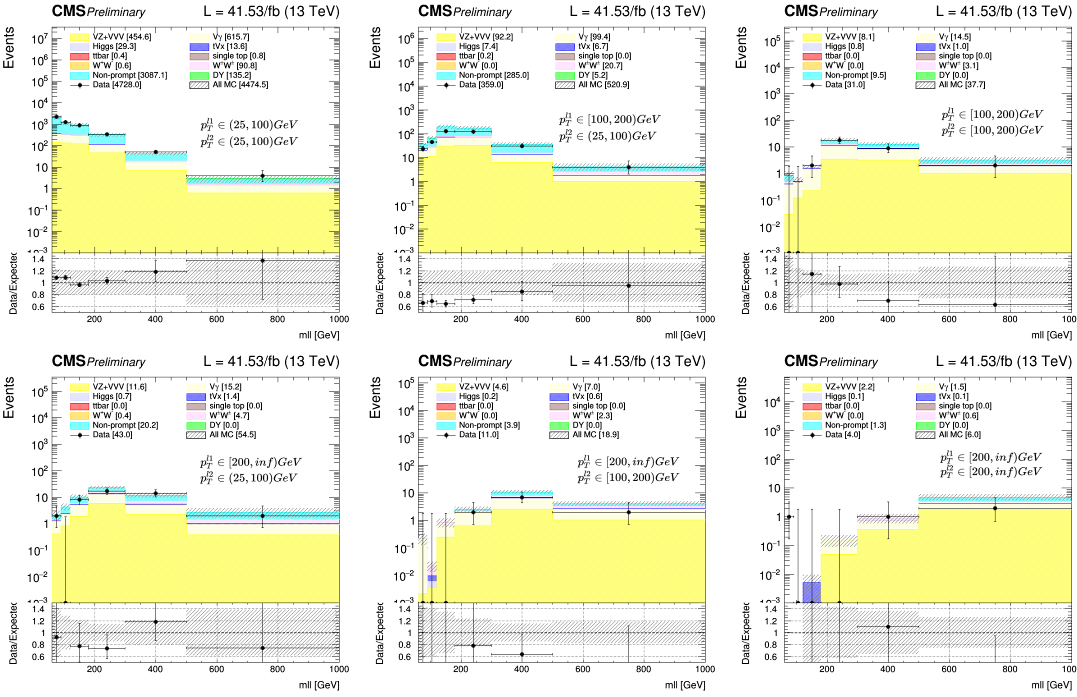

Figure A.8 $m_{\ell\ell}$ distributions of 2017 SS events for different lepton p_{T} selections in (25,100), (100,200), (200,inf) GeV.

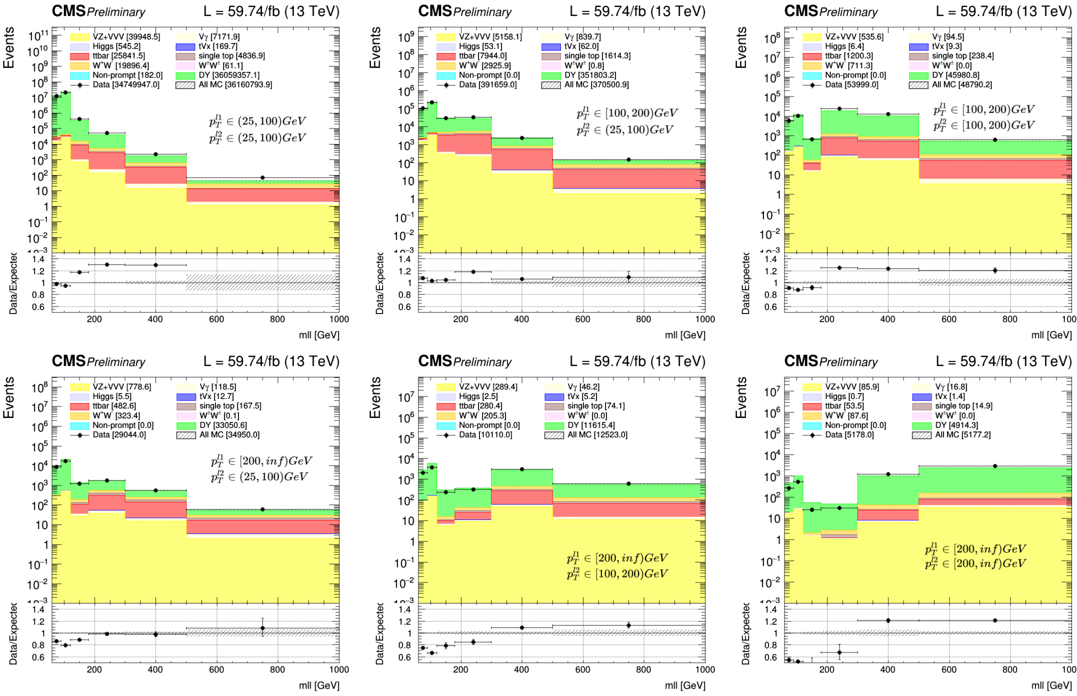

Figure A.9 $m_{\ell\ell}$ distributions of 2018 OS events for different lepton p_{T} selections in (25,100), (100,200), (200,inf) GeV.

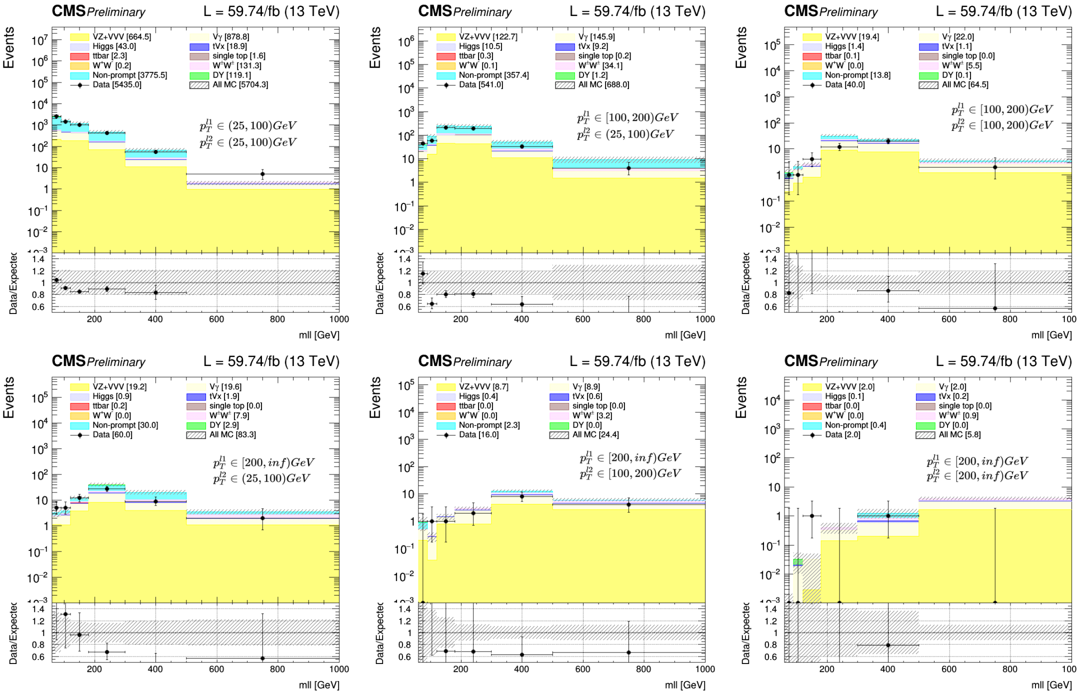

Figure A.10 $m_{\ell\ell}$ distributions of 2018 SS events for different lepton p_{T} selections in (25,100), (100,200), (200,inf) GeV.

$$\mathrm{sf}_{\mathrm{Yields}} = n_{Data}/n_{MC} \tag{A.3}$$

Then we plot the ratios $\frac{n_{SS}}{n_{SS}+n_{OS}}$ in 1D histograms, as shown in Figure A.11.

We fit to 6 bins in Figure A.11 for each year with three parameters simultaneously, each parameter represents the charge flip rate of different muon p_{T} bins. The charge flip rate in MC and in data and the scale factors for each year are in Table A.6. Because of low statistics, the charge flip rate of muons with $p_{\mathrm{T}} \in$ (200,inf) GeV have large error.

Table A.6 Charge flip rate of muons and scale factor between data and MC.

Year	p_{T} **range**	**MC**	**data**	**sf**
2016	(25,100) GeV	$2.63 \times 10^{-06} \pm 4.45 \times 10^{-07}$	$2.12 \times 10^{-06} \pm 4.63 \times 10^{-07}$	0.81 ± 0.22
	(100,200) GeV	$1.13 \times 10^{-06} \pm 8.47 \times 10^{-07}$	$5.70 \times 10^{-07} \pm 5.25 \times 10^{-07}$	0.50 ± 0.60
	(200,inf) GeV	$1.85 \times 10^{-04} \pm 1.83 \times 10^{-04}$	$1.02 \times 10^{-04} \pm 1.05 \times 10^{-04}$	0.55 ± 0.79
2017	(25,100) GeV	$2.72 \times 10^{-06} \pm 3.53 \times 10^{-07}$	$3.00 \times 10^{-06} \pm 7.15 \times 10^{-07}$	1.10 ± 0.30
	(100,200) GeV	$2.22 \times 10^{-07} \pm 2.15 \times 10^{-07}$	$1.55 \times 10^{-07} \pm 1.54 \times 10^{-07}$	0.70 ± 0.97
	(200,inf) GeV	$1.55 \times 10^{-05} \pm 1.55 \times 10^{-05}$	$1.35 \times 10^{-05} \pm 1.56 \times 10^{-05}$	0.87 ± 1.34
2018	(25,100) GeV	$1.72 \times 10^{-06} \pm 2.60 \times 10^{-07}$	$1.73 \times 10^{-06} \pm 4.14 \times 10^{-07}$	1.01 ± 0.29
	(100,200) GeV	$1.45 \times 10^{-06} \pm 8.29 \times 10^{-07}$	$9.15 \times 10^{-07} \pm 5.12 \times 10^{-07}$	0.63 ± 0.50
	(200,inf) GeV	$8.49 \times 10^{-07} \pm 9.43 \times 10^{-07}$	$4.28 \times 10^{-07} \pm 4.57 \times 10^{-07}$	0.50 ± 0.78

By applying the charge flip rate of 2016 and 2018 in the signal regions in Table A.6, the expected $H_{\mathrm{T}}/p_{\mathrm{T}}^{\ell 1}$ distributions are in Figure A.12, A.13, the wrong-sign contributions are tiny, can be negligible.

A.6 Additional materials for measurements of Wγ

A.6.1 Fake Photon Fraction and Weights Calculation

Figure A.14 through Figure A.16 are fitting plots in $|\eta| < 1$.

The resulting fake photon fractions for 2017, 2018 are in Tables A.7, A.8.Tables A.9, A.10 shows the extrapolation factors from the fakeable object photon selection to the tight photon selection of 2017 and 2018.

Table A.7 Fake photon fractions calculated from data for 2017.

η **range**	$20 < p_{\mathrm{T}} < 30\,\mathbf{GeV}$	$30 < p_{\mathrm{T}} < 40\,\mathbf{GeV}$	$40 < p_{\mathrm{T}} < 50\,\mathbf{GeV}$	$50\,\mathbf{GeV} < p_{\mathrm{T}}$
$\lvert\eta\rvert < 1$	0.406	0.165	0.124	0.101
$1 < \lvert\eta\rvert < 1.5$	0.397	0.167	0.141	0.127
$1.5 < \lvert\eta\rvert < 2$	0.311	0.157	0.137	0.108
$2 < \lvert\eta\rvert < 2.5$	0.215	0.111	0.100	0.066

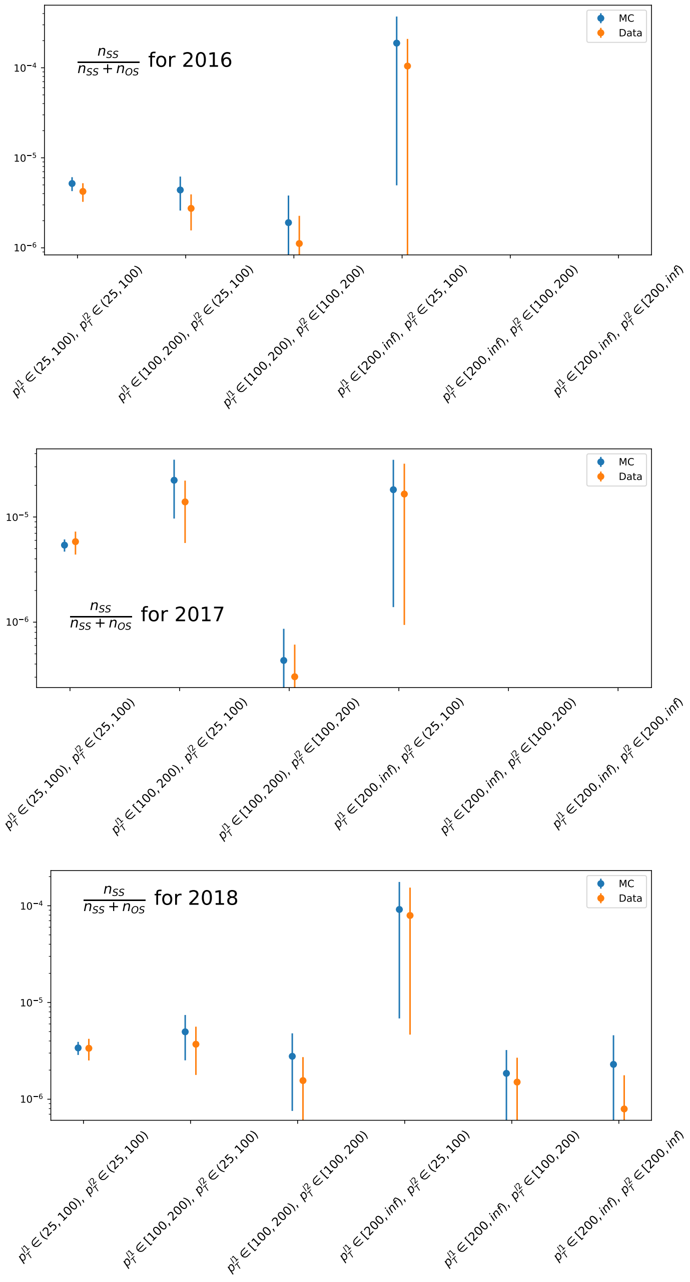

Figure A.11 The ratio $\frac{n_{SS}}{n_{SS}+n_{OS}}$ of 6 sub regions for 2016 (top), 2017 (middle) and 2018 (bottom). For 2016 and 2017 the value of last two bins are 0 due to no signal events.

Table A.8 Fake photon fractions calculated from data for 2018.

η **range**	$20 < p_T < 30$ **GeV**	$30 < p_T < 40$ **GeV**	$40 < p_T < 50$ **GeV**	50 **GeV** $< p_T$
$\lvert\eta\rvert < 1$	0.691	0.735	0.675	0.487
$1 < \lvert\eta\rvert < 1.5$	0.876	0.907	0.836	0.649
$1.5 < \lvert\eta\rvert < 2$	0.414	0.454	0.471	0.532
$2 < \lvert\eta\rvert < 2.5$	0.153	0.201	0.232	0.383

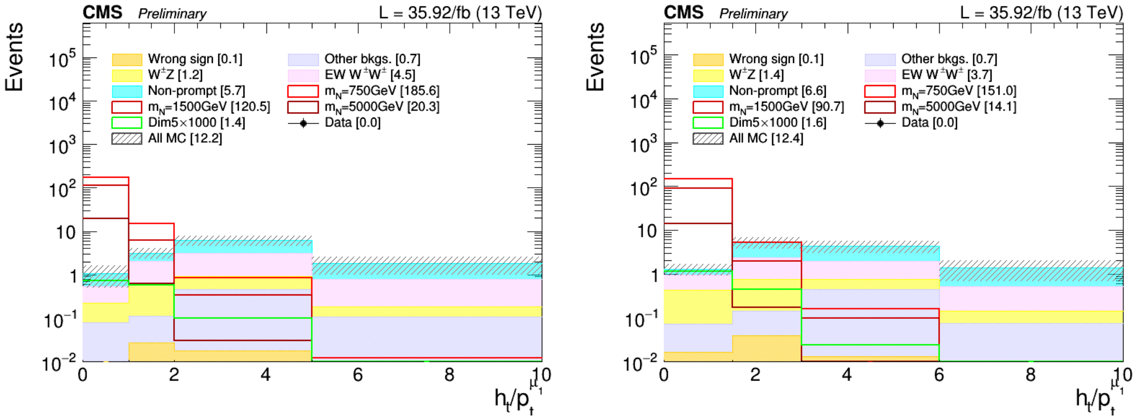

Figure A.12 In 2016, distributions of $H_{\mathrm{T}}/p_{\mathrm{T}}^{\ell 1}$ with wrong-sign component for SR1 (left) and SR2 (right), the wrong-sign contributions are tiny, can be negligible.

Table A.9 Fake photon weights calculated from data for 2017.

η **range**	$20 < p_{\mathrm{T}} < 30$ **GeV**	$30 < p_{\mathrm{T}} < 40$ **GeV**	$40 < p_{\mathrm{T}} < 50$ **GeV**	50 **GeV** $< p_{\mathrm{T}}$
$\lvert\eta\rvert < 1$	0.68	0.72	0.74	0.49
$1 < \lvert\eta\rvert < 1.5$	0.91	0.89	0.81	0.63
$1.5 < \lvert\eta\rvert < 2$	0.44	0.45	0.48	0.52
$2 < \lvert\eta\rvert < 2.5$	0.21	0.25	0.34	0.43

Table A.10 Fake photon weights calculated from data for 2018.

η **range**	$20 < p_{\mathrm{T}} < 30$ **GeV**	$30 < p_{\mathrm{T}} < 40$ **GeV**	$40 < p_{\mathrm{T}} < 50$ **GeV**	50 **GeV** $< p_{\mathrm{T}}$
$\lvert\eta\rvert < 1$	0.69	0.73	0.68	0.49
$1 < \lvert\eta\rvert < 1.5$	0.88	0.91	0.84	0.65
$1.5 < \lvert\eta\rvert < 2$	0.41	0.45	0.47	0.53
$2 < \lvert\eta\rvert < 2.5$	0.15	0.20	0.23	0.38

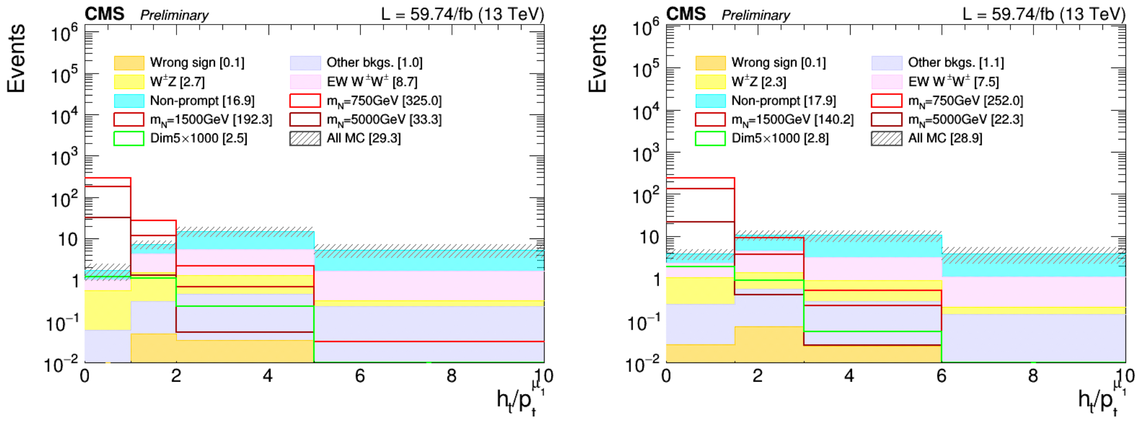

Figure A.13　In 2018, distributions of $H_T/p_T^{\ell 1}$ with wrong-sign component for SR1 (left) and SR2 (right), the wrong-sign contributions are tiny, can be negligible.

A.6.2　Fake Photon Closure Test

These fake photon event weights are compared to the true fake photon event weights (Tables A.11-A.13), and then the difference is added to the original fake photon event weights from the real data to create the alternative fake photon event weights (Tables A.14-A.16). In other words, the non-closure are added from a closure test to the nominal weights.

Table A.11　Fitted/true fake photon event weights for 2016.

η **range**	$20 < p_T < 30$ **GeV**	$30 < p_T < 40$ **GeV**	$40 < p_T < 50$ **GeV**	50 **GeV** $< p_T$
$\lvert\eta\rvert < 1$	0.69/0.79	0.75/0.78	0.62/0.81	0.40/0.56
$1 < \lvert\eta\rvert < 1.5$	0.84/0.91	0.84/1.32	0.82/0.96	0.57/1.13
$1.5 < \lvert\eta\rvert < 2$	1.14/0.91	0.98/1.32	1.37/0.96	0.87/1.13
$2 < \lvert\eta\rvert < 2$	0.78/0.59	0.56/1.10	0.97/1.54	1.12/1.58

Table A.12　Fitted/true fake photon event weights for 2017.

η **range**	$20 < p_T < 30$ **GeV**	$30 < p_T < 40$ **GeV**	$40 < p_T < 50$ **GeV**	50 **GeV** $< p_T$
$\lvert\eta\rvert < 1$	0.66/0.61	0.81/0.61	0.77/0.85	0.59/0.62
$1 < \lvert\eta\rvert < 1.5$	0.99/0.95	1.09/1.02	0.72/1.25	0.74/0.87
$1.5 < \lvert\eta\rvert < 2$	0.52/0.76	0.62/0.83	0.69/0.95	0.80/0.94
$2 < \lvert\eta\rvert < 2.5$	0.21/0.43	0.31/0.52	0.25/0.49	0.74/0.97

The per-fake photon weight variations for the second component are reported in Tables A.17-A.19.

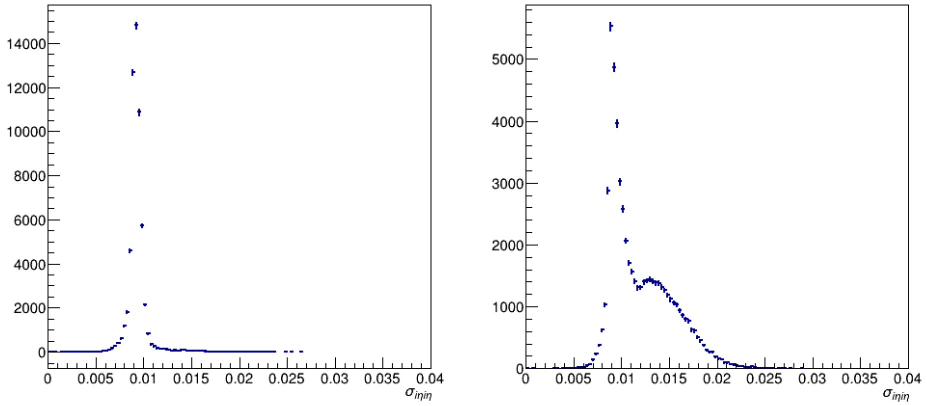

(a) Real photon template (b) Fake photon template

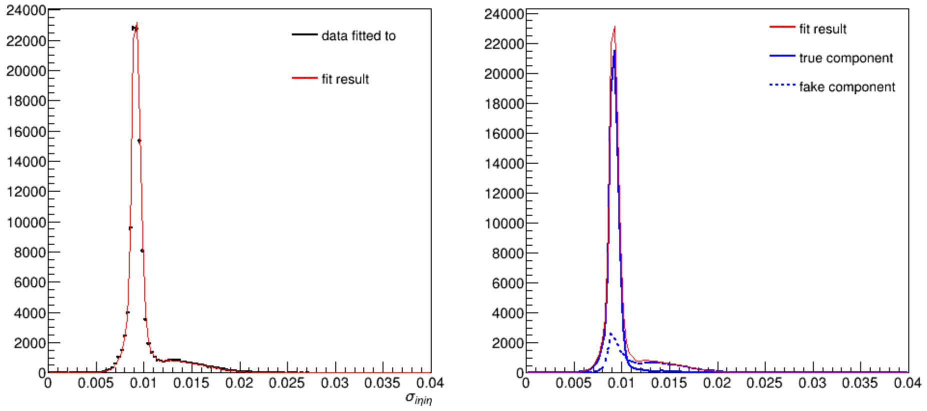

(c) Comparison between data and total fit (d) True and fake component after fitting

Figure A.14 Figures related to the fake photon fraction calculation for $|\eta| < 1$ range and p_{T} bin 30 to 40 GeV.

Table A.13 Fitted/true fake photon event weights for 2018.

η **range**	$20 < p_{\mathrm{T}} < 30\,\mathbf{GeV}$	$30 < p_{\mathrm{T}} < 40\,\mathbf{GeV}$	$40 < p_{\mathrm{T}} < 50\,\mathbf{GeV}$	$50\,\mathbf{GeV} < p_{\mathrm{T}}$
$\lvert\eta\rvert < 1$	0.77/0.74	0.86/0.73	0.78/0.66	0.51/0.70
$1 < \lvert\eta\rvert < 1.5$	0.99/0.94	1.03/1.39	0.56/0.86	0.51/0.67
$1.5 < \lvert\eta\rvert < 2$	0.50/0.81	0.54/0.79	0.55/0.53	0.67/0.77
$2 < \lvert\eta\rvert < 2.5$	0.21/0.35	0.29/0.51	0.17/0.64	0.16/0.60

Table A.14 Alternative fake photon event weights for component 1 for 2016.

η **range**	$20 < p_{\mathrm{T}} < 30\,\mathbf{GeV}$	$30 < p_{\mathrm{T}} < 40\,\mathbf{GeV}$	$40 < p_{\mathrm{T}} < 50\,\mathbf{GeV}$	$50\,\mathbf{GeV} < p_{\mathrm{T}}$
$\lvert\eta\rvert < 1$	0.79	0.68	0.74	0.55
$1 < \lvert\eta\rvert < 1.5$	0.93	1.32	0.89	1.10
$1.5 < \lvert\eta\rvert < 2$	0.90	1.47	0.61	1.24
$2 < \lvert\eta\rvert < 2.5$	0.49	1.28	1.35	1.34

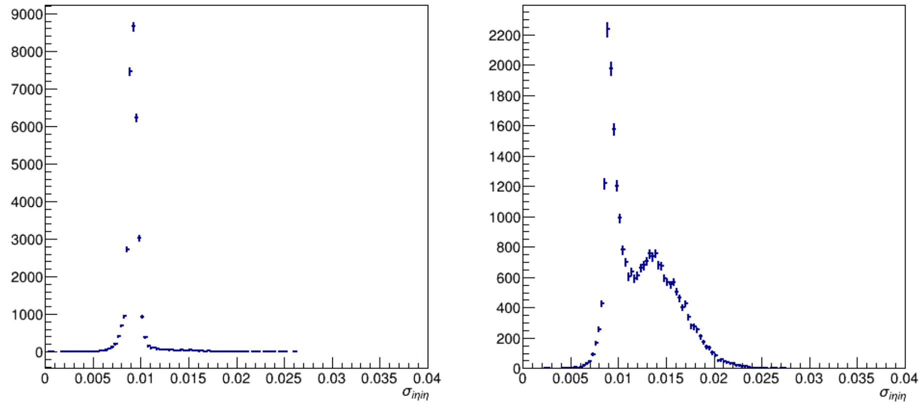

(a) Real photon template (b) Fake photon template

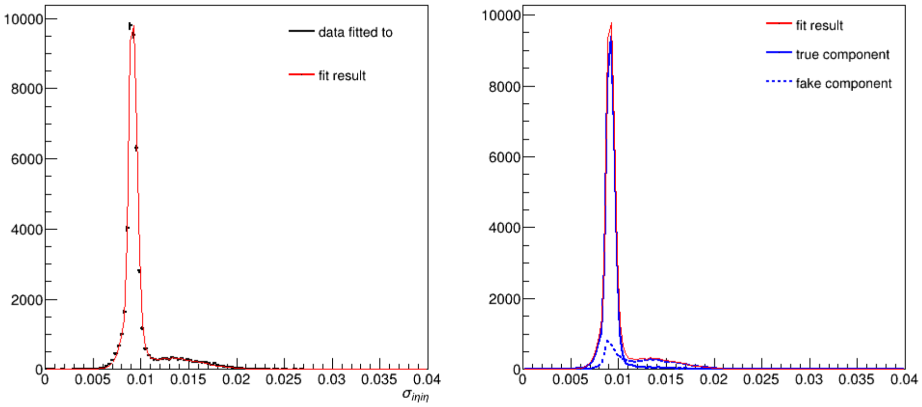

(c) Comparison between data and total fit (d) True and fake component after fitting

Figure A.15 Figures related to the fake photon fraction calculation for $|\eta| < 1$ and p_{T} bin 40 to 50 GeV.

Table A.15 Alternative fake photon event weights for component 1 for 2017.

η **range**	$20 < p_{\mathrm{T}} < 30$ **GeV**	$30 < p_{\mathrm{T}} < 40$ **GeV**	$40 < p_{\mathrm{T}} < 50$ **GeV**	50 **GeV** $< p_{\mathrm{T}}$
$\lvert\eta\rvert < 1$	0.63	0.51	0.72	0.52
$1 < \lvert\eta\rvert < 1.5$	0.87	0.81	1.33	0.77
$1.5 < \lvert\eta\rvert < 2$	0.67	0.66	0.74	0.67
$2 < \lvert\eta\rvert < 2.5$	0.43	0.46	0.58	0.66

Table A.16 Alternative fake photon event weights for component 1 for 2018.

η **range**	$20 < p_{\mathrm{T}} < 30$ **GeV**	$30 < p_{\mathrm{T}} < 40$ **GeV**	$40 < p_{\mathrm{T}} < 50$ **GeV**	50 **GeV** $< p_{\mathrm{T}}$
$\lvert\eta\rvert < 1$	0.66	0.61	0.56	0.68
$1 < \lvert\eta\rvert < 1.5$	0.82	1.27	1.13	0.80
$1.5 < \lvert\eta\rvert < 2$	0.73	0.71	0.44	0.64
$2 < \lvert\eta\rvert < 2.5$	0.30	0.42	0.70	0.82

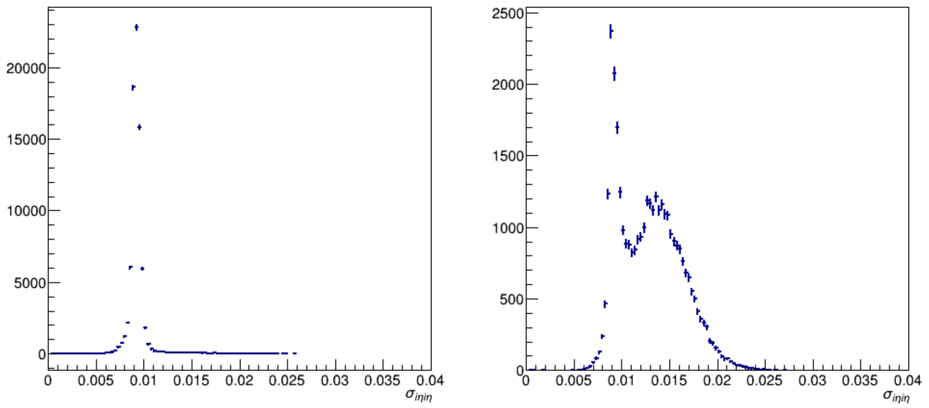

(a) Real photon template (b) Fake photon template

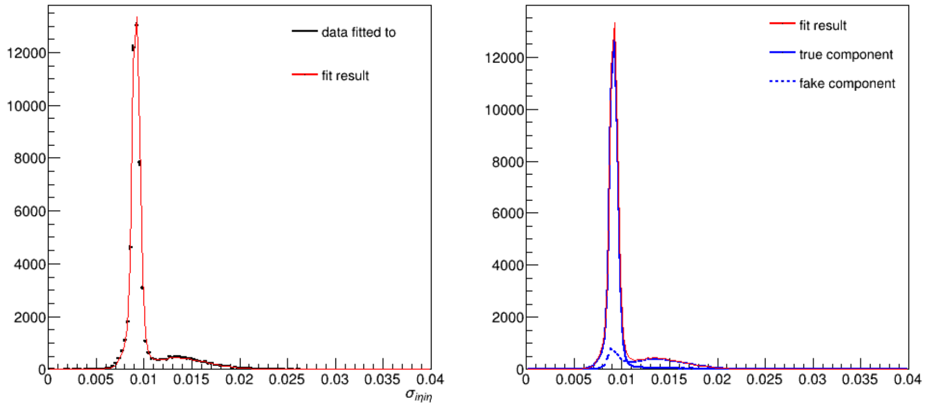

(c) Comparison between data and total fit (d) True and fake component after fitting

Figure A.16 Figures related to the fake photon fraction calculation for $|\eta| < 1$ and p_T bin > 50 GeV.

Table A.17 Alternative fake photon event weights for component 2 for 2016.

η **range**	$20 < p_T < 30$ **GeV**	$30 < p_T < 40$ **GeV**	$40 < p_T < 50$ **GeV**	50 **GeV** $< p_T$
$\lvert\eta\rvert < 1$	0.72	0.69	0.57	0.40
$1 < \lvert\eta\rvert < 1.5$	0.87	0.85	0.76	0.54
$1.5 < \lvert\eta\rvert < 2$	1.15	1.14	1.03	0.98
$2 < \lvert\eta\rvert < 2.5$	0.70	0.75	0.80	0.89

Table A.18 Alternative fake photon event weights for component 2 for 2017.

η **range**	$20 < p_T < 30$ **GeV**	$30 < p_T < 40$ **GeV**	$40 < p_T < 50$ **GeV**	50 **GeV** $< p_T$
$\lvert\eta\rvert < 1$	0.72	0.75	0.67	0.51
$1 < \lvert\eta\rvert < 1.5$	0.93	0.90	0.82	0.64
$1.5 < \lvert\eta\rvert < 2$	0.46	0.47	0.50	0.55
$2 < \lvert\eta\rvert < 2.5$	0.23	0.27	0.37	0.47

Table A.19 Alternative fake photon event weights for component 2 for 2018.

η **range**	$20 < p_\mathrm{T} < 30$ **GeV**	$30 < p_\mathrm{T} < 40$ **GeV**	$40 < p_\mathrm{T} < 50$ **GeV**	50 **GeV** $< p_\mathrm{T}$
$\lvert\eta\rvert < 1$	0.73	0.77	0.70	0.50
$1 < \lvert\eta\rvert < 1.5$	0.90	0.93	0.85	0.66
$1.5 < \lvert\eta\rvert < 2$	0.43	0.47	0.49	0.56
$2 < \lvert\eta\rvert < 2.5$	0.16	0.22	0.25	0.42

Acknowledgement

As the five-year Ph.D. comes to an end, it is only the beginning, and the author still hopes to continue swimming in the ocean of physics. However, let him stop for a moment and reflect on what he has learned over the past five years.

The author could not have made it this far without all of those who have cared for him, helped him, and guided him over the past five years. He would like to thank all the teachers and students in the High Energy Experiment Group at Peking University, especially his supervisor, Prof. Qiang Li. Prof. Li is very knowledgeable and quick thinking and has been the author's research role model. Prof. Li can always think of exciting topics, and the author felt the joy of research. When the author encountered difficulties, Prof. Li always guided him carefully and patiently to solve the problems. He probably would not have wanted to continue his research without Qiang as his guide. Of course, there are so many people the author would like to thank for the family of Peking University High Energy Experiment Group. Thanks to Dr. Andrew M. Levin, without Andrew's patience and meticulous help, the author would not have been able to complete his analysis. The author would like to thank Meng Lu and Linwei Li for guiding him in his research, and of course, the author would like to thank them for inviting him to dinner from time to time. The author also thanks to his classmates Ying An and Yunxuan Song for their motivation, which has helped the author a lot in his study. Without their supervision, the author might not have finished his thesis yet. The author also thanks Guan Zhe for helping to generate samples and Congqiao Li for teaching him to use advanced analysis tools. The author is incredibly grateful to Sitian Qian. Sitian perfectly illustrated what it means to help a senior graduate. Sitian's intelligence has assisted the author in research and life without fail and has taught him to communicate more with people.

The author would also like to thank Prof. Pietro Govoni and Dr. Andrea Massironi for their careful guidance during his exchange in Milan. He does not know when he would have finished the first analysis without them. Of course, they have helped the author a lot in his studies and his life. He still remembers the food that Andrea recommended to him. He still remembers Pietro driving him to his place when the epidemic was severe. Although there was the shadow of the epidemic for most of his time in Milan, the author still witnessed Italy winning the European Cup. He also attended the first major offline-oriented meeting of the High Energy Physics Experiment since the outbreak, MBI2021, which would not have been

possible without the efforts and dedication of Pietro, Andrea, and the rest of the faculty and students at the University of Milan-Bicocca. The author is also grateful to Davide Valsecchi for helping him with machine learning.

The author is very grateful to everyone he met in Milan. Also, he knows his friends in Milan, such as Zhimeng Hu, Hongsheng Liu, Jiefeng Bi, Xin Zhang. During the epidemic, especially Zhimeng took good care of the author, and he missed the time to have dinner and talk with him. He is also thankful to Bi Jiefeng for listening to him from time to time and relieving his frustration. The author is also thrilled to have formed a vacation team with Jiefeng Bi and Xin Zhang. He was able to go to Venice for nice ice cream and a break after a long home life of studying, and he hopes there will be another time.

Of course, the author is also very grateful to his family, parents, grandparents, and uncle. Without their care, he would not be who he is today. He also thanks to his sister's family for talking with him from time to time, and he wishes them all happiness.

Finally, the author also thanks the anime ”Yuru Camp” for the warmth it passed on to him and for making him understand that sometimes people are alone, but their hearts are with people who care. It is time to plan the first camping trip. Well, he will stop there.